Numerical Simulation of the Precipitation Kinetics of Nitrides and Carbides in Microalloyed Steel

By

Dipl.-Ing. Rene Radis

Christian Doppler Laboratory 'Early Stages of Precipitation'

Vienna University of Technology

Univ. Prof. Dipl.-Ing. Dr. techn. Ernst Kozeschnik

Institute for Materials Science and Welding

Graz University of Technology

Univ. Prof. Dipl.-Ing. Dr. techn. Christof Sommitsch

A dissertation submitted for the degree

'Doktor der technischen Wissenschaften'

at the Faculty of Mechanical Engineering

GRAZ UNIVERSITY OF TECHNOLOGY

Graz, August 10, 2010

'Prediction is very difficult, especially about the future.'

Nils Bohr (1885-1962), Nobel laureate in Physics (1922)

'Everything should be made as simple as possible, but not simpler.'

Albert Einstein (1879-1955), Nobel laureate in Physics (1921)

for Mary

Preface

The present work is submitted for the degree 'Doktor der technischen Wissenschaften' at the 'Faculty of Mechanical Engineering' of the 'Graz University of Technology'. The work was carried out in the frame of the project 'Modelling and simulation of the early stages of precipitation of second phase particles in technically relevant structural high-performance materials' which was part of module B in the Christian Doppler Laboratory 'Early Stages of Precipitation'. The project was realised in the time between November 2007 and October 2010 under the supervision of Prof. Ernst Kozeschnik. It was financed by the 'Christian Doppler Forschungsgesellschaft (CDG)'.

I declare that I have authored this thesis independently, that I have not used other than the declared sources/resources, and that I have explicitly marked all material which has been quoted either literally or by content from the used sources.

Rene Radis

Graz, August 10, 2010

List of Publications

The author of this dissertation was also author or co-author of several papers, published during his time as a PhD student. The following list shows the references of these papers, which cover investigations on microalloyed steels, nickel-based superalloys and maraging steels.

Refereed Journal Publications:

1. R. Radis and E. Kozeschnik. Concurrent Precipitation of AlN and VN in Microalloyed Steel. *Steel Research International*, 81:681-685, 2010.

2. R. Radis and E. Kozeschnik. Kinetics of AlN Precipitation in Microalloyed Steel. *Modelling and Simulation in Materials Science and Engineering*, 18(055003):1-16, 2010.

3. R. Radis, G. A. Zickler, M. Stockinger, C. Sommitsch and E. Kozeschnik. Interaction of the Precipitation Kinetics of δ and γ' Phases in Nickel-Base Superalloy ATI Allvac®718Plus™. *Materials Science Forum*, 638-642:2712-2717, 2010.

4. R. Radis and E. Kozeschnik. Precipitation Kinetics of Aluminium Nitride in Austenite in Microalloyed HSLA Steels. *Materials Science Forum*, 636-637:605-611, 2010.

5. R. Radis, M. Schaffer, M. Albu, G. Kothleitner, P. Pölt and E. Kozeschnik. Multi-Modal Size Distributions of γ' Precipitates During Continuous Cooling of UDIMET 720 Li. *Acta Materialia*, 57:5739-5747, 2009.

6. M. Pudar, S. Zamberger, K. Spiradek-Hahn, R. Radis and E. Kozeschnik. Computational Analysis of Precipitation During Continuous Casting of Microalloyed Steel. *Steel Research International*, 81:372-380, 2010.

7. R. Schnitzer, R. Radis, M. Nöhrer, M. Schober, R. Hochfellner, S. Zinner, E. Povoden-Karadeniz, E. Kozeschnik and H. Leitner. Reverted Austenite in PH 13-8 Mo Maraging Steels. *Materials Chemistry and Physics*, 122:138-145, 2010.

8. G. A. Zickler , R. Radis, R. Schnitzer, E. Kozeschnik, M. Stockinger and H. Leitner. The Precipitation Behavior of Superalloy ATI Allvac®718Plus™. *Advanced Engineering Materials*, 12:176-183, 2010.

9. E. Kozeschnik, J. Svoboda, R. Radis and F. D. Fischer. Mean-Field Model for the Growth and Coarsening of Stoichiometric Precipitates at Grain Boundaries. *Modelling and Simulation in Materials Science and Engineering*, 18(015011):1-19, 2010.

10. G. A. Zickler, R. Schnitzer, R. Radis, R. Hochfellner, R. Schweins, M. Stockinger and H. Leitner. Microstructure and Mechanical Properties of the Superalloy ATI Allvac®718Plus™. *Material Science and Engineering A*, 523:295-303, 2009.

Conference Proceedings:

1. R. Radis, G. A. Zickler, M. Stockinger, Ch. Sommitsch and E. Kozeschnik. Numerical Analysis of the Simultaneous Precipitation of δ and γ' Phases in the Ni-Base Superalloy ATI Allvac®.718Plus™, In 7^{th} *International Symposium on Superalloy 718 & Derivatives*, Pittsburgh, Pennsylvania, USA, October 2010, in press.

2. R. Radis and E. Kozeschnik. Kinetics of AlN Precipitation in the Ferrite Phase Field of Microalloyed (HSLA) Steels. In 139^{th} *Annual Meeting & Exhibition TMS, Vol. 2: Materials Characterization, Computation, Modeling and Energy*, pages 341-348, Seattle, Washington, USA, February 2010.

3. R. Radis and E. Kozeschnik. Simulation of Concurrent AlN and VN Precipitation During Thermal Treatment of Microalloyed Steels. In 3^{rd} *International Conference on Simulation and Modelling of Metallurgical Processes in Steelmaking STEEL-SIM*, pages 326-331, Leoben, Austria, September 2009.

4. R. Radis, G. A. Zickler, M. Stockinger, C. Sommitsch and E. Kozeschnik. Interaction of the Precipitation Kinetics of δ and γ' Phases in Nickel-Base Superalloy ATI Allvac®718Plus™. In 6^{th} *International Conference on Processing & Manufacturing of advanced Materials THERMEC*, pages 2712-2717, Berlin, Germany, August 2009.

5. R. Radis and E. Kozeschnik. Numerical Analysis of AlN Precipitation Kinetics in Microalloyed Austenite. In 4^{th} *International Conference ASIA STEEL*, pages 13-24, Busan, South Korea, May 2009.

6. R. Radis and E. Kozeschnik. Precipitation Kinetics of Aluminium Nitride in Austenite in Microalloyed HSLA Steels. In *V International Materials Symposium MATERIAIS*, paper 224 on CD, Lisbon, Portugal, April 2009.

7. R. Radis, M.Schaffer, M. Albu, G. Kothleitner, P. Pölt and Ernst Kozeschnik. Evolution of Size and Morphology of γ' Precipitates in UDIMET 720 Li During Continuous Cooling. In *SUPERALLOYS 11*, pages 829-836, Seven Springs Mountain Resort, Pennsylvania, USA, September 2008.

8. R. Radis und E. Kozeschnik. Die Ausscheidungskinetik von Aluminiumnitrid in mikrolegierten Stählen. In *10. Werkstofftagung - Verarbeitungs- und Gebrauchseigenschaften von Werkstoffen - Heute und Morgen*, pages 89-91, Graz, Austria, March 2008.

9. S. Schwarz, R. Radis, E. Kozeschnik and G. Rumplmair. TEM Investigations of the Precipitation Kinetics of Mn(Cu)S and AlN in Microalloyed Steel. In *MICROSCOPY Conference 2009*, pages 253-254, Graz, Austria, September 2009.

Poster:

1. R. Radis and E. Kozeschnik. Kinetics of AlN Precipitation in the Ferrite Phase Field of Microalloyed (HSLA) Steels. 139^{th} *Annual Meeting & Exhibition TMS*, Seattle, Washington, USA, February 2010.

2. R. Radis and E. Kozeschnik. Simulation of Concurrent AlN and VN Precipitation During Thermal Treatment of Microalloyed Steels. 3^{rd} *International Conference on Simulation and Modelling of Metallurgical Processes in Steelmaking STEEL-SIM*, Leoben, Austria, September 2009.

3. R. Radis, M.Schaffer, M. Albu, G. Kothleitner, P. Pölt and E. Kozeschnik, Evolution of Size and Morphology of γ' Precipitates in UDIMET 720 Li During Continuous Cooling. *SUPERALLOYS 11*, Champion, Pennsylvania, USA, September 2008.

4. S. Schwarz, R. Radis, E. Kozeschnik, G. Rumplmair. TEM Investigations of the Precipitation Kinetics of Mn(Cu)S and AlN in Microalloyed Steel. *MICROSCOPY Conference 2009*, Graz, Austria, September 2009.

Supervised Master Thesis:

1. Ch. Schlacher, *Untersuchung der Versprödung von sprengverfestigten Manganhartstählen*, Graz University of Technology, March 2010.

Acknowledgment

The present work was carried out during my employment as a PhD student at the Christian Doppler Laboratory 'Early Stages of Precipitation' located at the 'Institute for Materials Science and Materials Technology' of the 'Vienna University of Technology'.
I am very grateful to Prof. Ernst Kozeschnik for enabling and supervising the present PhD thesis as well as for numerous interesting discussions while enjoying some beers together. You learned me a lot in these three years, also beside thermodynamics and precipitation kinetics.
I would like to acknowledge Prof. Christof Sommitsch and Em. Prof. Horst Cerjak for the possibility to work at the 'Institute of Materials Science and Welding' of the 'Graz University of Technology'.
I am deeply grateful to Prof. Matthias Militzer and Dr. Mehran Maalekian, who invited me to join their group at the University of British Columbia (UBC) as a scientific scholar. I enjoyed the time in Vancouver very much!
Furthermore, I would like to thank all colleagues from the 'Institute of Materials Science and Welding' in Graz, the Christian Doppler Laboratory 'Early Stages of Precipitation' in Vienna as well as all industrial partners for the good collaboration throughout this project.
Special thanks go to my girlfriend Maria, my family and my friends for their huge support during my time as a PhD student.

Abstract

The present thesis deals with the numerical simulation of the precipitation kinetics of nitrides and carbides during isothermal annealing of (HSLA) microalloyed steel. Therefore the thermodynamic data of the relevant phases are analysed with special emphasis on microalloyed steel and implemented in the thermodynamic database 'mc_steel'. Using the software package MatCalc, computer simulations of the precipitation kinetics of microalloy nitrides and carbides are performed. A newly developed model is employed, which takes into account the predominant precipitation of particles at grain boundaries, together with the classical treatment for randomly distributed precipitates in the grain interior. It is demonstrated, that the precipitation of nitrides and carbides can be modeled in a consistent way if simultaneous precipitation at grain boundaries and at dislocations is taken into account, dependent on chemical composition, grain size and annealing temperature. It it is also demonstrated that, for consistent simulations, it is necessary to account for several physical mechanisms that are often neglected in this type of simulations, among them the precipitate/matrix volumetric misfit, the temperature dependent Young's modulus, composition-, temperature- and size-dependent interfacial energies, as well as the ratio between bulk and grain boundary diffusion.
Finally, a new simulation approach is presented for the calculation of the precipitation kinetics of microalloying phases during casting. It is shown that segregation effects during solidification play an important role and must be considered when doing precipitation kinetics calculations. All precipitation kinetics simulations are compared to independent experimental results from literature.

Contents

Chapter 1

Introduction

The term 'microalloyed steel' came up prior to 1940 when niobium and/or vanadium were added to a class of higher strength low C steels. However, the absence of a market and the lack of understanding of the use of these microalloying additions discouraged any serious developments. Both, research and development of these steels started simultaneously in the late 1950s and the early 1960s [1]. 40 years later, before the turn of the century, microalloyed steels have found extensive applications and it is estimated that they represent 12% of world steel production [2]. The addition of essentially less than 0.1% of the alloying element increases the yield strength of these steels by two or three times compared to plain C-Mn steel. Therefore microalloyed steels are used for the production of e.g. crankchafts, connecting rods, drive couplings, pipeline tubes, pipe fittings or pistonshafts [3]. Especially in the automotive sector, a strong increase in the application of these materials is observed. While the weight fraction of iron and steel in an average family car has decreased from 74% in 1978 to 67% in 1997, that of high- and medium strength steels has increased from 3.7% to 9.1% within the same time period [4].

In addition to a significant increase of yield strength, compared to plain C-Mn steels, these materials provide toughness, hot ductility and hot workability. Moreover, due to the decrease of the C content, good weldability is obtained. These desired mechanical properties are reached by the precipitation of second phase precipitates, e.g. nitrides, carbides or complex carbonitrides. Small amounts of vanadium (V), niobium (Nb), ti-

tanium (Ti) and aluminium (Al) are used together with nitrogen (N) and carbon (C) to form these second phase particles. During the production process of microalloyed steel, the precipitation will take place at different stages [5]. Type I precipitates are very stable ones, which form in the liquid phase and during or after solidification. These coarse particles have no significant influence on microstructural properties. Type II particles precipitate in austenite after solution treatment or during hot deformation. This group of precipitates is made responsible for grain refinement of microalloyed steel. During or after the austenite to ferrite transformation, particles of Type III develop, nucleating on the γ/α interface and in ferrite. Usually, a fine precipitate dispersion is established in this stage, which contributes significantly to the strength by dispersion strengthening.
For achieving desired mechanical properties, it is necessary to control the chemical composition of the alloys as well as the precipitation process during the production procedure, e.g. continuous casting, hot strip rolling, compact strip production, thin slap casting and rolling or coiling of hot strips of microalloyed steels. Therefore, a sound understanding of the basic mechanism of the precipitation process is essential, including the description of the precipitation kinetics in terms of nucleation, growth and coarsening of particles. Studying these nucleation and diffusion processes experimentally is expensive. With the development of specialised simulation software, e.g. the thermo-kinetic software MatCalc [6–8], it is possible, nowadays, to investigate these complex processes with computational methods on the researchers desktop. Using these tools enables the development of new alloys and/or optimization of the heat treatment parameters for the production processes of existing ones. This is crucial for being competitive on a global steel market.

Chapter 2

Objectives

The major goal of the present thesis is the numerical description of the precipitation kinetics of various nitrides and carbides in (HSLA) microalloyed steels. Therefore, different investigations are carried out.

Firstly, the solubility products of nitrides and carbides are studied in detail with special emphasis on microalloyed steel and compared to different thermodynamic assessments. Appropriate phase descriptions are determined and implemented in the thermodynamic database 'mc_steel'.

Secondly, precipitation kinetics simulations are carried out, utilizing a newly developed model for predominant precipitation at grain boundaries together with the classical treatment of randomly distributed precipitates. Moreover, in addition to different nucleation sites, misfit strain energies between precipitate/matrix interfaces are taken into account. Therefore, the characteristics of both, the novel grain boundary model as well as the classical treatment of precipitation, are investigated in terms of parameter studies.

Thirdly, the precipitation kinetics of AlN and VN are calculated, considering simultaneous precipitation at grain boundaries and at dislocations. It is shown that, for a consistent description of AlN precipitation, it is necessary to account for several physical mechanisms that are often neglected in this type of simulations, among them the precipitate/matrix volumetric misfit, temperature dependent Young's modulus, composition-, temperature- and size-dependent interfacial energies, as well as the ratio between bulk

and grain boundary diffusion.

Finally, the precipitation processes of microalloying phases during casting are analysed, taking into account the microsegregation of alloying elements during solidification of microalloyed steel.

Chapter 3

Literature Review

3.1 Fundamentals of Microalloyed High Strength Low Alloy Steel

This section gives an overview of the fundamental characteristics of microalloyed steels. After a short historical review of the development, structure property relationships are discussed with special emphasis on the two main strengthening mechanism in microalloyed steels, fine grain hardening and precipitation strengthening.

3.1.1 The Development of Microalloyed Steel

The positive effect of adding small amounts of microalloying elements was discovered prior to 1940. However, the absence of a sophisticated market and the lack of understanding of the use of this observation discouraged any serious developments. After an introduction in the late 1950s, both, research and development started simultaneously in the early 1960s [1]. Different stages of the development of microalloyed steels, including external influences, are shown in figure 3.1. The graph shows, that the development of these materials was driven by three main environmental influences. First of all, there was an increasing demand on steels with low C content due to the development and expansion of modern welding methods. Traditionally, tensile strength was increased by increasing the C and/or Mn content. But these materials obviously showed poor

weldability in terms of weld cracking. With increasing yield strain by the addition of microalloying elements, much lower C contents could be realized with improved weldability [1].

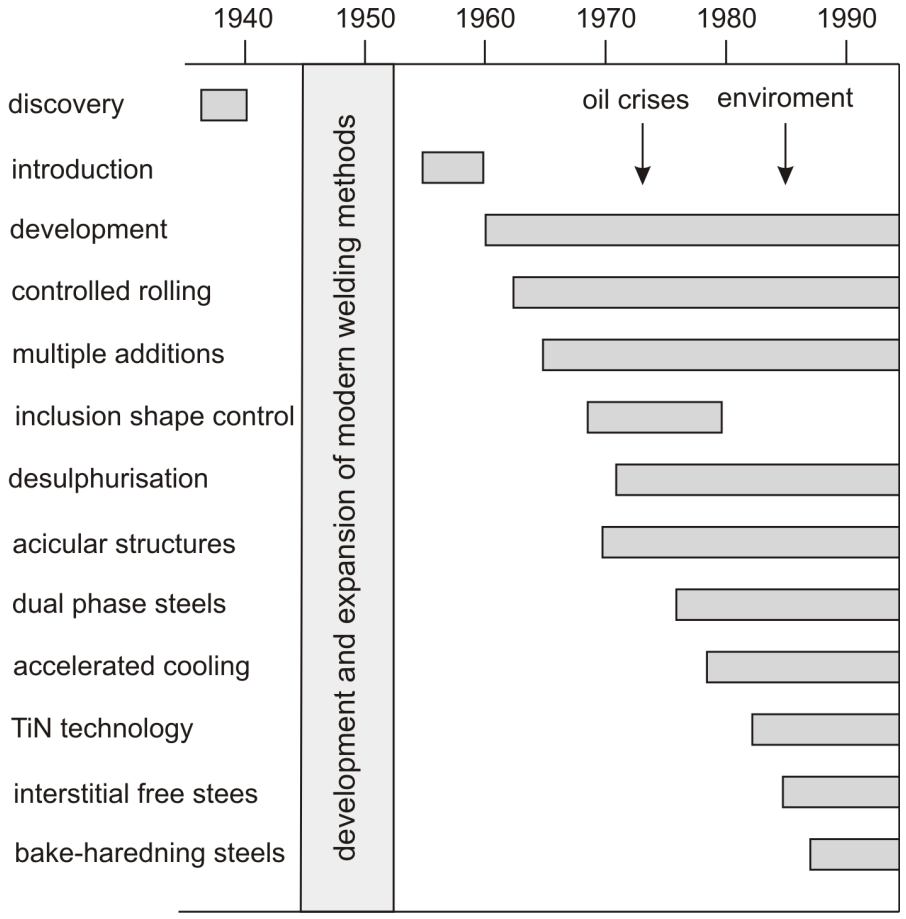

Figure 3.1: Historical review of the development of microalloyed steel with respect to major external influences [1].

Another major influence was the oil crises in 1973, which led to the development of lightweight vehicles with the aim of reducing the fuel consumption. Together with the substitution of lighter weight components by using aluminium and polymeric materials, microalloyed steels contributed significantly to vehicle weight reduction. And, last but not least, there was the ambition to reduce the environmental contamination and material conservation. Higher strength steels were substituted for other lower strength steels, the reduced material mass resulted in a substantially reduced materials requirement, with an attendant saving in energy required for iron extraction and steel refining [1].

3.1.2 Microstructure

Compared to classical high strength quenched and tempered martensitic steels, the microstructure of microalloyed (HSLA) steels consists of precipitation strengthened ferrite and pearlite containing simple stoichiometric nitrides and/or carbides as well as complex carbonitrides [3]. These desired microstructures are generally achieved during the production process, e.g. thermomechanical rolling. Thus, no further heat treatments are required to increase strength. The two major strengthening mechanism in microalloyed steels are fine grain hardening and dispersion strengthening [9]. While dispersion strengthening increases strength by hindering the movement of dislocations, fine grain hardening is made responsible for increasing strength, toughness, ductility and formability by controlling the grain size due to grain boundary pinning by second phase precipitates during the production process. Both mechanism are essential for achieving superior mechanical properties in microalloyed steels and are discussed subsequently.

3.1.3 Fine Grain Hardening

Grain refinement is extensively used as strengthening mechanism in the development of microalloyed steels. The quantitative relationship between grain size and yield strength was derived independently by Hall [10] and Petch [11] in the early 1950s. Today this relation is well established and known as the Hall-Petch relation,

$$\sigma_y = \sigma_0 + k_y d^{-1/2}, \tag{3.1}$$

where σ_y is the lower yield strength and d is the grain size. The quantities k_y and σ_0 are material constants. k_y is dependent on various solutes in iron. While C, N, Ni and Si increase k_y, no influence of Cr is observed [12]. The quantity σ_0 considers the starting stress for dislocation movement and the strengthening contribution of different solutes. Figure 3.2 shows the yield strength dependent on the final ferrite grain size for an air-cooled C-Mn steel containing 1.0% Mn, 0.25% Si and 0.01% N. In addition to the basic strength σ_0, which includes solid solution strengthening contributions of various

elements, a strong dependency on the final grain size is observed. While coarse grained materials show yield strengths in the range of 200 MPa, materials with approximately 5 μm ferrite grain size double the yield strength to about 400 MPa.

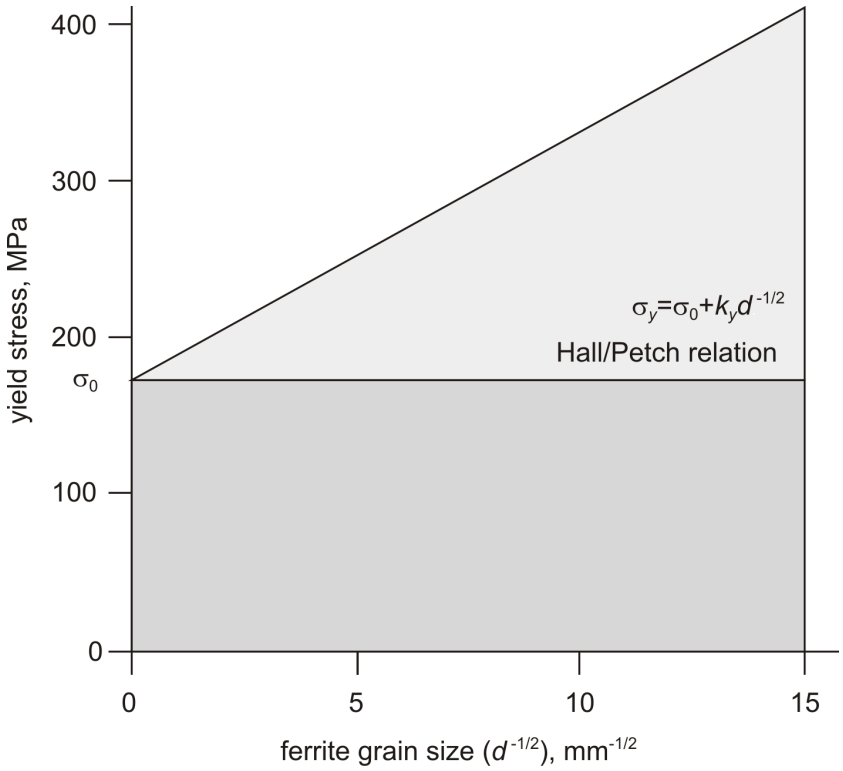

Figure 3.2: Dependency of yield stress on final ferrite grain size for an air-cooled C-Mn steel containing 1.0% Mn, 0.25% Si and 0.01% N [9].

In addition to the increase of yield strength, fine grain hardening improves mechanical properties like toughness, hot ductility and formability. Figure 3.3 shows the embrittlement vectors for various microstructural strengthening effects, defined by the change in the impact transition temperature per unit increase in yield strength. The vectors, depicted in this figure relate to ferrite-pearlite structures such as found in the matrix of low C structural steels [1]. The image clearly demonstrates that in addition to the positive strengthening effects (see Figure 3.2), grain refinement is the most effective way for reducing the impact transformation temperature and hence improving mechanical properties in terms of toughness or formability.

In microalloyed steel, this grain refinement effect is realized by pinning of grain bound-

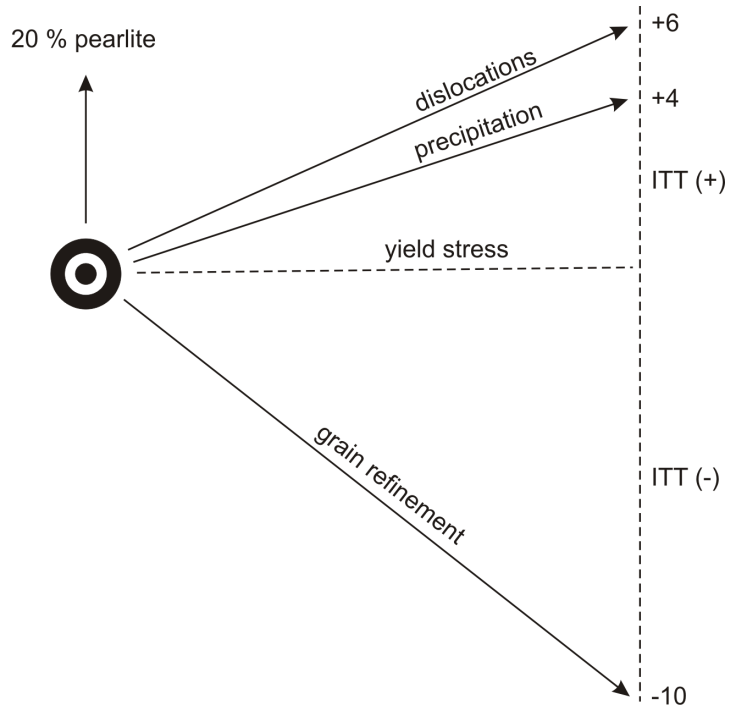

Figure 3.3: The embrittlement vectors, defined by the change in the impact transition temperature per unit increase in yield strength for various microstructural strengthening mechanism [1].

aries. This mechanism is well known for many years and essential for controlling grain growth, especially in the austenite phase field. Several theoretical descriptions of grain growth in particle containing materials have been developed, by Zener [13], Gladman [14], Heallman and Hillert [15], Elst et al. [16] and Rios [17]. The mathematical descriptions of these models as well as a comparison of the results with experimental data can be found in the work of Gao and Baker [18].

3.1.4 Dispersion Strengthening

Apart from fine grain hardening, dispersion strengthening is another very important strengthening mechanism in microalloyed steels. Shear stress induced dislocation movement in a dispersion hardened system, such as bcc ferrite, will cease when it meets one or several hard undeformable precipitates along its length. Two different dislocation particle interactions are made responsible for hindering the movement of dislocations, see

Figure 3.4. Depending on the precipitate size, smaller or larger than R_0, the dislocation will overcome the precipitate by cutting or bypassing it. R_0 indicates the critical radius, where the increase of yield strength is maximised. Due to the hardness of the microalloy nitrides and carbides, the transition from a cutting mechanism to the bypassing mechanism will occur at rather small precipitate size [1]. Thus, the latter mechanism, called Orowan [19] type, is the major type of dispersion strengthening in these materials.

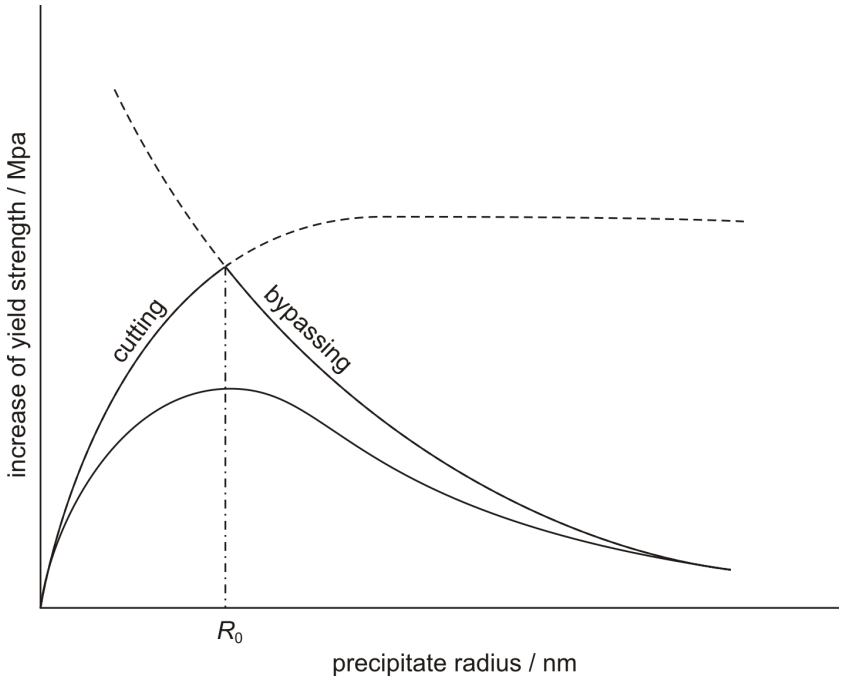

Figure 3.4: Relationship between particle radius and yield strength, considering cutting or bypassing of precipitates by dislocations [20].

This strengthening effect of hard carbides and/or nitrides can be described with theories based on dislocation bypassing. In the original work, Orowan developed his theory assuming a regular array of precipitates, which leads to an overestimation of the required stress for dislocation bypassing of the precipitates. Ashby [21] extended the work of Orowan taking into account that particles are arranged randomly as well as considering surface to surface interparticle distances rather than center to center spacing. According to that, the Ashby-Orowan [21] relationship is given with

$$\Delta\sigma_y = MCGb\frac{1}{\lambda}\ln\left(\frac{r_a}{r_i}\right), \tag{3.2}$$

where M is the Taylor factor, C is a constant, G is the shear modulus, b is the Burgers-vector, λ is the mean particle distance and r_i and r_a are the inner- and outer cut-off radii, respectively. Figure 3.5 shows the calculated increase of yield strength as a function of the volume fraction and diameter of precipitates according to equation 3.2. The graph clearly demonstrates the increase of yield strength with increasing volume fraction of small precipitates.

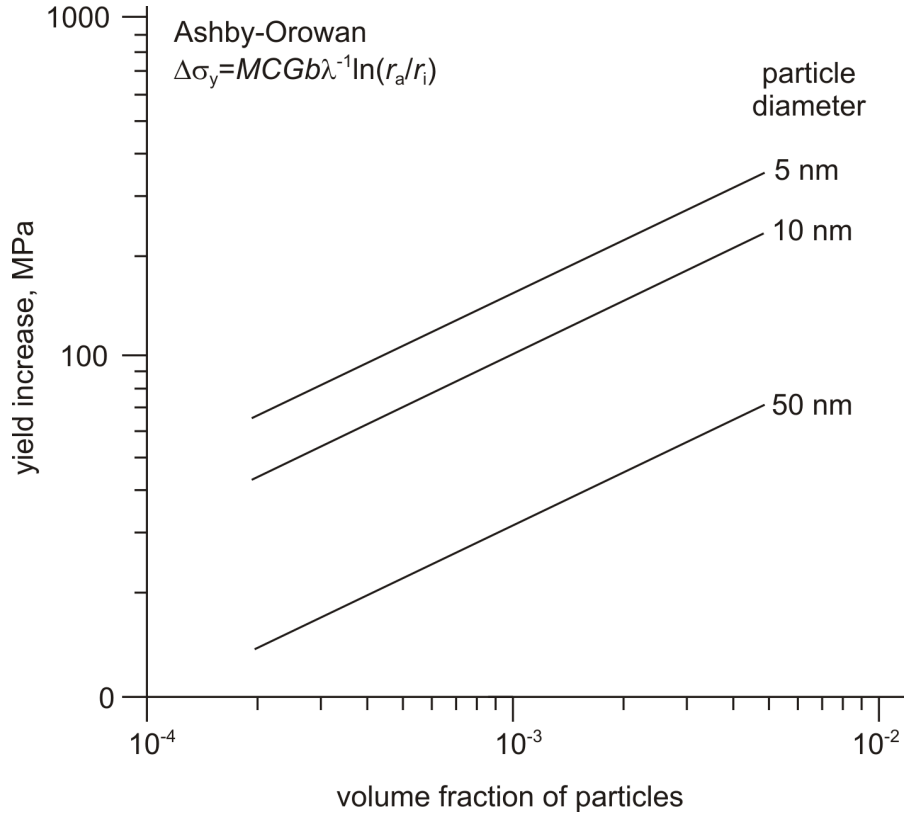

Figure 3.5: Calculated increase of yield strength by the addition of small volume fractions of particles of different sizes according to the Ashby-Orowan [21] relationships [1].

3.2 Precipitates in Microalloyed Steels

The precipitation of second phase particles, e.g. nitrides, carbides or complex carbonitrides, plays an important role in the production process of high-strength low-alloy (HSLA) steel. This section deals with the effect of various alloying elements on microalloyed steel with special emphasis on the precipitation of second phase particles. Furthermore, the influences of these second phase particles on the mechanical properties of microalloyed steel are presented.

3.2.1 Microalloying Elements and their Precipitates

The major microalloying elements in steel are Al, V, Nb and Ti. The content of these elements in microalloyed steel is rather low and generally below 0.1 wt%. These microalloying elements are added solely or in combination and precipitate in different matrix phases as simple carbides, nitrides or complex carbonitrides. Genereally, microalloying additions have higher affinity to N compared to C, thus, all these elements prefer the precipitation in form of nitrides [1]. Since V, Nb and Ti have all fcc structure these elements have mutual solubility in each other, leading to the precipitation of complex carbonitrides.

3.2.1.1 Aluminium

Al is often used for deoxidation during casting of Al killed steels. Therefore, the use of Al as a microalloying element can be seen as byproduct which is free of charge. However, important mechanical and technological properties, such as hot ductility [22–24], impact toughness [24], deep drawability [25] or weldability [26] can be improved by microalloying additions of Al. On the other hand, precipitation of AlN can cause embrittlement and induce cracking phenomena, such as, e.g. rock candy fracture [27–33]. Some authors [34] report that AlN without any other trace element has no influence on hot ductility of high purity iron. A summary of the effects of AlN in steel can be found in the extensive review of Wilson and Gladman [26].

The most significant effect of AlN in steel is in grain size control [24, 35–37], which

directly influences these properties. Especially in the austenite phase field, AlN precipitates predominatly at austenite grain boundaries [38–43]. Therefore, in austenite, grain growth can be effectively controlled by AlN precipitation. For instance, Militzer et al. [44] show that, in the presence of AlN precipitation, there is very little grain growth (40 μm after 10 min.) during isothermal annealing at temperatures below 1100 °C, whereas there is fast grain growth at 1150 °C (200 μm after 10 min.). They suggested that complete dissolution of AlN above 1100 °C is responsible for the large grain size in their steel. And also Gao and Baker [18] claim that the presence of AlN precipitates is responsible for grain size control in Al-V-N steel. In addition to AlN precipitates at the austenite grain boundaries, AlN is also found at ferrite grain boundaries [41].

The equilibrium crystallographic structure of AlN is the hexagonal wurtzite structure with a lattice constant of a=0.311 nm and c=0.4978 nm. At the early stages of precipitation, also, simple cubic structure with a=0.412 nm is observed [43, 45–47]. A detailed investigation of the two crystallographic structures can be found in reference [48].

Depending on the heat treatment and processing conditions, the morphology of AlN precipitates cover a wide range of different precipitate shapes. AlN particles can be dendritic (up to several hundred microns in lenght), large plates, rod, needle shaped, rectangular/cuboidal or simple finley distributed within the matrix ($<$ 5 nm). A large number of references summarizing these different morphologies, can be found in reference [26].

It should be noted that Al differs from other microalloying elements, like V, Nb and Ti, since it does not form a carbide in steel. Due to the hexagonal wurtzite structue of AlN precipitates, there is no mutual solubility with the carbides/nitrides of V, Nb and Ti, which all have NaCl cubic crystal structure [49].

3.2.1.2 Vanadium

World-wide, 94 % of the total V is used for alloying of steel and cast iron [50]. Compared to Al, the postive influences of V are not related to grain size control but to dispersion strengthening effects due to precipitation of finley distributed particles in a ferritic matrix (see section 3.1.4). Li et al. [51] showed that the dispersion plus dis-

location strengthening in V-microalloyed steels is in the range of 80 - 250 MPa, and Lagneborg et al. [49] concluded in their extensive review, that in a 0.12 % V-steel, the precipitation hardening potential is typically in the range of 6 MPa per 0.001 % N. Therefore, V microalloyed steels are widley used for forging steels, providing high strength as well as good fatique resistance, which is essential for applications for structures, machine and vehicle parts [3]. Furthermore V strengthened cold rolled steels are used in the automotive sector. According to Scott et al. [52], the ideal microalloying element for cold rolled steels should have following properties:

- Large precipitates formed in slabs can be redissolved during reheating
- No significant increase in hardness during hot rolling and no decrease in hot ductility
- No precipitation during finishing and coiling
- Intense precipitation during continuous annealing
- Precipitation should occur predominantly in the ferrite phase field
- Precipitation should be intergranular
- The number density should be as high as possible

These points require that the precipitating phase is sufficiently soluble in austenite, but shows a maximum possible precipitation driving force to generate a high particle nucleation density in ferrite. Considering all above mentioned criteria, the microalloying element which best satisfies these constraints is V [52]. In addition to these excellent properties for the production of cold rolled sheets, V provides also excellent metallurgical properties for production of hot rolled sheet products. Therefore, the important aspects can be summarized as, the high solubility of V(C,N) in austenite, the low solute drag coefficient [53] of V in austenite and the fact that N is the preferred element in V(C,N) precipitation [54].

3.2.1.3 Niobium

Nb has become a preferred microalloying element in HSLA steels sheet, since it increases the strength without reducing toughness. Therefore, the predominate strengthening mechanism is grain refinement of the ferrite grains, whereas other microalloying additions apply the strengthening mechanism dispersion strengthening to a major extent (Ti) or completly (V). Furthermore, compared to Nb, higher amounts of Ti or V are needed to obtain the same increase in strength [55,56]. Consequently, Nb is widely used in civil construction, automobile and line pipe applications. Plate sheets are produced by applying thermomechanical rolling, a technique that simultaneously increases strength and toughness by grain refinement. The most important role of Nb as a microalloying element in thermomechanically rolled steel is the retardation of austenite recrystallization, which provides more nuclei for the α/γ transformation and thus a finer ferrite grain size [57]. Two reasons can be attributed to this important effect [58]. Firstly, Nb in solid solution can retard the austenite recrystallization after deformation through the solute drag [53] effect as a consequence of its relatively large atom size. Secondly, and more important, Nb can also retard the recrystallization process by the precipitation of finely dispersed NbC particles. Depending on the hot rolling parameters, like deformation, temperature and interpass time, NbC precipitation is generally incomplete in the austenite phase field and does not reach its thermodynamical equilibrium state. Consequently, part of Nb retained in solid solution may form nanometer sized particles during or after the γ/α transition, which increases strength by precipitation hardening.

3.2.1.4 Titanium

Ti is often used to stabilize the N in liquid steel and it is well established that Ti has a very low solubility in steel. Therefore, it forms nitrides during and/or early after solidification in Ti-V and Ti-Nb microalloyed steels, providing a significant contribution in grain growth inhibition [49], see also figure 3.7. Furthermore it is also well known that there is a significant contribution of precipitation strengthening by the precipitation of fine dispersed TiN to the matrix strength of ferrite in microalloyed steel [59]. And,

especially, in Ti containing microalloyed steels, precipitation of complex carbonitrides with inhomogeneous element distribution is observed. The particles, which precipitate in the high temperature range, act as nucleation sites for nitrides and/or carbides with higher solubility. Thus, core/shell constructions of precipitates are observed with a TiN rich core surrounded by other microalloying elements, e.g. V, Nb(C,N) [60–62]. The morphology of pure TiN or Ti-rich complex carbonitrides are plates and cuboids, see e.g. [63, 64]. TiN is mainly used for the production of high strength steels sheets, e.g. in thin strip produced by compact strip production or hot strip rolling.

3.2.2 Effects of Microalloying on the Properties of Microalloyed Steels

The previous sections demonstrated the different characteristics of the microalloying additions. This section now deals with the influence of different precipitate phases on the mechanical properties of microalloyed steels in terms of fine grain hardening (section 3.1.3) and dispersion strengthening (section 3.1.4). Figure 3.6 shows a comparison of the effects of classical microalloying elements on the properties of hot strips, after Hulka [55]. The x-axis represents the amount of microalloying additions, whereas the y-axis shows the influences on the mechanical properties, strength and toughness. The letters P and F indicate the increase or decrease of the mechanical properties due to precipitation strengthening (P) and/or fine grain hardening (F). Both, Nb as well as Ti show big influences on the strength caused by both strengthening mechanism (P and F), whereas V is a solely precipitation strengthening element. Compared to Ti and V, there are much less additions of Nb required to achieve the same increase in strength. Furthermore, the graph shows that Nb is the only element enhancing considerable the toughness by fine grain hardening. However, Hulka [55] neglected in his comparison the positive influence of AlN on toughness.

Speich et al. [65] also compared the positive effects of microalloying additions on fine grain hardening. They suggested, that, next to Ti additions, Al is maybe the most effective element in avoiding grain coarsening at high temperatures, see figure 3.7. Con-

sequently the precipitation of AlN provides positive influences on toughness and embrittlement.

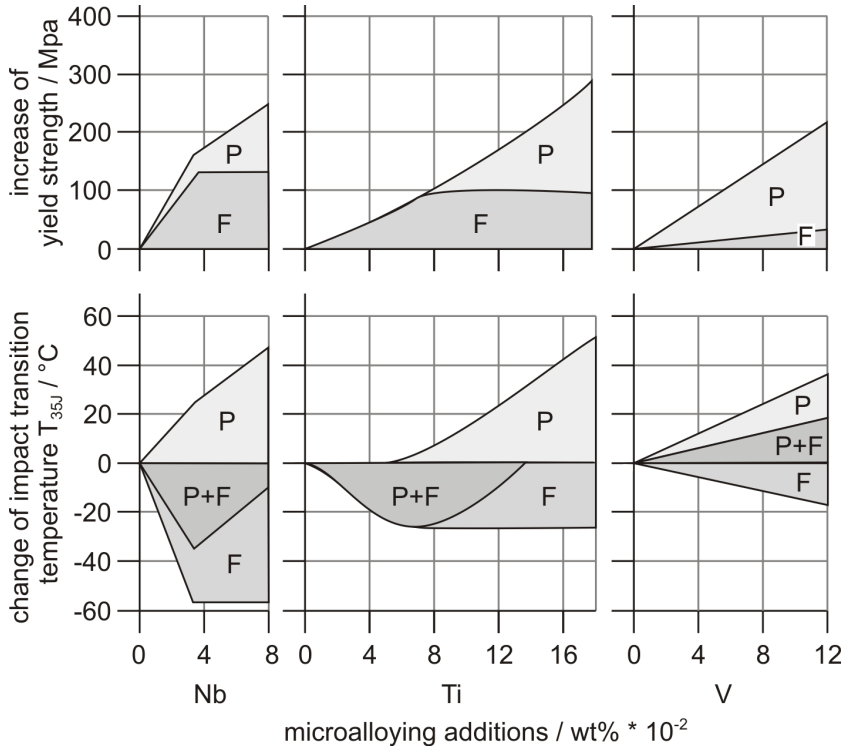

Figure 3.6: Effect of microalloying on the properties of hot strip [55].

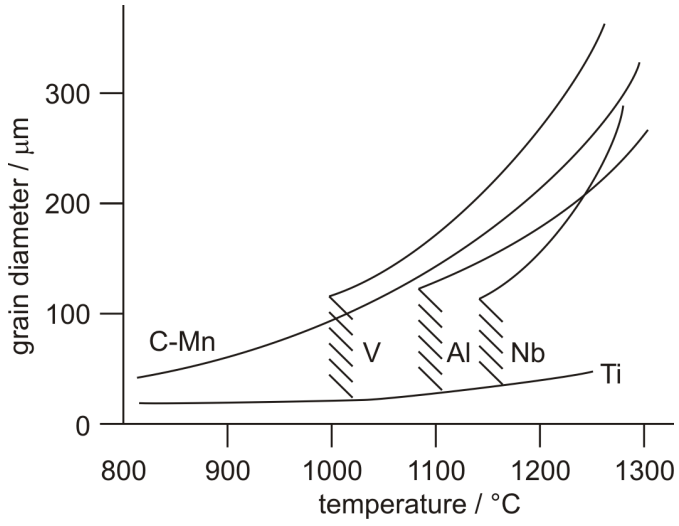

Figure 3.7: Austenite grain growth characteristics in steels containing various microalloying additions [65].

Another comparison of the microalloying elements was made by Morrison [2] with special emphasis on the achievement of different desired microstructures during various production processes, see table 3.1.

Table 3.1: Roles of the classical microalloying elements V, Nb and Ti, after Morrison [2].

microalloying element	V	Nb	Ti
precipitation strengthening after hot rolling	VN, VC	NbCN	TiC
precipitation strengthening after normalising	VC	-	-
influences recrystallisation during hot rolling	-	Nb, NbCN	-
refines grain size on normalising	VN	NbCN	TiC
refines grain size during high temperature austenitising	-	-	TiN
influences transformation characteristics after hot rolling	-	Nb	-

Morrison [2] also neglected the important role of Al in his summary. However, previous sections of this work as well as detailed investigations of other authors, e. g. Wilson and Gladman [26], show the high significance of this element, providing fine grain hardening and hence, enhanced toughness properties.

3.2.3 The Solubility of Nitrides and Carbides in Steel

In order to control the strengthening mechanisms, dispersion strengthening and fine grain hardening, it is necessary to understand the dissolution and precipitation processes. Fine ferrite grain sizes are generally achieved by controlling the austenite grain size in the high temperature range prior to the γ/α transformation. Thus, the precipitation of particles at sub-solvus temperatures as well as particles remaining undissolved in the austenite phase field are required. On the other hand, the precipitation of fine dispersed particles (3-5 nm in diameter) in the ferrite phase field after transformation is essential to increase strength by dispersion hardening. Therefore, such nitrides and/or carbides should be dissolved in the austenite region. In order to achieve the desired metallurgical

states, a detailed knowledge of the solubilities of the microalloy carbides and nitrides is required, together with a knowledge of their precipitation behavior [1].

3.2.3.1 The Solubility Product

The reaction between a microalloying element M with an interstitial X to give a compound MX at a given temperature T is given with

$$[M] + [X] \leftrightarrow (MX), \tag{3.3}$$

where [M] and [X] represent the concentrations of the microalloying element and the interstitial, dissolved in the matrix, whereas (MX) stands for the compound. The equilibrium constant, also known as the solubility product can be written as

$$k_s = \frac{a_{[M]} \cdot a_{[X]}}{a_{(MX)}}, \tag{3.4}$$

where $a_{[M]}$ and $a_{[X]}$ represent the activity of the dissolved elements and $a_{(MX)}$ is the activity of the compound. These activities can be expressed by the products of the elemental concentrations and the activity coefficients γ leading to

$$a_{[M]} = \gamma_{[M]}[M], \tag{3.5}$$

and hence

$$k_s = \frac{\gamma_{[M]}[M] \cdot \gamma_{[X]}[X]}{a_{(MX)}}. \tag{3.6}$$

In a rather empirical manner, it is assumed that the activity coefficients $\gamma_{[M]}$ and $\gamma_{[X]}$ are equal to unity and of course the activity of the product (MX) is unity [1]. Thus it can be written

$$k_s = [M][X]. \tag{3.7}$$

$[M]$ and $[X]$ should be the molare fractions. Since the concentrations are very low, traditionally, these element contents are expressed in weight percentage, which has only minor influence on the value of k_s.
The temperature dependence can be expressed using an Arrhenius relationship

$$ln\ k_s = -\left(\frac{Q}{RT}\right) + C, \tag{3.8}$$

where R represents the universal gas constant, Q the heat of dissolution, T the temperature and C a constant. Historically, metallurgist used the equation

$$log\ k_s = A - \frac{B}{T}, \tag{3.9}$$

where A and B are system constants, and T stands for the temperature in K. Combining equations 3.7 and 3.9 leads to the universal definition of the solubility product

$$log\ k_s = log[M[wt\%]] \cdot [X[wt\%]] = A - \frac{B}{T}. \tag{3.10}$$

Additional information on the deduction of the solubility product can be found in reference [1].

3.2.3.2 Solubility Products of Various Stoichiometric Phases

Different microalloying phases show a wide range of different solubility products. Figure 3.8 shows a comparison of the solubility data of different microalloy nitrides and carbides in austenite [49], since this is the temperature range of prime importance, when doing precipitation kinetics calculations.

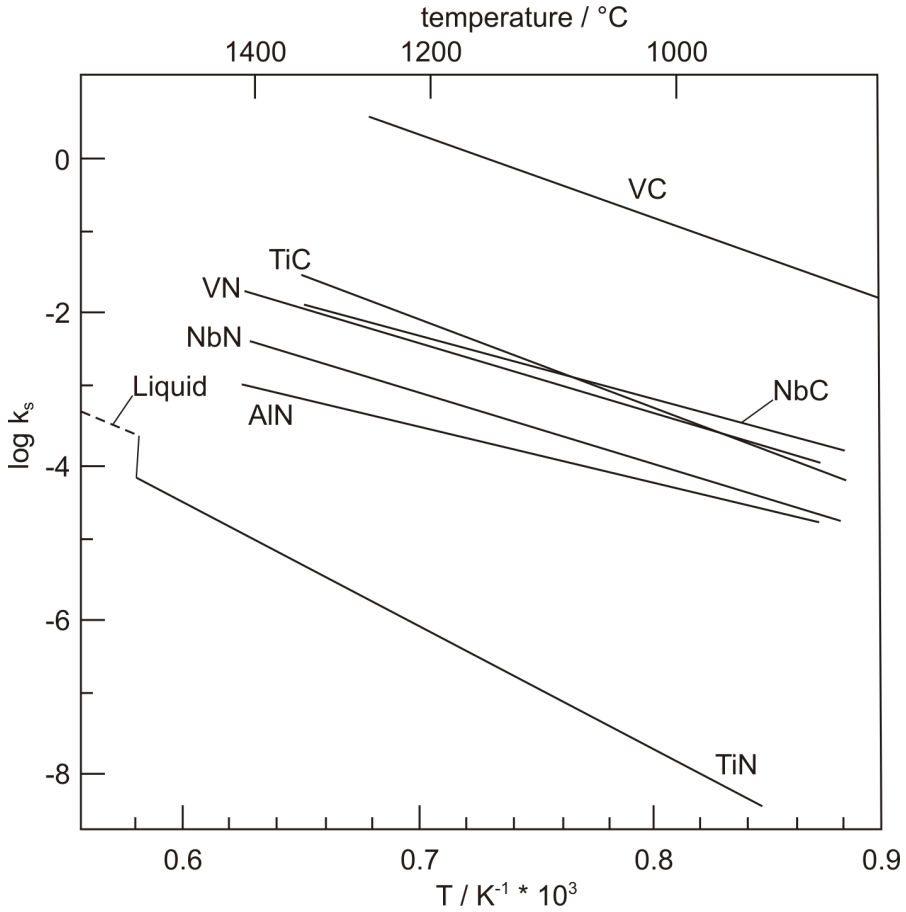

Figure 3.8: Comparison of the solubility products of the microalloy carbides and nitrides, in austenite [49].

Despite the variations in cited solubility product equations summarized in section 4.2 Gladman [1] proposed several important conclusions.

- In the austenite phase field, all microalloyed nitrides are more stable than their corresponding carbide. Large differences in solubility between the microalloy nitride and carbide are observed for the elements V and Ti, whilst the difference between the solubilities of NbN and NbC is much less. The solubility of AlN is slightly less compared to the solubility of NbN. However, AlC has never been reported to occur in steel, even in steel with considerable Al and C contents.
- Most of the microalloying carbides and nitrides show broadly similar solubility in austenite, with two exceptions. TiN is more stable by a factor of 1000, and VC is

far more soluble by a factor of 1000, than other microalloy carbides and nitrides.

- The solubility of TiN in liquid at temperature up to 1600 °C is similar to the solubility of most other microalloy nitrides and carbides in austenite at around 1200 °C.

The knowledge of these individual solubilities of microalloy compounds give a clear direction for the selection of microalloying elements for special applications. While the high solubility of VC suggests the use of V in normalised steels and high C steels, Ti and Al are the preferred grain refining elements in the austenite phase field as a direct consequence of their higher phase stability.

3.3 Theory of Precipitation

Precipitation is a special case of phase transformation where a new phase grows on the expense of an existing one. If we are talking from precipitates, we talk from particles, which are very small (few nanometers to few micrometers) compared to the parent phase (matrix phase). Typical precipitates are intermetallic phases or oxides, sulphides, nitrides and carbides [66]. The present work deals exclusively with the precipitation of nitrides and carbides, which are the essential precipitates in microalloyed steel.
In general, precipitation occurs when the amount of alloying elements exceeds the soluble equilibrium amount of elements in an alloying system. Apart from the dependence on chemical composition and temperature these precipitation processes are strongly time dependent, which is why we are talking of kinetics. The precipitation process can be divided into three different stages, compare for instance [66]:

- **Nucleation:** The initial stages in precipitate life. Stochastic process driven by microscopic thermal and compositional fluctuations.
- **Growth:** Controlled attachment of atoms to the precipitate. Deterministic process driven by chemical and/or mechanical driving forces.
- **Coarsening:** Dissolution of small precipitates in favor of larger ones. Driven by curvature-induced pressure, also called the Gibbs-Thomson effect.

Figure 3.9 shows the volume fraction f_T, the precipitate diameter d_T and the interparticle spacing λ_T versus time, indicating the three different stages, nucleation, growth and coarsening, during isothermal annealing at a given temperature T. After the incubation time τ, precipitates are generated with a critical precipitate diameter d^*. After this nucleation process, the particles pass through the stage of growth. The volume fraction f_T increases along with the increase of the particle diameter d_T. In the special case of randomly distributed precipitates, which is depicted in figure 3.9, the increase of the diameter goes with $t^{\frac{1}{2}}$. When the equilibrium phase fraction f_T is reached, stage three begins. Big precipitates grow at the expense of smaller ones, while the volume fraction

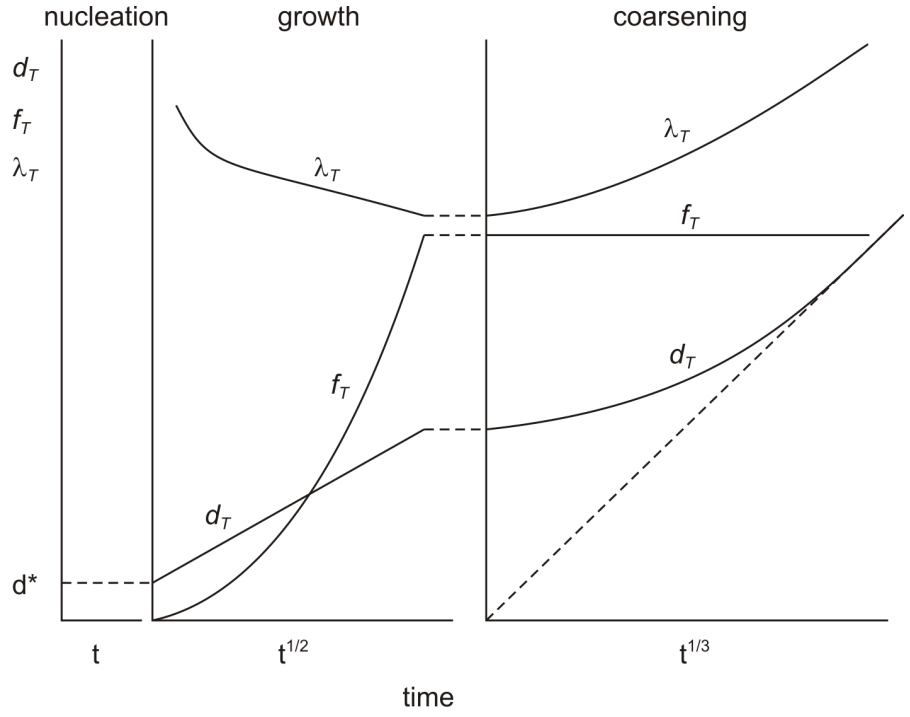

Figure 3.9: Development of precipitate diameter d_T, interparticle distance λ_T and phase fraction f_T versus time during isothermal annealing at a given temperature T [67].

f_T remains nearly constant. This stage is known as the coarsening stage and the precipitate diameter obeys $t^{\frac{1}{3}}$ if the particles are distributed randomly in the matrix phase. It is worthy to note here again that the parabolic growth law as well as the cubic coarsening law, describing the development of the mean radius during isothermal annealing, are only fulfilled in the special case of randomly distributed precipitates. This is the case for homogeneous precipitation in the bulk and in the broadest sense for heterogeneous precipitation at one or two dimensional lattice defects (e.g. dislocations), due to their nearly random arrangement. These laws are clearly not fulfilled when precipitation occurs predominantly at grain boundaries, which is demonstrated later on in the present work.

3.4 Precipitation Kinetics Models Embedded in the Software MatCalc

MatCalc [6–8] is a thermo-kinetic software package developed for the simulation of the precipitation kinetics of various metallurgical phases. The characteristics of this program can be summarized as a mean-field treatment of nucleation, growth and coarsening of multi-component, multi-phase and multi particle systems. This approach is based on the Onsager thermodynamic extremal principle [68,69], assuming that a thermodynamic system evolves along the particular kinetic path, where maximum entropy is produced. The theory is described by Svoboda et al. [6] and the treatment of the numerical implementation in the software package MatCalc was done by Kozeschnik et al. [7]. The basis for the calculation of the thermodynamics of the system are CALPHAD type databases [70], providing chemical potentials of the phases as well as diffusivities of the alloying elements on the basis of the chemical composition of the alloy and the present temperature. The following sections give a brief introduction on the basic models incorporated in the software package MatCalc.

3.4.1 Classical Nucleation Theory for Multi-Component Systems

In the software package MatCalc [6–8], the nucleation kinetics of precipitates is calculated from Classical Nucleation Theory (CNT) [71] extended for multi-component systems [6, 66, 72]. Accordingly, the transient nucleation rate J is given as

$$J = N_0 Z \beta^* \cdot exp\left(\frac{-G^*}{k \cdot T}\right) \cdot exp\left(\frac{-\tau}{t}\right). \tag{3.11}$$

J describes the rate, at which nuclei are created per unit volume and time. N_0 represents the total number of potential nucleation sites. The Zeldovich factor Z takes into account that the nucleus is destabilized by thermal excitation as compared to the inactivated state, and it is given with [71]

$$Z = \left[\frac{-1}{2\pi kT} \frac{\partial^2 \Delta G}{\partial n^2} \bigg|_{n^*} \right]^{\frac{1}{2}}. \tag{3.12}$$

ΔG represents the total free energy change on nucleus formation, n is the number of atoms in the nucleus, k is the Boltzmann constant and T is temperature. The derivative of ΔG is taken at the critical nucleus size n^*.

The atomic attachment rate β^* takes into account the long-range diffusive transport of atoms, which is needed for nucleus formation if the chemical composition of the matrix is different from the chemical composition of the precipitate. A suitable multi-component equation for β^* has been derived by Svoboda et al. [6], and it is given with

$$\beta^* = \frac{4\pi\rho^{*2}}{a^4\Omega} \left[\sum_{i=1}^{n} \frac{(c_{ki} - c_{0i})^2}{c_{0i} D_{0i}} \right]^{-1}, \tag{3.13}$$

where ρ^* is the critical nucleation radius, a is the atomic distance, Ω is the molar volume, c_{ki} and c_{0i} are the element concentrations in precipitate with index k and matrix, respectively, and D_{0i} is the diffusivity of element i in the matrix. The incubation time τ is given with [71]

$$\tau = \frac{1}{2\beta^* Z^2}, \tag{3.14}$$

and the critical energy for nucleus formation G^* is

$$G^* = \frac{16\pi}{3} \frac{\gamma^3}{(\Delta G_{vol} - \Delta G_s)^2}, \tag{3.15}$$

with the interfacial energy γ, the volume free energy change ΔG_{vol} and the misfit strain energy change ΔG_s. The interfacial energy γ is calculated using a generalized n-next nearest-neighbour broken-bond approach [73], assuming a planar and sharp interface, see also section 3.4.3. Corrections for the small size of the precipitate are taken into account according to reference [74].

It is important to note that G^* is a most essential quantity in nucleation theory, when compared to the other quantities occurring in equation 3.11. Since G^* appears in the exponent of the nucleation rate equation 3.11, small changes in γ and/or $\Delta G_{vol} - \Delta G_s$ can lead to huge variations in J, which has been demonstrated recently for γ'-precipitation in Ni-base superalloy UDIMET 720 Li [75–77].
Finally, the misfit strain energy is given with

$$\Delta G_s = \frac{E}{1-\nu}\epsilon^2, \tag{3.16}$$

where E is the Young's modulus and ν the Poisson constant of the matrix. ϵ is the linear misfit strain, approximately given as

$$\epsilon = \frac{1}{3}\frac{V_{mol}^P - V_{mol}^M}{V_{mol}^M}, \tag{3.17}$$

where V_{mol}^P and V_{mol}^M are the molar volumes of the precipitate and the matrix, respectively.

3.4.2 Growth and Coarsening - The SFFK Model

Once a precipitate is nucleated, its further growth is evaluated based on the evolution equations for the radius and composition of the precipitate derived by Svoboda et al. [6] in a mean-field approach utilizing the thermodynamic extremal principle [68, 69], also known as the SFFK model. The next two sections give a brief overview of this approach for randomly distributed precipitates (section 3.4.2.1) and precipitates arranged at grain boundaries (section 3.4.2.2).

3.4.2.1 Randomly Distributed Precipitates

The SFFK model [6] enables the treatment of multi-component, multi-phase and multi-particle systems. Figure 3.10 shows a schematic precipitate distribution for random

precipitation of particles with different size and chemical composition, surrounded by spherical diffusion fields (shaded areas).

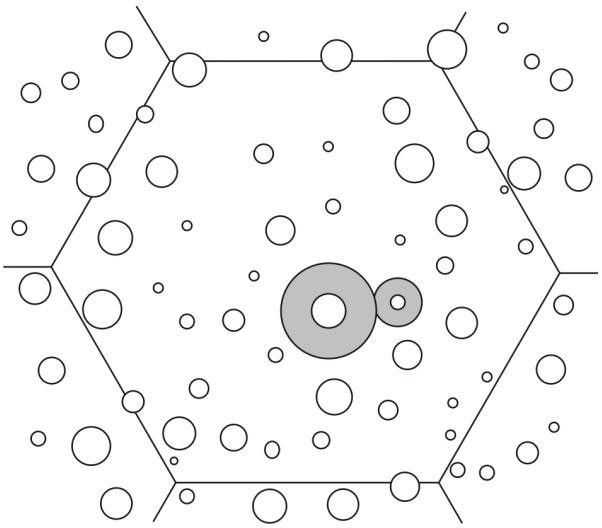

Figure 3.10: Schematic precipitate distributions and diffusion fields (shaded areas) for random precipitation in 2D [78].

In a system containing n chemical elements and m randomly distributed precipitates with spherical diffusion fields, the total free energy of the system can be written as [6,8]

$$G = \sum_{i=1}^{n} N_{0i}\mu_{0i} + \sum_{k=1}^{m} \frac{4\pi\rho_k^3}{3}\left(\lambda_k + \sum_{i=1}^{n} c_{ki}\mu_{ki}\right) + \sum_{k=1}^{m} 4\pi\rho_k^2\gamma_k, \tag{3.18}$$

where μ_{0i} $(i = 1, ..., n)$ is the chemical potential of component i in the matrix and μ_{ki} $(k = 1, ..., m, i = 1, ..., n)$ is the chemical potential of component i in the precipitate k. The chemical potentials are expressed as functions of the concentrations c_{ki} $(k = 0, ..., m, i = 1, ..., n)$. γ is the interface energy density and λ_k takes into account the contribution of the elastic energy and plastic work due to the volume change of precipitates. Therefore, equation 3.18 contains only mean values and no concentration profiles are considered. Thus, the SFFK model is a classical approximation procedure and can be seen as a 'mean-field approach'.

In the formulation of the total free energy (equation 3.18), each of the three terms can be related to a particular energy contribution [66]. Accordingly,

- The first term describes the Gibbs energy of the matrix by summing up the product of all moles of components N_{0i} with the corresponding chemical potentials μ_{0i}.
- The second term is related to the sum of the bulk free energy of all m precipitates, where the specific quantities for the mechanical free energy contribution λ_k and the chemical free energy $\sum_{i=1}^{n} c_{ki}\mu_{ki}$ are multiplied with the precipitate volume $4/3\pi\rho_k^3$. The summation over k in the second term is performed over all m precipitates.
- The third term takes into account the energy contribution of the precipitate-matrix interfaces. The specific interfacial energy γ_k is multiplied by the precipitate surface area $4\pi\rho_k^2$ and summation is performed over all m precipitates.

According to equation 3.18, the formulation of the total free energy of the system in the present state, is defined by the independent state parameters ρ_k and c_{ki}. The other parameters can be determined, using the mass conservation law for each component i [66],

$$N_i = N_{0i} + \sum_{k=1}^{m} \frac{4\pi\rho_k^3}{3} c_{ki} \tag{3.19}$$

and the global mass conservation

$$\sum_{i=1}^{n} N_i = N. \tag{3.20}$$

If a thermodynamic system evolves to a more stable state, the difference in free energy between initial and the final stage is dissipated. The classical products of this reaction are entropy and transformation heat. Three different dissipation effects are considered in the SFFK model [66]:

- Q_1 - Dissipation due to interface movement
- Q_2 - Dissipation due to diffusion inside the precipitate
- Q_3 - Dissipation due to diffusion inside the matrix

Dissipation due to interface movement can be related to the resistance against the driving pressure for interface migration and can be written as

$$Q_1 = \sum_{k=1}^{m} \frac{4\pi\rho_k^2}{M_k}\dot{\rho}_k^2, \tag{3.21}$$

where M_k stands for the interface mobility.

Dissipation due to diffusion inside the precipitate is given with

$$Q_2 = \sum_{k=1}^{m}\sum_{i=1}^{n}\int_0^{\rho_k} \frac{RT}{c_{ki}D_{ki}} 4\pi r^2 j_{ki}^2 dr, \tag{3.22}$$

where R is the universal gas constant. j_{ki} and D_{ki} are the flux and the diffusion coefficient of component i in the precipitate k.

Dissipation due to diffusion inside the matrix can be expressed as

$$Q_3 = \sum_{k=1}^{m}\sum_{i=1}^{n}\int_{\rho_k}^{Z} \frac{RT}{c_{0i}D_{0i}} 4\pi r^2 J_{ki}^2 dr, \tag{3.23}$$

assuming that the distance between the individual precipitates is sufficiently large and their diffusion profiles do not overlap. Thereby, Z represents a characteristic length between two precipitates. The flux J_{ki} can be determined using the mass conservation law across the interface.

Finally, the total rate of dissipation is calculated by summing up the expressions of the individual contributions

$$Q = Q_1 + Q_2 + Q_3. \tag{3.24}$$

Applying the thermodynamic extremal principle after Onsager [6], the growth rate $\dot{\rho}_k$ and the rate of change of chemical composition $\dot{c}_{ki}$ of the precipitate with index k are obtained from solution of the linear system of equations

$$A_{ij} y_j = B_i, \tag{3.25}$$

where the variable y_j represents the rates $\dot{\rho}_k$ and $\dot{c}_{ki}$, as well as the Lagrange multipliers from the stoichiometry constraints (see reference [6]). The index i comprises the variables for radius and chemical composition of the precipitate as well as the stoichiometry boundary conditions implied from the crystal structure of the precipitate phase. The system of equations 3.25 is solved for each precipitate k separately. The full expressions for the coefficients A_{ij} and B_i, as used in the present work, are given in reference [8]. The numerical time integration of $\dot{\rho}_k$ and $\dot{c}_{ki}$ is performed in the software MatCalc, based on the classical numerical Kampmann - Wagner approach [79], see section 3.4.4.

3.4.2.2 Precipitates Arranged at Grain Boundaries

If precipitation occurs predominantly at grain boundaries, the assumption of randomly distributed precipitates with spherical diffusion fields is not valid anymore. There are two reason for the predominant precipitation of particles at grain boundaries. Firstly, grain boundaries are preferred nucleation sites due to less misfit strain energies, compared to nucleation sites with larger precipitate-matrix lattice mismatch. Secondly, grain boundaries represent very efficient short circuit diffusion paths with diffusivities several orders of magnitude larger than in the bulk [80]. Thus, different diffusion coefficients D_{gi} and D_{bi} must be considered, representing the diffusivities of component i at grain boundaries and in the bulk, respectively.
Figure 3.11 shows a schematic arrangement of precipitates aligned at grain boundaries. Two processes are assumed to occur parallel in the system [78]:

- Growth of precipitates on the account of components dissolved in the matrix
- Coarsening of precipitates by means of redistribution of the fixed total volume of the grain boundary precipitates amongst precipitates of different sizes

According to this image, the model takes into account two different diffusion geometries,

indicated by arrows. On the one hand, the slow diffusion from the grain interior towards the grain boundary is considered. On the other hand, the model takes into account the many orders of magnitude faster diffusion along the grain boundaries [78].

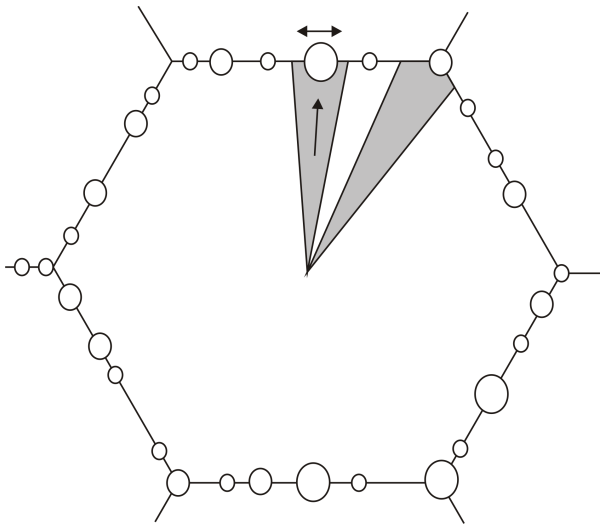

Figure 3.11: Schematic precipitate distributions for heterogeneous precipitation at grain boundaries in 2D, indicating the diffusional zone in the bulk and in the grain boundary (arrows) [78].

According to the treatment of randomly distributed precipitates with spherical diffusion fields, one can find the formulation of the total Gibbs free energy of the system as well as the corresponding dissipation equations. In the case of predominant precipitation at grain boundaries, two different dissipation mechanism are considered in the model [78]:

- Q^g - Dissipation due to diffusion in the grain boundary
- Q^b - Dissipation due to diffusion in the grain

By applying the thermodynamic extremal principle after Onsager, the growth rate $\dot{\rho}_k^g$ and the rate of coarsening $\dot{\rho}_k^c$ of each precipitate with index k can be determined, similar to the approach for randomly distributed precipitates. The corresponding equations can be found in reference [78].

3.4.3 Calculation of the Interfacial Energy

Apart from Gibbs energies and diffusion rates, the interfacial energy γ is another important, and maybe also the most uncertain, ingredient when doing precipitation kinetics simulations. Since the critical energy for nucleus formation G^* (equation 3.15) contains the cube of the interfacial energy and G^* appears in the exponent of the nucleation rate equation J (equation 3.11), small changes in γ lead to huge variations in J. Thus, precipitation kinetics simulations are very sensitive to this input quantity, which is often used in literature as 'fit - parameter' to adjust the simulations to experimental data.

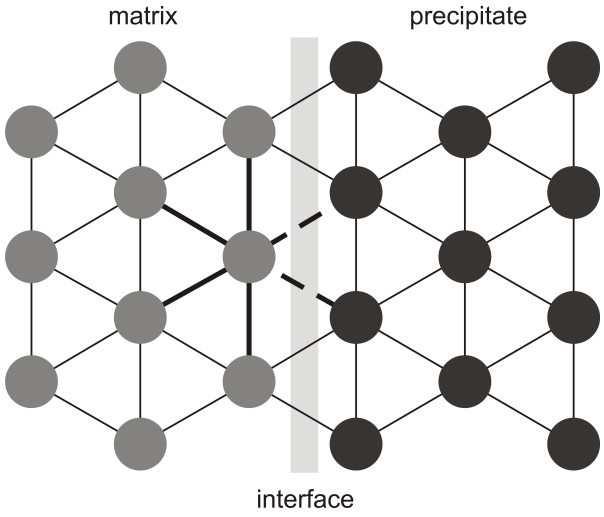

Figure 3.12: Two-dimensional interface with nearest-neighbor broken bonds [66].

Recently, Sonderegger and Kozeschnik [73] extended the classical 'Nearest-Neighbor-Broken-Bond' (NNBB) approach for the calculation of the interfacial energy γ to an n-next nearest-neighbor generalization of the NNBB concept, which is incorporated in the software package MatCalc [6–8]. Based on thermodynamic input data, this approach evaluates the interfacial energy, assuming a planar and sharp interface between precipitate and matrix, see figure 3.12. According to this image, the classical treatment of the 'NNBB' model considers only the first-nearest-neighbors, whereas the new extended approach takes also into account the second, third, ... n-nearest neighbors, which provides higher accuracy of the prediction.

The interfacial energy for a planar sharp interface γ_0 is calculated as [73]

$$\gamma_0 = \frac{n_s \cdot z_{S,eff}}{N \cdot z_{L,eff}} \Delta E_{sol}, \tag{3.26}$$

where ΔE_{Sol} is the enthalpy of solution, n_s the number of surface atoms per unit area within the surface plane and N the Avogardo number. $z_{s,eff}$ represents the number of broken bonds across the interface per atom and $z_{L,eff}$ accounts for the number of neighbors of an atom. The subscript 'eff' stands for effective structural parameters, accounting also the second, third, ... n-nearest neighbors.

However, corrections regarding the spherical shape of the nucleus and entropic contributions from finite interface thickness must be considered in the interfacial energy. Thus, the curvature dependency of the interfacial energy is treated according to [74]

$$\gamma' = \alpha \cdot \gamma_0 \tag{3.27}$$

and

$$\alpha = 1 - \frac{6}{11} \cdot \frac{r_1}{\rho} + 0.08921 \cdot \frac{r_1^2}{\rho^2} + 0.045 \cdot \ln\left(\frac{10}{3} \cdot \frac{\rho}{r_1}\right) \cdot \frac{r_1^2}{\rho^2}, \tag{3.28}$$

where ρ is the precipitate radius and r_1 is the nearest-neighbor interatomic distance. The corresponding curve is shown in figure 3.13. For large precipitate radii, the correction function converges towards unity, which corresponds to a planar interface. With

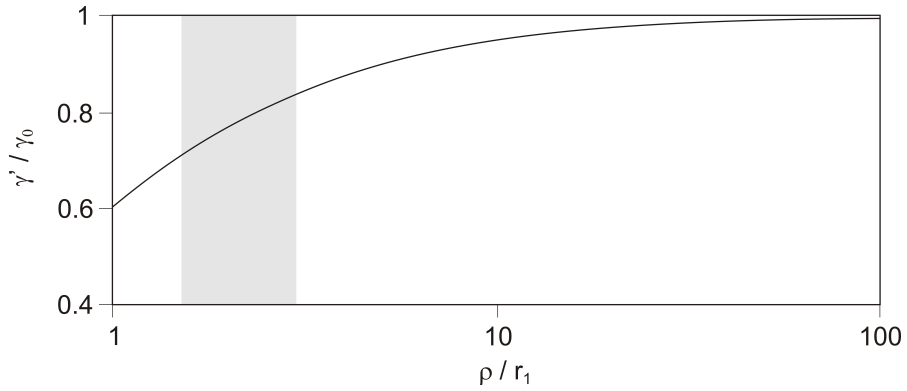

Figure 3.13: Size correction function (equation 3.28) [74].

decreasing radii, the size-correction function predicts a decrease in interfacial energy. The shaded area indicates critical nucleation radii with a size of 1.5 to 3 times r_1, which are typical cluster radii in the nucleation stage. The correction factor α varies between 0.7 and 0.85 for these critical nucleation radii.

Particularly, close to the solution temperature, the effect of entropic contributions from finite interface thickness can become prominent. This behaviour of the interfacial energy has been observed in a previous work by Pudar et al. [81] and also treated theoretically in reference [82]. Hence, at temperatures close to the solution temperature of the precipitates, an additional correction factor β must be taken into account. Finally, the calculation of the interfacial energy can be summarized as,

$$\gamma = \gamma_0 \cdot \alpha \cdot \beta. \tag{3.29}$$

3.4.4 Numerical Treatment of the Evolution Equations

The fact that both, classical nucleation theory (CNT) (section 3.4.1) as well as the growth laws for the evolution of the precipitate radius (section 3.4.2) are differential equations, makes it necessary to integrate these expressions over time.

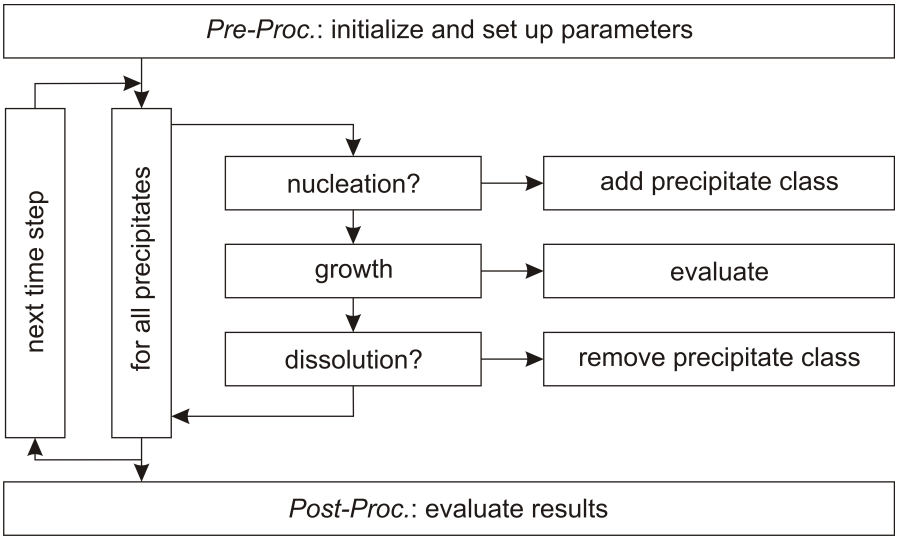

Figure 3.14: Flow chart for numerical integration of the evolution equations for precipitate nucleation and growth [7].

This is realized in MatCalc applying a numerical treatment of the evolution equations similar to the classical Kampmann - Wagner approach [79], according to the flow chart in figure 3.14. In the solution procedure, the time is discretised and the precipitate distribution is subdivided into different precipitate classes. All precipitate evolution equations are calculated for every precipitate class within each time step, determining all precipitate parameters. A detailed explanation of this algorithm can be found in reference [66].

Chapter 4

Results and Discussion

In this chapter, the models, previously introduced in section 3.4, are applied for the investigation of the precipitation of nitrides and carbides in microalloyed steel, using the thermo kinetic software MatCalc (version 5.30).

Starting with an analysis of the thermodynamic information in three different databases demonstrates, that there is room for improvement of the thermodynamic data. Therefore, the solubility products of several microalloy nitrides and carbides are studied in detail with special emphasis on microalloyed steel. Appropriate phase descriptions are determined and implemented in the thermodynamic database 'mc_steel' (version 1.86) [83]. Additional essential ingredients for modeling and simulation of precipitation kinetics are analysed, among them the precipitate/matrix volumetric misfit, the temperature dependent Young's modulus, as well as the ratio between bulk and grain boundary diffusion, and temperature dependent formulations are presented. Performing detailed parameter studies, predominant precipitation at grain boundaries as well as the precipitation of randomly distributed particles are analysed, with special emphasis on the sensitivity of the calculations on these input quantities.

With the knowledge of the model characteristics of both, the novel grain boundary model (GBDG) as well as the classical treatment of randomly distributed precipitates with spherical diffusion fields (RSDG), together with the established input parameters, the precipitation kinetics of AlN and VN are calculated, considering simultaneous precipitation at grain boundaries and at dislocations. The calculations are carried out for

15 different chemical compositions at various different annealing temperatures, in ferrite as well as austenite, and compared to independent experimental data from literature. Finally, the precipitation processes of TiN, TiC and NbC during casting are analysed, taking into account the microsegregation of alloying elements during solidification of microalloyed steel. A new approach is presented, which allows calculating the precipitation parameters locally at every point of the dendrite.

4.1 Thermodynamic Information in Three Different Databases

When doing precipitation kinetics simulation, the main input quantity is the thermodynamic information. These thermodynamic data are generated from experimental investigations and summarised in thermodynamic databases. Hence, the thermodynamic assessments of different sources can show some discrepancies. The following section deals with a preliminary investigation of three different databases. In addition to the MatCalc database 'mc_steel' (version 1.18) [83], the thermodynamic information in the commercial databases 'TCFE3' [84] and 'Fe-data6' [85] are analysed and compared to each other. Therefore, equilibrium calculations of microalloying phases in three alloys are carried out [86]. The chemical compositions of the alloys are given in table 4.1.

Table 4.1: Chemical composition of three typical microalloyed steels.

steel no.	C	Si	Mn	Al	Ti	V	N	Nb
1	0.22	0.243	1.2	0.025	0.002	0.001	0.0061	0.36
2	0.16	0.300	1.5	0.033	0.015	0.065	0.0097	0.03
3	0.40	0.590	1.4	0.030	0.021	0.150	0.0170	-

The simulations are performed using the description of the 'complex solution phase' (MX phase) of the three different databases. This complex solution phase is modeled according to the CALPHAD approach [70] as a part of the fcc matrix phase. For the simulation of microalloying phases with fcc structure, composition sets are defined

with microalloying elements as major constituents. However, minor amounts of other interstitial as well as substitutional elements are considered in the phase description, this is why we are talking of 'complex solution phases'.

Figures 4.1 to 4.3 show the calculated equilibrium phase fractions of the microalloy phases versus temperature, using the three different databases [86].

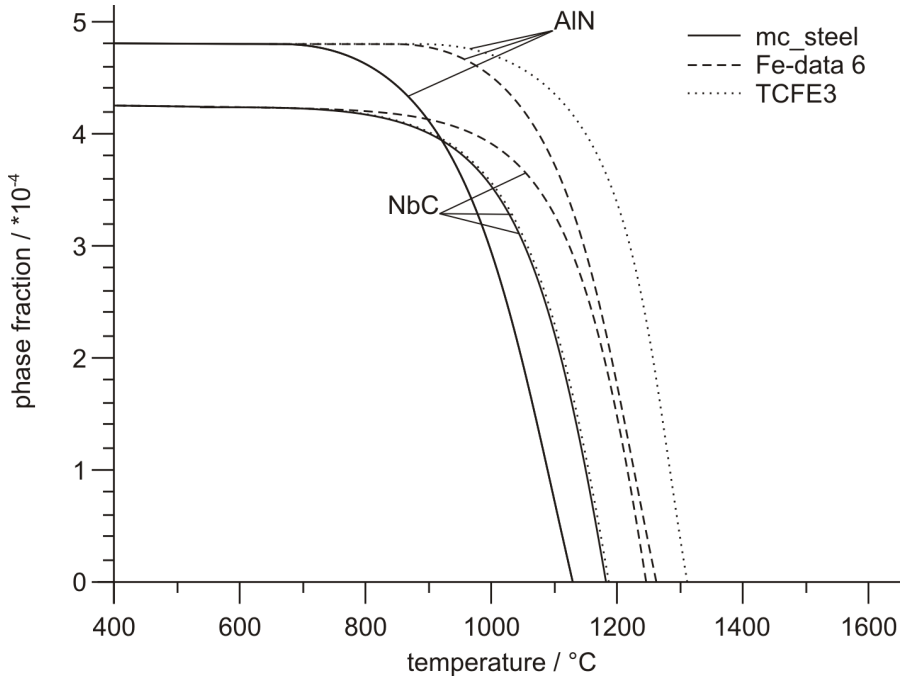

Figure 4.1: Comparison of the calculated phase fractions versus temperature of the phases NbC and AlN in steel 1, using three different databases.

Depending on the investigated alloy, precipitation of VC, NbC, Ti(C,N) or AlN is observed. The solution temperature for Ti(C,N) is calculated very similar, using the different databases. However, essential discrepancies in the calculated phase fraction of Ti(C,N) are observed with decreasing temperature. The database 'Fe-data6' provides generally smaller values compared to the other two databases. Additionally, it should be noted, that the chemical composition of Ti(C,N) differs also in a wide range, depending on the database used for the calculation.

Apart from Ti(C,N), most similar values concerning the solution temperature are calculated for NbC. The calculations with the databases 'mc_steel' and 'Fe-data6' deliver quite similar results and the database 'TCFE3' calculates a value, which is only 70°C

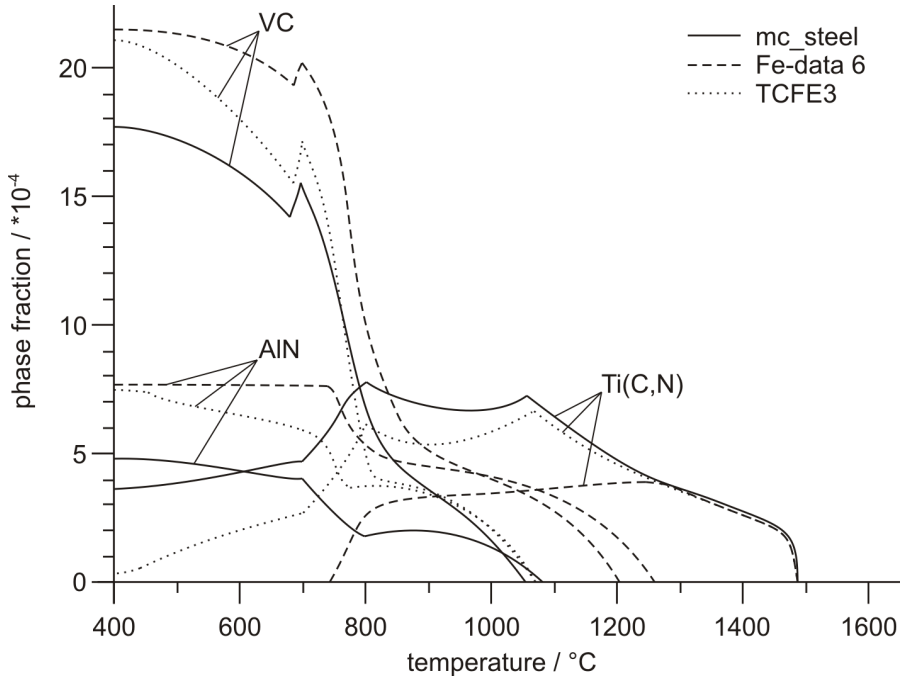

Figure 4.2: Comparison of the calculated phase fractions versus temperature of the phases VC, Ti(C,N) and AlN in steel 2, using three different databases.

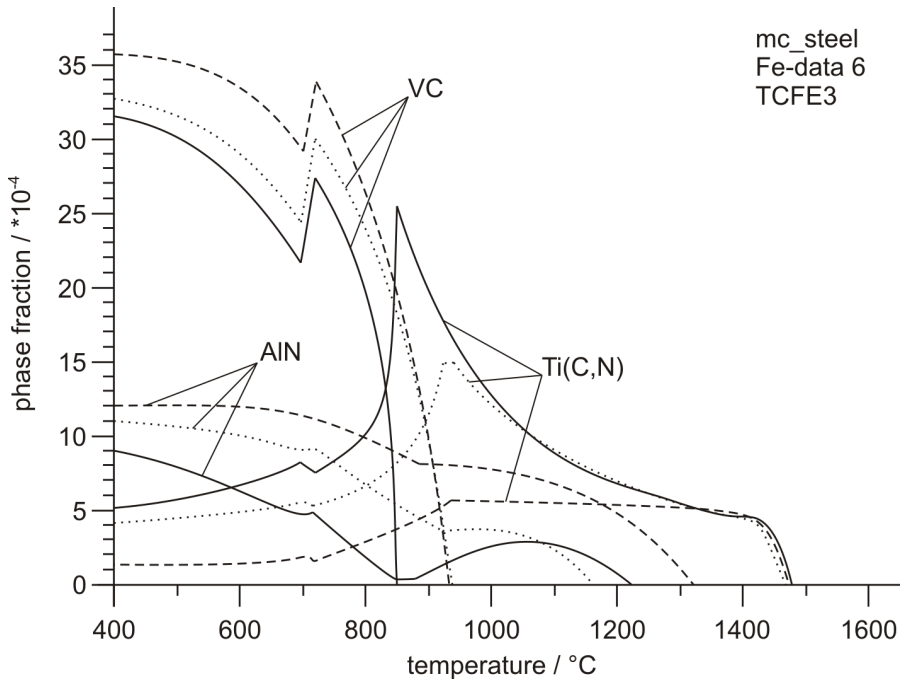

Figure 4.3: Comparison of the calculated phase fractions versus temperature of the phases VC, Ti(C,N) and AlN in steel 3, using three different databases.

higher, see figure 4.1.

The discrepancies of the predicted solution temperature are much more pronounced in the case of VC. Considering steel 2, the databases 'mc_steel' and 'TCFE3' predict a solution temperature of 1050 °C, while the database 'Fe-data6' calculates 1200 °C.

Most dramatic differences are observed by the calculation of the equilibrium phase fraction of AlN. In the case of steel 1, the database 'TCFE3' calculates a solution temperature of 1315 °C, 'Fe-data6' predicts 1260°C and the calculation with the database 'mc_steel' delivers 1125 °C. Thus, the difference in the predicted solution temperatures of AlN, using the databases 'TCFE3' and 'mc_steel', is about 190 °C.

Substantial discrepancies are also observed regarding the predicted equilibrium phase fraction of the microalloy phases when using the different databases, especially for the calculation at low temperatures. These preliminary investigations clearly demonstrate the sensitivity of the calculations on the thermodynamic input data and thus the importance of the accuracy of these data. Therefore, the solubility of different stoichiometric phases is investigated in detail subsequently.

4.2 Solubility Products in Austenite

For microalloyed steels, it is common to express the solubility of nitrides and carbides using so-called solubility products, see section 3.2.3. With these data, thermodynamic parameters can be adjusted by comparing equilibrium calculations of solution temperatures of a nitride or carbide with the values obtained from the solubility product. The present section deals with the investigation of the solubility products of stoichiometric microalloy nitrides and carbides in the austenite phase field. Furthermore, the solution temperatures are calculated based on the thermodynamic databases 'TCFE3' [84], 'Fe-data6' [85] and 'mc_steel' (version 1.86) [83] and compared to the solubility products given in literature. For the calculation of the solution temperatures, the ratio between the amount of the interstitial element (e.g. N) and the substitutional element (e.g. Al) is assumed to be 1/10.

4.2.1 Aluminium Nitride

A large number of papers are published on the solubility of AlN in austenite. Authors carried out experimental investigations [24, 29, 87–92] as well as thermodynamic calculations [93, 94] and determined various expressions for the description of the solubility of AlN in austenite. Table 4.2 and figure 4.4 summarize these data. In addition to the classical description of the solubility product (no. 1-14), Mayrhofer [89] introduced a formulation accounting for high Al contents (solubility product 15).

Unfortunately, the data obtained by the different authors show a very large scatter. This large scatter in the available solubility products for AlN precipitation gave motivation for detailed investigations already two decades ago. Wilson and Gladman [26] studied the solubility products published by different authors. Based on their assessment, they identified solubility product 5 [87] listed in table 4.2 as a 'most likely' one. They found support by the work of Irvine et al. [36], who report that their results are in close agreement with the results of Erasmus [24] and König et al. [88]. Particularly, the work of König et al. [88] seems to be much substantiated, because they investigated the solubility product of AlN using several different chemical compositions. In the present

assessment, we base our analysis on the experiments reported in references [41, 88, 89], where AlN precipitates have been clearly detected after different solution treatments, indicated by dots in figure 4.4, and have not been identified in treatments at higher temperature. The chemical compositions and different heat treatment temperatures are considered as the lower limit for the solubility product of AlN in austenite.

Table 4.2: Available solubility products of AlN.

no.	$\log k_s$	ref.
1	$4.382 - 11085/T$	[94]
2	$0.528 - 5938/T$	[90]
3	$1,79 - 7184/T$	[91]
4	$4,5989 - 11568/T$	[95]
5	$1,03 - 6770/T$	[87]
6	$1,95 - 7400/T$	[92]
7	$0,725 - 6180/T$	[24]
8	$0,309 - 6015/T$	[24]
9	$1,48 - 7500/T$	[35]
10	$1,8 - 7750/T$	[88]
11	$3,577 - 10020/T$	[29]
12	$2,923 - 9200/T$	[29]
13	$3,079 - 9295/T$	[29]
14	$6,4 - 14356/T$	[93]
15	$0,18 - 5675/T + 2,4 \cdot Al[wt\%]$	[89]

Together with the data of Saunders [96] and Zhang [97] for Al in the Fe matrix phases, following expression for the Gibbs energy of the AlN phase has been found most suitable for the simulations in the present work and is implemented in the database 'mc_steel'.

$$G(FCC\_A1, AL:N;0)\ 298.15\ + GHSERAL\# + GHSERNN\# + 80 \cdot T;$$
$$6000.00\ N$$
$$G(FCC\_A1, AL, FE:VA;0)\ 298.15\ - 76066.1 + 18.6758 \cdot T;\ 6000.00\ N$$

$$G(FCC\_A1, AL, FE : VA; 1)\ 298.15\ +21167.4 + 1.3398 \cdot T;\ 6000.00\ N$$

$$G(BCC\_A2, AL : N; 0)\ 298.15\ +23000 + 10 \cdot T + GHSERAL\#$$
$$+ 3 \cdot GHSERNN\#;\ 6000.00\ N$$

$$G(BCC\_A2, AL, FE : VA; 0)\ 298.15\ -122960 + 31.9888\dot{T};\ 6000.0\ N$$

$$G(BCC\_A2, AL, FE : VA; 1)\ 298.15\ +3089.2;\ 6000.0\ N$$

$$G(ALN, AL : N; 0)\ 298.15\ -262982 + 63 \cdot T + GHSERAL\#$$
$$+ GHSERNN\#;\ 6000.00\ N$$

The corresponding curve is shown as solid bold line in figure 4.4.

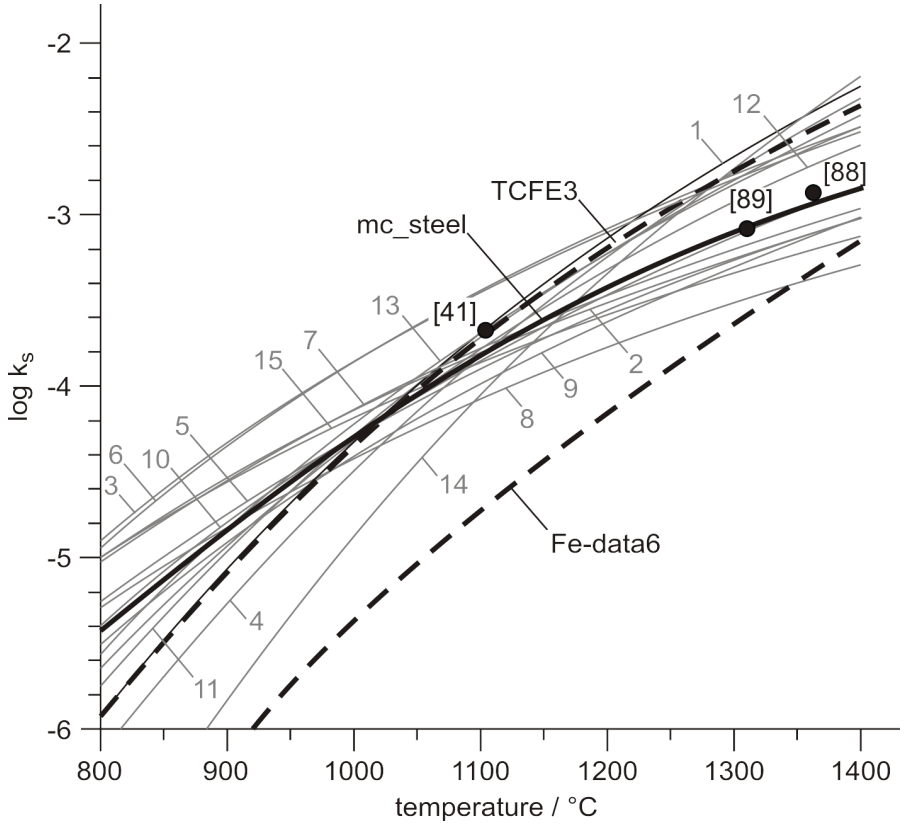

Figure 4.4: Comparison of solubility products and thermodynamic data of AlN.

4.2.2 Vanadium Nitride

The solubility of VN in the austenite phase field has been investigated using different experimental techniques [36,98,99] as well as thermodynamic calculations [49,100]. The corresponding relations are summarized in table 4.3 and figure 4.5. Nevertheless, it has been reported that, in V-microalloyed steels, the effect of Mn on the activity of V is especially important [36,49]. Mn is known to increase the activity coefficient of V and, at the same time,. decrease the activity coefficient of C [49]. Therefore, the solubility product of VN in austenite increases slightly with increasing content of Mn [1]. Thus, Irvine et al. [36] suggested to take into account the Mn content, according to solubility product 1 in table 4.3, especially for microalloyed steels with significant Mn contents. All three databases predict the same solution behavior for VN in austenite. However, especially in the low temperature range of the austenite, they show some discrepancies compared to the experimental data [36,98,99] being in reasonable agreement.

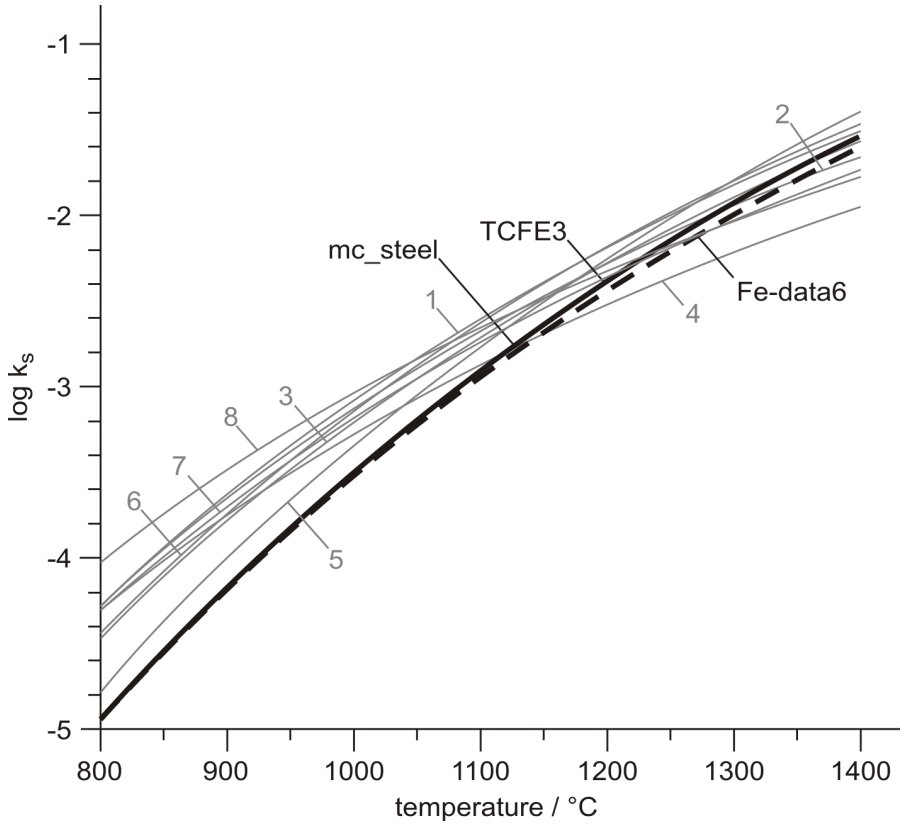

Figure 4.5: Comparison of solubility products and thermodynamic data of VN.

Table 4.3: Available solubility products of VN.

no.	$\log k_s$	ref.
1	$3.4 - 8330/T + 0.12 \cdot Mn[wt\%]$	[36]
2	$3.02 - 7840/T$	[98]
3	$3.63 - 8700/T$	[99]
4	$2.27 - 7070/T$	[100]
5	$-10.34 - 7600/T + 1.8 \cdot \ln T + 7.2 \cdot 10^{-5} T$	[49]
6	$3.84 - 8890/T$	[49]
7	$2.86 - 7700/T$	[27]
8	$2.21 - 6680/T$	[101]

The thermodynamic database 'mc_steel' incorporates the assessments of Ohtani and Hillert [102, 103], which reads

$$
\begin{aligned}
&G(FCC\_A1, V:N;0)\ 298.15\ -215000 + 101\cdot T - 2.22\cdot T\cdot LN(T)\\
&\qquad + 0.00073\cdot T^2 + GHSERVV\# + GHSERNN\#;\ 6000.00\ N\\
&G(FCC\_A1, FE, V:VA;0)\ 298.15\ -15291 - 4.138\dot{T};\ 6000.00\ N\\
&G(FCC\_A1, FE, V:N;0)\ 298.15\ -60000;\ 6000.00\ N\\
&G(FCC\_A1, FE, V:N, VA;0)\ 298.15\ -120000;\ 6000.00\ N\\
&G(FCC\_A1, V:N, VA;0)\ 298.15\ -131000 + 47.1\cdot T;\ 6000.00\ N\\
&G(BCC\_A2, V:N;0)\ 298.15\ +843000 + GHSERVV\# + 3\cdot GHSERNN\#;\\
&G(BCC\_A2, V:N, VA;0)\ 298.15\ -1680000 + 325\cdot T;\ 6000.00\ N\\
&G(BCC\_A2, FE, V:VA;0)\ 298.15\ -23674 + 0.465\cdot T;\ 6000.00\ N\\
&G(BCC\_A2, FE, V:VA;1)\ 298.15\ +8283;\ 6000.00\ N\\
&G(VN, V:N;0)\ 298.15\ -215000 + 101\cdot T - 2.22\cdot T\cdot LN(T)\\
&\qquad + 0.00073\cdot T^2 + GHSERVV\# + GHSERNN\#;\ 6000.00\ N\\
&G(VN, V:VA;0)\ 298.15\ +7500 + 1.7\cdot T + GHSERVV\#;\ 4000.00\ N\\
&G(VN, V:N, VA;0)\ 298.15\ -131000 + 47.1\cdot T;\ 6000.00\ N.
\end{aligned}
$$

Only solubility product 5, introduced by Lagneborg et al. [49], is in acceptable agreement with the three thermodynamic databases. However, this solubility product is not representative, because it is also deduced from the assessment of Ohtani and Hillert [102].

4.2.3 Vanadium Carbide

The solubility of VC in the austenite phase field is significantly higher than those of the other microalloy carbides and nitrides. However, the description of VC is a little more complicated due to stoichiometric effects. There is some evidence that the chemical formula for vanadium carbide is close to V_4C_3 [1,104]. Therefore, the solubility product may be defined as

$$k_s = \frac{[V]^{4/3}[C]}{a^{1/3}_{(V_4C_3)}}, \tag{4.1}$$

rather than equation 3.7. However, not all authors accepted this definition. For instance Narita [99] based his solubility product on the classical formulation according to 3.7, whereas Bungardt et al. [105], Wriedt et al. [104] and Aronsson [106] use equation 4.1 assuming the formation of V_4C_3. The different expressions for the solubility product of VC are listed in table 4.4 and pictured in figure 4.6.

Table 4.4: Available solubility products of VC.

no.	$\log k_s$	ref.
1	$6.72 - 9500/T$	[99]
2	$4.45 - 6560/T$	[104]
3	$7.06 - 10800/T$	[105]
4	$5.35 - 8000/T$	[106]
5	$3.685 - 5531/T$	[60]
6	$1.32 - 2980/T + (1160/T - 0.2) \cdot C[wt\%]$	[107]

Especially, the work of Wriedt et al. [104] (solubility product 2) seems to be substantiated, since they investigated several alloys with different V/C ratios. Acevedo et al. [60]

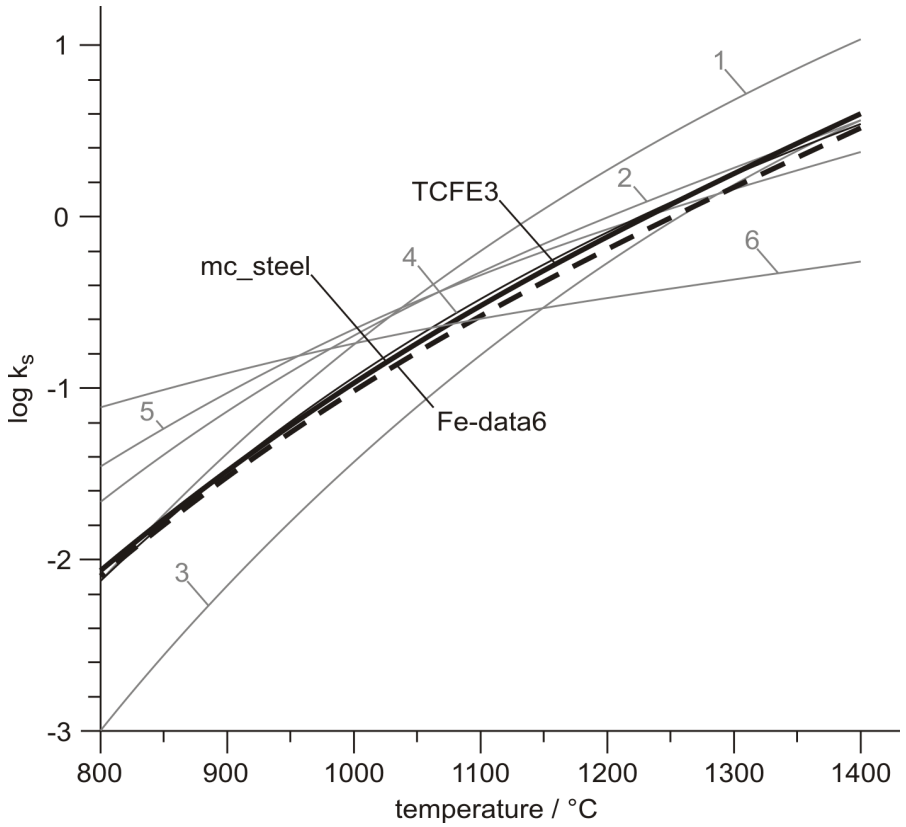

Figure 4.6: Comparison of solubility products and thermodynamic data of VC.

identified the formation of V_6C_5 carbides by doing TEM investigations and, therefore, they introduced solubility product 5. Ohtani et al. [107] related their expression of the solubility of VC to the C content, see solubility product 6.

Similar to the observations for VN, all three databases predict the same solution behavior for VC in austenite, which is in close agreement to solubility product 4 [106].

The database 'mc_steel' contains the thermodynamic assessment of Huang [108], which describes the solubility of VC with

$$G(FCC\_A1, V:C; 0)\ 298.15\ -117302 + 262.57 \cdot T - 41.756 \cdot T \cdot LN(T) - 0.00557101 \cdot T^2 + 590546 \cdot T^{-1};\ 6000.00\ N$$

$$G(FCC\_A1, V:C, VA; 0)\ 298.15\ -74811 + 10.201 \cdot T;\ 6000.00\ N$$

$$G(FCC\_A1, V:C, VA; 1)\ 298.15\ -30394;\ 6000.00\ N$$

$$G(FCC\_A1, FE, V:VA; 0)\ 298.15\ -15291 - 4.138 \cdot T;\ 6000.00\ N$$

$G(FCC\_A1, FE, V:C; 0)\ 298.15\ -7645.5 - 2.069 \cdot T;\ 6000.00\ N$

$G(FCC\_A1, FE, V:C; 1)\ 298.15\ -7645.5 - 2.069 \cdot T;\ 6000.00\ N$

$G(FCC\_A1, FE, V:C, VA; 0)\ 298.15\ -40000;\ 6000.00\ N$

$G(BCC\_A2, V:C; 0)\ 298.15\ +108449 + GHSERVV\# + 3 \cdot GHSERCC\#;$
$6000.00\ N$

$G(BCC\_A2, V:C, VA; 0)\ 298.15\ -297868;\ 6000.00\ N$

$G(BCC\_A2, FE, V:VA; 0)\ 298.15\ -23674 + 0.465 \cdot T;\ 6000.00\ N$

$G(BCC\_A2, FE, V:VA; 1)\ 298.15\ +8283;\ 6000.00\ N$

$G(BCC\_A2, FE, V:C; 0)\ 298.15\ -23674 + 0.465 \cdot T;\ 6000.00\ N$

$G(BCC\_A2, FE, V:C; 1)\ 298.15\ +8283;\ 6000.00\ N$

$G(VC, V:C; 0)\ 298.15\ -117302 + 262.57 \cdot T - 41.756 \cdot T \cdot LN(T)$
$-0.00557101 \cdot T^2 + 590546 \cdot T^{-1};\ 6000.00\ N$

$G(VC, V:VA; 0)\ 298.15\ +7500 + 1.7 \cdot T + GHSERVV\#;\ 4000.00\ N$

$G(VC, V:C, VA; 0)\ 298.15\ -74811 + 10.201 \cdot T;\ 6000.00\ N$

$G(VC, V:C, VA; 1)\ 298.15\ -30394;\ 6000.00\ N.$

4.2.4 Niobium Nitride

Several authors have reported about the solubility product of NbN in austenite. The equations are summarized in table 4.5 and figure 4.7. Whereas the solubility products 1-4 are determined experimentally [99, 109–111] (e.g. chemical separation of particles), others are determined by thermodynamic calculations, e.g. solubility product 7 [112]. However, solubility product 7 is an approximate expression for the chemical compound $NbN_{7/8}$. All other authors formulated the solubility of NbN based on the stoichiometric compound NbN. Gladman [1] recommends to use solubility product 1, determined by Narita [99], which is in very close agreement with the data of Smith [109], Mori et al. [111] and Klinkenberg et al. [57].

The thermodynamic database 'TCFE3' reproduces these recommended values best. The databases 'Fe_data6' and 'mc_steel calculate approximately the same results, which show

Table 4.5: Available solubility products of NbN.

no.	$\log k_s$	ref.
1	$2.8 - 8500/T$	[99]
2	$4.04 - 10230/T$	[109]
3	$3.7 - 10800/T$	[110]
4	$3.79 - 10150/T$	[111]
5	$1.71 - 7000/T$	[49]
6	$6.63 - 12500/T$	[49]
7	$2.86 - 7927/T$	[112]
8	$4.2 - 10000/T$	[113]
9	$3.82 - 9940/T$	[57]
10	$5.09 - 11880/T$	[101]

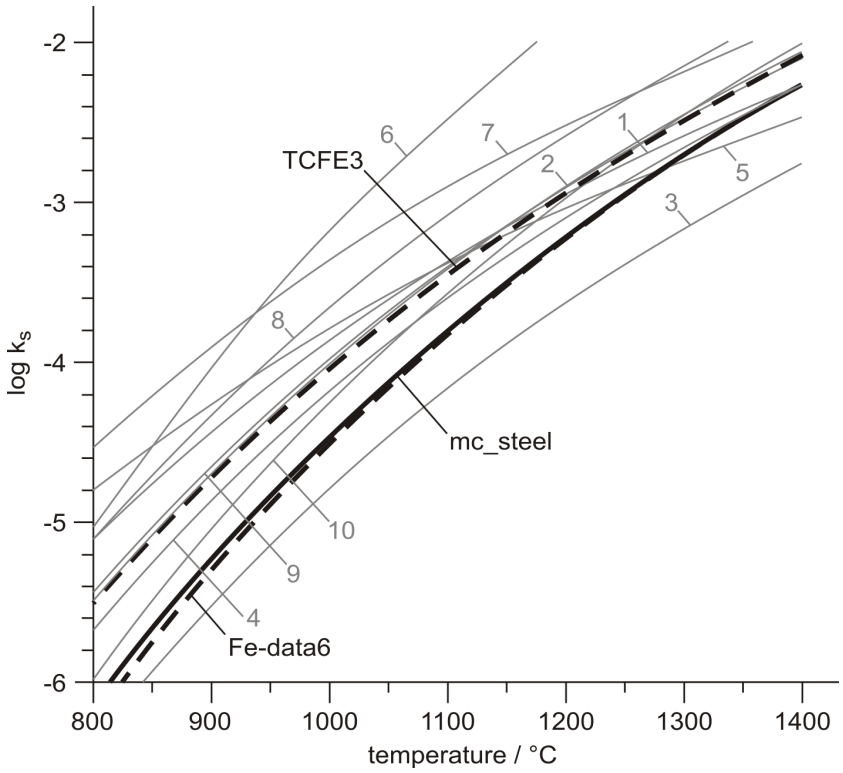

Figure 4.7: Comparison of solubility products and thermodynamic data of NbN.

some discrepancies to the experimentally obtained and recommended solubility products. However, the basis for the calculation of NbN in the database 'mc_steel' is the thermodynamic assessment after Lee [114], which is given with

$$G(FCC\_A1, NB:N;0)\ 298.15\ -227779+120.567\cdot T-4\cdot T\cdot LN(T)$$
$$+GHSERNB\#+GHSERNN\#;\ 6000.00\ N$$
$$G(FCC\_A1, NB:N,VA;0)\ 298.15\ -65218;\ 6000.00\ N$$
$$G(FCC\_A1, FE,NB:VA;0)\ 298.15\ -2000;\ 6000.00\ N$$
$$G(BCC\_A2, NB:N;0)\ 298.15\ -207283+110.085\cdot T+GHSERNB\#$$
$$+3\cdot GHSERNN\#;\ 6000.00\ N$$
$$G(BCC\_A2, NB:N,VA;0)\ 298.15\ -357277+129.474\cdot T;\ 6000.00\ N$$
$$G(BCC\_A2, FE,NB:VA;0)\ 298.15\ -4400+6.333\cdot T;\ 6000.00\ N$$
$$G(NBN, NB:N;0)\ 298.15\ -227779+120.567\cdot T-4\cdot T\cdot LN(T)$$
$$+GHSERNB\#+GHSERNN\#;\ 6000.00\ N$$
$$G(NBN, NB:VA;0)\ 298.15\ +13500+1.7\cdot T+GHSERNB\#;\ 5000.00\ N$$
$$G(NBN, NB:N,VA;0)\ 298.15\ -65218;\ 6000.00\ N.$$

4.2.5 Niobium Carbide

Most papers have been published on the solubility of NbC in austenite. The determination methods cover many experimental techniques as well as thermodynamic calculations or statistical treatments of existing solubility products. Lots of them are summarized in the work of Palmiere et al. [115]. The different solubility products for NbC in austenite are given in table 4.6 and shown in figure 4.8.

Different authors report about different chemical formulas, similar to the case of VC. Whereas some authors assume the stoichiometric compound NbC [99,107,115–119,122–124], others [111,112,120,121] base the formulation of their solubility product on $NbC_{7/8}$. Palmiere et al. [115] performed detailed atom probe investigations and demonstrated that precipitates ranging in size from 0.5 to 10 nm have compositions ranging from $NbC_{8/10}$ to stoichiometric NbC. However, they suggested to use a stoichiometric de-

Table 4.6: Available solubility products of NbC.

no.	$\log k_s$	ref.
1	$2.06 - 6700/T$	[115]
2	$-0.63 - 2500/T$	[116]
3	$3.04 - 7290/T$	[117]
4	$3.7 - 9100/T$	[118]
5	$3.42 - 7900/T$	[99]
6	$4.37 - 9290/T$	[119]
7	$3.18 - 7700/T$	[111]
8	$3.11 - 7520/T$	[120]
9	$2.96 - 7510/T$	[120]
10	$3.4 - 7200/T$	[120]
11	$2.81 - 7019.5/T$	[112]
12	$3.4 - 7920/T$	[121]
13	$2.26 - 6670/T$	[36]
14	$3.89 - 8030/T + (1150/T - 0.05) \cdot C[wt\%]$	[122]
15	$1.18 - 4880/T + (1590/T - 0.1) \cdot C[wt\%]$	[107]
16	$1.74 - 5600/T + (1380/T - 0.027) \cdot C[wt\%]$	[123]
17	$3.31 - 7970/T + (1371/T - 0.9) \cdot Mn[wt\%] - (75/T - 0.0504) \cdot Mn^2[wt\%]$	[124]
18	$3.31 - 7970/T - (735/T - 0.348) \cdot Si[wt\%]$	[124]
19	$3.31 - 7970/T + (1113/T - 0.691) \cdot Cr[wt\%] - (38/T - 0.0228) \cdot Cr^2[wt\%]$	[124]
20	$3.31 - 7970/T + (148/T - 0.0904) \cdot Ni[wt\%] + (8.5/T - 0.0068) \cdot Ni^2[wt\%]$	[124]

scription according to solubility product 1. Compared to other solubility products in figure 4.8, this description predicts markedly lower solubility levels of Nb in austenite. Therefore, the authors argued that the measured data using the atom probe yielded a

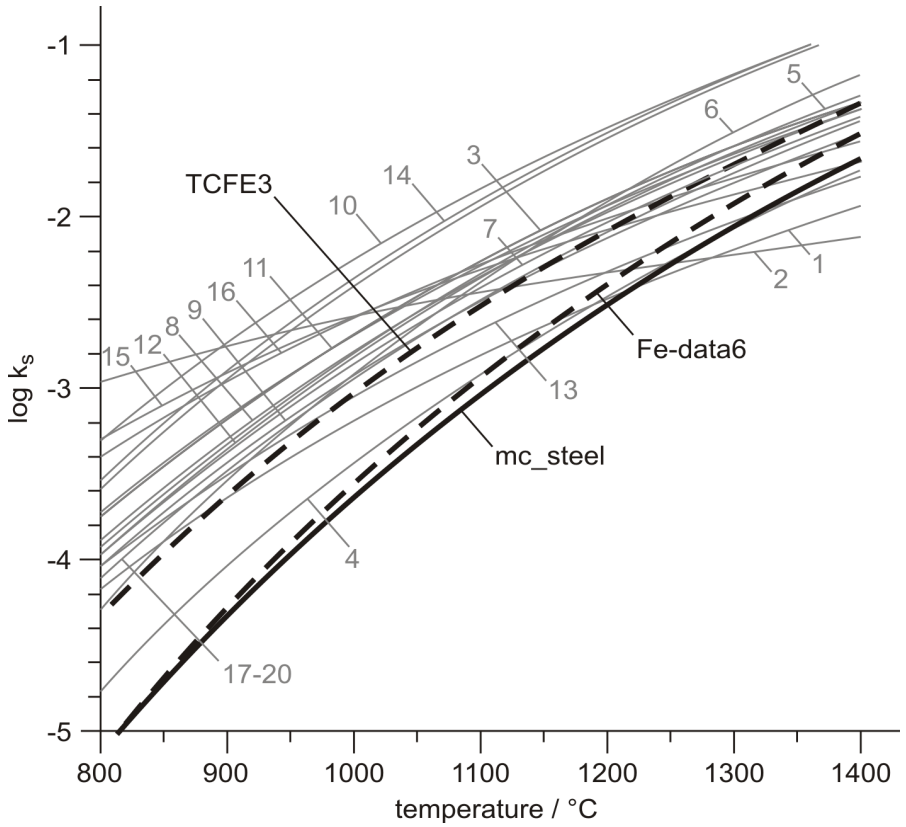

Figure 4.8: Comparison of solubility products and thermodynamic data of NbC.

more reliable description of the solution behavior compared to other techniques employed for previous investigations. Nordberg and Aronsson [120] did statistical investigations of existing solubility products using the method of least squares. Table 4.6 shows three different solubility products provided by these authors. Solubility product 8 is based on the assumption of the formation of $NbC_{7/8}$, whereas solubility product 9 underlies the stoichiometric compound of NbC. In addition to the statistical analysis, they performed thermodynamic calculations resulting in solubility product 10, which is also based on the formation of $NbC_{7/8}$. Some authors extended the classical description of the solubility product (equation 3.7) by an additional term, considering ternary interaction parameters. Therefore, Balasubramanian et al. [122] as well as Ohtani et al. [107, 123] added a term taking into account the C-concentration and the strong interactions between Nb and C at higher C concentrations, see solubility products 14-16. Moreover, Koyama et al. [124] studied the influence of Mn, Si, Cr and Ni on the solubility of NbC in the

austenite phase field, see solubility products 17-20. Mn and Cr increase the solubility of NbC remarkably. Also, Ni increases the solubility of NbC in austenite at comparatively low temperatures, while the effect is weak at higher temperatures. On the other hand, additions of Si decrease the solubility of NbC. Koyama et al. [124] attributed these effects to the effect of each element on the activity of Nb as well as that of C.
The three thermodynamic databases predict lower solubilities for NbC in austenite compared to most of the solubility products. This is in agreement with the atom probe investigation of Palmiere et al. [115]. Furthermore, the slope of the curves of the thermodynamic assessments differ significantly from those of most solubility products, which is related to deviations in entropic contributions. The thermodynamic database 'mc_steel' contains the description of Povoden et al. [125] given with

$$
\begin{aligned}
&G(FCC\_A1, NB:C;0)\ 298.15\ -162000+283.912\cdot T-46.34274\cdot T\cdot LN(T)\\
&\qquad -0.0029287\cdot T^2-1.02788144\cdot 10^9\cdot T^{-3}+563374\cdot T^{-1};\ 6000.00\ N\\
&G(FCC\_A1, FE, NB:VA;0)\ 298.15\ -2000;\ 6000.00\ N\\
&G(FCC\_A1, FE, NB:C, VA;0)\ 298.15\ -40000;\ 6000.00\ N\\
&G(FCC\_A1, NB:C, VA;0)\ 298.15\ -83000+20\cdot T;\ 6000.00\ N\\
&G(FCC\_A1, NB:C, VA;2)\ 298.15\ -61342+25.207\cdot T;\ 6000.00\ N\\
&G(BCC\_A2, NB:C;0)\ 298.15\ +520879-70.807\cdot T\\
&\qquad +GHSERNB\#+3\cdot GHSERCC\#;\ 6000.00\ N\\
&G(BCC\_A2, NB:C, VA;0)\ 298.15\ -588143;\ 6000.00\ N\\
&G(NBC, NB:C;0)\ 298.15\ -162000+283.912\cdot T-46.34274\cdot T\cdot LN(T)\\
&\qquad -0.0029287\cdot T^2-1.02788144\cdot 10^9\cdot T^{-3}+563374\cdot T^{-1};\ 6000.00\ N\\
&G(NBC, NB:VA;0)\ 298.15\ +13500+1.7\cdot T+GHSERNB\#;\ 5000.00\ N\\
&G(NBC, NB:C, VA;0)\ 298.15\ -83000+20\cdot T;\ 6000.00\ N\\
&G(NBC, NB:C, VA;2)\ 298.15\ -61342+25.207\cdot T;\ 6000.00\ N,
\end{aligned}
$$

which is deduced from the assessment of Huang et al. [126, 127].

4.2.6 Titanium Nitride

Studies of the solubility of TiN have shown that, from all microalloy carbides and nitrides, TiN is by far the most stable one [1]. Different expressions of solubility products have been obtained by experimental investigations [99, 128–131] as well as thermodynamic analysis [131–133]. The results are presented in table 4.7 and illustrated in figure 4.9.

Table 4.7: Available solubility products of TiN.

no.	$\log k_s$	ref.
1	$3.82 - 15020/T$	[99]
2	$4.35 - 14890/T$	[131]
3	$0.32 - 8000/T$	[128]
4	$8.48 - 12900/T + 1.457 \cdot \ln T + 0.00028 \cdot T$	[132]
5	$5.19 - 15490/T$	[129]
6	$5 - 14400/T$	[133]
7	$5.15 - 13925/T$	[129]
8	$4.94 - 14400/T$	[130]
9	$5.4 - 15791/T$	[27]

The data of Wada and Pehlke [130] are in very good agreement with those of Roberts [133] (solubility products 6 and 8). Furthermore, the values of Kunze [129] are very similar to those used by Turkdogan [27] (solubility products 5 and 9). The lowest solubility of TiN in austenite is predicted by Narita [99] (solubility product 1), whereas the highest values are proposed by using an estimation after Roberts [133], reported in the work of Kunze [129] (solubility product 7). Furthermore, figure 4.9 shows that the solubility data of the different authors underlie a wide spread. The scatter can perhaps be attributed to the low solubility of TiN in austenite, bearing in mind that TiN can precipitate in considerable amounts in liquid steel. However, apart from the data of Matsuda and Okumura [128], the slope of the curves are similar and parallel to each other, but the intercept varies significantly. All three databases predict the same

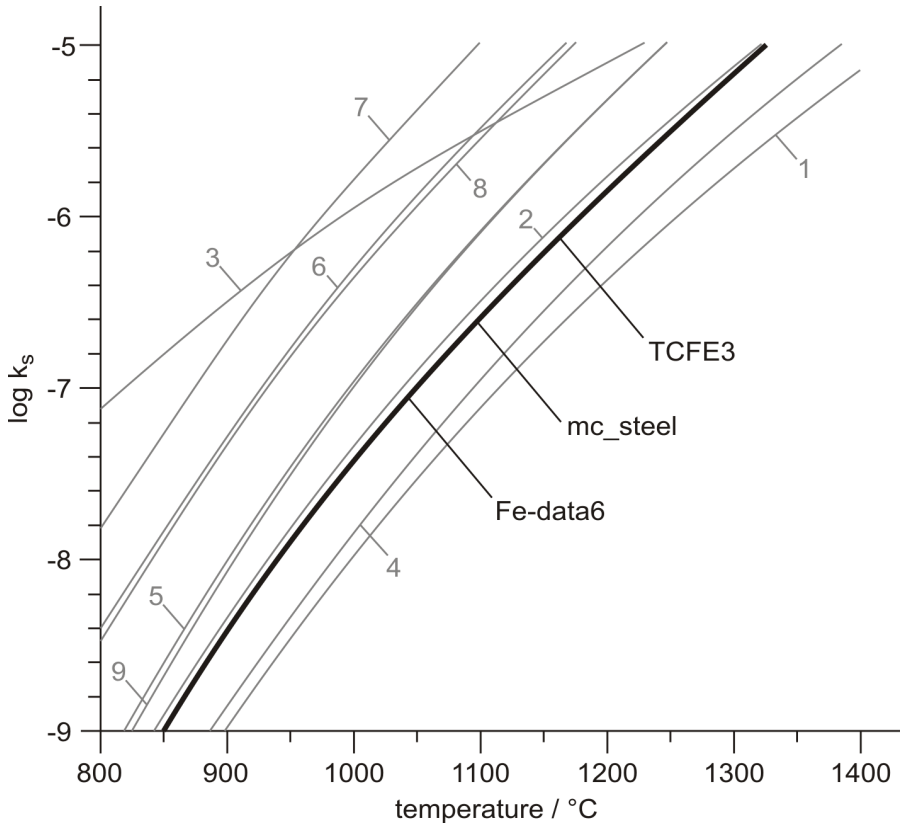

Figure 4.9: Comparison of solubility products and thermodynamic data of TiN.

solubility temperatures for TiN in austenite. The thermodynamic database 'mc_steel' contains thermodynamic information of Lee [114] and Frisk [134], which is given with

$$G(FCC\_A1, TI:N;0)\ 298.15\ GHSERTIN\#;\ 6000.00\ N$$

$$G(FCC\_A1, TI:N,VA;0)\ 298.15\ -42704;\ 6000.00\ N$$

$$G(FCC\_A1, TI:N,VA;1)\ 298.15\ -13989;\ 6000.00\ N$$

$$G(FCC\_A1, FE,TI:VA;0)\ 298.15\ -51136+10.4\cdot T;\ 6000.00\ N$$

$$G(FCC\_A1, FE,TI:VA;1)\ 298.15\ -1950-6\cdot T;\ 6000.00\ N$$

$$G(FCC\_A1, FE,TI:VA;2)\ 298.15\ +14875;\ 6000.00\ N$$

$$G(BCC\_A2, TI:N;0)\ 298.15\ +2604202+118.04\cdot T+GHSERTIN\#$$
$$+2\cdot GHSERNN\#;\ 6000.00\ N$$

$$G(BCC\_A2, TI:N,VA;0)\ 298.15\ -3215338;\ 6000.00\ N$$

$$G(BCC\_A2, FE,TI:VA;0)\ 298.15\ -59098+11.5\cdot T;\ 6000.00\ N$$

$G(BCC\_A2, FE, TI : VA; 1)\ 298.15\ -1796 + 1 \cdot T;\ 6000.00\ N$

$G(BCC\_A2, FE, TI : VA; 2)\ 298.15\ +5602 + 3.5 \cdot T;\ 6000.00\ N$

$G(TIN, TI : N; 0)\ 298.15\ GHSERTIN\#;\ 6000.00\ N$

$G(TIN, TI : VA; 0)\ 298.15\ +6000 - 0.1 \cdot T + GHSERTI\#;\ 3000.00\ N$

$G(TIN, TI : N, VA; 0)\ 298.15\ -42704;\ 6000.00\ N$

$G(TIN, TI : N, VA; 1)\ 298.15\ -13989;\ 6000.00\ N.$

The calculations with these input data are in very good agreement with the work of Inoue et al. [131] (solubility product 2), who did experimental investigations as well as thermodynamic calculations.

4.2.7 Titanium Carbide

The solubility product equations for TiC in austenite are listed in table 4.8 and are shown graphically in figure 4.10.

Table 4.8: Available solubility products of TiC.

no.	$\log k_s$	ref.
1	$5.33 - 10475/T$	[99]
2	$2.75 - 7000/T$	[36]
3	$5.12 - 10300/T$	[1]
4	$4.03 - 8720/T$	[113]
5	$4.1 - 9070/T + (1205/T + 0.24) \cdot C[wt\%]$	[135]
6	$4.2 - 8970/T + (1600/T + 0.2) \cdot C[wt\%]$	[107]
7	$3.23 - 7430/T + (1300/T + 0.03) \cdot C[wt\%]$	[136]

Experimental investigations have been performed by Narita [99], Irvine et al. [36] and Balasubramanian et al. [113,135] (solubility products 1-5), while thermodynamic calculations are done by Ohtani et al. [107,136] (solubility products 6-7). Compared to the data for TiN (see figure 4.9), the results of the different authors are in good agreement. However, Gladman [1] suggested that some difficulties associated with TiC solubility

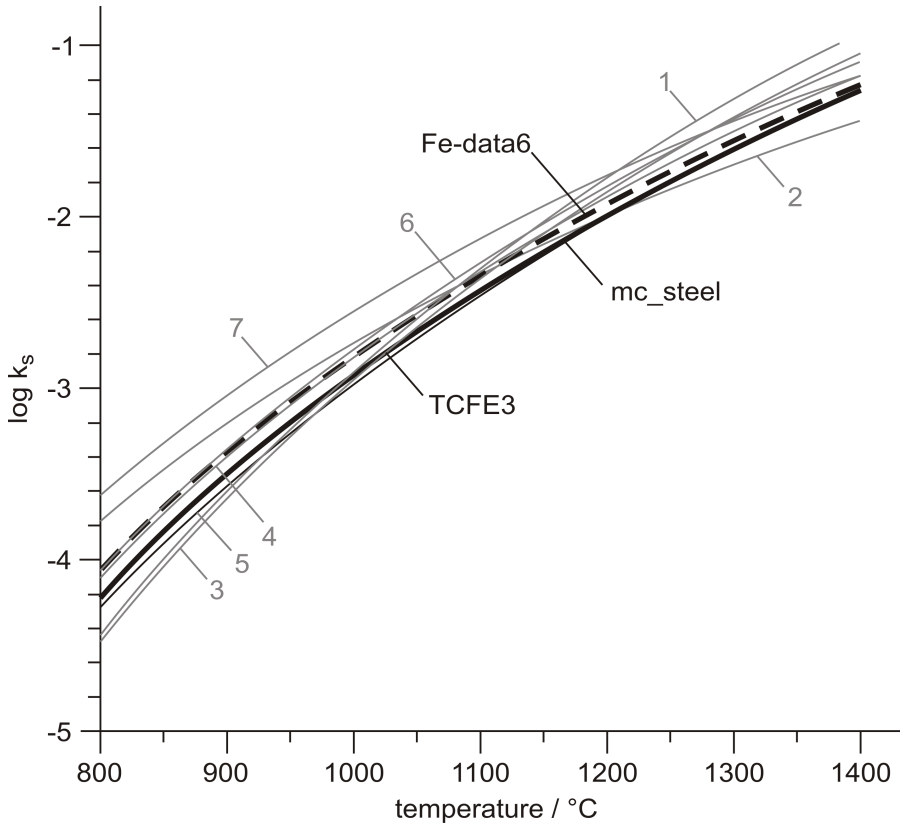

Figure 4.10: Comparison of solubility products and thermodynamic data of TiC.

data is related to the presence of N in the steels used. In section 4.2.6, it is already mentioned that TiN is extremely stable and needs to be considered when interpreting experimental results. Similar to the expressions for NbC (see table 4.6), Balasubramanian et al. [135] as well as Ohtani et al. [136] added a term to the solubility product accounting for the C-concentration by taking into account the strong interactions between Ti and C at higher C concentrations.

The databases 'mc_steel' and 'TCFE3' predict the same solution temperatures and are very close to the data calculated with the database 'Fe-data6'. The database 'mc_steel' contains thermodynamic information of Lee [114] and Frisk [134], which reads

$$G(FCC\_A1, TI:C; 0)\ 298.15\ +GTIC\#;\ 6000.00\ N$$

$$G(FCC\_A1, TI:C, VA; 0)\ 298.15\ -40219.8-18.25\cdot T;\ 6000.00\ N$$

$$G(FCC\_A1, TI:C, VA; 1)\ 298.15\ -108521+12.735\cdot T;\ 6000.00\ N$$

$$G(FCC\_A1, FE, TI:VA; 0)\ 298.15\ -51136+10.4\cdot T;\ 6000.00\ N$$

$G(FCC\_A1, FE, TI : VA; 1)\ 298.15\ -1950 - 6 \cdot T;\ 6000.00\ N$

$G(FCC\_A1, FE, TI : VA; 2)\ 298.15\ +14875;\ 6000.00\ N$

$G(FCC\_A1, FE, TI : C, VA; 0)\ 298.15\ -180000;\ 6000.00\ N$

$G(FCC\_A1, FE, TI : C, VA; 1)\ 298.15\ +318559 + 39.74 \cdot T;\ 6000.00\ N$

$G(FCC\_A1, FE, TI : C, VA; 2)\ 298.15\ -318559 - 39.74 \cdot T;\ 6000.00\ N$

$G(BCC\_A2, TI : C; 0)\ 298.15\ +2 \cdot GHSERCC\# + GTIC\# + 600000;$

$4000.00\ N$

$G(BCC\_A2, TI : C, VA; 0)\ 298.15\ -957000 + 75 \cdot T;\ 6000.00\ N$

$G(BCC\_A2, FE, TI : VA; 0)\ 298.15\ -59098 + 11.5 \cdot T;\ 6000.00\ N$

$G(BCC\_A2, FE, TI : VA; 1)\ 298.15\ -1796 + 1 \cdot T;\ 6000.00\ N$

$G(BCC\_A2, FE, TI : VA; 2)\ 298.15\ +5602 + 3.5 \cdot T;\ 6000.00\ N$

$G(TIC, TI : C; 0)\ 298.15\ -168261 + 293.73187 \cdot T - 48.0195 \cdot T \cdot LN(T)$

$- 0.00272 \cdot T^2 + 819000 \cdot T^{-1} - 2.03 \cdot 10^9 \cdot T^2 - 3;\ 6000.00\ N$

$G(TIC, TI : VA; 0)\ 298.15\ +6000 - 0.1 \cdot T + GHSERTI\#;\ 3000.00\ N$

$G(TIC, TI : C, VA; 0)\ 298.15\ -52702 - 4.6 \cdot T;\ 6000.00\ N$

$G(TIC, TI : C, VA; 1)\ 298.15\ -121367 + 31.5 \cdot T;\ 6000.00\ N.$

The results of all three databases are in good agreement with the solubility products listed in table 4.8.

4.2.8 Solubility Data Calculated with the Database 'mc_steel'

Figure 4.11 summarises the solubility of microalloy carbides and nitrides calculated with MatCalc (version 5.30) using the thermodynamic database 'mc_steel (version 1.86)'. The results are similar to the data proposed by Lagneborg et al. [49], see figure 3.8 in section 3.2.3.2. Accordingly, all microalloying nitrides are more stable than their corresponding carbides. The solubility products of the different phases in austenite range from 1 to -9. Furthermore, the order of the solubility of the nitrides and carbides corresponds to the data proposed by Lagneborg et al. [49]. Thus, TiN is an extremely stable microalloying

phase, whereas VC is characterized by high solubility. The solubility of the other phases is somewhere in between these two extrema.

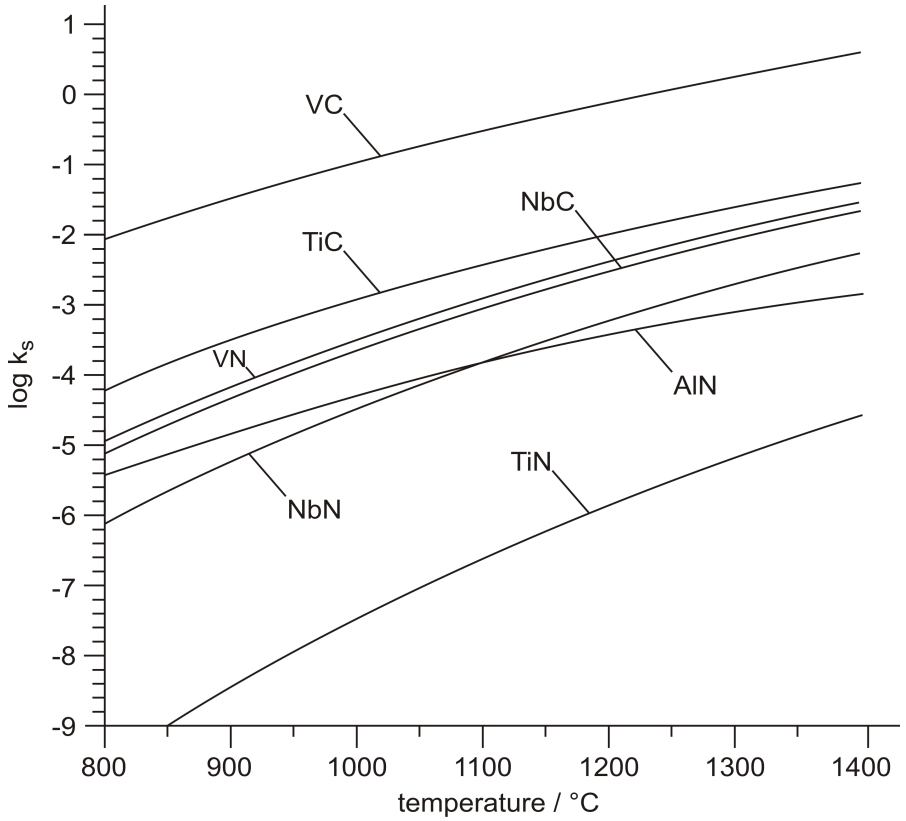

Figure 4.11: Comparison of the solubility of various carbides and nitrides, calculated with the thermodynamic database 'mc_steel (version 1.86)'.

Due to the different solubility characteristics of the nitrides and carbides, depicted in figure 4.11, Gladman [1] proposed several important conclusions, which are summarized in section 3.2.3.2.

4.2.9 Discussion

The solubility data of various nitrides and carbides have been determined by many workers using different theoretical or experimental (direct or indirect) methods. However, the evaluation of the solubility product by different authors show scatter to a greater or lesser extent, depending on the investigated phase, see section 4.2.1 to section 4.2.7. One reason for these discrepancies can be related to the variety of methods used in ob-

taining the given solubility, as each approach has its own assumptions and limitations. Typical methods for determining solubility products of nitrides or carbides are briefly summarised in the following [115]:

- thermodynamic calculations
- chemical separation and isolation of precipitates
- equilibrating a series of steels with different concentrations of the microalloying element, after which the C or N contents are analyzed
- hardness measurements
- thermoelectric power measurements
- statistical treatment of existing solubility products

Thermodynamic calculations of solubility products often neglect any interaction between elements. Only few authors [107, 122, 135] consider these interaction parameters to account for the effect of alloying elements on the solubility of nitrides or carbides in austenite.

Experimental techniques, which indirectly account for these chemical interactions, have other limitations. One problem of the separation method is that very fine particles may not be included in the analysis. Particularly, the Beeghly method [137], which is used by numerous authors, seems to be critical for a reliable detection of fine precipitates [138]. Other methods, e.g. the equilibrating method, assume stoichiometric or nonstoichiometric compounds, not accounting for the exact chemical composition of the precipitate. Finally, indirect methods like hardness measurements or thermoelectric power measurements are questionable since they are based on the assumption that an increase in hardness or thermoelectric power is directly related to the precipitation of nitrides and/or carbides, not accounting other effects, e.g. fine grain hardening, solid solution hardening or dislocation strengthening [115].

Apart the limitations of the investigation methods, there exist other problems related to the chemical composition of the investigated alloys. Erasmus et al. [24] demonstrate that the AlN solution temperature in a 3,5 % Ni steel is about 100°C higher compared

to a plain C steel due to the lower solubility of N in austenite. Furthermore, Höner and Baliktay [29] determined three different solubility products for AlN in austenite for three different alloys, see table 4.2. And Mayrhofer [89] and Koyama et al. [124] related their solubility products to the presence of Al, Mn, Cr, Si and Ni. Furthermore the discreapances can be related to the mutual solubility of different carbides or nitrides. The higher affinity of microalloying elments to N should be mentioned, which can be related to difficulties in the determination of various carbides, if N is present in the investigated steel. Also, the substitution of an element in the precipitate by other alloying elements, e.g. Al is replaced by Cr, is reported [45] as well as core shell structures of particles [60–62] in the presence of extremly stable compounds, e.g. TiN.

Another reason can be attributed to the presence of different crystallographic structures. Whereas the equilibrium crystallographic structure of AlN is the hexagonal wurtzite structure, in the early stages of precipitation cubic structure is observed [43,45–47]. Different crystallographic structures are also observed in the case of NbN. Mori et al. [139] measured NbN particles with cubic structure but also precipitates with hexagonal structures.

All these reasons account to a more or less extent for the discrepancies observed in the solubility data in section 4.2. However, the thermodynamic database 'mc_steel' (version 1.86) [83] is in fair agreement with most of the reported solubility products, thus representing reasonable mean values.

4.3 Simple versus Complex Solution Phases

'Complex solution phases' (MX phases) with fcc structure are modeled as a part of the fcc matrix phase, according to the CALPHAD approach [70]. For the simulation of these phases, composition sets are defined with the microalloying elements as major constituents. However, these phase descriptions consider also minor amounts of other elements, this is why we call them 'complex solution phases'. The complex character of these phases can sometimes cause numerical difficulties and phase instabilities when performing precipitation kinetics calculations.

In some cases, if the chemical composition of the precipitates is rather stoichiometric, the description of the precipitation phases can be simplified to so-called 'simple solution phases'. Thus, simple phase descriptions are introduced in our database 'mc_steel', which contain only the alloying elements of the desired phase, see section 4.2. The usage of these thermodynamic models lead to an enhancement of the stability of the calculations as well as to a reduction of computing time.

However, it is worthy to note once more that the usage of simple phases is a simplification for enhancing the stability of the calculations. Thus, before pure phases can be used, it must be clarified which phases are stable in a system by finding the miscibility gaps using the description of the complex solution phases (MX phase). Once the phases are defined, and the composition is rather stoichiometric, these complex phases can be substituted by the description of simple phases.

Figures 4.12 to 4.16 show the comparison of the calculations of three alloys (see table 4.1) using the simple phase description in 'mc_steel' (version 1.18) as well as the description of the complex solution phase (MX phase) of this database. In addition to the calculated phase fractions of the microalloying phases (figures 4.12, 4.13 and 4.15), figures 4.14 and 4.16 show the calculated chemical composition of the complex solution phases Ti(C,N), (V,Nb)C and V(C,N) in alloys 2 and 3.

Since the thermodynamic model of AlN is stoichiometric in both cases and there are no additional alloying elements except Nb and C in steel 1 the calculated phase fraction of AlN and NbC are identically, see figure 4.12.

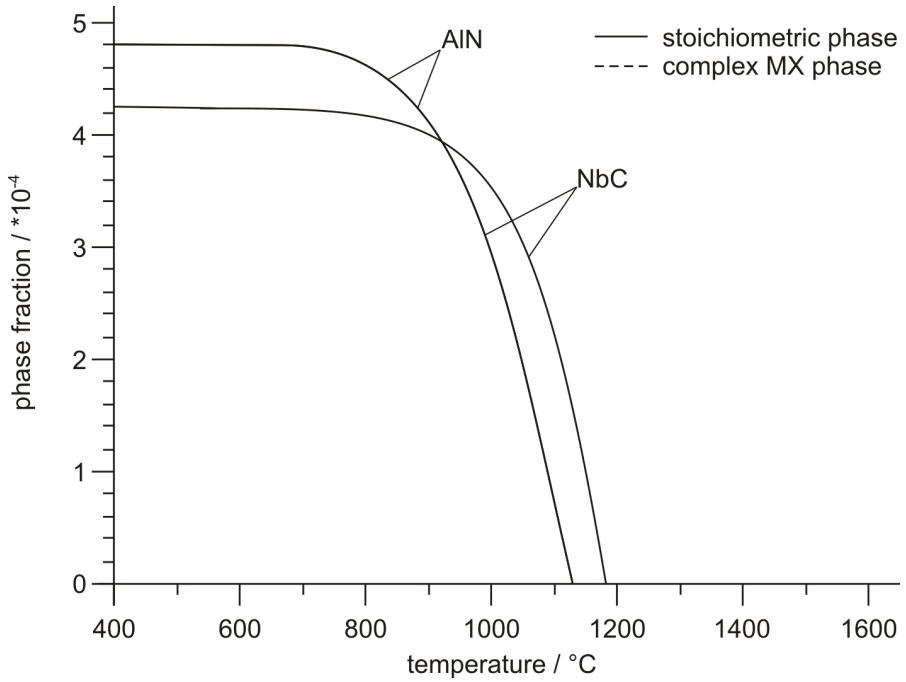

Figure 4.12: Equilibrium calculation of the phases NbC and AlN in steel 1, using the description of simple phases and complex solution phases in 'mc_steel'.

The calculated solution temperatures of TiN in alloy 1 and 2 are in good agreement, see figures 4.13 and 4.15. However, there are some discrepancies in the phase fraction of TiN in the temperature range between 600 °C and 1200 °C, whereas the equilibrium phase fraction at low temperatures coincide well. This discrepancies can be explained by looking at the chemical compositions of the Ti(C,N) phases, see figures 4.14 and 4.16. In both cases, the Ti(C,N) precipitates are rater stoichiometric phases at high temperatures as well as at low temperatures. However, in the temperature range from 600°C to 1200°C the composition of the alloy 2 and 3 are more (Ti,V,Nb)(C,N) and (Ti,V)(C,N), respectively, rather then a simple TiN.

Using the stoichiometric VC phase description shows, that the calculated solution temperature as well as the phase fraction is in good agreement with the values obtained with the complex MX phase, in the case of steel 3 (figure 4.15). Dramatic discrepancies are only observed by the comparison of the two approaches concerning the VC in steel 2, see figure 4.13. This deviation can be attributed to the different number of stable phases, depending on the thermodynamic model. Whereas the complex phase descrip-

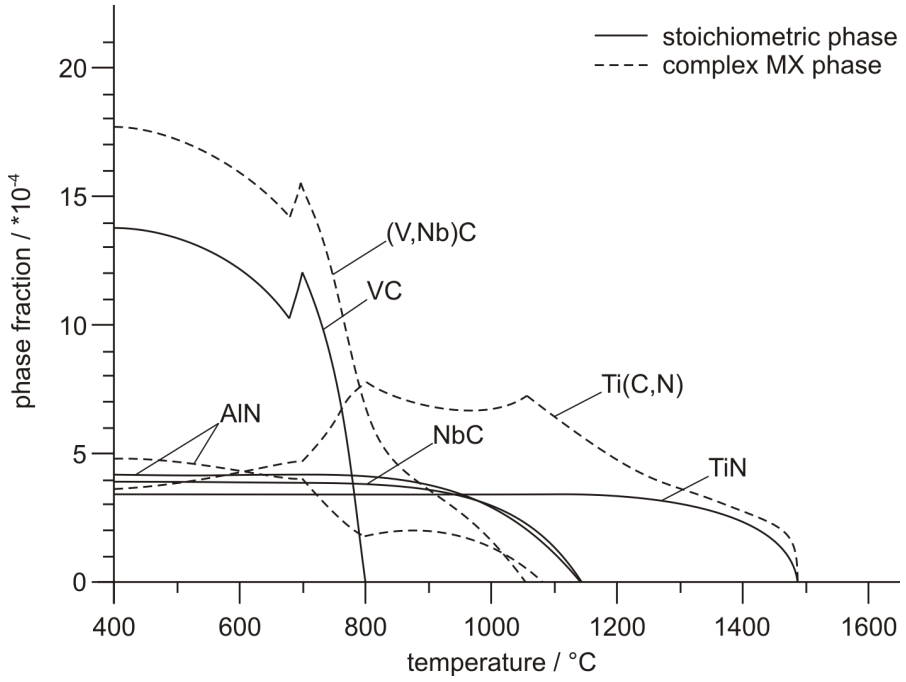

Figure 4.13: Equilibrium calculation of the phases VC, NbC, TiN and AlN in steel 2, using the description of simple phases and complex solution phases in 'mc_steel'.

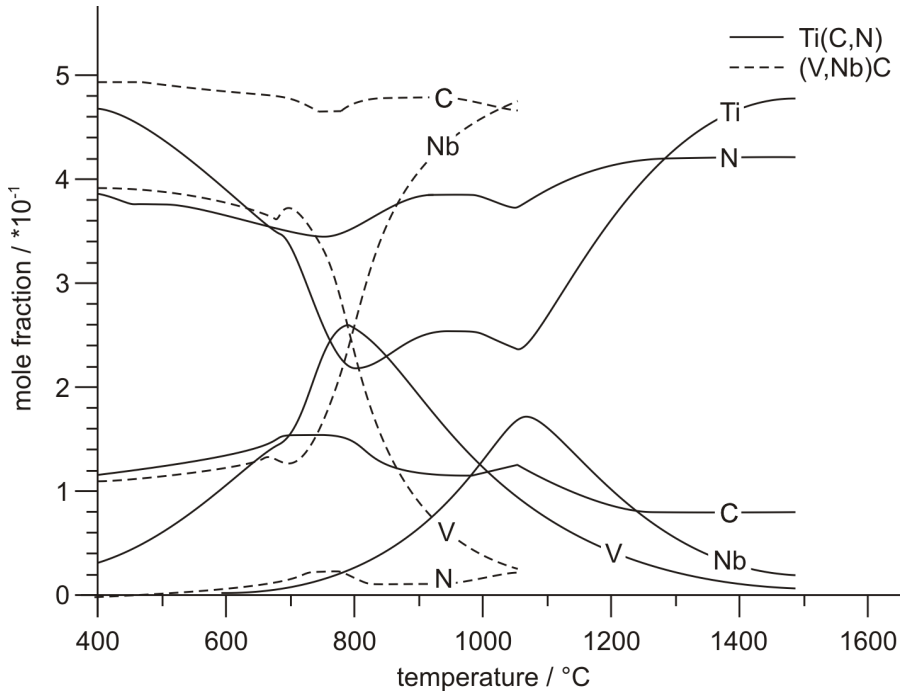

Figure 4.14: Equilibrium calculation of the chemical composition of the phases (V,Nb)C and Ti(C,N) in steel 2, using the description of complex solution phases in 'mc_steel'.

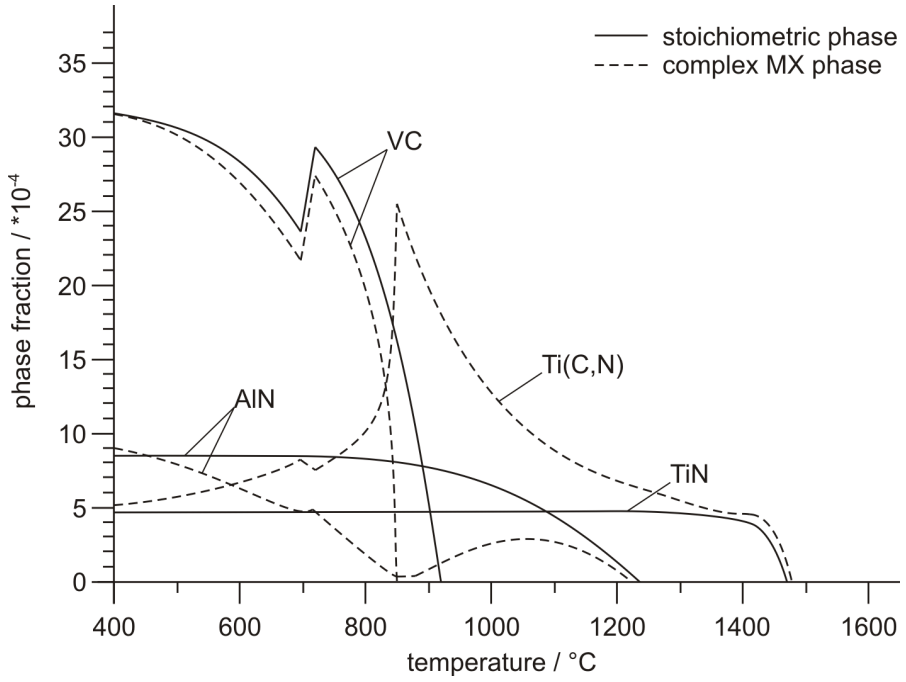

Figure 4.15: Equilibrium calculation of the phases VC, TiN and AlN in steel 3, using the description of simple phases and complex solution phases in 'mc_steel'.

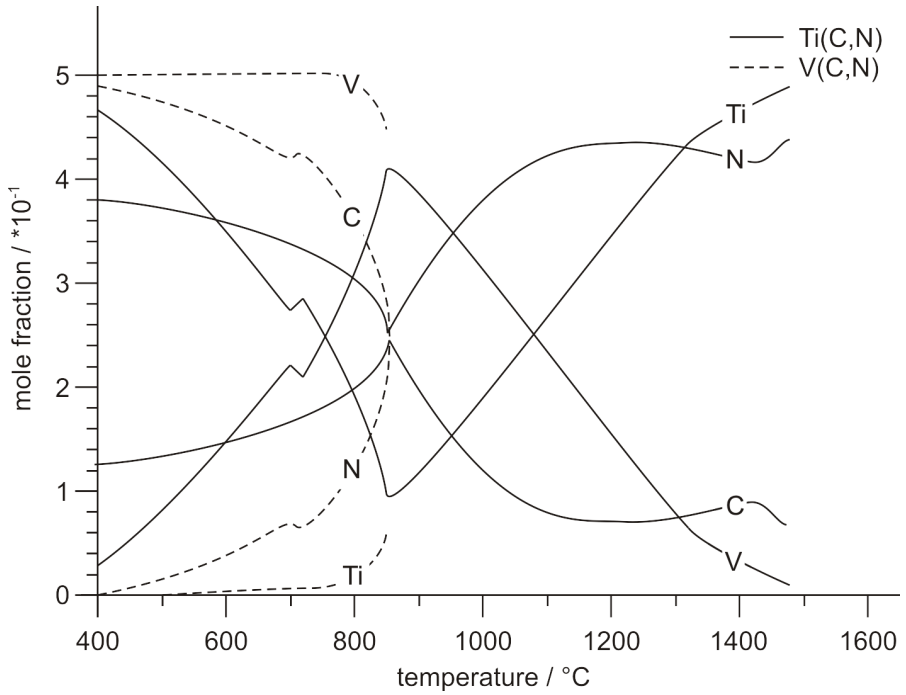

Figure 4.16: Equilibrium calculation of the chemical composition of the phases VC and Ti(C,N) in steel 3, using the description of complex solution phases in 'mc_steel'.

tion predicts a (V,Nb)C, this phase is replaced by the two separate phases VC and NbC, when using the simple pure phases. Since the calculation of the chemical composition of the complex (V,Nb)C predicts a NbC at approximately 1000°C and a VC at temperatures below 700°C, it seems to be likely that both phases are stable depending on the temperature. In this special case it can not be clarified yet which description is more serious, since it is possible that there is a very sensitive miscibility gab which cannot be determined with the complex MX phase description.

The equilibrium calculations of the three alloys demonstrate, that the prediction of simple pure phases is in good agreement with the complex description in many cases. Thus, this simplification enables to run stable precipitation kinetics calculations.

4.4 Essential Ingredients for Modeling Precipitation Kinetics

For a consistent description of the precipitation kinetics of various nitrides and/or carbides, several important input parameters must be taken into account. Apart the main input quantities thermodynamic and diffusion data, it is necessary to account for several physical mechanisms that are often neglected in this type of simulations, among them the precipitate/matrix volumetric misfit and the temperature dependent Young's modulus, composition-, temperature- and size-dependent interfacial energies, as well as the ratio between bulk and grain boundary diffusion. The present section introduces these important quantities.

- **Thermodynamic input data:** The thermodynamic data is the basis of every precipitation kinetics calculation, providing chemical potentials and Gibb's free energies. Consequently the accuracy of the thermodynamic input data is of great importance, see section 4.2. For the kinetic calculations in the present work, the thermodynamic database 'mc_steel' (version 1.50) [83] is used, unless stated otherwise.
- **Diffusion data:** The diffusion database is another very important basic ingredient, when doing precipitation kinetics calculations, providing mobility data of the elements in various phases. For the present kinetic calculations the information of the database 'mc_sample_fe' (version 1.03) [140] is used.
- **Interfacial energy:** The interfacial energy is calculated from the generalized n-next nearest-neighbour broken-bond approach [73], taking into account the influence of the precipitate size during nucleation [74], see also section 3.4.3.
- **Different nucleation sites:** Does precipitation occur heterogenously at grain boundaries, dislocations or also homogeneously in the bulk? Depending on the volumetric misfit between precipitate and matrix at various nucleation sites, different types of precipitates nucleate on different nucleation sites.
- **Different diffusion geometries:** Different nucleation sites makes it necessary

to take into account different diffusion geometries. In the present work, a new model [78] for grain boundary precipitation is employed, which takes into account fast short-circuit diffusion along grain boundaries as well as slower bulk diffusion inside the grain, together with the classical treatment for randomly distributed precipitates with spherical diffusion fields.

- **Ratio between diffusion along grain boundaries D_{gi} and diffusion in the bulk D_{bi}:** Since grain boundaries represent very efficient short-circuit diffusion paths with diffusivities several orders of magnitude larger than in the bulk, it is necessary to take into account the ratio between diffusion at grain boundaries D_{gi} and in the bulk D_{bi}.
- **Grain size:** Another important input parameter is the grain size, which strongly influences the calculated results by applying the model for predominant precipitation at grain boundaries.
- **Dislocation densities:** If nucleation of precipitates occurs at dislocations, the dislocation density is of prior importance. For the present calculations dislocation densities are used according to [141].
- **Volumetric misfit:** As already mentioned, different precipitates nucleate on different nucleations sites depending on the volumetric misfit between particle and matrix. How big is the misfit between precipitate and matrix at different nucleation sites?
- **Young's Modulus:** In addition to the volumetric misfit, the calculation of the misfit strain energies requires a temperature dependent description of the Young's modulus of the fcc and bcc iron matrix phases. The precipitates are assumed to be a rigid body. The temperature dependence of the Young's modulus of the precipitates is therefore neglected.
- **Quenched in vacancies:** Depending on the heat treatment parameters (e.g. solution treatment and subsequent quenching) the effect of quenched in vacancies must not be neglected. Although, this effect is well-known and heavily utilized in aluminium alloys (e.g. [142]) it is assumed to be not relevant in the case of microalloyed steels.

These aspects are investigated in detail and descriptions are presented subsequently. Some of these descriptions are valid for the precipitation of different phases (e.g. ratio between grain boundary diffusion and bulk diffusion or temperature dependent Young's modulus), whereas others have to be studied for each phase (e.g. thermodynamic data or misfit between matrix and precipitate phase) or for each application (e.g. grain size) separately. The next sections deal with the introduction of temperature dependent functions, used independently of the precipitating phases.

4.4.1 Ratio Between Grain Boundary Diffusion and Lattice Diffusion

An important ingredient for treatment of precipitation of nitrides and carbides with the new grain boundary precipitation model [78] is the grain boundary diffusional mobility.

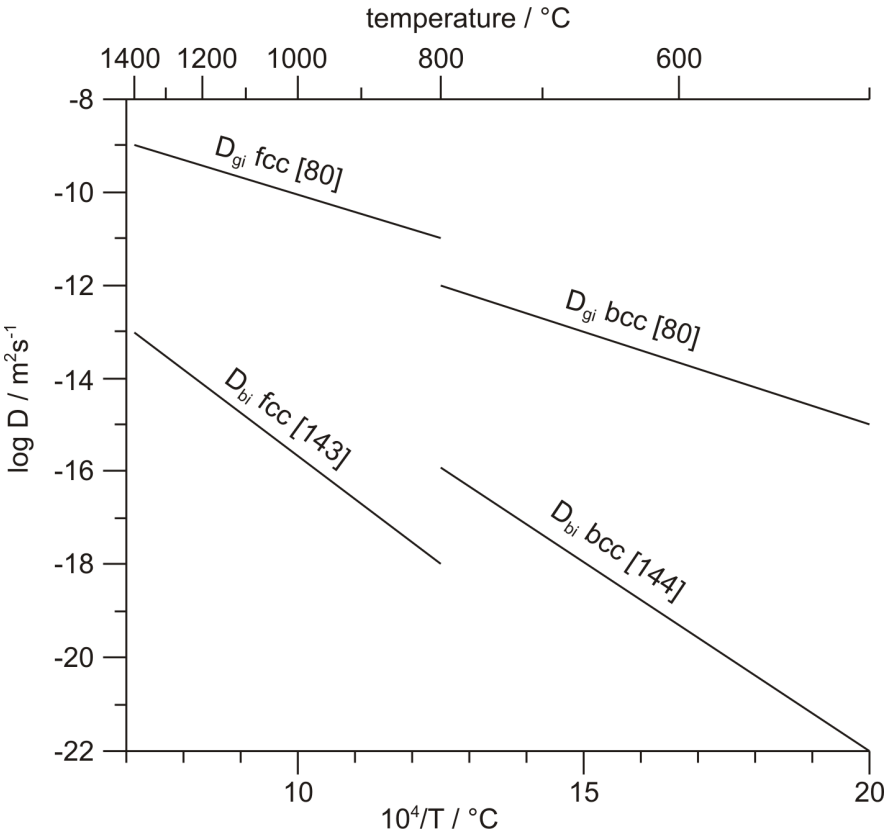

Figure 4.17: Temperature dependent self diffusion coefficients of Fe in the bulk (D_{bi}) and at grain boundaries (D_{gi}) [80, 143, 144].

Figure 4.17 shows the temperature dependent diffusion coefficients in the bulk and at the grain boundaries in bcc and fcc Fe. The ratios D_{gi}/D_{bi} are in the range of 10^7 to 10^4 for temperatures between 500 °C to 800 °C and 800 °C to 1400 °C, for ferrite and austenite, respectively. According to the approximated relations

$$\left(\frac{D_{gi}}{D_{bi}}\right)_{fcc} = 10^{(11-0.005\cdot T)} \tag{4.2}$$

and

$$\left(\frac{D_{gi}}{D_{bi}}\right)_{bcc} = 10^{(12-0.01\cdot T)} \tag{4.3}$$

these temperature dependent ratios D_{gi}/D_{bi} are taken into account for γ and α iron, respectively. Both equations consider the temperature T in °C.

4.4.2 Temperature Dependent Young's Modulus

Considering misfit strain energies in precipitation kinetics calculations makes it necessary to take into account the temperature dependence of the Young's modulus (see equation 3.16). Several authors have reported about this quantity in the ferrite phase field [145–154], whereas considerably less attention was paid to the austenite phase field [146, 154], see figure 4.18. Differences in the results are mainly attributed to different investigation methods [146], different chemical compositions [148] or different pre-treatment [149]. Most of the authors used the high frequency resonance method, e.g. [148, 149]. Fukuhara et al. [146] analyzed a plain low C steel using the ultrasonic pulse sing-around method. Both methods deliver accurate results, but Fukuhara et al. [146] mention in their discussion, that the ultrasonic pulse sing-around is the only technique for the determination of the elastic parameters in the higher temperature range beyond the recrystallization temperature.

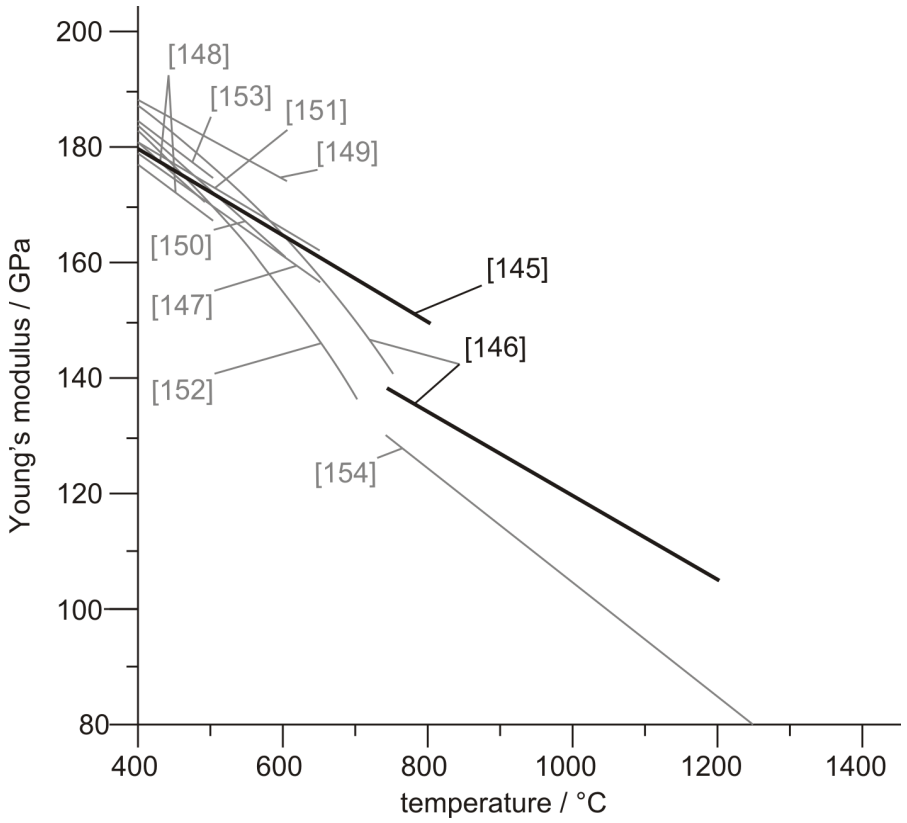

Figure 4.18: Temperature dependent Young's modulus.

In the present work, the Young's modulus of austenite is used according to

$$E_{fcc} = -75 \cdot T + 210000, \tag{4.4}$$

following the description of Fukuhara et al. [146]. The description for the ferrite phase field reads

$$E_{bcc} = -73.33 \cdot T + 193000, \tag{4.5}$$

following the results of Peil and Wichers [145], which are similar to the observations of Takeuti et al. [151], in between the lower and upper limits of Date [148] and a linear regression of the ultrasonic pulse sing-around investigations of Fukuhara et al. [146]. Also these equations for the temperature-dependent Young's modulus, accept the temperature T in °C. The relations are indicated by bold lines in figure 4.18.

4.5 Precipitation at Grain Boundaries

This section deals with the treatment of predominant precipitation of particles at grain boundaries, utilizing a newly developed model [78]. Therefore, the model characteristics are investigated in the present section on the example of AlN precipitation in microalloyed steels. The iron-rich corner of the Fe-Al-N system in the fcc + AlN phase field of the Fe-Al-N phase diagram represents a classical example, where nucleation of precipitates occurs predominantly at grain boundaries and is almost entirely suppressed elsewhere [26]. This model system has, therefore, been selected for investigation of the features and characteristics of the present model. The analysis is carried out in the form of a parameter study. The comparison of the calculations with experimental data will be subject of section 4.7.

4.5.1 Growth of Equi-Sized Precipitates

First, the growth characteristics of individual precipitates are explored utilizing an ensemble of identical particles located at the grain boundaries of unit volume of polycrystalline material with given grain radius. In this setup, the kinetics of a single particle is representative for the kinetics of the whole system.

The first set of simulations is initialized with a constant number of precipitates ($N_0 = 10^{18}\ m^{-3}$) with supercritical nucleation radius according to classical nucleation theory [71]. The precipitates are assumed to be homogeneously distributed over the entire grain boundary area. The simulations are carried out for different austenite grain radii between $R = 1\ \mu$m and $R = 250\ \mu$m at a temperature $T = 1000\ °C$. The composition of the system is taken to be 0.05 wt% Al, 0.005 wt% N, balance Fe, which are typical values for microalloyed steel. It is further assumed that the diffusion of elements in the grain boundaries is 10^4 times faster than diffusion in the matrix.

Figure 4.19 shows the calculated growth kinetics of a constant number of equi-sized AlN precipitates ($N_0 = 10^{18}\ m^{-3}$) using the new grain boundary diffusion geometry (GBDG) formalism at hand. Plot (a) displays the evolution of the phase fraction of AlN precipitates versus time, whereas plot (b) shows the evolution of the precipitate radius.

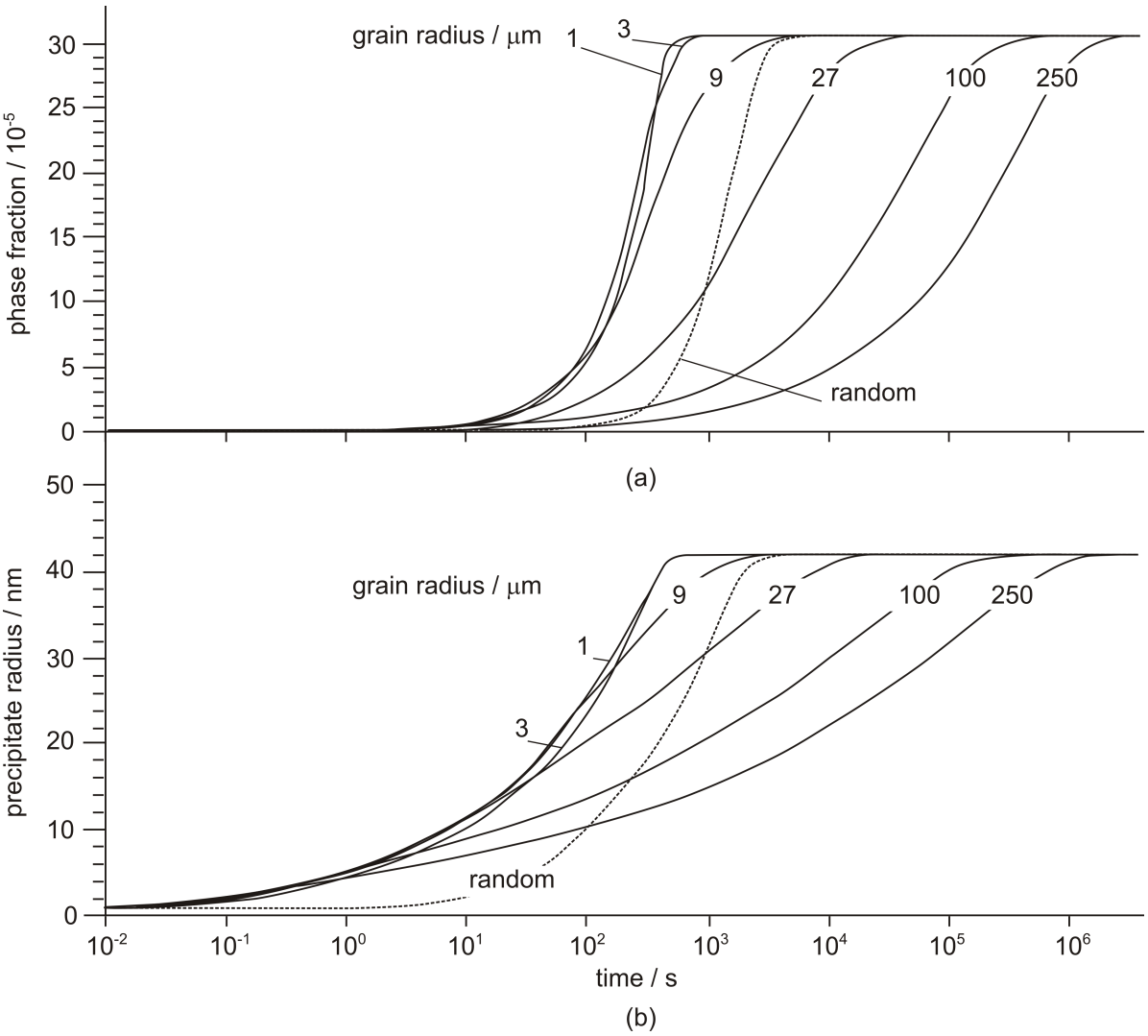

Figure 4.19: Evolution of phase fraction and radius of a constant number of identical AlN precipitates for different grain radii. Al=0.05 wt%, N=0.005 wt%, T=1000 °C, $D_{gi} = 10000 \cdot D_{bi}$.

In accordance with expectation, the growth kinetics of grain boundary precipitates is the faster the smaller R is. The leftmost curve in the phase fraction plot is computed for a grain radius of $R = 1$ μm. The corresponding particle density at the grain boundary is 8 precipitates per grain with a mean diffusion field radius Λ of approximately 700 nm. The precipitate radius evolution shows a rapid increase in the early stages of the growth process and an almost constant growth rate until soft impingement hinders further growth. If R is increased from $R = 1$ μm to 9 μm, while holding the total

number of precipitates constant, the precipitate density at the grain boundary increases from 8 precipitates per grain to a value of 5200. This increase leads to a significant decrease of the mean diffusion field width Λ from 700 nm to 250 nm and, together with the increased diffusion distance from the grain center R, to a slower growth rate in the final stages of the growth process. This effect is even more pronounced, if R is further increased to $R = 250$ μm, where the decreasing growth rate is already visible for medium size precipitates. For the largest R, a precipitate density of $9 \cdot 10^7$ precipitates per grain is observed with a mean diffusion field radius of $\Lambda \approx 50$ nm.

In the phase fraction evolution shown in plot (a) of figure 4.19, the different growth kinetics with increasing grain radius and precipitate density are clearly reflected in a change of the slope of the phase fraction versus time curves. This becomes most obvious in comparing also to the classical parabolic growth behavior observed in the random-distribution spherical diffusion field geometry (RSDG). This curve is shown in dashed line for comparison.

The second set of simulations is carried out for variable grain radius and constant precipitate density of 10000 precipitates per grain. This constraint is maintained by proper adaptation of the total number of precipitates with variable grain radius. The results are summarized in figure 4.20. Image (a) displays the evolution of the phase fraction versus time, showing that the time to reach full precipitation is strongly retarded in larger grains. Since the diffusion field radius Λ is approximately constant in this simulation setup (one precipitate always shares the same amount of grain boundary area), this effect is mainly due to the increased diffusion distances from the grain center to the grain boundary as well as the fact that the precipitates grow to considerably larger size (mass conservation). For the six values $R = 1,\ 3,\ 9,\ 27,\ 100$ and 250 μm used in figure 4.20, the corresponding number densities are $2 \cdot 10^{21},\ 7 \cdot 10^{19},\ 3 \cdot 10^{18}, 1 \cdot 10^{17}, 2 \cdot 10^{15}$ and $1.5 \cdot 10^{14}$ m^{-3}. These results reflect the well-known fact that grain boundary precipitation (viewed in terms of phase fraction) can be effectively controlled by the parent phase grain radius.

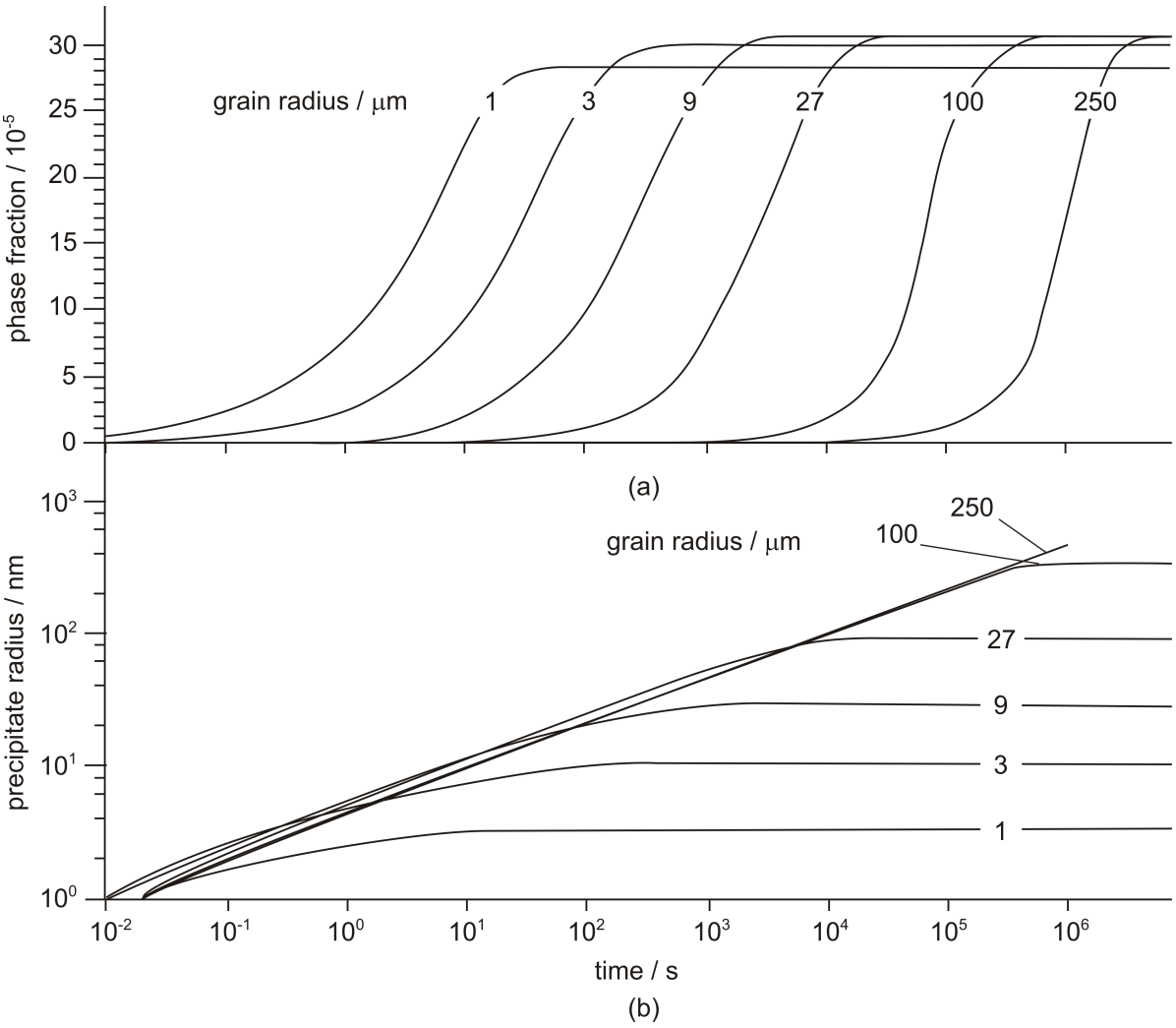

Figure 4.20: Evolution of phase fraction and radius computed in grain boundary diffusion geometry (GBDG) for constant precipitate density of 10000 precipitates per grain. Al=0.05 wt%, N=0.005 wt%, T=1000 °C, $D_{gi} = 10000 \cdot D_{bi}$.

4.5.2 Evolution of Non-Equi-Sized Precipitates

All simulations start with a pre-defined initial size distribution of precipitates (Gaussian distribution) and a total precipitate phase fraction of 1/1000 of the equilibrium value. The simulations are carried out for a composition of 0.1 wt% Al, 0.01 wt% N, balance Fe, and a temperature T=1000 °C.

Figure 4.21 summarizes the results of the simulations for various grain radii between $R = 1$ and $R = 1000$ μm. The major difference given by these simulation conditions

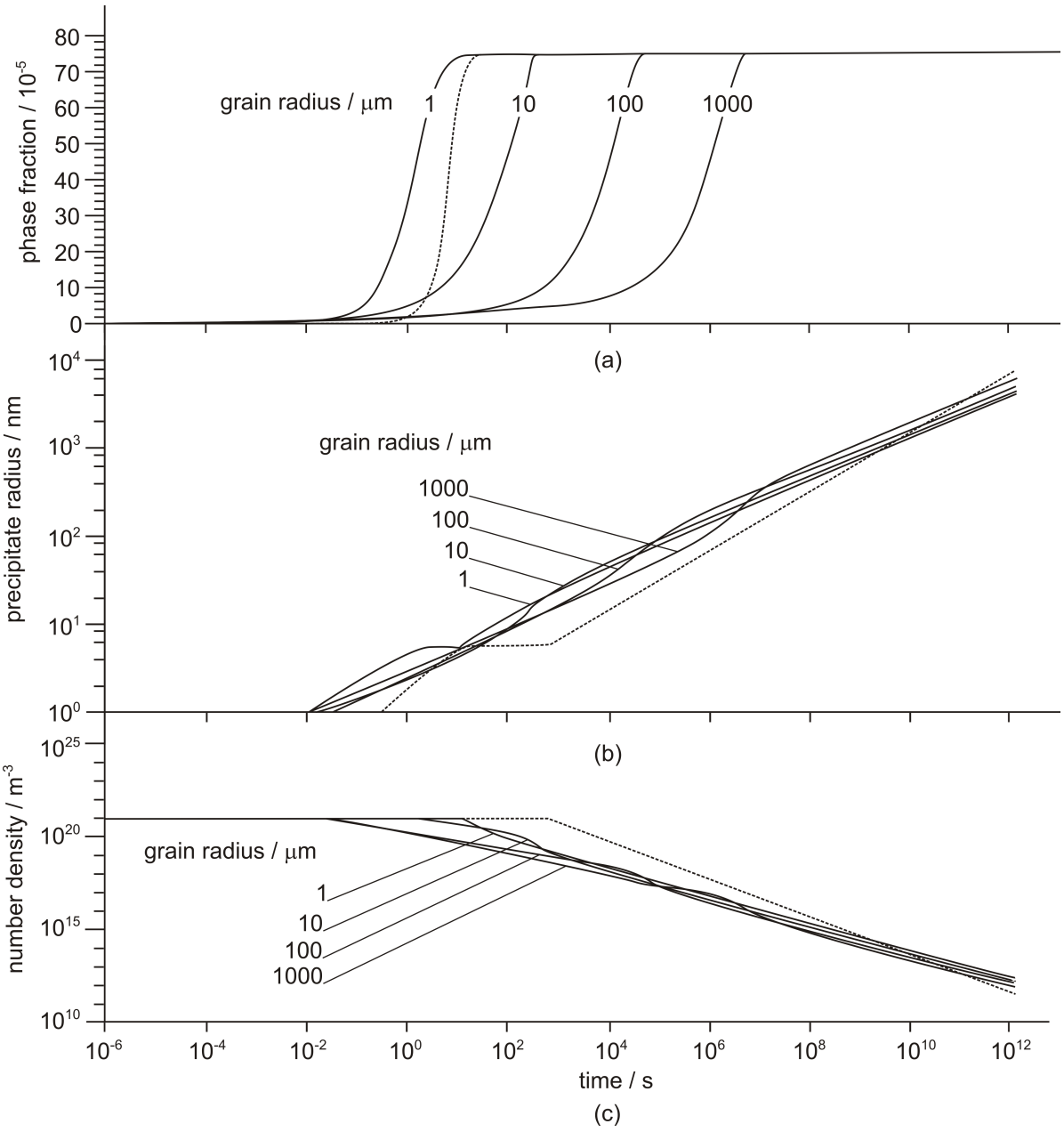

Figure 4.21: Phase fraction, mean radius and number density of AlN precipitates as a function of grain radius ($R = 1,\ 10,\ 100,\ 1000\ \mu$m). Dashed line indicates simulation with random precipitate distribution and radial diffusion fields (RSDG). Al=0.1 wt%, N=0.01 wt%, $T = 1000\ °C$, $D_{gi} = 10000 \cdot D_{bi}$.

is the average number of precipitates per grain, which varies from approximately 10^5 precipitates per grain for $R = 1\ \mu$m to 10^{15} precipitates per grain for $R = 1000\ \mu$m. Investigating the evolution of the phase fraction for this simulation setup in figure 4.21,

similar characteristics are observed as in the simulations shown in figure 4.19. The evolution of the radius, however, is more complex since it involves interaction of precipitates with different sizes. The curves for the smallest grain radius of $R = 1$ μm as well as the curve for the RSDG treatment (dashed lines) exhibit a clear distinction of the growth stage from the coarsening regime. The two regions are separated by a plateau indicating the transient region after completion of growth and before onset of coarsening. For grain radii $R = 10$ μm and more, this transient region disappears due to a significant overlapping of precipitate growth and coarsening by short-circuit diffusion in the grain boundary. This observation is discussed in the following section.

Figure 4.22 displays two typical precipitate distributions observed at different stages of coarsening. Since the number of precipitates per grain changes continuously during coarsening, no stationary precipitate distribution is achieved for the entire simulation time. Instead, for sufficiently long time, a distribution corresponding to classical Ostwald ripening of grain boundary precipitates [155–160] is observed, with a time exponent of approximately 1/4.2 - 1/4.0 for the evolution of the mean precipitate radius. This is in good accordance with theory, predicting a value of 1/4 for purely grain boundary diffusion driven coarsening. The left plot in figure 4.22 shows a typical numerical distribution obtained with the present model compared to the theoretical precipitate distribution for the limit of zero phase fraction, given as [157]

$$g(u) = \left(\frac{3}{4}\right)^4 u^3 \left(1 - \frac{3u}{4}\right)^{-19/6} \left(\frac{3u^2}{16} + \frac{u}{2} + 1\right)^{-23/12} \cdot$$
$$exp\left\{\frac{1}{2} - \frac{\frac{2}{3}}{\left(\frac{4}{3} - u\right)} - \frac{1}{6\sqrt{2}} \cdot \left[tan^{-1}\left(\frac{1 + \frac{3u}{4}}{\sqrt{2}}\right) - tan^{-1}\frac{1}{\sqrt{2}}\right]\right\};\ u < \frac{4}{3}, \tag{4.6}$$

where the normalized number density $g(u)$ is plotted over the normalized precipitate radius u.

Higher values of the time exponent up to 1/3 are predicted [158, 159], if solute transfer occurs by volume and grain boundary diffusion simultaneously. This occurs typically at higher temperatures. Lower values down to 1/5 are observed experimentally [161–163]

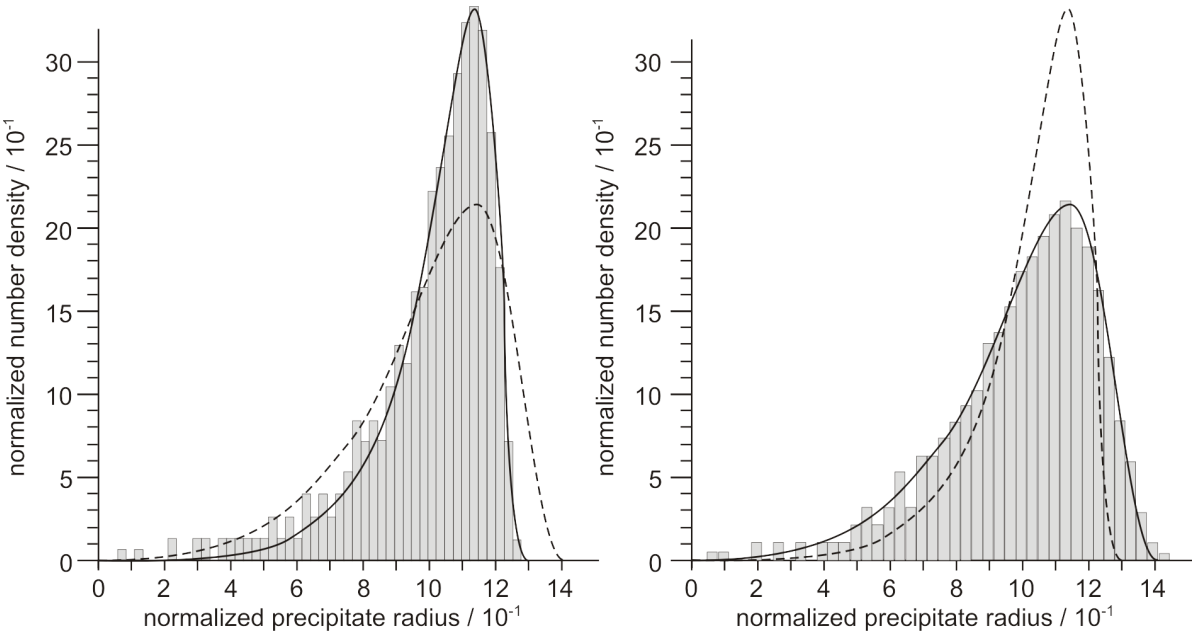

Figure 4.22: Typical precipitate distributions observed during coarsening. Left image: $t^{1/4}$-coarsening distribution. Right image: classical $t^{1/3}$-LSW distribution.

and theoretically [157], if the diffusional transport occurs via pipe diffusion through a dislocation network of, e.g., a low-angle grain boundary. In the simulations, the time exponent for the evolution of the number density is observed with approximately 1/1.4. For approximately two orders of magnitude in time, the distribution changes its shape and closely resembles the classical LSW-distribution [164,165] for coarsening of randomly distributed precipitates, theoretically expressed as

$$g(u) = \frac{4u^2}{9}\left[\frac{3}{3-2u}\right]^{-11/3}\left[\frac{3}{3+u}\right]^{-7/3} \cdot exp\left[\frac{-2u}{3-2u}\right];\ u < \frac{3}{2}. \tag{4.7}$$

This region is characterized by a 'hump' in the mean radius and the total number of precipitates curves, as clearly visible in figure 4.21. The right plot in figure 4.22 compares a corresponding distribution with the theoretical LSW distribution. In our simulations, the particular region, where this progression occurs, is always found at the position, where the precipitate density adopts values of approximately $10^4 - 10^5$ precipitates per grain.

4.5.3 Influence of Grain Boundary and Bulk Diffusion

In this section, the growth kinetics and interactions of an ensemble of grain boundary precipitates of different size are investigated. By changing the ratio between the diffusional mobilities of all elements in the bulk and the grain boundaries, D_{gi}/D_{bi}, the important influence of this quantity on the overall precipitation kinetics is explored. In contrast to the numerical analyses in the previous sections, the present simulations are carried out without pre-existing nuclei. The formation of new precipitates follows a numerical procedure based on classical nucleation theory, see section 3.4. The simulations are performed with a maximum of 500 size classes. A constant grain radius of $R = 250$ μm is used, and the ratio between grain boundary and bulk diffusional mobility of all elements D_{gi}/D_{bi} is varied between 1 and 10^6. If the diffusivities in the grain boundary and the bulk are assumed to be similar, this would correspond to temperatures close to the melting point. If they are assumed to be different by several orders of magnitude, this would correspond to situations commonly observed at relatively low temperatures, when the bulk diffusion is already sluggish and most diffusional transport occurs along short-circuit diffusion paths such as dislocations and grain boundaries [80]. Figure 4.23 shows the evolution of the AlN phase fraction, the mean radius and the precipitate density for various values of D_{gi}/D_{bi} while leaving the values of D_{bi} unchanged. The maximum precipitate density is limited to approximately 10^{20} m^{-3} according to the saturation of nucleation sites. The slowest precipitation kinetics is observed for the lowest values of D_{gi}/D_{bi}, which is easily attributed to the slow transport velocity of atoms towards the precipitate. With increasing ratio D_{gi}/D_{bi}, this transport is speeded up together with the entire precipitation process. In the diagram for the phase fraction of AlN versus time (figure 4.23 (a)), the kinetics of precipitation is increased significantly, if the grain boundary diffusivity is increased starting at low values. Interestingly, at a given point, this increase comes to a stop, and only the shape of the diagram changes. The faster the diffusion in the grain boundary is, the flatter is the slope of the phase fraction increase. This observation can be understood on the basis of the evolution of the other precipitation parameters shown in figures 4.23 (b) and 4.23 (c). The curves

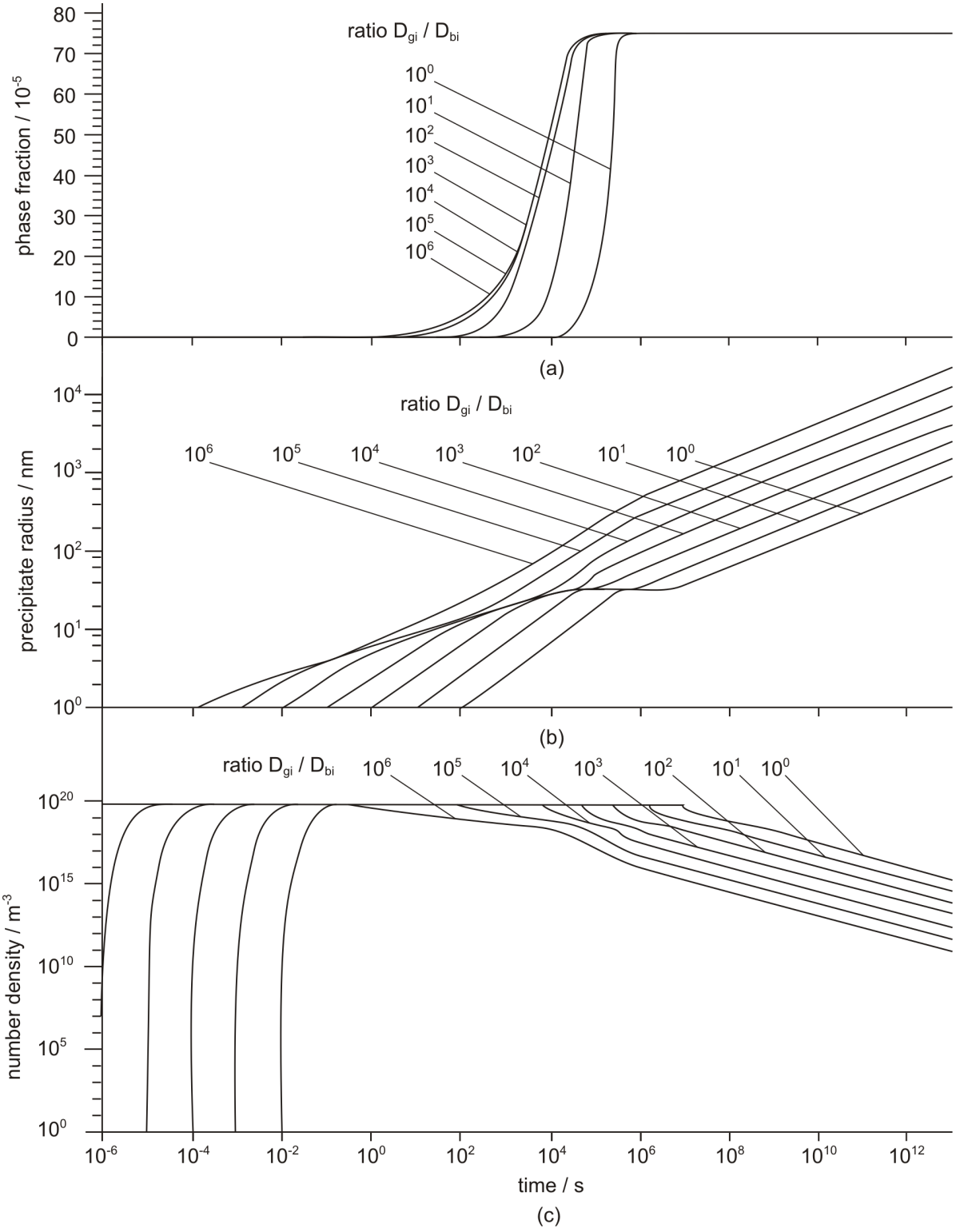

Figure 4.23: Phase fraction, mean radius and number density of AlN precipitates as a function of the ratio between grain boundary and bulk diffusion coefficient D_{gi}/D_{bi}.

for the precipitate mean radius and number density are continuously shifted to shorter times with increasing ratio D_{gi}/D_{bi}. This observation is attributed to the fact that the nucleation process of precipitates is mainly controlled by the diffusional mobility of elements within the grain boundary. With increasing D_{gi}/D_{bi}, the transport of atoms inside the grain boundary becomes faster, and growth of precipitates speeds up. An increase of D_{gi}/D_{bi} thus simultaneously shifts the start time of nucleation and the curves for mean radius and number density.

On closer investigating the evolution of the precipitate mean radius, we find that the growth of precipitates occurs approximately with a slope of 1/2 in the case of a low ratio of D_{gi}/D_{bi}. This corresponds to the well-known parabolic growth laws for diffusion-controlled transformations. If the grain boundary diffusivity becomes faster, the coarsening contribution to $\dot{\rho}_k$ starts to dominate over the growth contribution (see section 3.4.2.2 for the two parallel processes), and the slope of the precipitate mean radius evolution starts to decrease to a value of approximately 1/3 to 1/4 for values of $D_{gi}/D_{bi} > 10$. A comparable decrease in the time exponent for the precipitate mean radius evolution is also observed in the case of classical precipitate coarsening [155, 159, 164, 165]. The higher the ratio D_{gi}/D_{bi} is, the earlier occurs coarsening inside the grain boundary and the smaller becomes the contribution from diffusional transport through the bulk to the grain boundaries. This fact is reflected in the phase fraction curves for higher ratio D_{gi}/D_{bi}. The curves are not shifted to shorter times. Instead, the slope of the curves changes, once a critical value of D_{gi}/D_{bi} is reached. In this case, growth and coarsening occur simultaneously, with increasing dominance of the coarsening contribution with increasing ratio D_{gi}/D_{bi}. It should be emphasized that this latter effect of change of slope occurs in addition to the effect described in the previous section based on the variation of the precipitate diffusion zone radius Λ in the grain boundary.

4.5.4 Time-Temperature-Precipitation (TTP) Diagram

This section deals with the comparison of the time-temperature-precipitation diagram for AlN precipitation in austenite using the GBDG model and the RSDG model.

Figure 4.24 shows that the TTP plot calculated with the GBDG model deviates significantly from the TTP plot evaluated with the RSDG model. A grain radius R = 50 μm and a dislocation density of 10^{12} m^{-2} have been assumed in these calculations. Although both models predict approximately the same upper temperature limit for the start of AlN precipitation, the nose of the C-curve for the grain boundary diffusion model is shifted to higher temperature by almost 100°C. At lower temperatures, the model with radial diffusion fields predicts faster kinetics by several orders of magnitude in time for the end of precipitation. This effect is attributed to the long diffusion distances from the grain interior to the grain boundary precipitates for completion of the precipitation process.

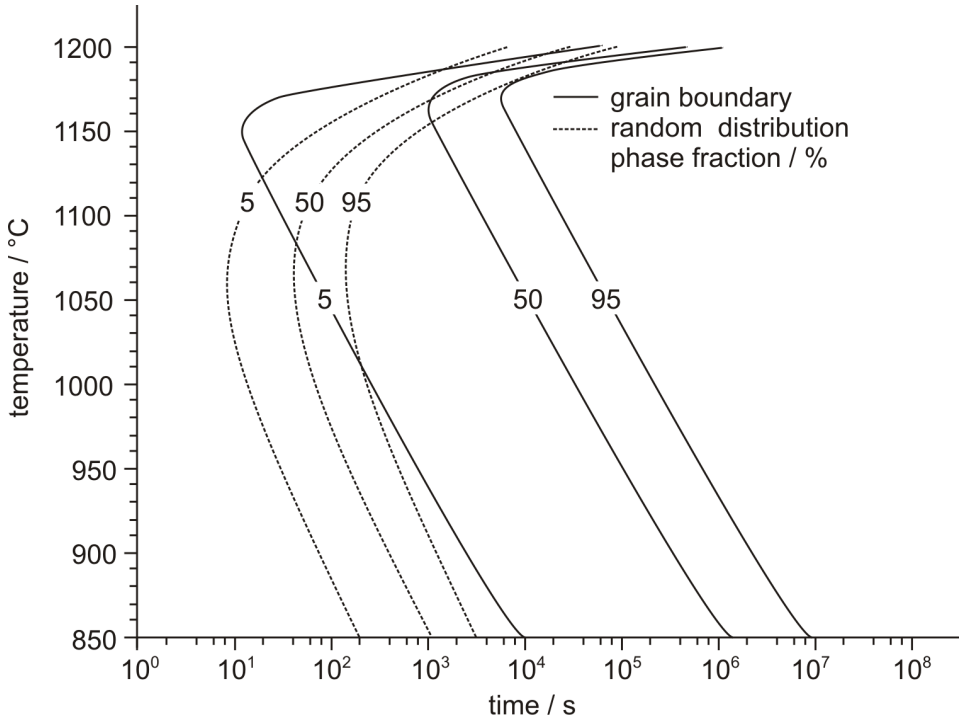

Figure 4.24: Calculated time-temperature-precipitation diagram for AlN precipitation in austenite. The solid lines represent the result using the GBDG model, while the dashed lines indicate the treatment with radial diffusion fields (RSDG model).

4.6 Influence of Volumetric Mismatch and Young's Modulus

Precipitation at dislocations is simulated using the classical model assuming randomly distributed precipitates surrounded by spherical diffusion fields (RSDG model), see section 3.4.2.1. Due to differences in lattice parameters, in some cases (e.g. AlN), high volumetric misfits between microalloy precipitates and the steel matrix are observed. This makes it necessary to take into account the elastic strain energy G_s. Especially, in the nucleation stage, this energy contribution can substantially reduce the total free energy change (see equation 3.15) and, thus, the nucleation rate (equation 3.11). In addition to the volumetric misfit, the Young's modulus is an important ingredient for the calculation of the elastic strain energy G_s, see equation 3.16.

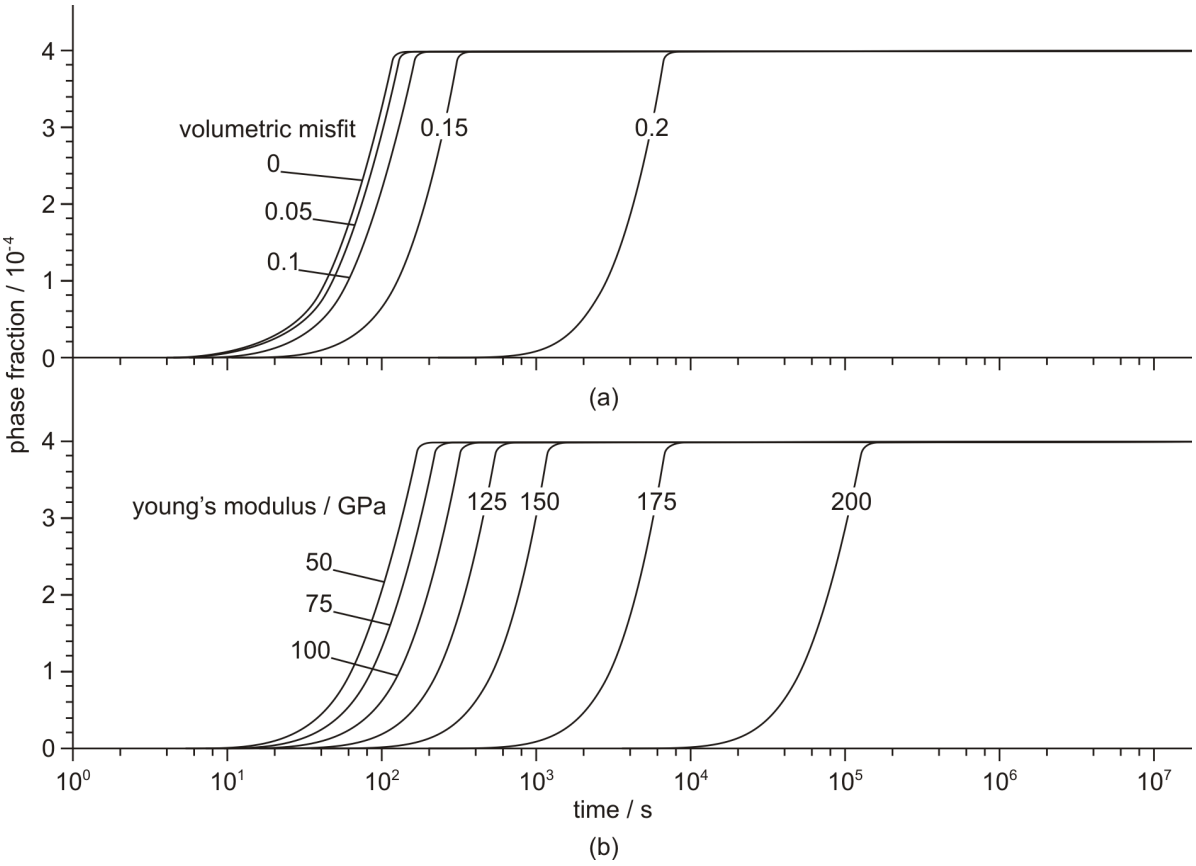

Figure 4.25: Sensitivity of the calculations of precipitation at dislocations on the parameters (a) volumetric misfit and (b) Young's modulus.

For the analysis of the sensitivity of the calculation of precipitation at dislocation on the volumetric misfit energy contribution, an alloy containing 0.05 % Al and 0.005 % N is isothermally heat-treated at a temperature of 700 °C. Figure 4.25 indicates the influence of the values of the volumetric misfit and the Young's modulus on the simulation results. The volumetric misfit is varied between 0 and 0.2 in 0.05 steps (figure 4.25 (a)) and the Young's modulus is varied between 50 GPa and 200 GPa in 25 GPa steps (figure 4.25 (b)). Both, the volumetric misfit as well as the Young's modulus show a high influence on the precipitation kinetics calculations. An increase of these parameters can retard the precipitation to longer times by several orders of magnitude. While the temperature-dependent Young's moduli of the matrix phases fcc and bcc are well established (see section 4.4.2), the volumetric misfit has to be analysed for each microalloying phase at each nucleation site.

4.7 Kinetics of AlN Precipitation in Microalloyed Steel

It is already mentioned in section 3.2.1.1 that Al is an essential ingredient for the production of microalloyed high strength steels. The predominant precipitation of AlN is made responsible for grain refinement, which increases strength as well as toughness, see section 3.1.3. To achieve the desired mechanical properties, it is essential to control the precipitation of AlN carefully during the production process, and thus to understand the precipitation of these important precipitates.

Several authors have reported about theoretical treatments of AlN precipitation in microalloyed steel. Duit et al. [166] carried out calculations of AlN precipitation in ferrite based on the Avrami equation. Cheng et al. [41, 95, 167] model the precipitation of AlN in microalloyed steel. In [41, 95], these authors treat the coarsening and growth stages not accounting for the nucleation process. In reference [167], they also consider the nucleation stage, but they verify their model only on a single chemical composition. Technology-oriented treatments are available for AlN precipitation during compact strip production (CSP) [93], thin slab casting and rolling (TSCR) [168] or coiling of hot strips of microalloyed steels [169]. Zolotorevsky et al. [170] as well as Kozeschnik et al. [171] investigated the competing processes of AlN precipitation and recrystallization during batch annealing of low C steel. Biglari et al. [47] model the precipitation kinetics of AlN during internal nitridation with special emphasis on the crystallographic structure. Using thermodynamic calculations, they demonstrate that, in recrystallized specimens, the precipitation of incoherent, hexagonal AlN is favoured, whereas the precipitation of coherent cubic precipitates is preferred in cold rolled specimens.

However, despite this high number of computational studies available in literature, there is no comprehensive and rigorous description of the precipitation kinetics available for AlN precipitation. The present section deals with the numerical simulation of the precipitation kinetics of AlN, taking into account that AlN precipitation can occur simultaneously at grain boundaries and on dislocations [172–176]. The computed results are compared to independent experimental data from literature, spanning a wide range of

different chemical compositions and various isothermal annealing temperatures.

4.7.1 Materials

The numerical simulations are compared to experimental data from nine literature sources [45, 87–89, 138, 166, 168, 177, 178]. The Al and N contents are given in table 4.9 and table 4.10 for ferrite and austenite, respectively, and sorted according to the value of their solubility product. These alloys cover a wide range of different Al and N contents representative for conventional microalloyed steel.

Table 4.9: Chemical composition of the alloys investigated in ferrite.

alloy	Al / wt%	N / wt%	Log k_s	T_{sol} / °C	grain size / μm	ref.
1	0.046	0.0067	-3.51	1187	15	[138]
2	0.059	0.0051	-3,52	1187	10	[177]
3	0.058	0.0050	-3,54	1181	7	[45]
4	0.058	0.0038	-3,66	1150	7	[178]
5	0.030	0.0070	-3.67	1143	15	[168]
6	0.047	0.0043	-3,69	1142	10	[166]
7	0.016	0.0065	-3,98	1072	5	[177]
8	0.035	0.0029	-3,99	1072	10	[177]
9	0.060	0.0017	-3,99	1074	15	[177]
10	0.019	0.0039	-4,13	1040	7	[177]

Table 4.10: Chemical composition of the alloys investigated in austenite.

alloy	Al / wt%	N / wt%	Log k_s	T_{sol} / °C	grain size / μm	ref.
11	0.055	0.0240	-2,88	1417	50	[88]
12	0.120	0.0057	-3,16	1327	100	[89]
13	0.079	0.0072	-3,25	1262	50	[87]
14	0.058	0.0058	-3,47	1198	100	[87]
15	0.030	0.0070	-3.67	1143	150	[168]

4.7.2 Weight Percent Versus Volume Percent

Most of the experimental references [45, 87–89, 138, 166, 168, 177, 178] report about measured phase fractions in weight percent or the amount of N in wt% bound to AlN, see e.g. König et al. [88]. However, performing numerical simulations with MatCalc delivers phase fractions of carbides and/or nitrides in mole percent. Therefore, the experimental data has to be transformed from measured N bounded to AlN in wt% to the phase fraction of AlN in mol%. This section deals with a short explanation on how to handle this transformation on the example of AlN.

Let us assume that a numerical simulation with MatCalc delivers a calculated phase fraction for AlN of 0.056 mol%. This means that 0.056% of all atoms are Al and N atoms. Let us further assume that AlN is a stoichometric compound. Thus, 0.056 mol% AlN consist of 0.028 mol% N and 0.028 mol% Al. The major amount of atoms in a microalloyed steel is represented by Fe. Therefore, the atomic weight of the measured N (14 g mol^{-1}) has to be related to the atomic weight of Fe (56 g mol^{-1}). Finally the relation of calculated AlN in mol% and measured N in wt% bound to AlN can be expressed as

$$AlN\ [mol\%] = \frac{m_{Fe}}{m_N} \cdot x_{stoch} \cdot N[wt\%], \tag{4.8}$$

where m_{Fe}/m_N represents the differences in atomic weight and x_{stoch} takes into account the stoichiometric compound. Thus a factor of 8 ($4 \cdot 2$) must be considered when comparing the calculated phase fraction of AlN in mol% to the measured amount of N in wt% bound to AlN.

4.7.3 Simulation Setup

Precipitation of AlN in ferrite and austenite is assumed to occur simultaneously on grain boundaries and dislocations. Therefore, two separate populations of AlN precipitates are considered in the simulations, different in the type of nucleation site and the value for the volumetric misfit. Figure 4.26 shows the volumetric misfit (solid line) along with

the molar volumes of the bcc, fcc and AlN phases (dashed lines) versus temperature.

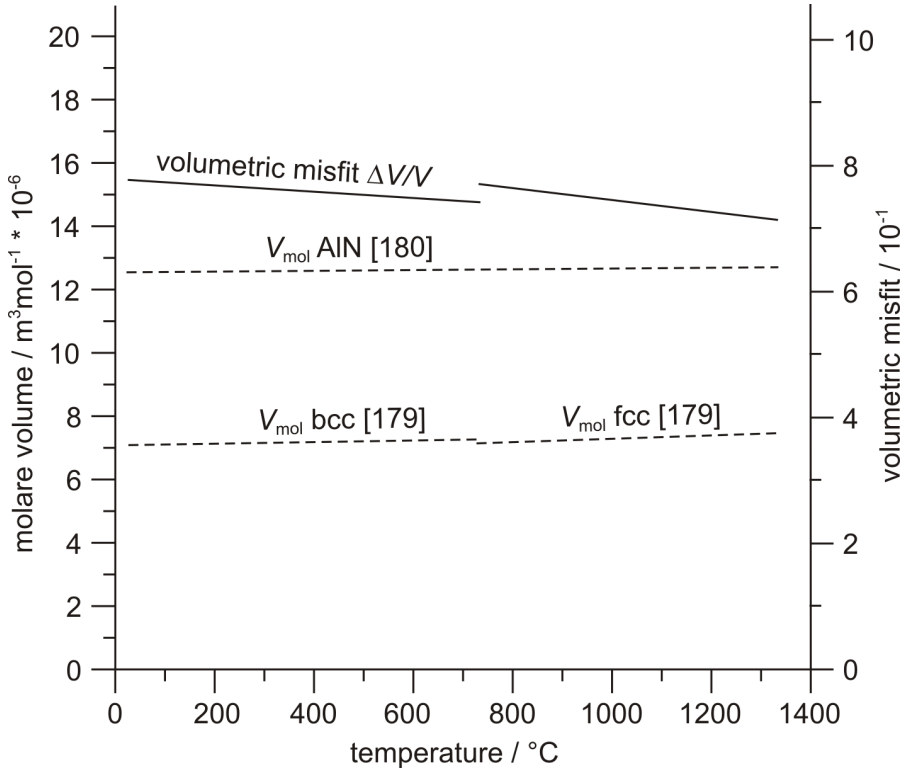

Figure 4.26: Volumetric misfit of the phases bcc, fcc, AlN and the calculated volumetric misfit [179, 180].

Accordingly, the misfit is relatively constant over the entire temperature range and varies between 71 % and 77 %. However, these values represent the precipitate/matrix mismatch in an undisturbed crystal lattice and represent the so-called unconstrained misfit, which corresponds to the difference in lattice parameters of isolated bcc, fcc and AlN phases. In a precipitate/matrix composite, the matrix and precipitates will be elastically stressed, which leads to a so-called constrained misfit [181]. This effect reduces the effective volumetric mismatch that must be inserted for calculation of the misfit energy. Moreover, the misfit strain energy between AlN nuclei and matrix is strongly influenced by lattice defects, such as dislocations and grain boundaries. For the former, precipitates can accommodate some of the volumetric misfit strain in the dislocation regions with either compressive or tensile local stresses. For the latter, we assume that the grain boundary represents a heavily disturbed lattice region with almost amorphous

structure. The precipitate nuclei can form with incoherent phase boundary, where lattice vacancies can easily be created or annihilated, and relaxation of misfit strains [182] can occur almost simultaneously with nucleus formation.

The simulations have shown that a constant value of 19* % effective volumetric misfit for precipitates located at dislocations delivers good results for the calculation of precipitation of AlN in ferrite as well as in austenite. No volumetric mismatch is considered for the precipitates at grain boundaries due to the assumed immediate stress relaxation caused by vacancy creation or annihilation at the precipitate/matrix interface. Using a value of 70 % mismatch for coherent bulk nucleation entirely suppresses the nucleation of AlN in all situations considered in the present work, consistent with experimental evidence. For the calculation of the misfit strain energy, temperature dependent Young's moduli are used according to equations 4.4 and 4.5 for austenite and ferrite, respectivley. For the calculations of precipitates at dislocations, dislocation densities of 10^{12} m^{-2} and 10^{11} m^{-2} are assumed for annealed ferrite and austenite, respectively [141].

Furthermore, figure 4.17 shows the temperature dependent ratios between diffusion at grain boundaries and in the bulk D_{gi}/D_{bi}, used for grain boundary precipitation [78]. Equations 4.2 and 4.3 are incorporated in the present simulation setup.

The only variable input parameter in the simulations is the grain size, which is unfortunately widely unknown for the various experiments. The grain sizes assumed in the calculations are summarized in table 4.9 and table 4.10 and are between 5 and 15 μm for ferrite and 50 and 150 μm for austenite. All simulations presented subsequently are otherwise performed with the same identical set of simulation parameters.

4.7.4 Phase Fraction of AlN Versus Time

The following figures show the calculated phase fraction versus time curves of AlN precipitated in 15 different alloys at various temperatures.

*The effective volume misfit of AlN at dislocations, originally determined with 0.19 in ref. [172] and as used in this thesis, must be replaced by 0.27 when using MatCalc versions 5.40 and higher. Due to a software bug, the misfit value has erroneously been taken twice in older versions.

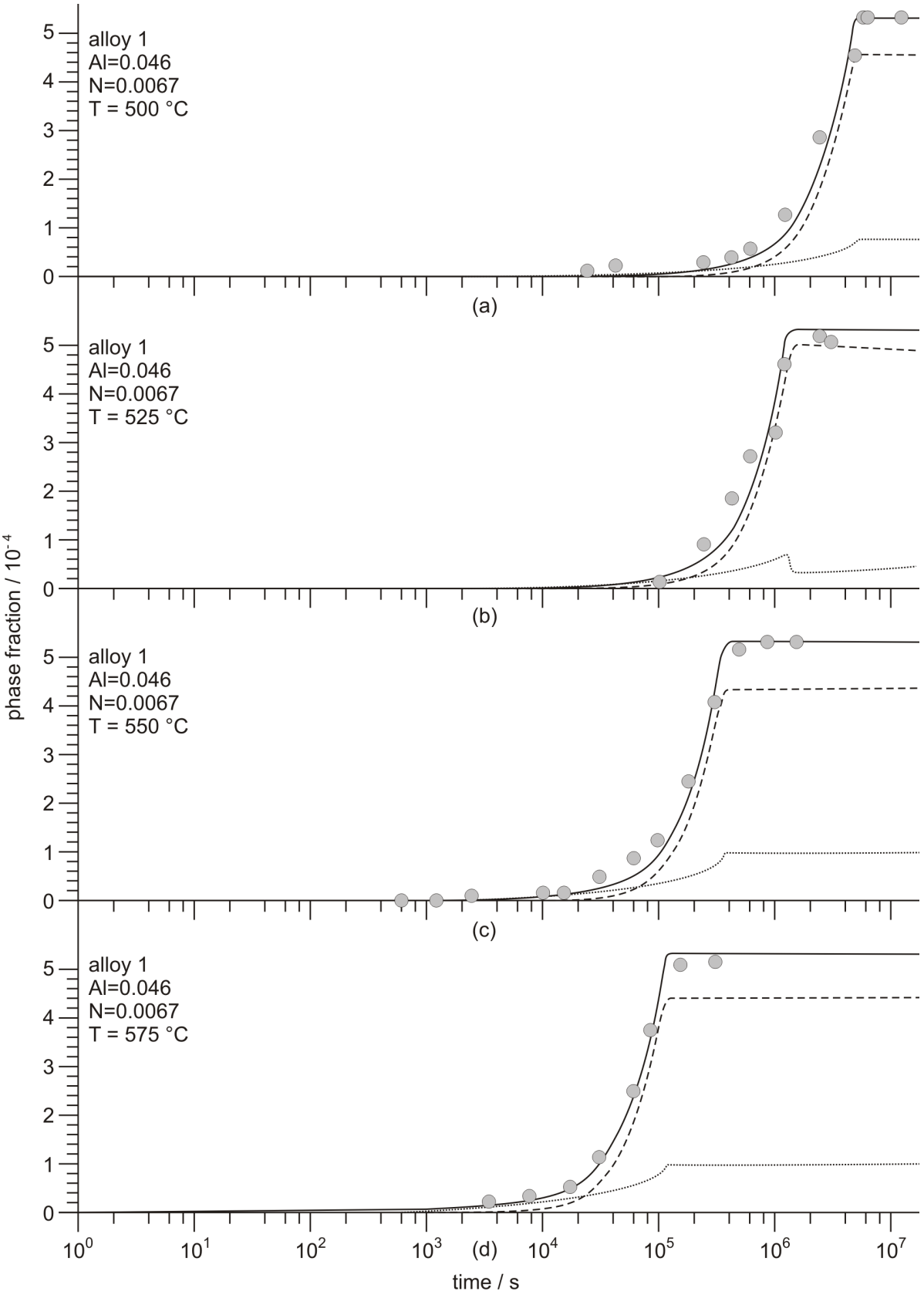
alloy 1
Al=0.046
N=0.0067
T = 500 °C
(a)
alloy 1
Al=0.046
N=0.0067
T = 525 °C
(b)
alloy 1
Al=0.046
N=0.0067
T = 550 °C
(c)
alloy 1
Al=0.046
N=0.0067
T = 575 °C
(d)
phase fraction / 10-4
time / s

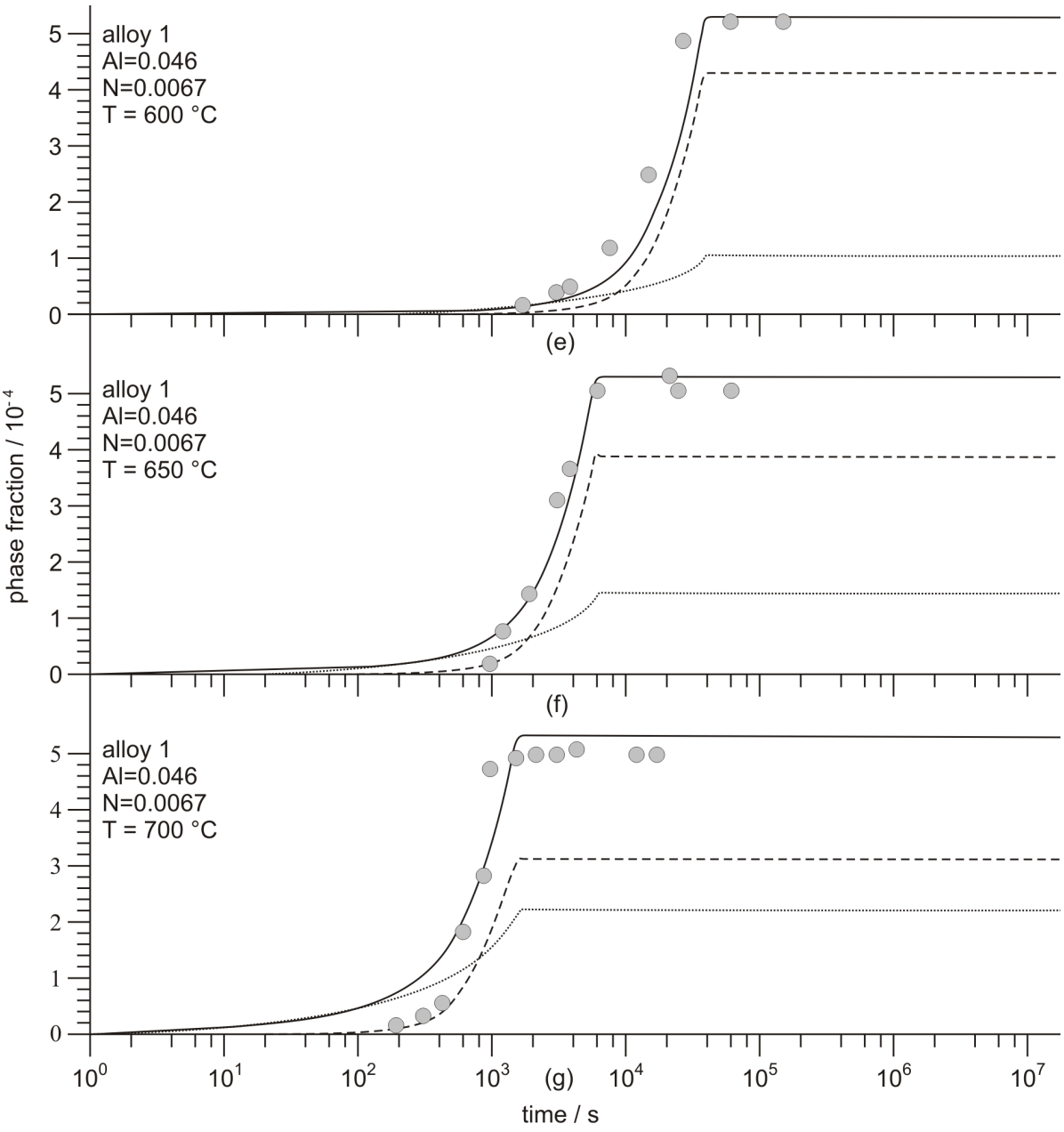

Figure 4.27: Calculated and experimental precipitation kinetics of AlN in ferrite for alloy 1 at several temperatures.

For ten alloys, precipitation occurred in the ferrite phase field, see figures 4.27 - 4.36. The simulation of the precipitation kinetics in the austenite phase field is shown in figures 4.37 - 4.41, using five different chemical compositions.

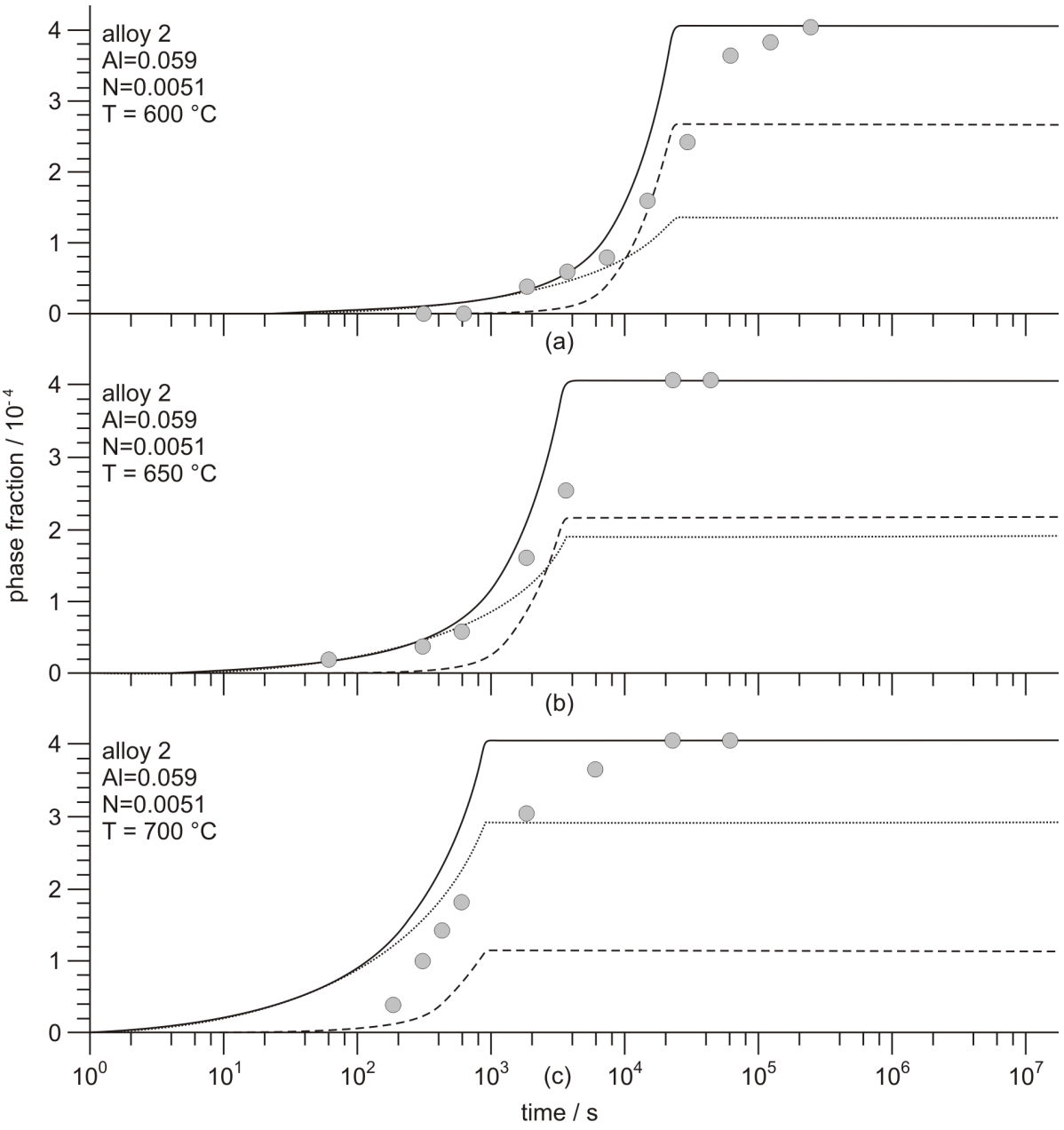

Figure 4.28: Calculated and experimental precipitation kinetics of AlN in ferrite for alloy 2 at the temperatures 600 °C, 650 °C and 700 °C.

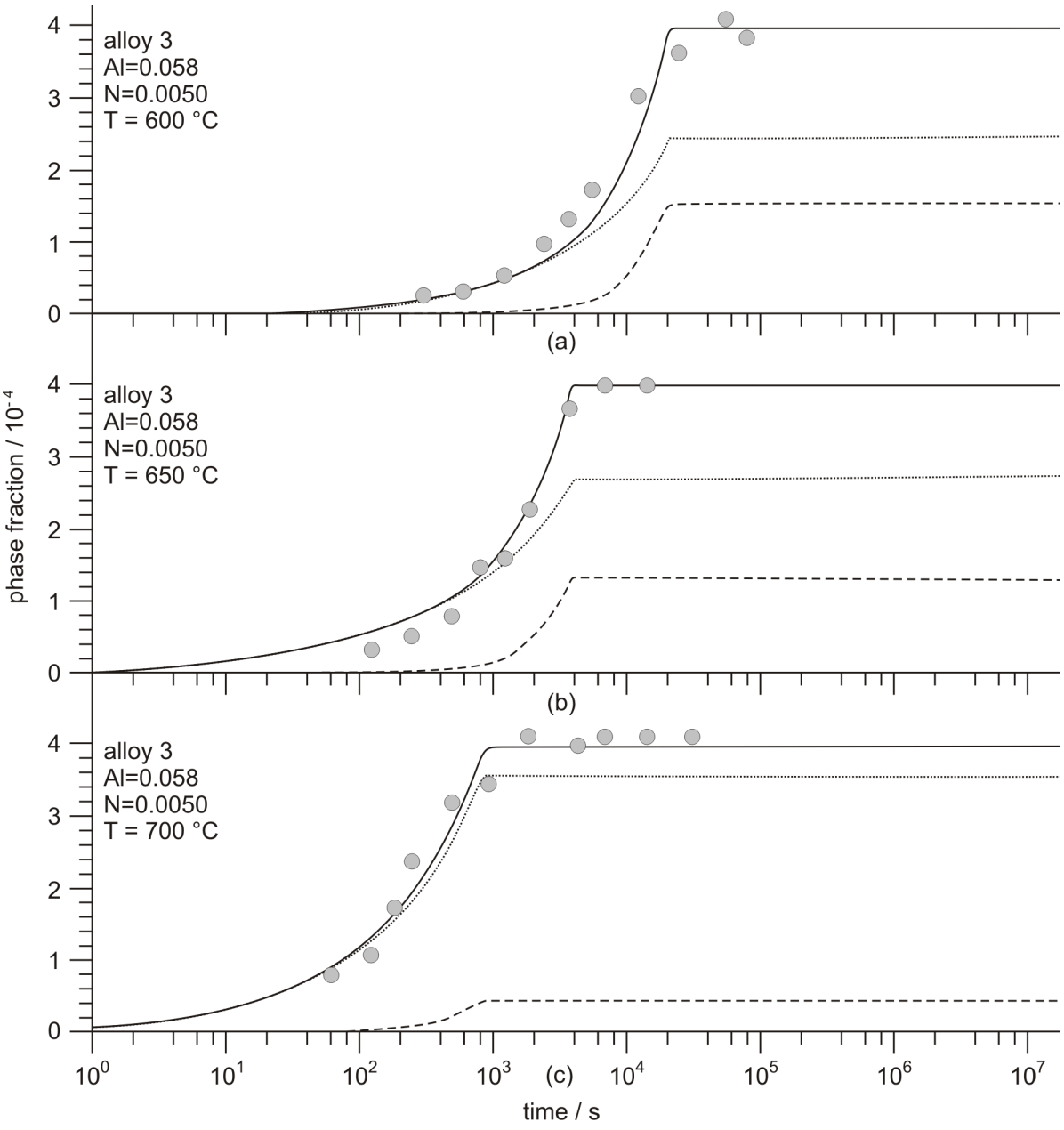

Figure 4.29: Calculated and experimental precipitation kinetics of AlN in ferrite for alloy 3 at the temperatures 600 °C, 650 °C and 700 °C.

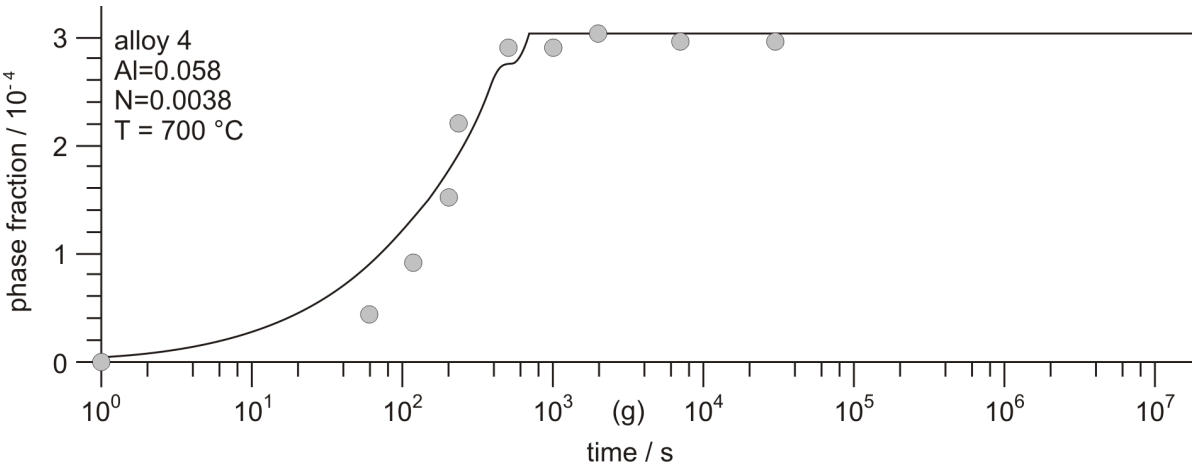

Figure 4.30: Calculated and experimental precipitation kinetics of AlN in ferrite for alloy 4 at a temperature of 700 °C.

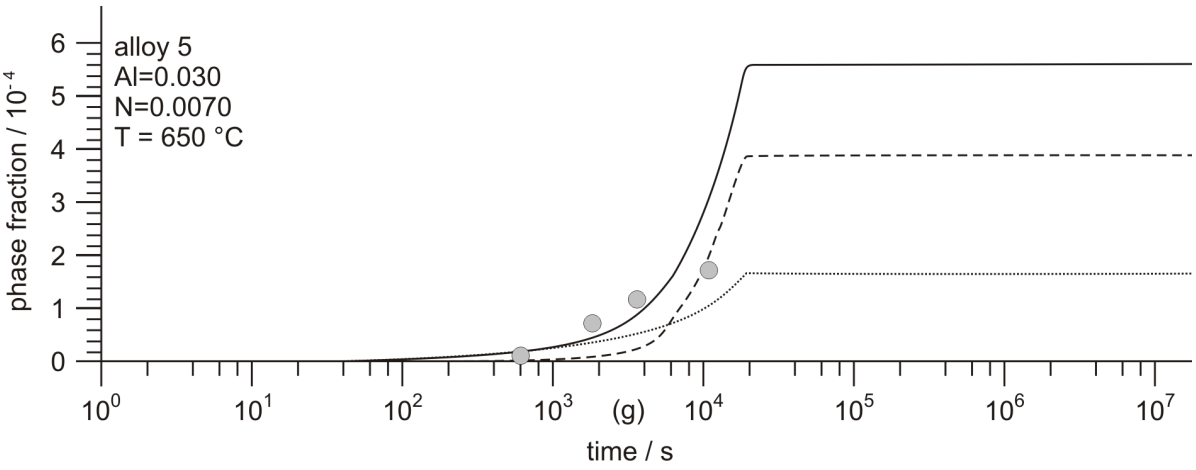

Figure 4.31: Calculated and experimental precipitation kinetics of AlN in ferrite for alloy 5 at a temperature of 650 °C.

The grain sizes used for the calculations are given in table 4.9 and table 4.10. The dashed lines represent precipitates formed at dislocations, whereas the dotted lines represent precipitates formed at grain boundaries. The sum of both phase fractions corresponds to the solid lines. Again, the alloys are sorted according to decreasing Al and N contents, which decrease from alloy 1 to 10 and from alloy 11 to 15 for the calculations in ferrite and austenite, respectively.

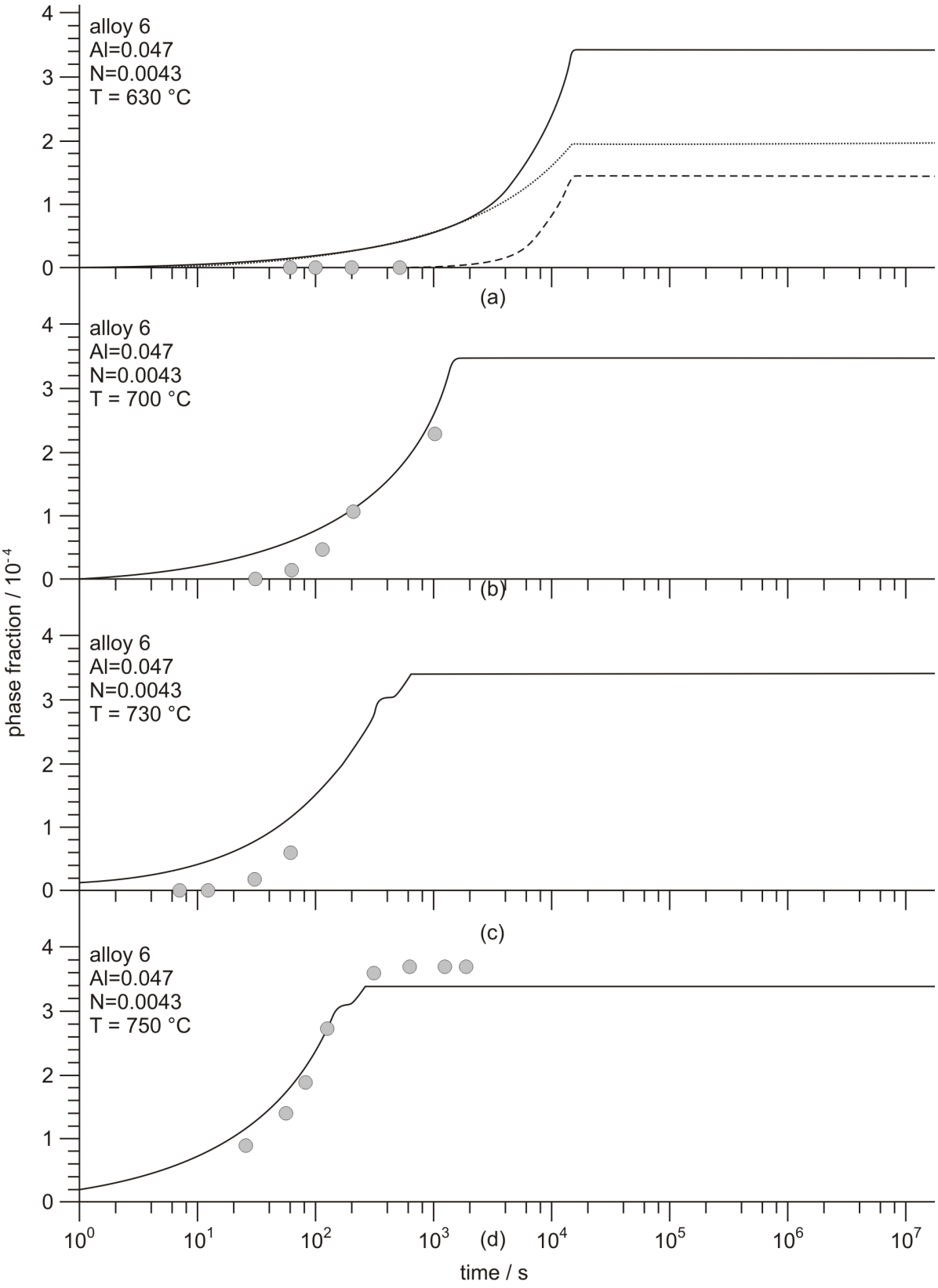
alloy 6
Al=0.047
N=0.0043
T = 630 °C
(a)
alloy 6
Al=0.047
N=0.0043
T = 700 °C
(b)
alloy 6
Al=0.047
N=0.0043
T = 730 °C
(c)
alloy 6
Al=0.047
N=0.0043
T = 750 °C
(d)
phase fraction / 10-4
time / s

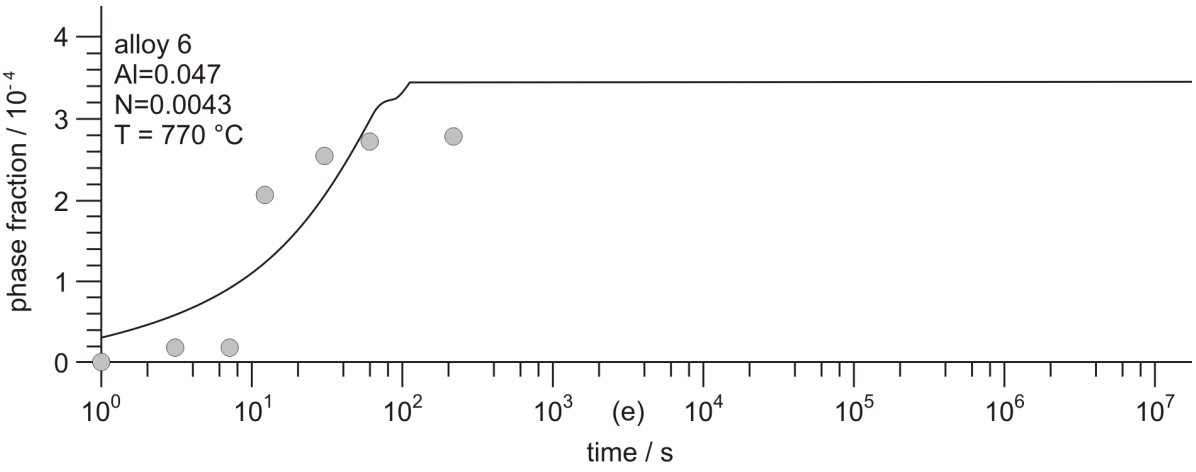

Figure 4.32: Calculated and experimental precipitation kinetics of AlN in ferrite for alloy 6 at at several temperatures.

Depending on chemical composition and annealing temperature, the calculations show only precipitation at grain boundaries or simultaneous precipitation at grain boundaries and dislocations. Especially in alloys with high Al and N contents, precipitation is observed at both nucleation sites, which is shown in figures 4.27 - 4.31, 4.32(a), 4.33(a), 4.34(a), 4.35(a) for precipitation in ferrite, and in figures 4.37(a,b) for precipitation in austenite.

Moreover, a strong dependency of nucleation site selection on the isothermal annealing temperature is observed. Whereas, at low temperatures and with higher driving forces, the majority of precipitates is located at dislocations, at higher annealing temperatures, precipitation at grain boundaries becomes predominant, see figures 4.27 - 4.29. For steels with low Al and N additions (see alloy 6-10), which have solubility products smaller than approximately -3.7, a clear preference for precipitation at ferrite grain boundaries is observed, see figures 4.32 - 4.36.

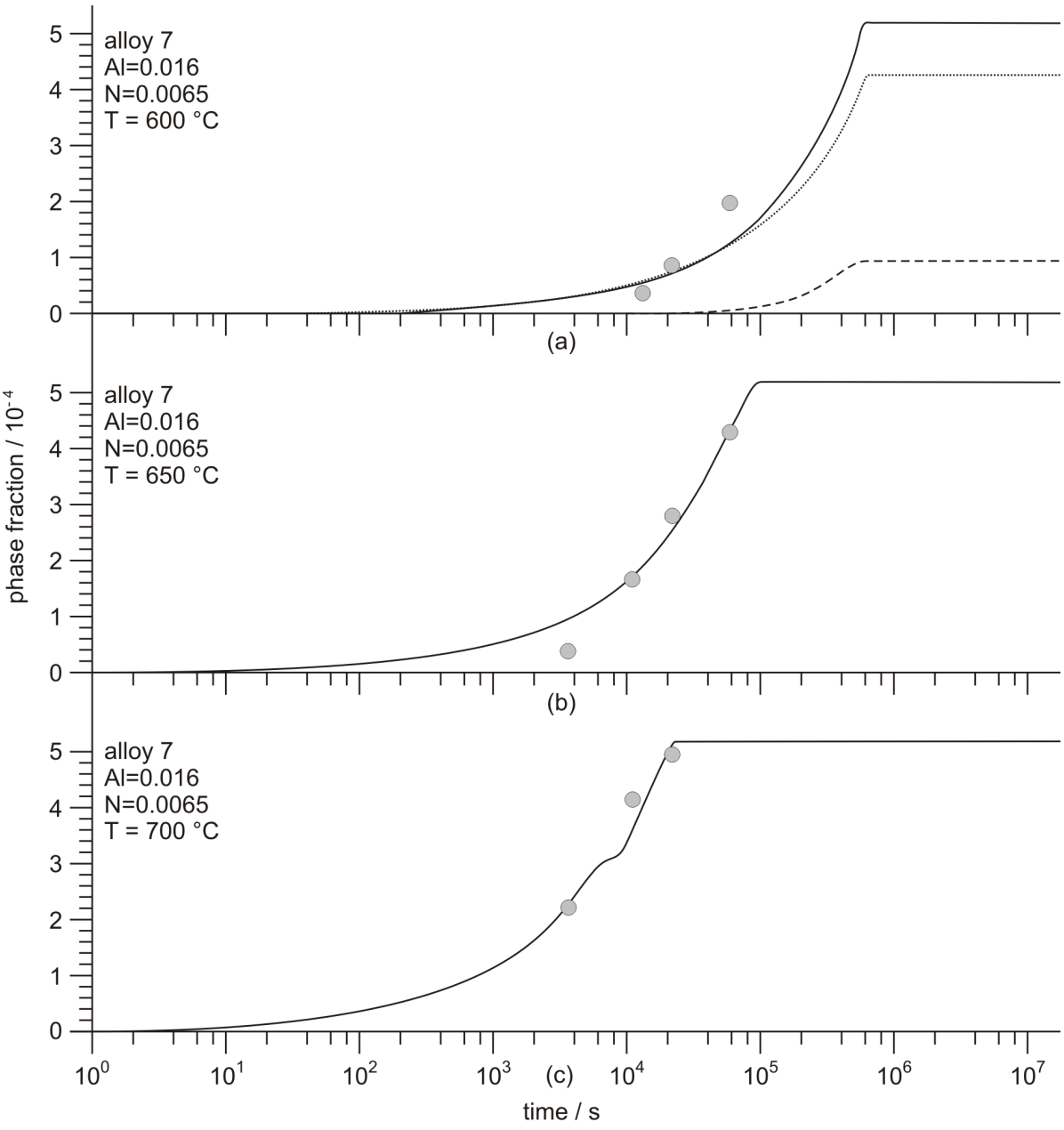

Figure 4.33: Calculated and experimental precipitation kinetics of AlN in ferrite for alloy 7 at the temperatures 600 °C, 650 °C and 700 °C.

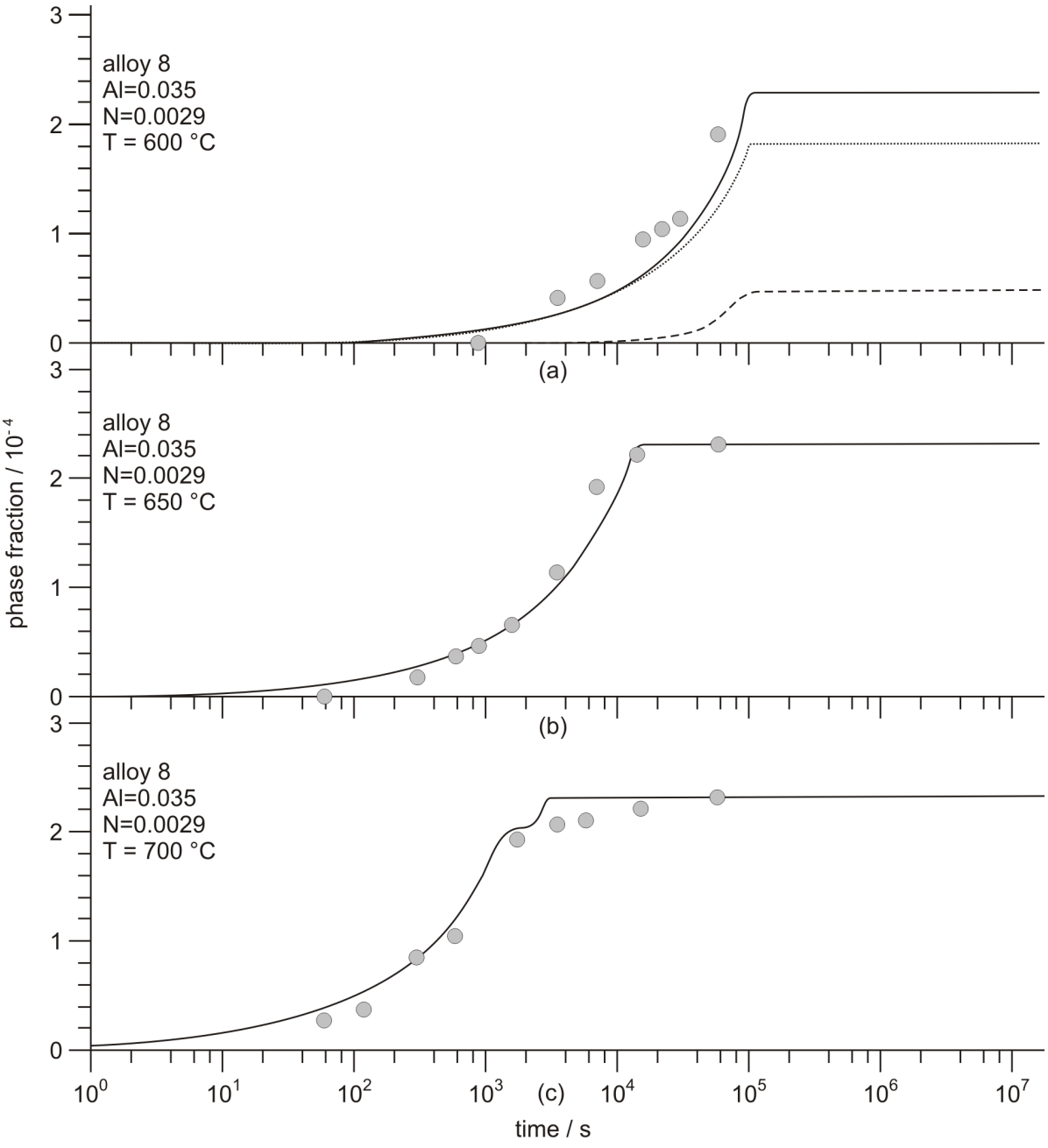

Figure 4.34: Calculated and experimental precipitation kinetics of AlN in ferrite for alloy 8 at the temperatures 600 °C, 650 °C and 700 °C.

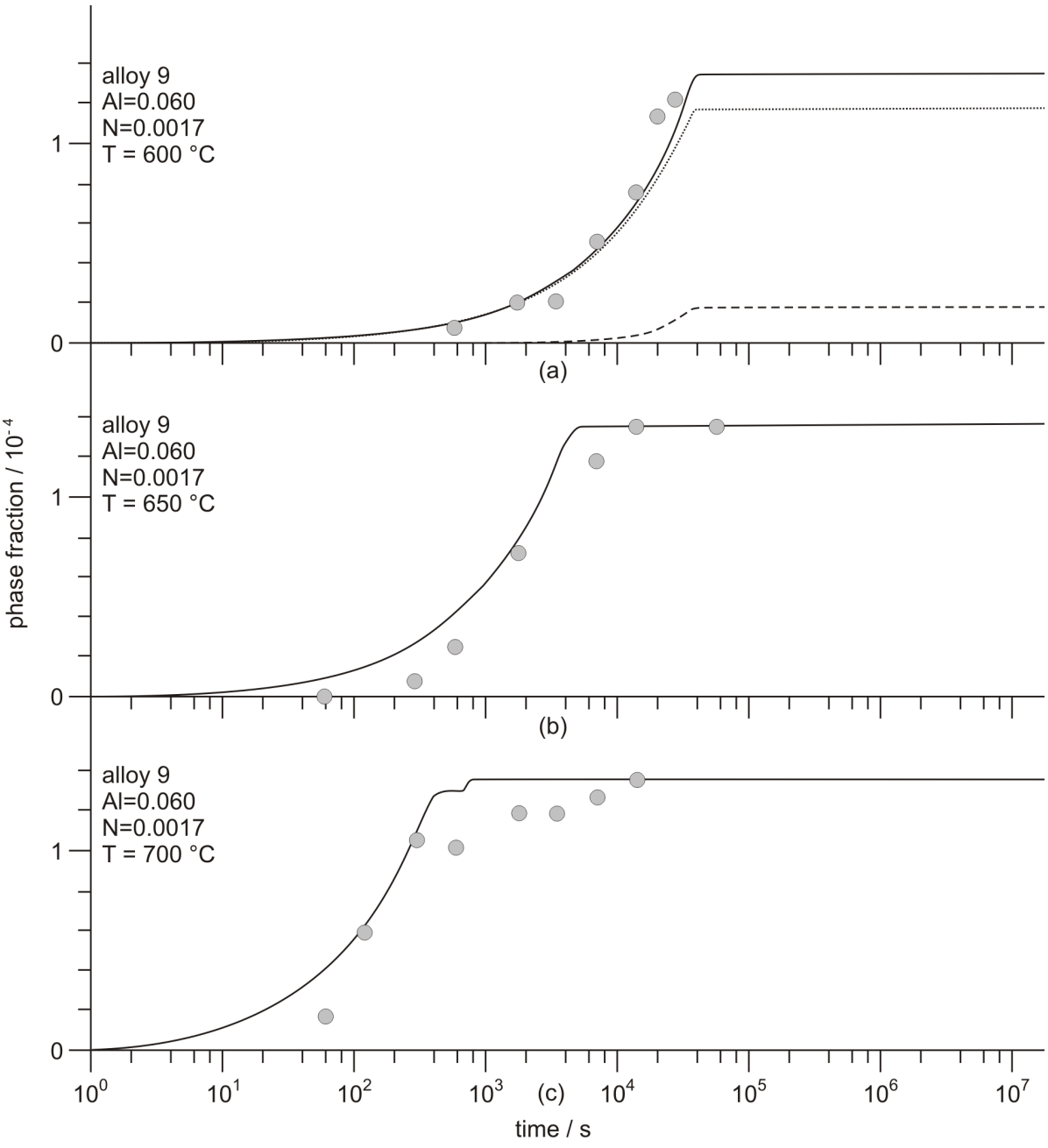

Figure 4.35: Calculated and experimental precipitation kinetics of AlN in ferrite for alloy 9 at the temperatures 600 °C, 650 °C and 700 °C.

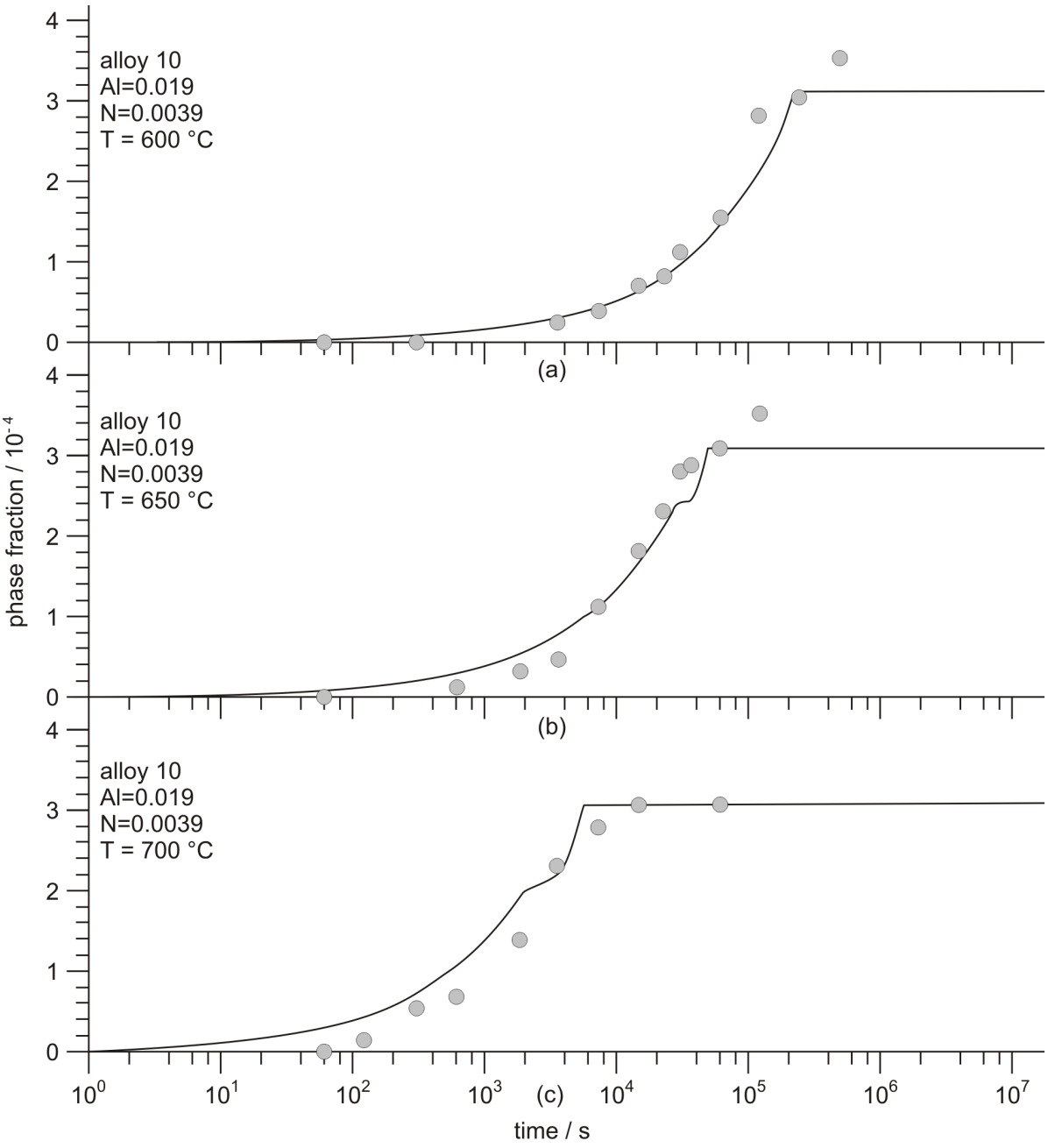

Figure 4.36: Calculated and experimental precipitation kinetics of AlN in ferrite for alloy 10 at the temperatures 600 °C, 650 °C, 700 °C.

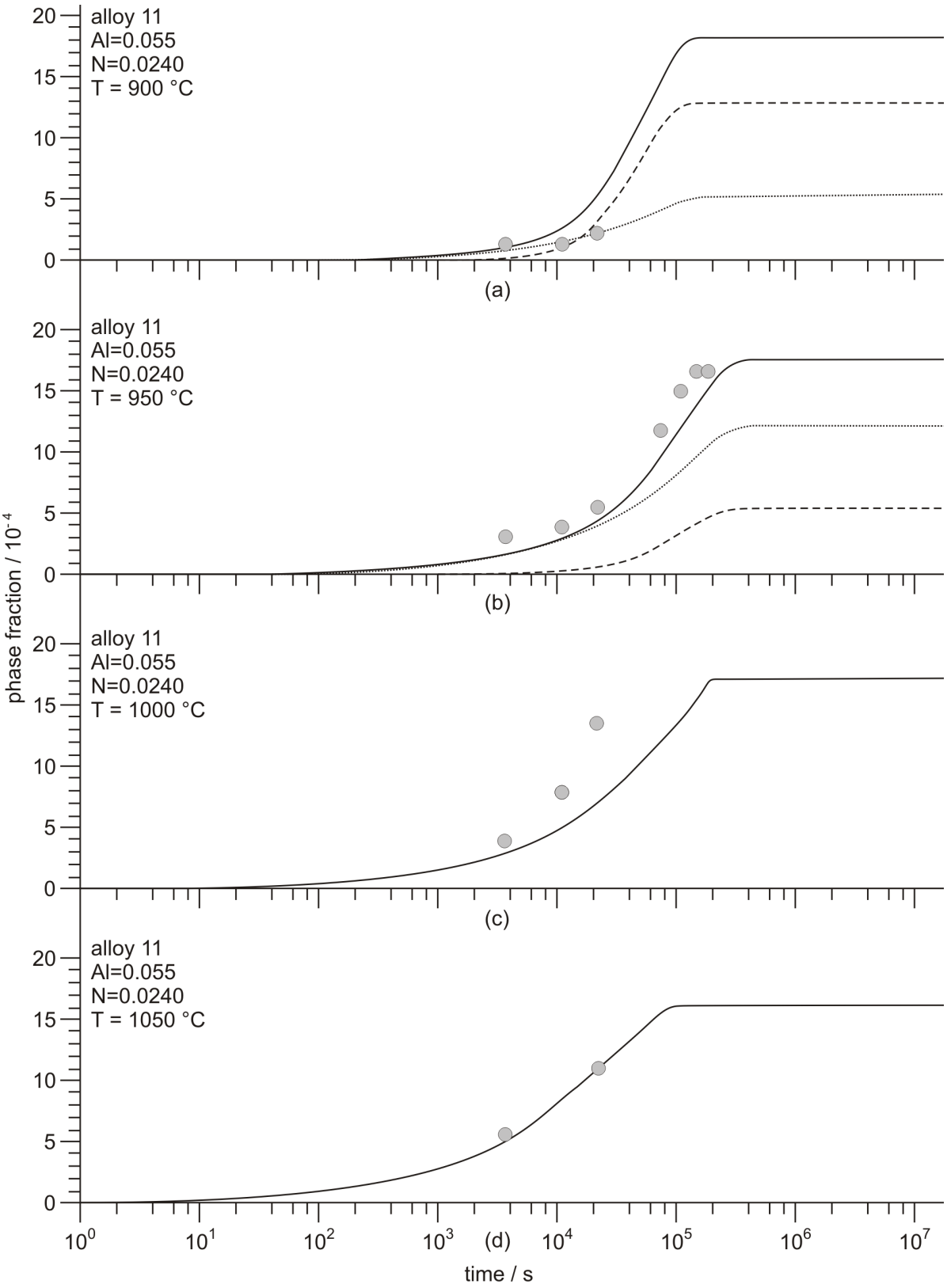
alloy 11
Al=0.055
N=0.0240
T = 900 °C
(a)
alloy 11
Al=0.055
N=0.0240
T = 950 °C
(b)
alloy 11
Al=0.055
N=0.0240
T = 1000 °C
(c)
alloy 11
Al=0.055
N=0.0240
T = 1050 °C
(d)
phase fraction / 10-4
time / s

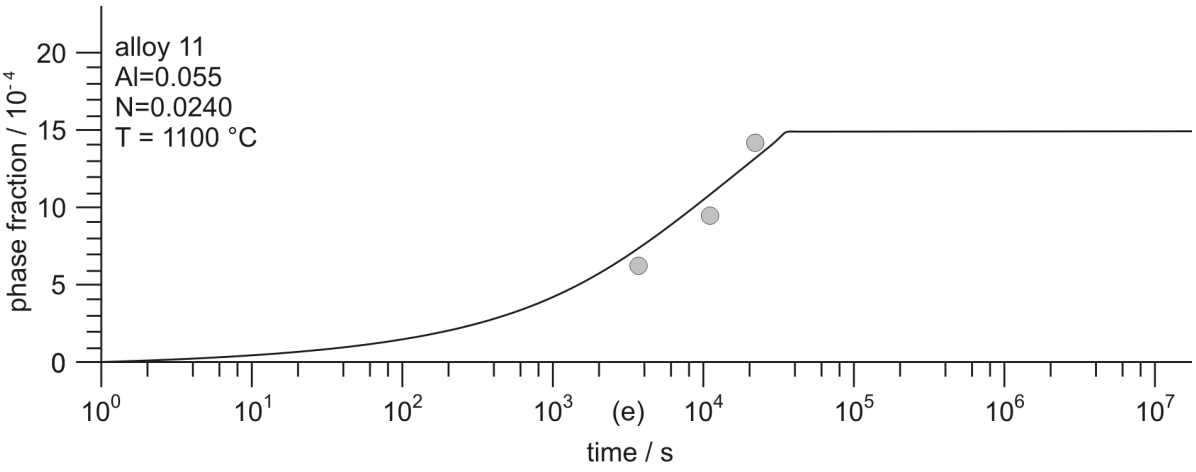

Figure 4.37: Calculated and experimental precipitation kinetics of AlN in austenite for alloy 11 at at several temperatures.

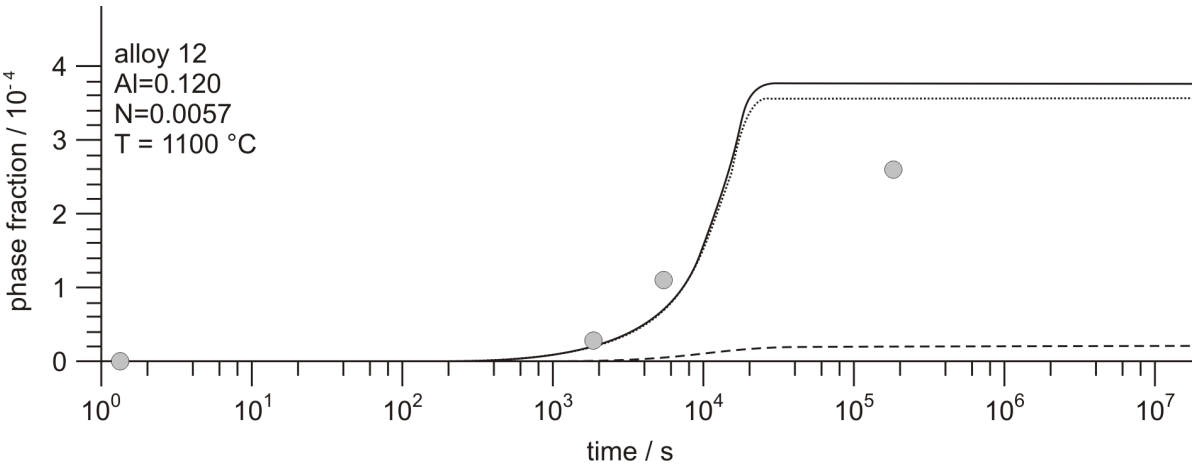

Figure 4.38: Calculated and experimental precipitation kinetics of AlN in austenite for alloy 12 at a temperature of 1100 °C.

This observation is even more pronounced in the case of precipitation in austenite, in agreement with thermodynamic calculations of Cheng et al. [167], who have also showed that G^* is much higher for homogeneous nucleation compared to nucleation at grain boundaries. These authors concluded that AlN nucleates predominantly at austenite grain boundaries. Apart from alloy 11, this is also observed in this work, see figures 4.37 - 4.41. However, alloy 11 has a very high solubility product of -2.88. This leads to the predicted additional precipitation at dislocation for temperatures below 950 °C.

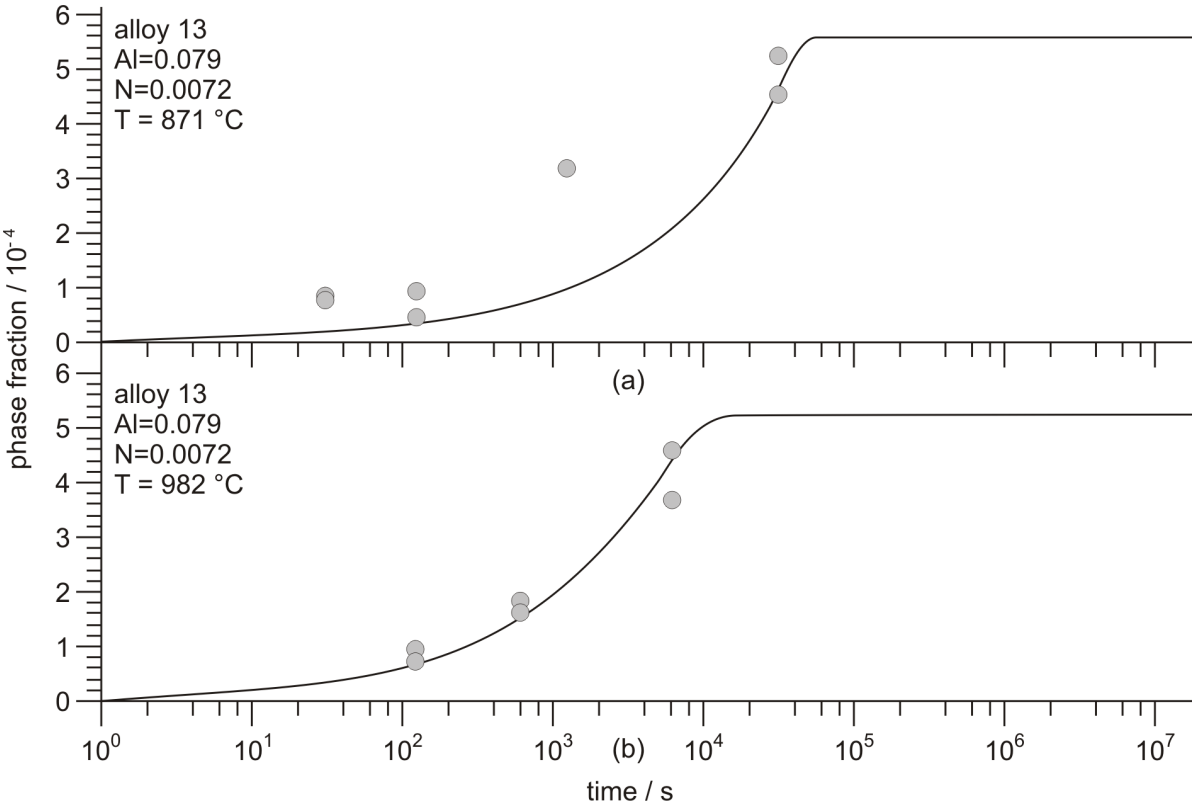

Figure 4.39: Calculated and experimental precipitation kinetics of AlN in austenite for alloy 13 at the temperatures 871 °C and 982 °C.

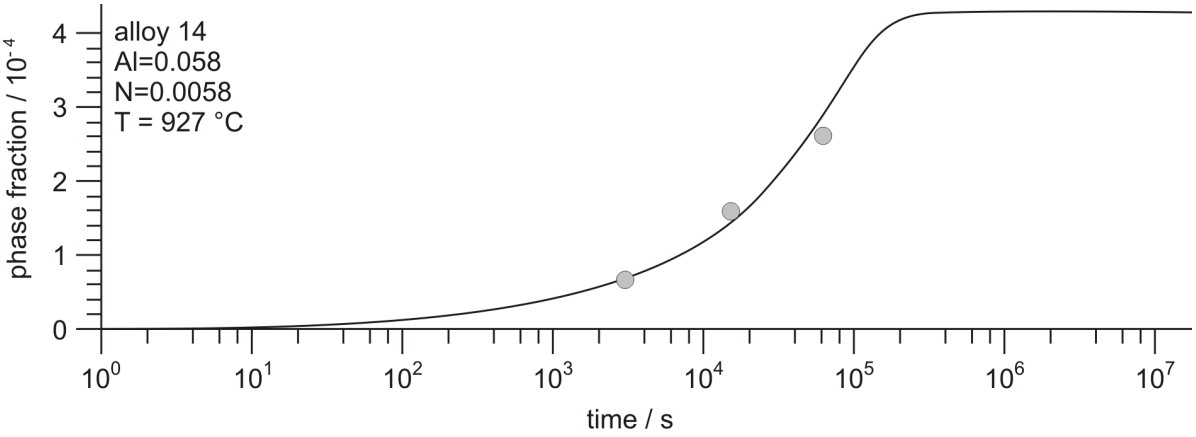

Figure 4.40: Calculated and experimental precipitation kinetics of AlN in austenite for alloy 14 at a temperature of 927 °C.

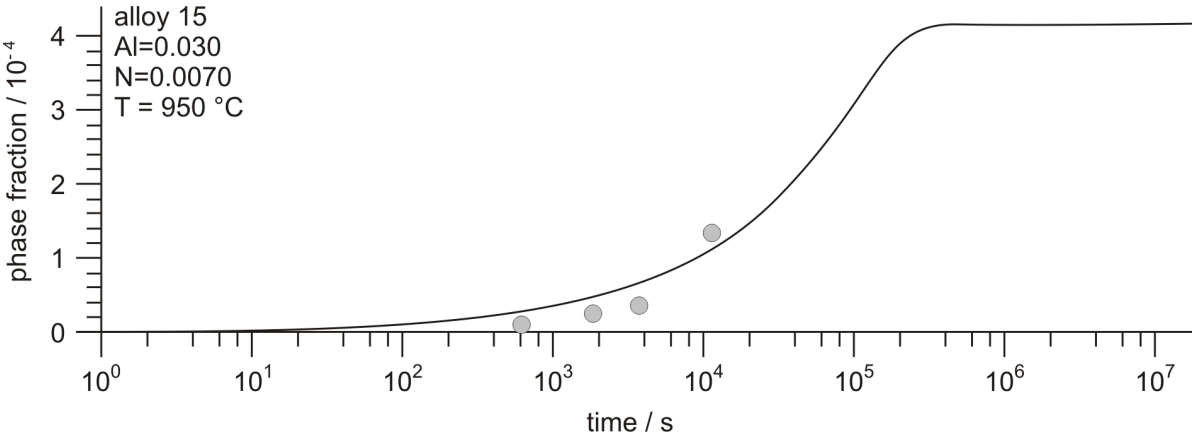

Figure 4.41: Calculated and experimental precipitation kinetics of AlN in austenite for alloy 15 at a temperature of 950 °C.

4.7.5 Time-Temperature-Precipitation Plots for AlN in Steel

Figures 4.42 and 4.43 show a comparison of the precipitation kinetics of the alloys with lowest (alloy 10) and highest (alloy 11) amount of Al and N, depicted in time-temperature-precipitation (TTP) diagrams. In the simulations, the allotropic transformation from austenite to ferrite is assumed to occur at 800 °C. The calculations are performed with a grain size of 10 μm for the ferritic matrix and 100 μm for the austenitic matrix, respectively. Similar to figures 4.27 - 4.41, the grain boundary precipitates are represented by dotted lines, whereas dashed lines indicate the precipitates formed at dislocations. For both populations, the time for 5 % and 95 % precipitation (relative phase fraction) is displayed.

The two TTP diagrams reflect the features discussed for the previous figures. Whereas, for alloy 10, the solution temperature of AlN is calculated with 1040 °C, the solution temperature for alloy 11 is calculated with 1417 °C. As a consequence, in alloy 10, the precipitation of AlN is only observed at temperatures below 900 °C. Especially in austenite, precipitation occurs after long annealing times, e.g. $t_{0.05} = 2 * 10^4\ s$ with a nose temperature of 825 °C. Moreover, above 600 °C, precipitation of AlN is observed only at grain boundaries (dotted lines). Nucleation at dislocations is only predicted for temperatures below 600 °C (dashed lines) with rather small volume fractions.

In alloy 11 (figure 4.43), the nose temperature for precipitation in austenite is calculated

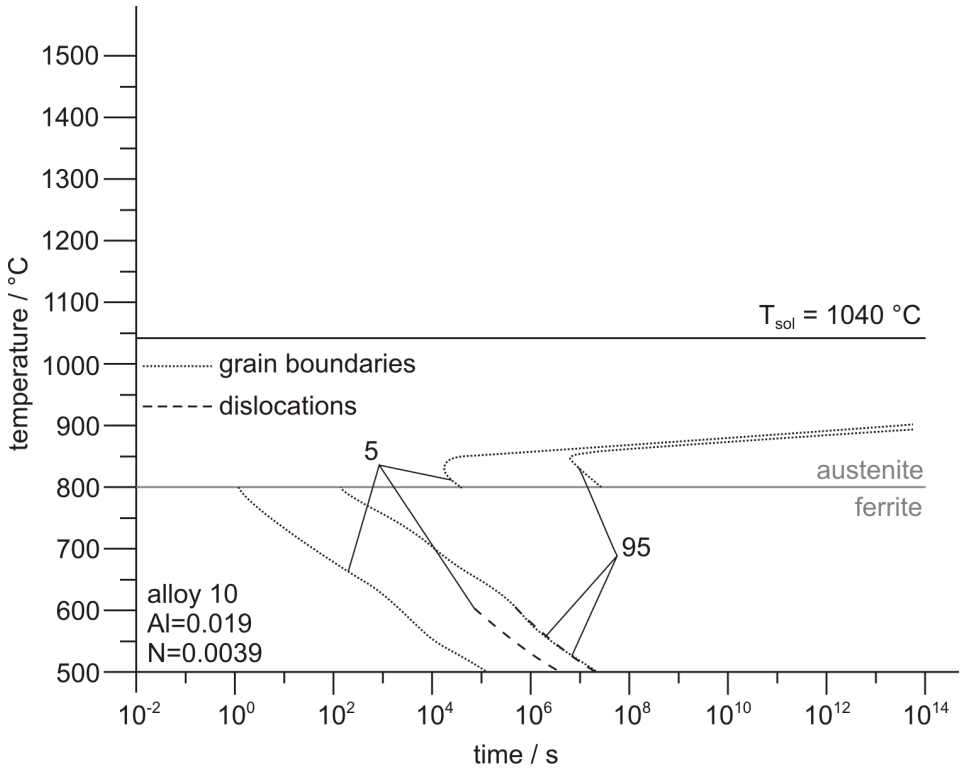

Figure 4.42: Calculated TTP diagram for alloy 10.

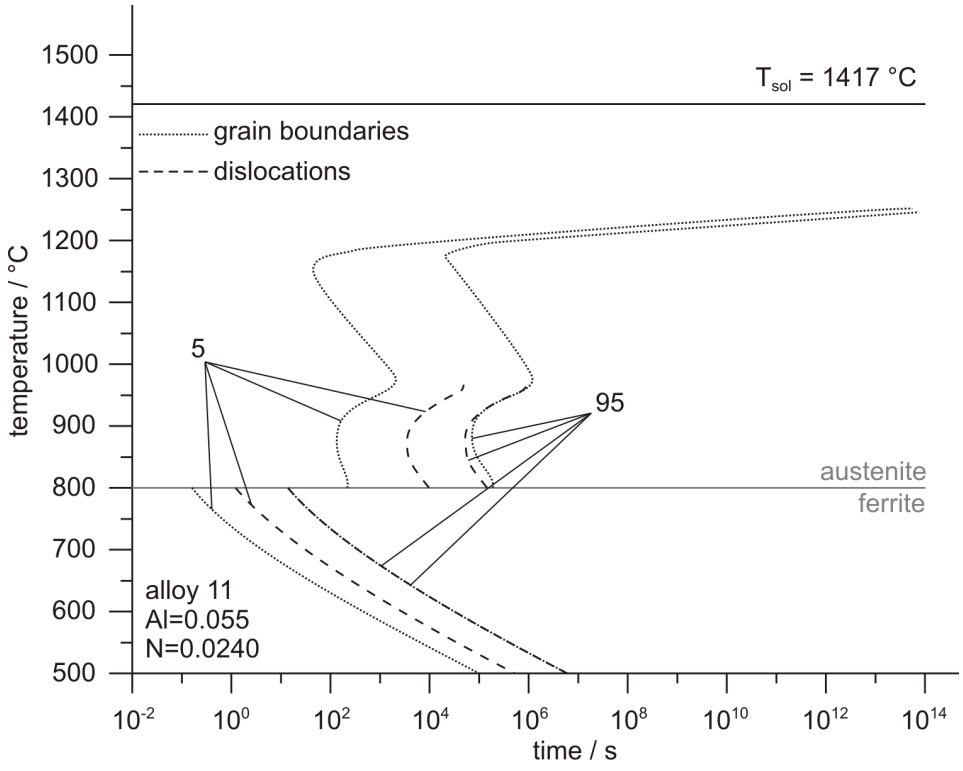

Figure 4.43: Calculated TTP diagram for alloy 11.

with 1150 °C. At this temperature, precipitation at grain boundaries occurs after 43 s. The discontinuity in the C-curve of the time-temperature-precipitation diagram for precipitation at austenite grain boundaries is attributed to the simultaneous precipitation of AlN at dislocations below a temperature of 1000 °C. Due to the change from major precipitation at grain boundaries to favored precipitation at dislocation, the total phase fraction of grain boundary precipitates is strongly reduced. Thus, the 5 % and 95 % phase fraction lines are shifted to shorter times. The fastest AlN precipitation kinetics is observed at a temperature of 800 °C for both alloys, which is the temperature of the assumed austenite to ferrite transformation. At this temperature, the precipitation of 5 % of the equilibrium phase fraction is completed after 1.5 s and 0.15 s for alloy 10 and alloy 11, respectively. Consequently, the present calculations suggest that AlN precipitation occurs almost immediately after austenite has transformed into ferrite.

4.7.6 Discussion

In order to get good agreement of our simulations with the available experimental data based on a single, identical set of input parameters, several physical mechanisms and several simulation steps had to be considered. First, the thermodynamic basis for AlN formation has been reassessed and a revised Gibbs energy expression has been developed, see section 4.2.1. Comparison of this expression with solubility products reported in literature shows that the new description delivers solubility products, which are close to the 'recommended' solubility products of Wilson and Gladman [26]. Although there exists some discrepancy with the assessment of Hillert and Jonsson [94] in terms of the entropy of AlN, the revised expression is capable of reproducing the necessary driving forces for AlN precipitation in austenite and ferrite in a satisfying manner. This agreement could not be achieved with any of the alternative thermodynamic descriptions of other databases. It is not clear whether there exists any influence of the crystal structure (simple cubic or hexagonal) of the AlN nuclei on the precipitation kinetics.

The present analysis demonstrates that, for the numerical description of AlN precipitation in microalloyed steel, it is essential to account for the predominant precipitation of

AlN at grain boundaries as well as at dislocations. The numerical simulations show that precipitation at grain boundaries starts very quickly in the early stages of the precipitation process due to fast diffusion of atoms along grain boundaries. However, the kinetics becomes significantly more sluggish in the later stages because of increasingly wide diffusion distances from the grain interior to the grain boundaries, see section 4.5 [78]. This effect is clearly reflected in the shape of the volume fraction versus time curves. Especially in alloys with high Al and N contents, simultaneous precipitation of AlN at grain boundaries and dislocations is observed in the present simulations. The reason for this is founded in the assumption that the misfit strain energy for the critical nucleus at dislocations is higher compared to the values at grain boundaries. Thus, the activation barrier for dislocation nucleation is only overcome in alloys with higher Al and N contents. The preferred precipitation at dislocations at lower temperatures can be attributed to higher driving forces caused by higher undercooling and faster growth of dislocation precipitates characterized by approximately spherical diffusion fields. This issue has been discussed in section 4.5, where the model characteristics of the GBDG model and the RSDG model are compared.

4.8 Concurrent Precipitation of AlN and VN in Microalloyed Steel

The goal of the present section is the investigation of the simultaneous precipitation of AlN and VN in austenite [183, 184]. The presence of both types of precipitates combines the positive effects of AlN (section 3.2.1.1) and VN (section 3.2.1.2). The predominant precipitation of AlN at grain boundaries is made responsible for grain size control (section 3.1.3), whereas VN increases strength by precipitation of fine dispersed distributed particles in the grain interior (section 3.1.4). Therefore, a proper control of these precipitation reactions is necessary to achieve the desired mechanical properties. Hence, it is essential to understand the precipitation process of both, AlN and VN, as well as their kinetic interactions.

4.8.1 Materials

Two different alloys are used for the analysis of the concurrent precipitation of AlN and VN in the austenite phase field of microalloyed steels. The chemical compositions as well as the calculated solution temperatures for the phases AlN and VN are given in table 4.11.

Table 4.11: Chemical composition of the investigated alloys [88].

alloy	Al / wt%	V / wt%	N / wt%	T_{sol}^{AlN} / °C	T_{sol}^{VN} / °C
16	0.052	0.14	0.023	1404	1018
17	0.010	0.14	0.024	1197	1177

While both alloys contain similar amounts of V and N, the additions of Al differ significantly.

4.8.2 Simulation Setup

The calculation of the precipitation kinetics of AlN is carried out according to the description given in section 4.7.3. A default grain diameter (gs) of 50 μm is used,

unless stated otherwise. In addition to the precipitation of AlN particles, a separate population of VN precipitates is introduced. The nucleation of VN is assumed to occur at dislocations, mainly, with an assumed dislocation density in austenite of 10^{11} m^{-2} [141]. The interfacial energy is evaluated from the generalized n-nearest-neighbour broken-bond approach [73, 74]. A brief description of this method is given in section 3.4.3. Figures 4.44 and 4.45 illustrate the calculated interfacial energy for a planar sharp interface as well as the corrections regarding the interfacial curvature. The solid lines represent the values for the interfacial energy of AlN, the dashed lines that of VN. The filled circles stand for the calculated interfacial energy of a planar sharp interface, whereas the squares indicate the corrections due to the spherical shape of the nucleus.

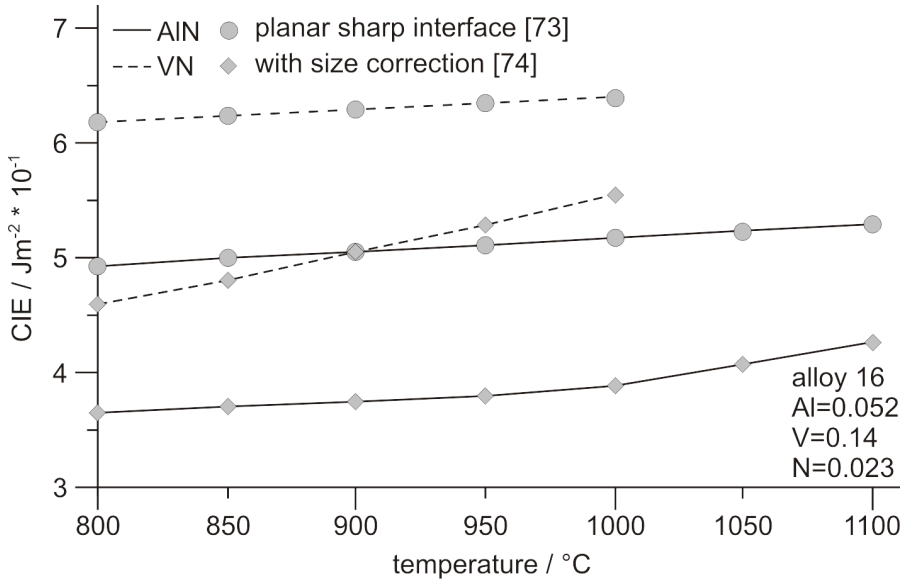

Figure 4.44: Calculated interfacial energy (CIE) for a planar sharp interface [73] and including corrections for interfacial curvature [74] for alloy 16.

In addition to the precipitate size correction, corrections accounting for entropic contributions from finite interface thickness must be considered in the calculation of the interfacial energy for the precipitate/matrix interface between VN and austenite. Particularly, close to the solution temperature, these contributions can become prominent. Therefore, an additional multiplicative temperature-dependent correction factor β is introduced, as described in section 3.4.3 and shown in figure 4.46. No corrections are made

for the precipitation of AlN at the austenite grain boundaries, except the corrections concerning the interfacial curvature [74].

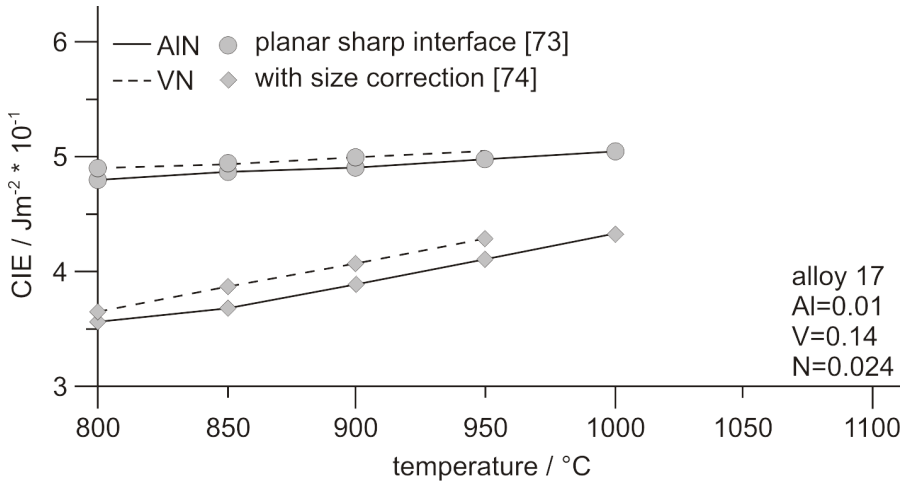

Figure 4.45: Calculated interfacial energy (CIE) for a planar sharp interface [73] and including corrections for interfacial curvature [74] for alloy 17.

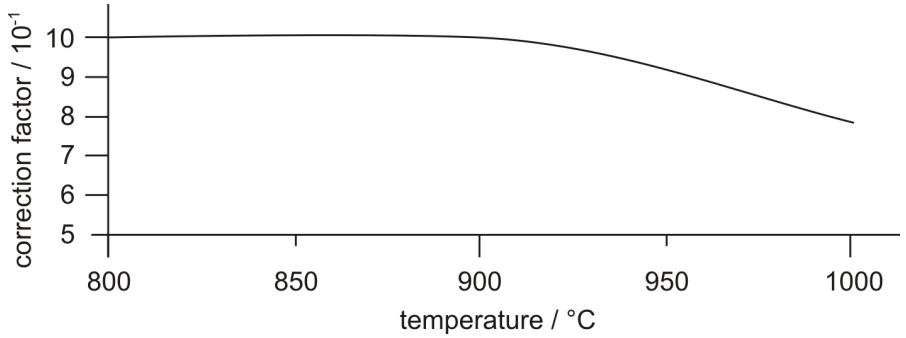

Figure 4.46: Temperature-dependent correction factor β to the calculated sharp interface energy of VN, in addition to the size correction α for interfacial curvature (see also section 3.4.3).

4.8.3 Phase Fraction of AlN and VN Versus Time

The precipitation kinetics of AlN and VN is simulated for two different alloys at various different temperatures. While the importance of using the new GBDG model for the precipitation of AlN was demonstrated in sections 4.5 and 4.7, figure 4.47 shows now the

simultaneous precipitation of AlN and VN in alloy 16 using the two different approaches. Figure 4.47(a) presents the treatment with randomly distributed precipitates, whereas figure 4.47(b) shows the calculated results assuming predominant precipitation of AlN at austenite grain boundaries. The solid lines represent the phase fraction of AlN, whereas the dashed lines represent the phase fraction of VN.

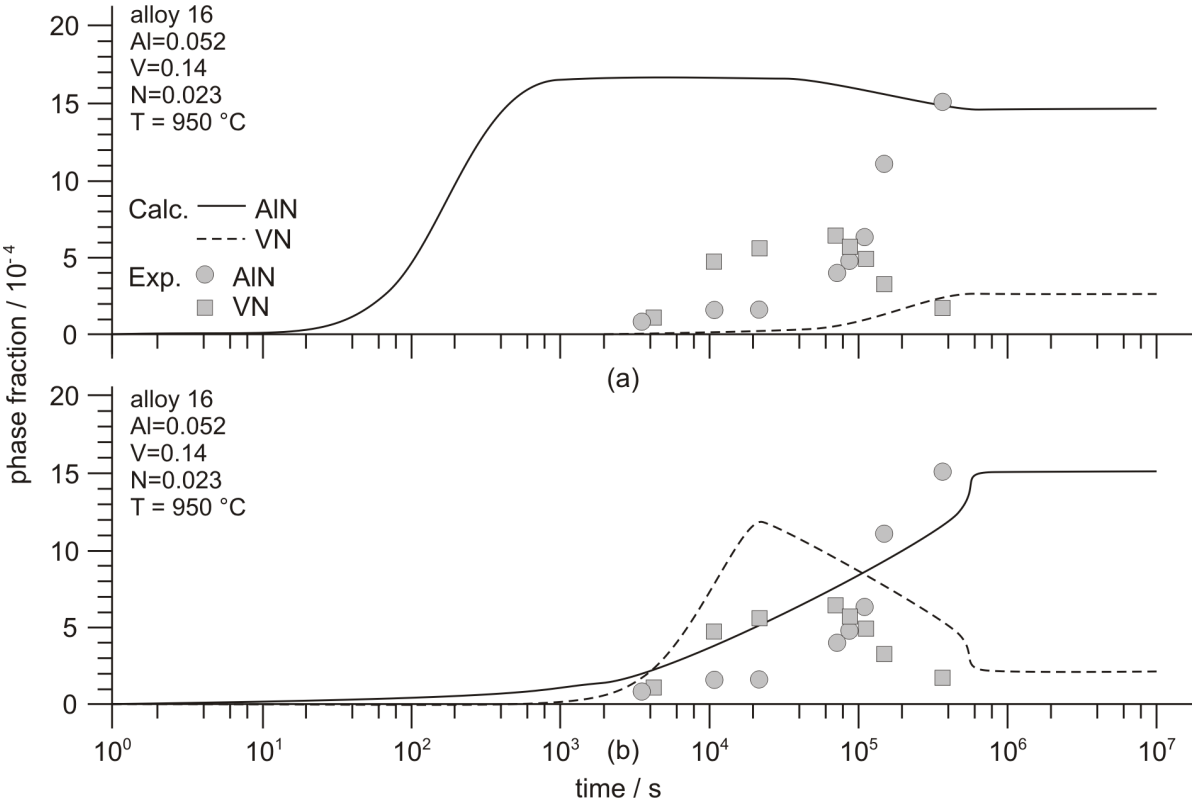

Figure 4.47: Comparison of the calculated phase fractions versus time and experimental data [88] for alloy 16 at 950 °C (a) assuming randomly distributed precipitates or (b) assuming AlN precipitation at grain boundaries.

Figures 4.48 and 4.49 show the calculated phase fraction versus time plots for both alloys and the comparison with experimental results from König et al. [88].

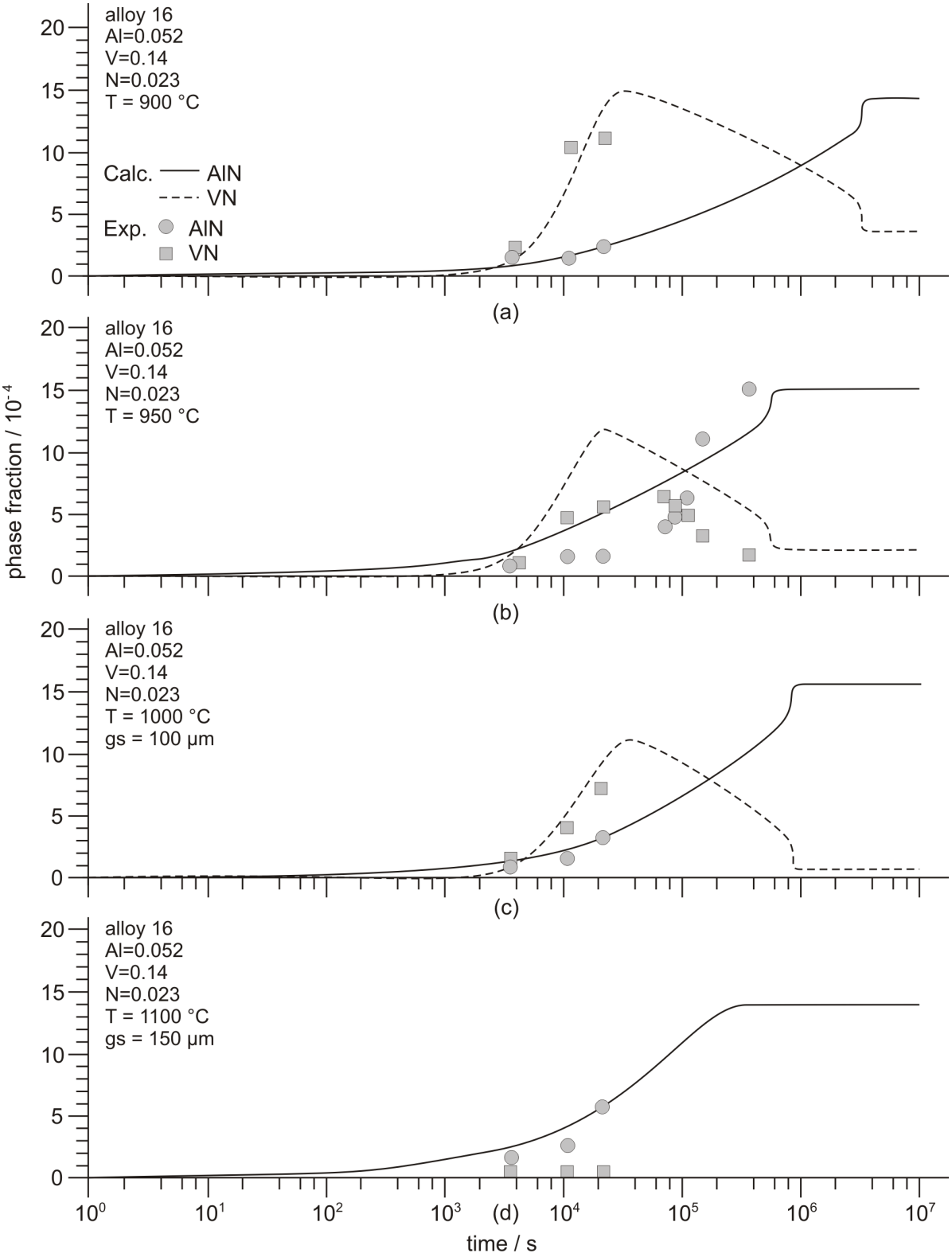

Figure 4.48: Calculated and experimental precipitation kinetics of AlN and VN in austenite for alloy 16 at the temperatures 900 °C, 950 °C, 1000 °C and 1100 °C.

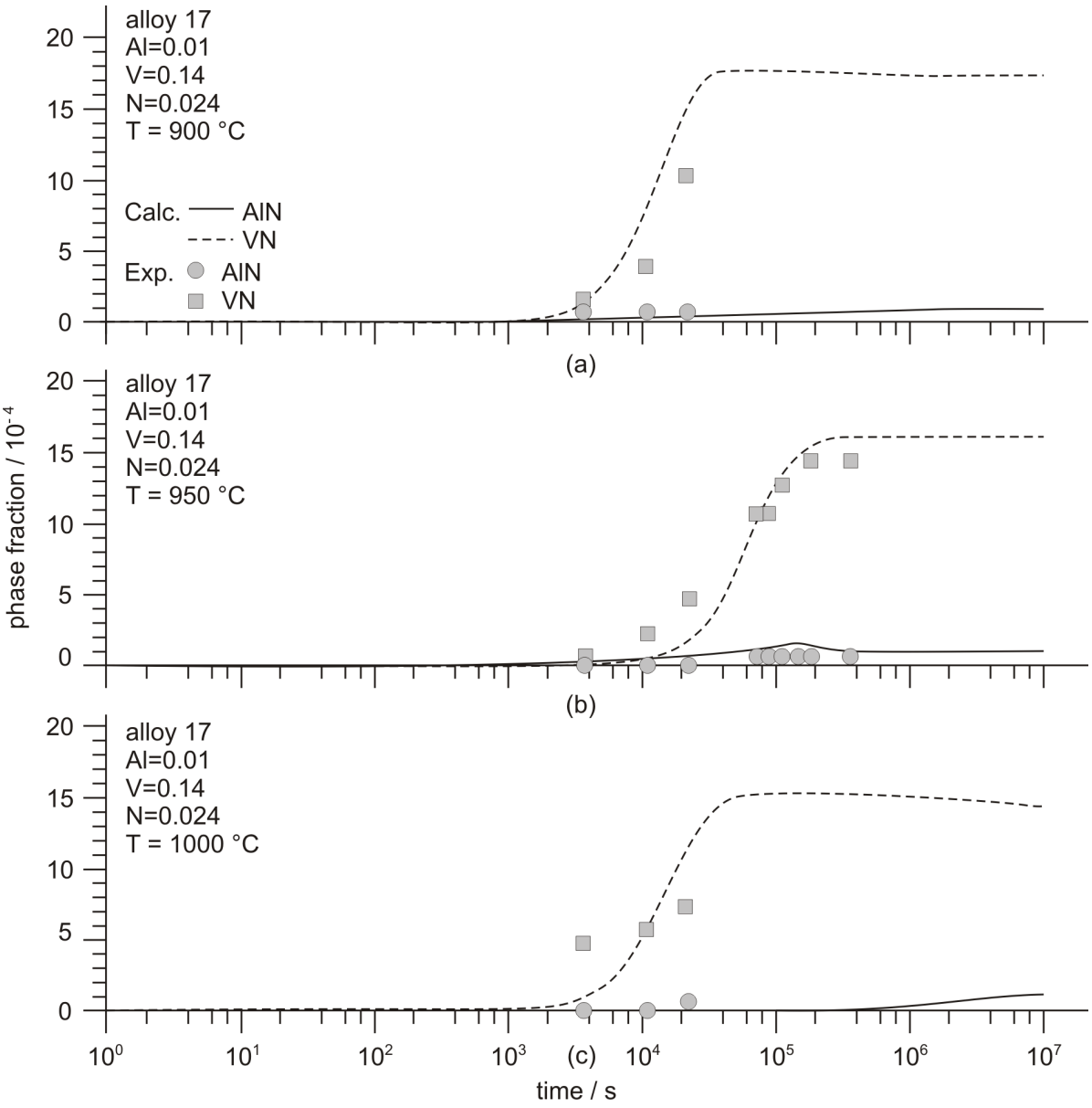

Figure 4.49: Calculated and experimental precipitation kinetics of AlN and VN in austenite for alloy 17 at the temperatures 900 °C, 950 °C and 1000 °C.

4.8.4 Time-Temperature-Precipitation Plots for AlN and VN in Steel

Figures 4.50 and 4.51 shows the time-temperature-precipitation (TTP) plots for AlN and VN precipitation in both investigated alloys. The solid lines represent the precipitation of AlN, whereas the dashed lines stand for VN.

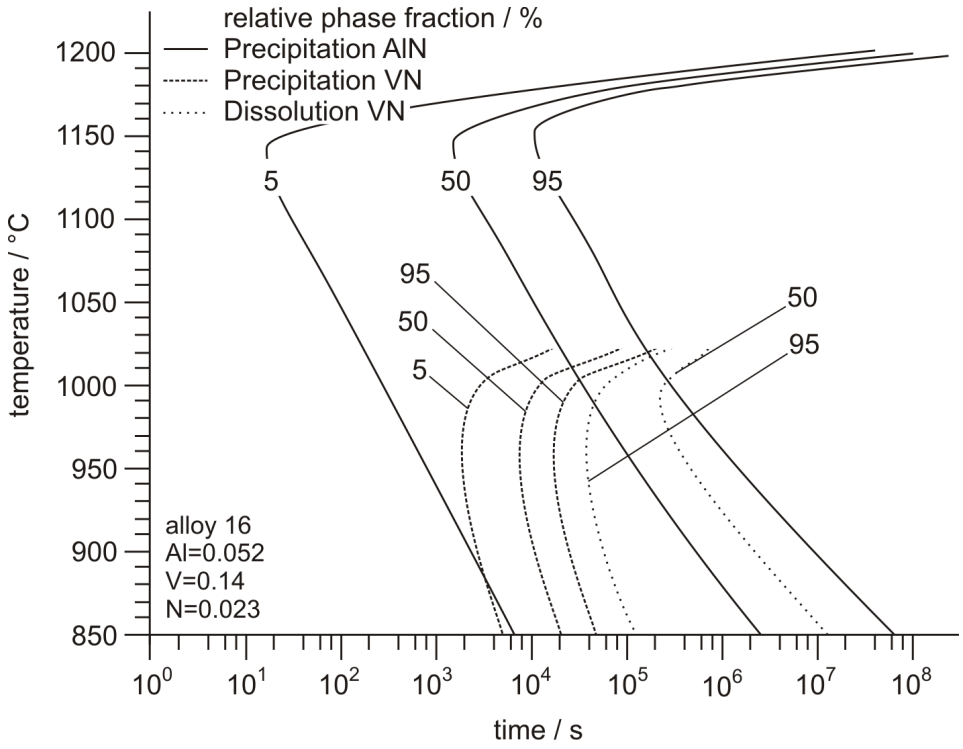

Figure 4.50: Calculated TTP diagram of AlN and VN for alloy 16.

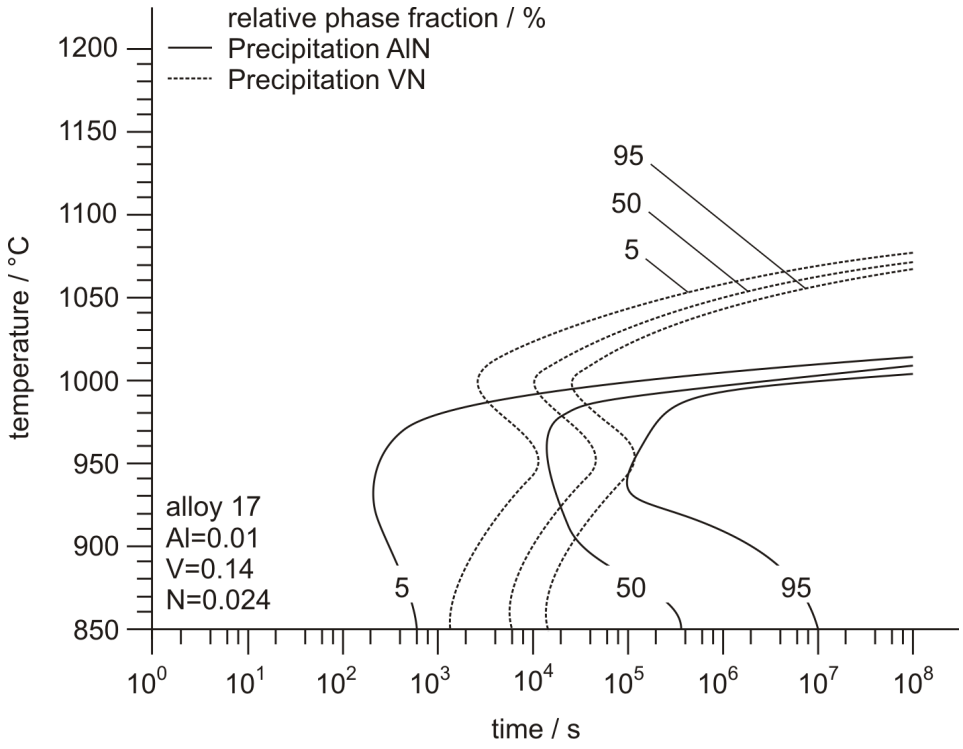

Figure 4.51: Calculated TTP diagram of AlN and VN for alloy 17.

Figure 4.51 additionally shows the predicted dissolution lines of VN, indicated by dotted lines. The lines are labelled with numbers corresponding to the relative phase fractions at each temperature.

4.8.5 Discussion

The present section emphasizes the importance of considering the predominant precipitation of AlN on austenite grain boundaries, not only for the calculation of the precipitation kinetics of AlN (see also sections 4.5 and 4.7), but also for the correct prediction of the precipitation kinetics of VN. Figure 4.47 show that the classical model with randomly distributed precipitates and spherical diffusion fields strongly overestimates the precipitation kinetics of AlN. In addition, the precipitation of VN is completely suppressed if grain boundary precipitation is not taken into account correctly, see figure 4.47(a). Taking into account AlN precipitation at austenite grain boundaries leads to a good agreement between calculation and experimental observation, see figures 4.48 and 4.49. Moreover, in alloy 16, due to the decelerated precipitation of AlN at the grain boundaries, pronounced precipitation of metastable VN inside the austenite grains is observed, dissolving again, however, in favour of the thermodynamically more stable AlN. Figures 4.50 and 4.51 show the predicted TTP-plots for AlN and VN precipitation in the investigated alloys. Below 950°C, the precipitation of AlN is shifted to longer times, which is indicated by the change of the slope of the TTP curves. Although, there are only small quantities of Al present in alloy 17, the TTP diagram clearly reproduces the deceleration of the VN precipitation kinetics below approximately 1000°C. Furthermore, the TTP plots for both alloys show that the distances between the curves, which represent 5, 50 and 95 % of the relative phase fraction, are larger in the case of AlN precipitation compared to VN. This is again an indication for the experimentally observed flatter slope of the phase fraction curves for AlN precipitation at grain boundaries, see also figure 4.48.

4.9 Precipitation Kinetics Considering Microsegregation During Solidification

During the production process of steel, e.g. continuous casting, solidification of steel occurs within a given temperature interval. After cooling below solidification temperature, first, solid crystals nucleate, which finally represent the cores of new dendrites. During further solidification, a composition gradient from the regions where the solidification started (centre of the dendrite) to the areas where the last liquid solidified (outer shell of the dendrite) develops [185]. Consequently, in as-cast material, the precipitation behavior of nitrides and carbides is expected to be totally different at different regions of the solidification microstructure. The precipitation kinetics is very sluggish in the regions corresponding to the dendrite core, while it is many orders of magnitude faster in the outer shell of the dendrite. Pudar et al. [186, 187] studied the segregation of alloying elements as well as the precipitation behavior in the dendrite core and in the residual liquid after final solidification. However, his precipitation kinetics calculations concentrated on the prediction of maximum precipitate sizes in the dendrite core and in between the dendrites. The authors did not take into account the phase fraction of precipitates in the region between the dendrite center and the region of final solidification separately. This first approach is extended in this section to be applicable for the prediction of phase fractions in segregated microalloyed steels, too.
The new approach, which is presented subsequently, deals with the prediction of phase fractions, particle sizes and number densities locally at every point of the promary solidification microstructure as well as the accumulated phase fractions, particle sizes and number densities globally in the whole microstructure.

4.9.1 Simulation Procedure

The numerical procedure of the calculation of the precipitation process during solidification is subdivided into two calculations [188]. First, the calculation of the segregation of alloying elements during solidification, and, second, the calculation of the precipi-

tation kinetics of the nitrides and carbides in the regions of different chemistry. The calculations are performed using the thermodynamic database 'mc_steel' [83] (version 1.20). The numerically computed results are compared to independent experimental data [189]. The chemical compositions of the investigated alloy is given in table 4.12.

Table 4.12: Chemical composition of the investigated alloy [189].

alloy	C	Si	Mn	Al	V	Ti	Nb	N
18	0.175	0.014	1.46	0.032	0.006	0.0151	0.013	0.004

4.9.1.1 Segregation of Alloying Elements During Solidification

For the calculation of the segregation of alloying elements during solidification, 'Scheil-Gulliver' simulations are performed [190, 191]. In the simulations, the phases LIQUID, BCC, FCC, AlN, NbN, NbC, TiN, TiC, VN and VC are considered. These calculations deliver the fraction and composition of all phases during solidification step by step from the liquidus temperature to the temperature where final solidification of the residual liquid phase occurs.

On the basis of these results (see section 4.9.2.2), the composition profile of the dendrites is divided into eight different zones, one core, six shells and 5% residual liquid, which represent the composition gradient from the dendrite center to the region of final solidification. Figure 4.52 shows a schematic image of such dendrites. The darker the zone, the more alloying elements are in solution and available for precipitation of nitrides and carbides. The content of alloying elements is drawn as a function of the phase fraction of the solid phase in figure 4.53 for the case of Ti. With ongoing solidification, the content of Ti increases in the solidifying shells as well as in the residual liquid phase. The chemical compositions of the different zones are weighted according to figure 4.53. Thus, the core and the first shell are weighted with 25%, the following four shells with 10% and the last shell and the residual liquid are weighted with 5%, respectively.

To determine the mean composition of each zone, the mean content of each alloying element is calculated and multiplied with the weighting coefficient. Summarizing these

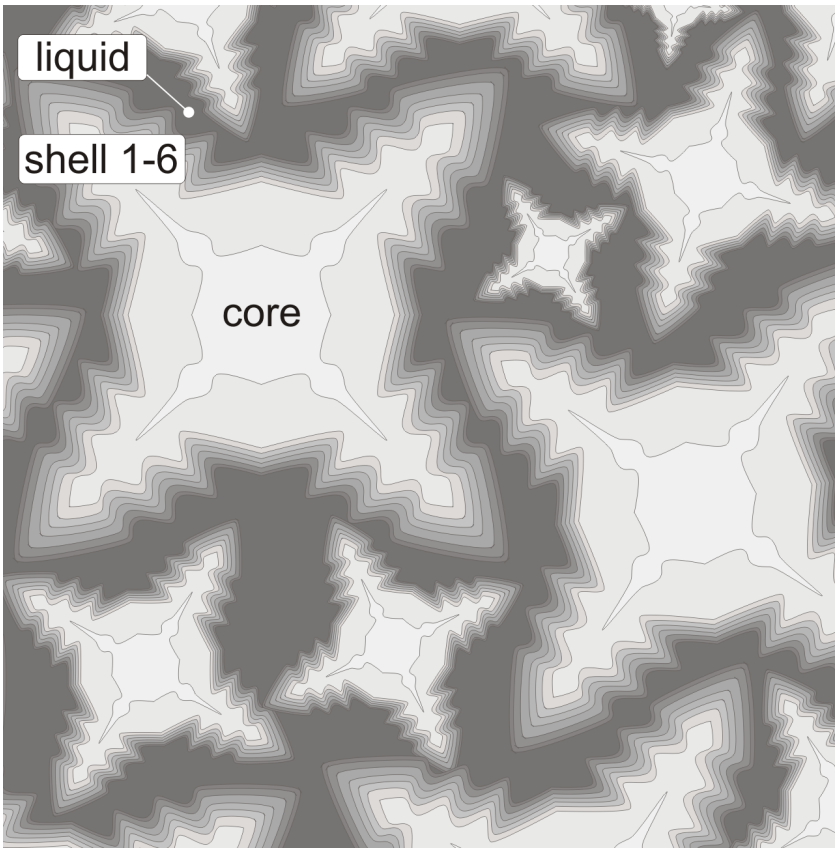

Figure 4.52: Dendrites with zones of different chemical compositions.

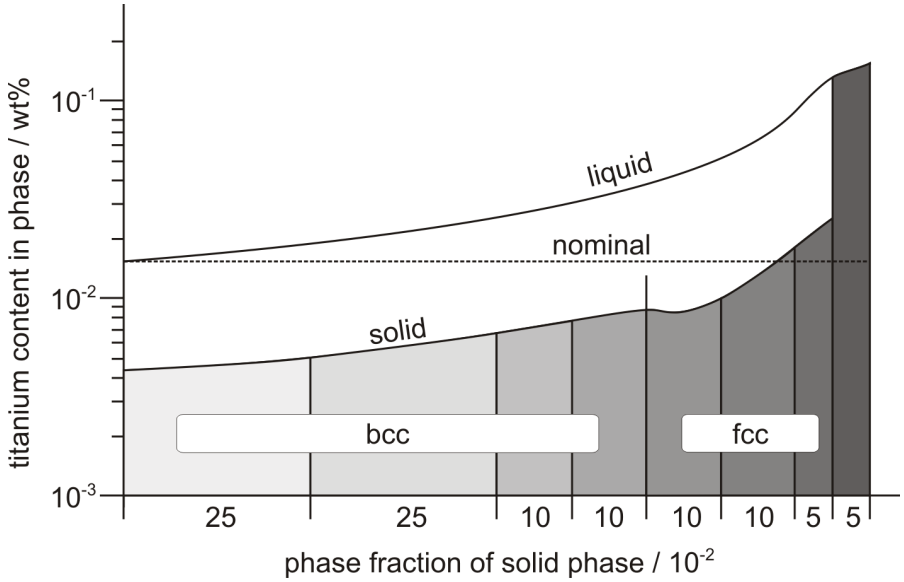

Figure 4.53: Ti content in different zones as function of the phase fraction of the solid phase.

weighted chemical compositions of all zones deliverers the nominal composition of the steel.

4.9.1.2 Precipitation Kinetics in Regions of Different Chemistry

AThe heat treatment used in the present simulations is shown in figure 4.54. After a linear cooling from 1300°C to 900°C the material is isothermally annealed for 4 h. Subsequently, a series of calculations with different chemical compositions, according to the results of the 'Scheil-Gulliver' simulations (see section 4.9.2.2) are performed. Thus, the precipitation kinetics for every zone of the dendrite is determined.

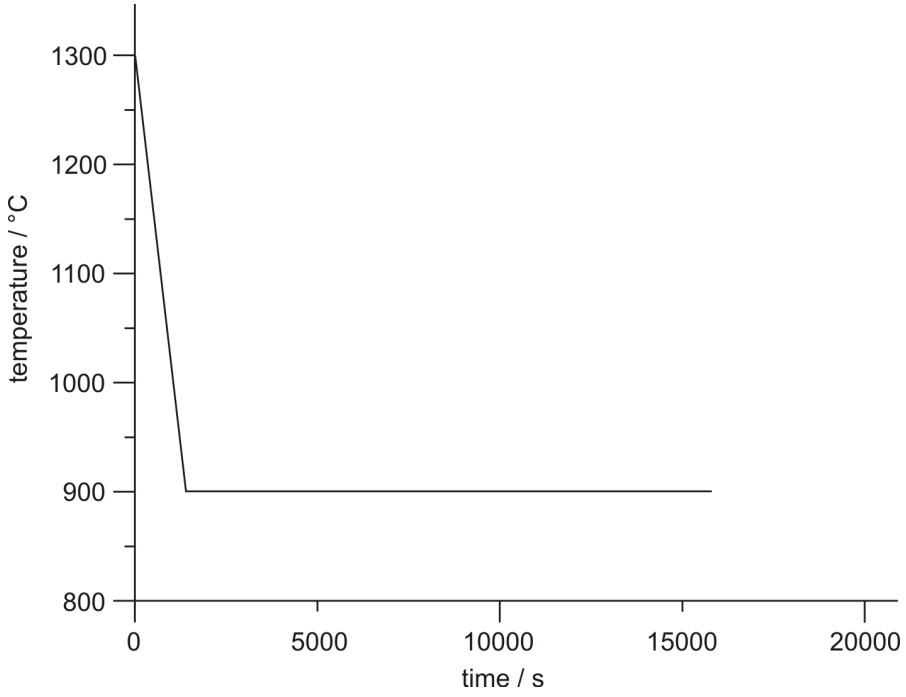

Figure 4.54: Heat treatment used for the precipitation kinetics simulations.

Finally, the individual phase fractions of all zones are summarised and compared to the experimental investigations. This is done after accumulating the amount of the carbides and nitrides of one microalloying element because the amount of Ti and Nb delivered in the experimental studies is also an accumulated quantity and gives no information whether the alloying element is bonded to a nitride or carbide. The comparison of the calculated volume fractions of TiN, TiC and NbC with the measured weight fractions

of Ti and Nb is done according to the procedure described in section 4.7.2.

4.9.2 Results

After some equilibrium considerations of alloy 18 the segregation of alloying elements is calculated. With the results of these prior segregation calculations, precipitation kinetics calculations are performed in different chemical regions of the dendrites.

4.9.2.1 Equilibrium Calculations

For a rough estimation about stable nitrides and carbides in alloy 18, an equilibrium calculation is performed using the nominal composition, given in table 4.12.

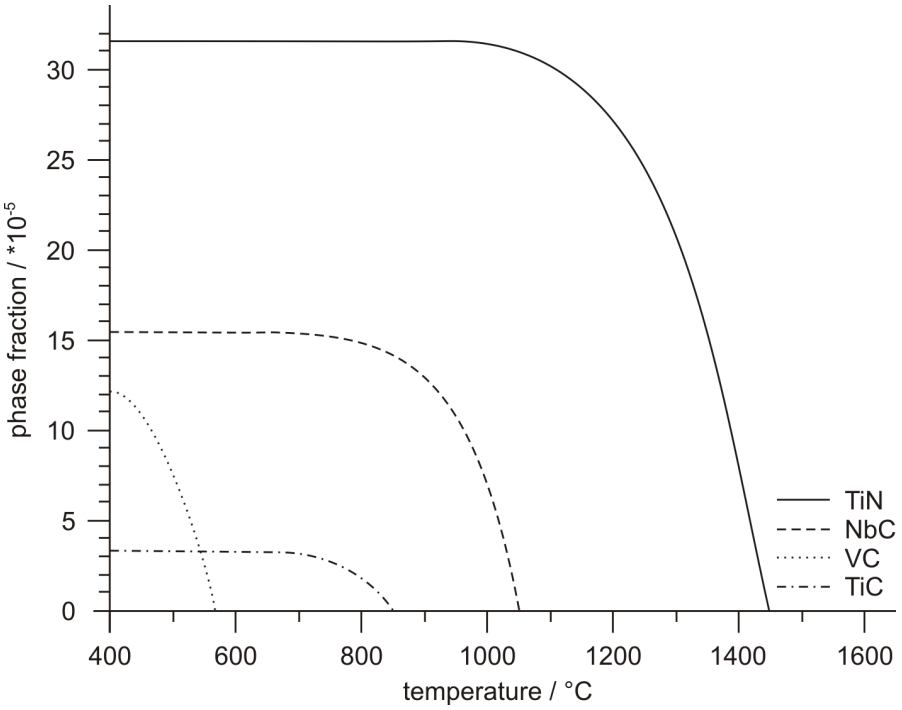

Figure 4.55: Equilibrium phase fractions versus temperatures of alloy 18.

Several nitrides (AlN, NbN, TiN, VN) and carbides (NbC, TiC, VC) are considered in the simulation. Figure 4.55 shows that, in equilibrium, the second phase precipitates TiN, NbC, TiC and VC are stable below solution temperatures of 1446°C, 1052°C, 850°C and 568°C, respectively. Thus, after isothermal annealing of alloy 18 for infinitely long time at a temperature of 900°C, only the precipitation of TiN and NbC should occur.

4.9.2.2 Segregation of Alloying Elements During Solidification

After casting, the samples are quenched and reheated to 1300°C, afterwards directly cooled from 1300°C to 900°C and isothermally annealed at this temperature for 4h [189].

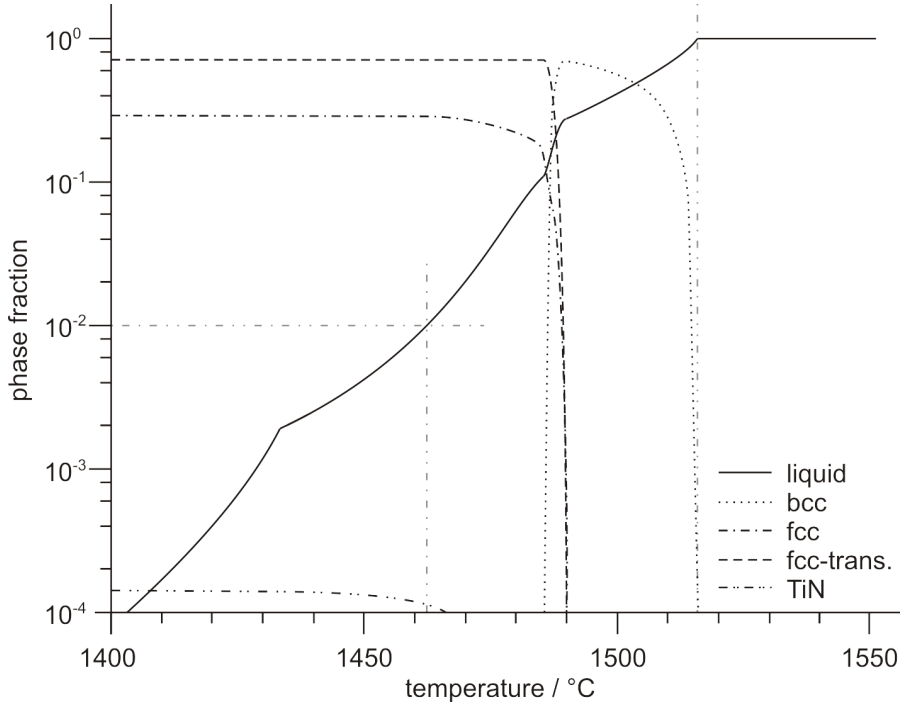

Figure 4.56: Scheil-Gulliver simulation of alloy 18.

Since we expect strong segregation during solidification and no time for diffusion to level out the composition gradients, the precipitation kinetic calculations for the as-cast material cannot be carried out with the nominal compositions of the steels. Instead, 'Scheil-Gulliver' simulations are performed (4.9.1.1) to estimate the segregation of the alloying elements during solidification. Figure 4.56 shows the result of the 'Scheil-Gulliver' calculation for alloy 18. The solidification range is between 1517°C and 1463°C, if solidification of the residual liquid is assumed to occur at 1%. If this is the case, some coarse primary TiN precipitates are likely to be present in this steel.

Table 4.13 shows the chemical composition of each zone in the dendrite obtained from the 'Scheil-Gulliver' simulation. The mean values of alloying elements at different residual liquid states are calculated in the different matrix phases.

Table 4.13: Calculated amount of alloying elements (wt-ppm) in the different zones (dendrite core, shells, residual liquid) of the primary solidification microstructure.

shell	residual	measured	amount of alloying elements in shell / wt-ppm							
no.	liquid	in phase	Mn	C	Nb	Ti	Si	Al	V	N
7	0.05	liquid	31400	5321	1592	1262	317	336	174	67
6	0.076	fcc	20940	1512	160	211	205	291	82	39
5	0.177	fcc	17246	1442	80	111	162	264	59	43
4	0.256	fcc	15776	1404	59	83	146	252	51	46
3	0.354	bcc	13810	621	51	79	133	325	54	21
2	0.457	bcc	12938	525	42	68	123	331	52	19
1	0.612	bcc	12020	426	34	57	114	336	49	15
0	0.867	bcc	11000	326	26	46	103	342	46	12

Table 4.14: Corrected and weighted amount of alloying elements (wt-ppm) in the different zones (dendrite core, shells, residual liquid) of the primary solidification microstructure.

shell	residual	weight	amount of alloying elements in shell / wt-ppm							
no.	liquid		Mn	C	Nb	Ti	Si	Al	V	N
7	0.05	0.05	1598	502	82	71	16	17	9	5
6	0.076	0.05	1066	143	8	12	11	15	4	3
5	0.177	0.1	1756	272	8	13	17	27	6	7
4	0.256	0.1	1606	265	6	9	15	25	5	7
3	0.354	0.1	1406	117	5	9	14	33	6	3
2	0.457	0.1	1317	99	4	8	13	33	5	3
1	0.612	0.25	3059	201	9	16	29	85	13	6
0	0.867	0.25	2800	153	7	13	27	86	12	5
sum			14607	1751	130	150	140	321	60	40
correction factor			1.018	1.885	1.035	1.132	1.03	1.008	1.04	1.62

Using mean values of the alloying elements leads to some discrepancies between the sum of alloying additions of all zones and the nominal composition. Therefore, correction factors are introduced, which are multiplied with the amount of each element in every area, see table 4.14. Generally, these factors are very small, except for the interstitial elements C and N. These achieve equilibrium (liquid and solid phases) due to rapid back-diffusion from the liquid phase into the solid phase [190]. In these cases, the correction factors are approximately in the order between 1,5 and 2. However, using these factors and weighting the amount of the elements with the width of the zones (dendrite core, shells and residual liquid), ensures mass conservation with respect to the nominal composition (see table 4.14).

4.9.2.3 Precipitation Kinetics in Regions of Different Chemistry

Several precipitation kinetics calculations are performed using the chemical composition of each zone presented in section 4.9.2.2 as input parameter. Figure 4.57 displays the summarized results of the calculations. The dashed lines indicate the individual phase fractions of TiN in the different zones (dendrite core, shells, residual liquid) of the dendrite. Whereas the precipitation of TiN is predicted in each zone of the dendrites, precipitation of TiC and NbC only occurs in the interdendritic regions. Finally, the sum of the individual phase fractions of TiN in each zone, as well as the sum of the phase fractions of TiN and TiC is depicted. The accumulation of the phase fractions of TiN and TiC is necessary, due to the fact that the amount of Ti and Nb provided from the experimental studies is given in total quantities and give no information whether the alloying element is bonded to a nitride or carbide. These total quantities are indicated by solid circles and squares for Ti and Nb, respectively.

4.9.3 Discussion

The precipitation kinetics calculations of alloy 18 performed in this study show that the proposed method leads to fair agreement between calculations and experimental observations. This could not be achieved with any calculations using the nominal com-

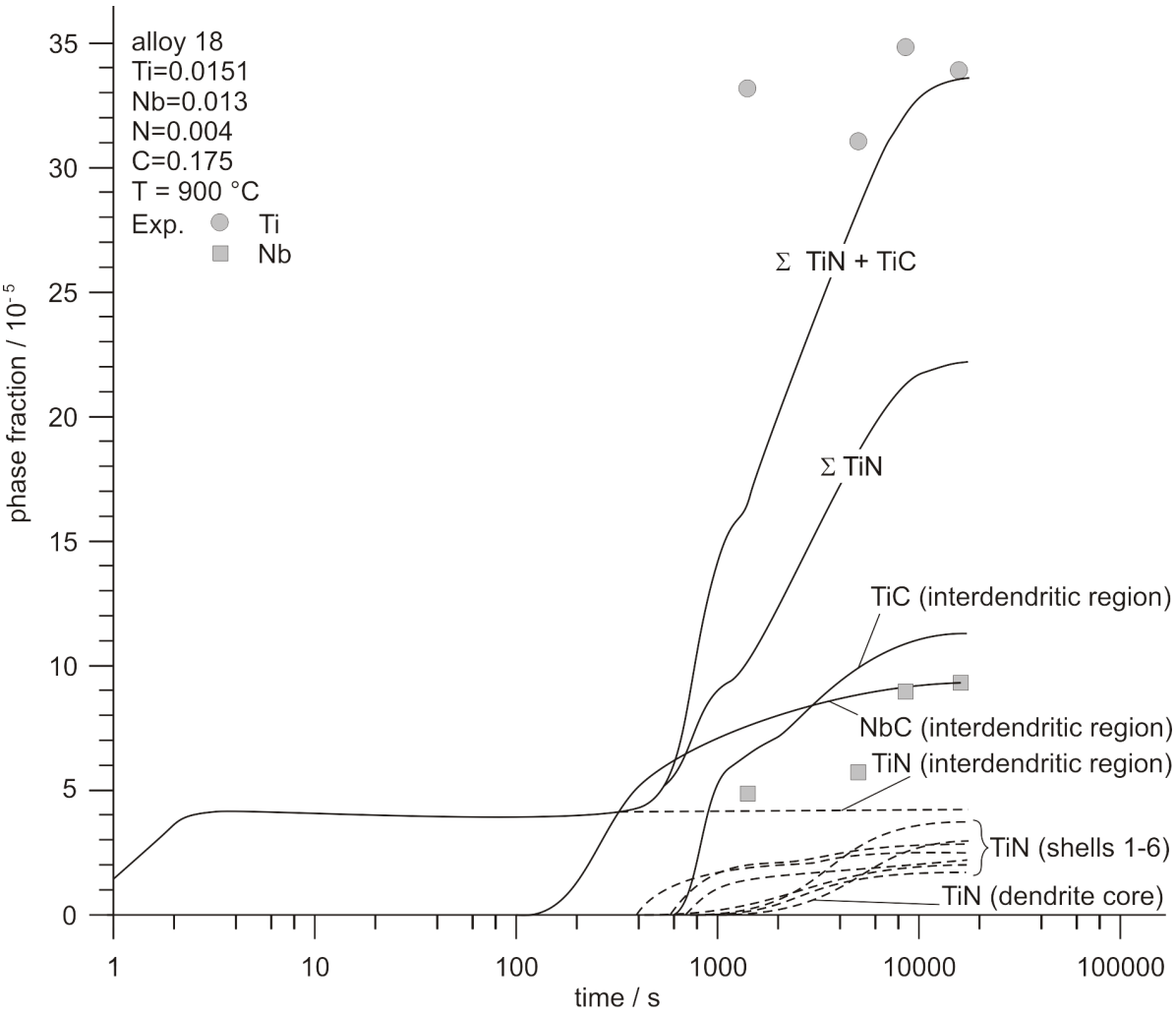

Figure 4.57: Calculated phase fractions of nitrides and carbides in alloy 18 at a temperature of 900°C.

position of alloy 18. Moreover, figure 4.55 shows that no TiC is stable in equilibrium when using the nominal composition. However, the measured amounts of Ti can only be reached, when considering both, TiN and TiC precipitated in different zones of the segregated dendrites, see figure 4.57. While the precipitation of TiN is observed in all regions of the dendrite (core, shells and residual liquid), precipitation of TiC and NbC is only observed in the interdendritic region.

It should be emphasized that the experimental results for Ti are compared to the sum of the results of the numerical calculations of two Ti containing phases. Thus, to match the experimental results, it is necessary that all the critical parameters, such as thermody-

namics, interfacial energies or diffusion constants, of the two phases must be reasonably accurate. Furthermore, it should be noted, that no adaptations of any of these parameters have been made. In this sense, the calculations can be considered as predictions and must be evaluated as good.

The calculations based on the proposed method also provide some information about the spatial arrangement of the particles. Particle sizes, number densities and phase fractions can be determined as a function of the distance from the core of a dendrite.

Chapter 5

Summary

The present thesis deals with the numerical simulation of the precipitation kinetics of various nitrides and carbides in (HSLA) microalloyed steel. The solubility data of all microalloy carbides and nitrides are reviewed and compared to different thermodynamic assessments. Reasonable descriptions of the thermodynamic properties of the nitrides and carbides are incorporated in the thermodynamic database 'mc_steel' in the form of simple phase descriptions.

Employing the software package MatCalc and the corresponding thermodynamic and diffusion databases, numerical precipitation kinetics simulations are performed using two different models. On the one hand, a new model for grain boundary precipitation is employed, which takes into account fast short-circuit diffusion along grain boundaries as well as slower bulk diffusion inside the grain. On the other hand, the classical treatment for randomly distributed precipitates with spherical diffusion fields is used. In the case of randomly distributed precipitates located at dislocations, volumetric misfit strain energies between precipitate/matrix interfaces are fully accounted for in the present calculations.

Detailed parameter studies are presented, describing the characteristics of both models. It is shown that the grain boundary model reproduces the well-known effect of grain size on the grain boundary precipitation kinetics, where large grain sizes significantly retard the overall precipitation process due to large inner grain diffusion distances. Moreover, depending on the ratio of grain boundary diffusion to bulk diffusion, simultaneous

growth and coarsening of precipitates can occur. In the case of high grain boundary diffusivity, the initial stage of precipitation is accelerated by fast nucleation and growth kinetics. Simultaneously, the phase fraction increase is significantly slower compared to the random distribution case. In the case of the classical treatment of randomly distributed precipitates, the parameter studies demonstrate the high sensitivity of the calculations on the input quantities volumetric misfit and Young's modulus.

The precipitation kinetics of AlN and VN is analyzed by the numerical simulation of isothermal annealing of microalloyed steels covering various chemical compositions. The simulations clearly demonstrate that AlN formation occurs by simultaneous precipitation at grain boundaries and at dislocations. Depending on chemical composition, grain size and annealing temperature, predominant precipitation at grain boundaries and/or at dislocations is predicted. With the application of the two models representing these two mechanisms, an excellent agreement between prediction and experimental data is achieved. Moreover, it is demonstrated, that for certain ratios between Al and V, after a temporary precipitation of VN, these precipitates dissolve again, in favour of the thermodynamically more stable AlN. It is also shown that, for a consistent description of these precipitation reactions, it is necessary to account for several physical mechanisms that are often neglected in this type of simulations, among them the precipitate/matrix volumetric misfit, the temperature dependent Young's modulus, as well as the ratio between bulk and grain boundary diffusion.

Finally, the precipitation kinetics of TiN and NbC is simulated, taking into account the microsegregation of these elements during solidification. A new approach is presented, which allows calculating the precipitation parameters locally at every point of the dendrite. The chemical concentration profile from the dendrite core to the segregated regions is simulated with 'Scheil-Gulliver' calculations of the microsegregation process during solidification. Using these chemical compositions, the precipitation parameters are calculated in each individual zone. Accumulation of phase fractions, particle sizes and number densities leads to the overall precipitation products in the whole material. The calculations and comparison with experimental data clearly demonstrate that these segregation effects must be taken into account.

Bibliography

[1] T. Gladman. *The Physical Metallurgy of Microalloyed Steels*. The Institute of Materials, London, United Kingdom, 1997.

[2] W. B. Morrison. Overview of Microalloying in Steel. In *The Use of Vadium in Steel, Procedings of the VANITEC Symposium*, pages 25–35, Guilin, China, November 2000.

[3] G. Krauss. Vanadium Microalloyed Forging Steels. In *The Use of Vanadium in Steel, Proceedings of the VANITEC Symposium*, Beijing, China, October 2001.

[4] M. Militzer, E.B. Hawbolt, and T.R. Meadowcroft. Microstructural Model for Hot Strip Rolling of High-Strength Low-Alloy Steels. *Metallurgical and Materials Transactions A*, 31A:1247–1259, 2000.

[5] S. Gündüz and R.C. Cochrane. Influence of Cooling Rate and Tempering on Precipitation and Hardness of Vanadium Microalloyed Steel. *Materials and Design*, 26:486–492, 2005.

[6] J. Svoboda, F.D. Fischer, P. Fratzl and E. Kozeschnik. Modelling of Kinetics in Multi-Component Multi-Phase Systems with Spherical Precipitates I - Theory. *Materials Science and Engineering*, A385:166–174, 2004.

[7] E. Kozeschnik, J. Svoboda, P. Fratzl and F.D. Fischer. Modelling of Kinetics in Multi-Component Multi-Phase Systems with Spherical Precipitates II - Numerical Solution and Application. *Materials Science and Engineering*, A385:157–165, 2004.

[8] E. Kozeschnik, J. Svoboda and F.D. Fischer. Modified Evolution Equations for the Precipitation Kinetics of Complex Phases in Multi-Component Systems. *CALPHAD*, 28:379–382, 2004.

[9] T. Gladman, D. Dulieu and I. D. McIvor. Structure-Property Relationships in High-Strength Microalloyed Steels. In *Proceedings of an International Symposium on High-Strength, Low-Alloy Steels*, Washington DC, USA, October 1975.

[10] E. O. Hall. The Deformation and Ageing of Mild Steel .3. Discussion and Results. *Proceedings of the Physical Society of London Section B*, 64(381):747–753, 1951.

[11] N. J. Petch. The Cleavage Strength of Polycrystals. *Journal of the Iron and Steels Institute*, 174(1):25–28, 1953.

[12] W. C. Leslie. *The Physical Metallurgy of Steels*. McGraw-Hill International Book Company, 1982.

[13] C. Zener, quoted by C. S. Smith. Grains, Phase, and Interphases - An Interpretation of Microstructure. *Transactions of the American Institute of Mining and Metallurgical Engineers*, 175:15–51, 1948.

[14] T. Gladman. On the Theory of the Effect of Precipitate Particles on Grain Growth in Metals. *Proceedings of the Royal Society of London Series A - Mathematical and Physical Sciences*, 294(1438):298–309, 1966.

[15] P. Hellman and M. Hillert. On the Effect of Second-Phase Particles on Grain Growth. *Scandinavian Journal of Metallurgy*, 4(5):211–219, 1975.

[16] R. Elst, J. van Humbeeck and L. Delaey. Evaluation of Grain Growth Criteria in Particle-Containing Materials. *Acta Metallurgica*, 36(7):1723–1729, 1988.

[17] P. R. Rios. Overview no. 62. A Theory for Grain Boundary Pinning by Particles. *Acta Metallurgica*, 35(12):2805–2814, 1987.

[18] N. Gao and T. N. Baker. Austenite Grain Growth Behaviour of Microalloyed Al-V-N and Al-V-Ti-N Steels. *ISIJ International*, 38(7):744–751, 1998.

[19] E. Orowan. Internal Stresses - Discussion. In *Symposium on Internal Stresses in Metals and Alloys*, pages 451–453, London - United Kingdom, 1948. The Institue of Metals.

[20] E. Hornbogen and H. Warlimont. *Metallkunde - Aufbau und Eigenschaften von Metallen und Legierungen*. Springer-Verlag, Berlin - Germany, 1991.

[21] M. F. Ashby. The Theory of the Critical Shear Stress and Work Hardening of Dispersion-Hardened Crystals. In *Metallurgical Society Conference*, volume 47, pages 143–205, New York - USA, 1968. Gordon and Breach.

[22] B. Mintz, J. R. Wilcox and D. N. Crowther. Hot Ductility of Directly Cast C-Mn-Nb-Al Steel. *Materials Science and Technology*, 2:589–594, 1986.

[23] R. Abushosha, S. Ayyad and B. Mintz. Influence of Cooling Rate on Hot Ductility of C-Mn-Al and C-Mn-Nb-Al steels. *Materials Science and Technology*, 14:346–351, 1998.

[24] L. A. Erasmus. Effect of Aluminium Additions on Forgeability, Austenite Grain Coarsening Temperature, and Impact Properties of Steel. *Journal of the Iron and Steel Institute*, 202:32–41, 1964.

[25] V. Massardier, V. Guétaz, J. Merlin and M. Solar. Study of the Role Played by Nitrogen on the Deep Drawing Properties of Aluminium Killed Steel Sheets Obtained After a Continuous Annealing. *Materials Science Forum*, 426-432:1267–1272, 2003.

[26] F. G. Wilson and T. Gladman. Aluminium Nitride in Steel. *International Materials Reviews*, 33(5):221–286, 1988.

[27] E. T. Turkdogan. Causes and Effects of Nitride and Carbonitride Precipitation During Continuous Casting. *Iron and Steelmaker*, 16(5):61–75, 1989.

[28] B. Mintz, S. Yue and J. J. Jonas. Hot Ductility of Steels and its Relationship to the Problem of Transverse Cracking During Continuous-Casting. *Internatinal Materials Reviews*, 36(5):187–217, 1991.

[29] K. E. Höner and S. Baliktay. Aluminiumnitridbildung im Stahlguß und deren Einfluß auf die Anfälligkeit für Primärkorngrenzenbruch. *Giesserei-Forschung*, 30(2):53–64, 1978.

[30] F. K. Naumann and E. Hengle. Muscheliger Bruch bei Stahl, seine Ursachen und Bildungsbedingungen. *Stahl und Eisen*, 82(10):612–621, 1962.

[31] K. Roesch and K. Zimmermann. Stahlguss. In *Band 17 aus der Reihe Stahleisen-Bücher*, Düsseldorf - Germany, 1966. Verlageisen Stahl mbH.

[32] K. Schwerdtfeger. *Rißanfälligkeit von Stählen beim Stranggießen und Warmumformen*. Verlag Stahleisen mbH, Düsseldorf - Germany, 1994.

[33] D. E. Dutcher. Understanding 'Rock Candy' Fracture in Steel Castings. *Modern Casting*, 89(2):46–49, 1999.

[34] P. Heritier, A. Fourdeux and A. Kobylanski. The Influence of Aluminium Nitride on the Hot Ductility of Ultra High Purity Steels. *Scripta Metallurgica*, 15:753–755, 1981.

[35] T. Gladman and F. B. Pickering. Grain-Coarsening of Austenite. *Journal of the Iron and Steel Institute*, 205(6):653–664, 1967.

[36] K. J. Irvine, F. B. Pickering and T. Gladman. Grain-Refined C-Mn Steels. *Journal of the Iron and Steel Institute*, 205(2):161–182, 1967.

[37] T. Gladman. Aluminium for Grain Size Control. *Heat Treatment of Metals*, 21(1):11–14, 1994.

[38] M. P. Sidey. Effects of Aluminium Nitride on the Properties of Steel. *Iron and Steel*, pages 168–171, 1967.

[39] E. L. Brown and A. J. DeArdo. Aluminium Nitride Precipitation in C-Mn-Si and Microalloyed Steels. In A. J. DeArdo, G. A. Ratz and P. J. Wray, editor, *Thermomechanical Processing of microalloyed Austenite*, pages 319–341, Warrendale, Pennsylvania, USA, 1982. The Metallurical Society of AIME.

[40] J. R. Wilcox, R. W. K. Honeycombe. Effect of Precipitation on Hot Ductility of Niobium and Aluminium Micralloyed Steels. *Materials Science and Technology*, 3:849–854, 1987.

[41] L. M. Cheng, E. B. Hawbolt and T. R. Meadowcroft. Dissolution and Coarsening of Aluminum Nitride Precipitates in Low Carbon Steel - Distribution, Size and Morphology. *Canadian Metallurgical Quaterly*, 39(1):73–86, 2000.

[42] J. F. Chávez-Alcalá, A. Rodríguez-Reyes, E. G. Navarrete-Ramos, H. J. Dorantes-Rosales, M. L. Saucedo-Munoz and V. M. López-Hirata. Microstructural Characterisation of Precipitation in an Isothermally Aged Nb-Containing Microalloyed Steel. *ISIJ International*, 41(12):1532–1534, 2001.

[43] S. Hanai, N. Takemoto and Y. Mizuyama. Precipitates of Cubic Structure Detected in Low-Carbon Alluminium-Killed Steels. *Transactions ISIJ*, 11(27):24–31, 1971.

[44] M. Militzer, A. Giumelli, E. B. Hawbolt and T. R. Meadowcroft. Austenite Grain Growth Kinetics in Al-Killed Plain Carbon Steels. *Metallurgical and Materials Transactions A*, 27:3399–3409, 1996.

[45] V. Massardier, V. Guétaz, J. Merlin and M. Solar. Kinetic and Mircostructural Study of Aluminium Nitride Precipitation in Low Carbon Aluminium-Killed Steel. *Materials Science and Engineering A*, 355:299–310, 2003.

[46] R. Ogawa, T. Fukutsuka and Y. Yagi. Precipitation Behaviour of AlN in Cold-Worked High Purity Fe-Al-N Alloy. *Transactions ISIJ*, 12:291–297, 1972.

[47] M. H. Biglari, C. M. Brakman, E. J. Mittemeijer and S. Van Der Zwaag. The Kinetics of the Internal Nitriding of Fe-2 At. Pct Al Alloy. *Metallurgical and Materials Transactions A*, 26:765–776, 1995.

[48] M. Sennour and C. Esnouf. Contribution of Advanced Microscopy Techniques to Nano-Precipitates Characterization: Case of AlN Precipitation in Low-Carbon Steel. *Acta Materialia*, 51:943–957, 2000.

[49] R. Lagneborg, T. Siwecki, S. Zajac and B. Hutchinson. The Role of Vanadium in Microalloyed Steels. *Scandanavian Journal of Metallurgy*, 28(5):186–238, 1999.

[50] P. S. Mitchell. The Use of Vanadium. In *The Use of Vadium in Steel, Procedings of the VANITEC Symposium*, pages 1–12, Beijing, China, October 2001.

[51] Y. Li, J. A. Wilson, A. J. Craven, P. S. Mitchel, D. N. Crowther and T. N. Baker. Dispersion Strengthening in Vanadium Microalloyed Steels Processed by Simulated Thin Slab Casting and Direct Charging Part 1 - Processing Parameters, Mechanical Properties and Microstructure. *Materials Science and Technology*, 23(5):519–527, 2007.

[52] C. Scott, F. Perrard and P. Barges. Microalloying with Vanadium for Improved Cold Rolled TRIP Steels. In *International Seminar on Application Technologies of Vanadium in Flat - Rolled Steels, Proceedings of the VANITEC Symposium*, pages 13–25, Suzhou, China, 2005.

[53] H. K. D. H. Bhadeshia. Considerations of Solute-Drag in Relation to Transformations in Steels. *Journal of Material Science*, 18:1473–1481, 1983.

[54] R. J. Glodowski. A Review of Vanadium Microalloying in Hot Rolled Steel Sheet Products. In *The Use of Vadium in Steel, Procedings of the VANITEC Symposium*, pages 43–51, Beijing, China, October 2005.

[55] K. Hulka und Ch. Klinkenberg. Nioblegierte Stähle - Stand und Entwicklungstendenzen. *Stahl und Eisen*, 125(7):19–23, 2005.

[56] K. Hulka. The Role of Niobium in Multi-Phase Steel. Technical report, Niobium Products Company GmbH, Düsseldorf, Germany, see Website: *http* : *//www.cbmm.com.br/portug/sources/techlib/report/novos/pdfs/the_role*2*.pdf*.

[57] Ch. Klinkenberg, K. Hulka and W. Bleck. Niobium Carbide Precipitation in Microalloyed Steel. *Steel Research International*, 75(11):744–752, 2004.

[58] M. Béres, T. E. Weirich, K. Hulka and J. Mayer. TEM Investigations of Fine Niobium Precipitates in HSLA Steel. *Steel Research International*, 75(11):753–758, 2004.

[59] J. Moon, S. Kim, J. Jang, J. Lee and C. Lee. Orowan Strenghtening Effect on the Nanoindentation Hardness of the Ferrite Matrix in Microalloyed Steels. *Material Science and Engineering A*, 487:552–557, 2008.

[60] D. Acevedo, M. Perez, T. Epicier, E. Kozeschnik, F. Perrard and T. Sourmail. Kinetics of Precipitation and Dissolution in Model FeCV and FeCVNb Alloy, and Microlloyed Ultra High Strength Spring Steel. In *Proc. of Conference on New Developments on Metallurgy and Applications of High Strength Steels*, volume 1-2, pages 987–999, Buenos Aires, Argentina, May 2008.

[61] S. Shanmugan, M. Tanniru, R. D. K. Misra, D. Panda and S. Jansto. Precipitation in V Bearing Microalloyed Steel Containig low concentarations of Ti and Nb. *Materials Science and Technology*, 21(8):883–892, 2005.

[62] T. Shiraiwa, N. Fujino and J. Murayama. Electron Probe Microanalysis of Titanium and Zirconium Carbonitride Inclusions in Steel. *Transactions of the Iron and Steel Institute Japan*, 10:406–412, 1970.

[63] H. Kejian and T. N. Baker. The Effects of Small Titanium Additions on the Mechanical Properties and the Microstructures of Controlled rolled Niobium-Bearing HSLA Plate Steels. *Materials Science and Engineering A*, 169:53–65, 1993.

[64] M. Bai, D. Liu, Y. Lou, X. Mao, L. Li and X. Huo. Effects of Ti Addition on Low Carbon Hot Strips Produced by CSP Process. *Journal of University of Science and Technology Beijing*, 13(3):230–234, 2006.

[65] G. R. Speich, L. J. Cuddy, C. R. Gordon and A. J. DeArdo. Formation of Ferrite From Control-Rolled Austenite. In A. R. Marderm and J. I. Goldstein, editor, *Phase Transformations in Ferrous Alloys*, pages 341–389, Warrendale, Pennsylvania, USA, 1984. The Metallurgical Society.

[66] K. G. F. Janssens, D. Raabe, E. Kozeschnik, M. A. Miodownik and B. Nestler. *Computational Materials Engineering - An Introduction to Microstructure Evolution*. Elsevier Academic Press, Burlington, Massachusetts, USA, 2007.

[67] R. Bürgel. *Handbuch Hochtemperatur - Werkstofftechnik*. Vieweg & Sohn Verlagsgesellschaft, Braunschweig, Germany, 2001.

[68] L. Onsager. Reciprocal Relations in Irreversible Processes I. *Physical Review*, 37(4):405–426, 1931.

[69] L. Onsager. Reciprocal Relations in Irreversible Processes II. *Physical Review*, 38(12):2265–2279, 1931.

[70] B. Sundman, H. L. Lukas and S. G. Fries. *Computational Thermodynamics: The Calphad Method*. Cambridge University Press, Cambridge, United Kingdom, 2007.

[71] K. Russell. Nucleation in Solids - The Induction and Steady-State Effects. *Advances in Colloid and Interface Science*, 13(3-4):205–318, 1980.

[72] E. Kozeschnik, J. Svoboda, F. D. Fischer. On the Role of Chemical Composition in Multi-Component Nucleation. In *Proceedings International Conference Solid-Solid Phase Transformations in Inorganic Materials*, pages 301–310, Pointe Hilton Squaw Peak Resort, Phoenix, Arizona, USA, 2005.

[73] B. Sonderegger and E. Kozeschnik. Generalized Nearest-Neighbor Broken-Bond Analysis of Randomly Oriented Coherent Interfaces in Multicomponent Fcc and

Bcc Structures. *Metallurgical and Materials Transactions A*, 40A(3):499–510, 2009.

[74] B. Sonderegger and E. Kozeschnik. Size Dependence of the Interfacial Energy in the Generalized Nearest-Neighbor Broken-Bond Aapproach. *Scripta Materialia*, 60(8):635–638, 2009.

[75] R. Radis. Untersuchung der Ausscheidungskinetik und der Teilchenverteilung in der Nickelbasis - Superlegierung UDIMET 720 Li. Master's thesis, Graz University of Technology, September 2007.

[76] R. Radis, M. Schaffer, M. Albu, G. Kothleitner, P. Pölt and E. Kozeschnik. Multi-Modal Size Distributions of γ' Precipitates During Continuous Cooling of Udimet 720 Li. *Acta Materialia*, 57:5739–5747, 2009.

[77] R. Radis and E. Kozeschnik. Evolution of Size and Morphology of γ' Precipitates in UDIMET 720 Li During Continuous. In *SUPERALLOYS 11*, pages 829–836, Seven Springs Mountain Resort, Pennsylvania, USA, September 2008. TMS.

[78] E. Kozeschnik, J. Svoboda, R. Radis and F. D. Fischer. Mean-Field Model for the Growth and Coarsening of Stoichiometric Precipitates at Grain Boundaries. *Modelling and Simulation in Materials Science and Engineering*, 18(015011):1–19, 2010.

[79] R. Kampmann and R. Wagner. Kinetics of Precipitation in Metastable Binary Alloys - Theory and Applications to Cu-1.9 at% Ti and Ni-14 at% Al. In *Decomposition of Alloys: The Early Stages, Proceedings of the 2nd Acta-Scripta Metallurgica Conference*, pages 91–103, Sonnenberg, Germany, 1983.

[80] R. W. Balluffi. Grain Boundary Diffusion Mechanisms in Metals. *Metallurgical Transactions A*, 13A:2069–2095, 1982.

[81] M. Pudar, E. Kozeschnik, A. Sormann and E. Parteder. Numerical Analysis of the Nb(C,N) Precipitation Kinetics in Microalloyed Steels. *Steel Research International*, 79(8):660–664, 2008.

[82] Y. W. Lee and H. I. Aaronson. Anisotropy of Coherent Interphase Boundary Energy. *Acta Materialia*, 28(4):539–548, 1980.

[83] Thermodynamic Database 'mc_steel', version 1.50, Institute of Materials Science and Technology, Vienna University of Technology.

[84] Thermodynamic Database TCFE3, version 3, ThermoCalc AB, Stockholm.

[85] Thermodynamic Database Fe-Data, version 6, Thermotech, Ltd., Surrey, United Kingdom.

[86] R. Radis and E. Kozeschnik. Berechnung der Phasenmengendiagramme im Gleichgewicht und der Änderung der Wärmekapazität hervorgerufen durch Ausscheidungen in vier verschiedenen Stählen. Technical Report B2-02, Christian Doppler Laboratory 'Early Stages of Precipitation', Vienna University of Technology, 2008.

[87] W. C. Leslie, R.L. Rickett, C. L. Dotson and C. S. Walton. Solution and Precipitation of Aluminum Nitride in Relation to the Structure of Low Carbon Steels. *Transactions of the ASM*, 46:1470–1499, 1954.

[88] P. König, W. Scholz und H. Ulmer. Wechselwirkung von Aluminium, Vanadium und Stickstoff in aluminiumberuhigten, mit Vanadin und Stickstoff legierten schweißbaren Baustählen mit rd. 02 % C und 1,5 % Mn. *Archiv für das Eisenhüttenwesen*, 32(8):541–556, 1961.

[89] M. Mayrhofer. Untersuchungen zur Auflösungs- und Ausscheidungskinetik von Al-Nitrid in Al-beruhigtem Stahl. *Berg- und Hüttenmännische Monatshefte*, 120(7):312–321, 1975.

[90] Ö. N. Dogan, G. M. Michal and H. W. Kwon. Pinning of Austenite Grain Boundaries by AlN Precipitates and Abnormal Grain Growth. *Metallurgical Transactions A*, 23A:2121–2129, 1992.

[91] T. Shimose and K. Narita. Influence of Heat Treatment on the Behaviour of AlN in Steel. *Tetso-to-Hagane (Journal of the Iron Steel Institue Japan)*, 40:242–243, 1954.

[92] L. S. Darken, R. P. Smith and E. W. Filer. Solubility of Gaseous Nitrogen in Gamma-Iron and the Effect of Alloying Constituents - Aluminium Nitride Precipitation. *Transactions of the American Institute of Mining and Metallurgical Engineers*, 191(12):1174–1179, 1951.

[93] Y. Kang, H. Yu, J. Fu, K. Wang and Z. Wang. Morphology and Precipitation Kinetics of AlN in Hot Strip of Low Carbon Steel Produced by Compact Strip Production. *Materials Science and Engineering*, A351:265–271, 2003.

[94] M. Hillert and S. Jonsson. An Assessment of the Al-Fe-N System. *Metallurgical Transactions A*, 23A:3141–3149, 1992.

[95] L. M. Cheng, E. B. Hawbolt and T. R. Meadowcroft. Modeling of Dissolution, Growth, and Coarsening of Aluminium Nitride in Low-Carbon Steels. *Metallurgical and Materials Transactions A*, 31A:1907–1916, 2000.

[96] N. Saunders. Thermochemical Database for Light Metal Alloys. *COST 507*, 2:23–27, 1998.

[97] L. Zhang and Y. Du. Thermodynamic Description of the Al-Fe-Ni System. *CALPHAD*, 31:529–540, 2007.

[98] W. Roberts and A. Sandberg. The Compositions of V(C,N) as Precipitated in HSLA Steels Microalloyed with Vanadium. Technical Report IM-1489, Swedish Institute for Metals, Stockholm, Sweden, 1980.

[99] K. Narita. Physical Chemistry of the Groups IVa (Ti, Zr), Va (V, Nb, Ta) and the Rare Earth Elements in Steel. *Transactions ISIJ*, 15:145–152, 1975.

[100] M. G. Frohberg and H. Graf. Die Löslichkeitsverhältnisse und die Ausscheidung von Vanadinnitrid im α- und γ-Gebiet des Systems Eisen-Stickstoff-Vanadin. *Stahl und Eisen*, 80(8):539–541, 1960.

[101] K. Inoue, N. Ishikawa, I. Ohnuma, H. Ohtani and K. Ishida. Calculation of Phase Equilibria between Austenite and (Nb, Ti, V)(C,N) in Microalloyed Steels. *ISIJ International*, 41(2):175–182, 2001.

[102] H. Ohtani and M. Hillert. A Thermodynamic Assessmant of the V-N System. *CALPHAD*, 15(1):11–24, 1991.

[103] H. Ohtani and M. Hillert. A Thermodynamic Asessment of the Fe-N-V System. *CALPHAD*, 15(1):25–39, 1991.

[104] H. A. Wriedt and H. Hu. Solubility Product of Vanadium Carbide in Austenite. In *Proceedings of a Symposium Sponsored by the TMS-AIME Physical Chemistry Committee*, Albany, Oregon, USA, 1981. The Metallurgical Society AIME.

[105] K. Bungardt, K. Kind and W. Oelsen. Solubility of Vanadium Carbide in Austenite. *Archiv für das Eisenhüttenwesen*, 27(1):61–66, 1956.

[106] B. Aronsson. Gefügeaufbau und Mechanische Eigenschaften einiger Martensitischer Stähle unter besonderer Berücksichtigung des Einflusses von Niob und Molybdän. In *Climax Molybdenum Special Publication*, pages 77–87, Dolder Grand Hotel, Zürich, Switzerland, 1969.

[107] H. Ohtani, T. Tanaka, M. Hasabe and N. Nishizawa. Solubility of NaCl-Type Carbides - NbC, VC, TiC - In Austenite. In *Japan-Canada Seminar on Secondary Steelmaking*, pages J7/1–J7/12. Iron and Steel Institute of Japan, 1985.

[108] W. Huang. Thermodynamic Properties of the Fe-Mn-V-C System. *Metallurgical Transactions*, 22A:1911–1920, 1991.

[109] R. P. Smith. Solubility of Niobium (Columbium) Nitride in Gamma Iron. *Transactions of the Metallurgical Society of AIME*, 224(1):190–191, 1962.

[110] T. M. Hoogendoorn and M. J. Spanraft. Quantifying the Effect of Microalloying Elements on Structures During Processing. In *Proceedings of the Conference of Microalloying 75*, pages 75–85, New York, USA, 1977. Union Carbide Corporation.

[111] T. Mori, M. Tokizane, K. Yamaguchi, E. Sunami and Y. Nakazima. Thermodynamik Properties of Niobium Carbides and Nitrides in Steel. *Tetsu to Hagane (Journal of the Iron and Steel Institute of Japan)*, 54:763–776, 1968.

[112] R. C. Sharma, V. K. Lakshmanan and J. S. Kirkaldy. Solubility of Niobium Carbide and Niobium Carbonitride in Alloyed Austenite and Ferrite. *Metallurgical Transactions A*, 15(3):545–553, 1984.

[113] K. Balasubramanian and J. S. Kirkaldy. Thermodynamic of Fe-Ti-C and Fe-Nb-C Austenites and Nonstoichiometric Titanium and Niobium Carbides. In *Proceedings of the International Symposium - Advance in Phase Transitions*, pages 37–51, Ontario, Canada, 1987. Department of Materials Science and Engineering, McMaster University, Pergamon Press, Oxford, United Kingdom.

[114] B. J. Lee. A Thermodynamic Assesment of the Fe-Nb-Ti-C-N. *Metallurgical and Materials Transactions*, 32A:2423–2439, 2001.

[115] E. J. Palmiere, C. I. Garcia and A. J. DeArdo. Compositional and Microstructural Changes which Attend Reheating and Grain Coarsening in Steels Containig Niobium. *Metallurgical and Materials Transactions A*, 25A:277–286, 1994.

[116] F. de Kazinczy, A. Axnas and P. Pachleitner. Some Properties of Niobium-Treated Mild Steel. *Jernkontorets Annaler*, 147(4):408–433, 1963.

[117] L. Meyer. On Dissolution Precipitation and Age Hardening Effect of Niobium in Plain Carbon Steel. *Zeitschrift für Metallkunde*, 58(5):334–339, 1967.

[118] R. P. Smith. Solubility of Niobium (Columbium) Carbide in Gamma Iron. *Transactions of the Metallurgical Society of AIME*, 236(2):220–221, 1966.

[119] T. H. Johansen, N. Christen and B. Augland. Solubility of Niobium (Columbium) Carbide in Gamma Iron. *Transactions of the Metallurgical Society of AIME*, 239(10):1651–1654, 1967.

[120] H. Nordberg and B. Aronsson. Solubility of Niobium Carbide in Austenite. *Journal of the Iron and Steel Institute*, 206:1263–1266, 1968.

[121] V. K. Laksmanan and J. S. Kirkaldy. Solubility Product for Niobium Carbide in Austenite. *Metallurgical Transactions A*, 15(3):541–544, 1984.

[122] K. Balasubramanian, A. Kroupa and J. S. Kirkaldy. Experimental Investigations of the Thermodynamics of Fe-Nb-C Austenite and Nonstoichiometric Niobium and Titanium Carbides (T=1273 to 1473 K). *Metallurgical Transactions A*, 23A:729–744, 1992.

[123] H. Ohtani, M. Hasebe and T. Nishizawa. Calculation of the Fe-C-Nb Ternary Phase-Diagram. *CALPHAD*, 13(2):183–204, 1989.

[124] S. Koyama, T. Ishil and K. Narita. Effects of Mn, Si, Cr and Ni on the Solution and Precipitation of Niobium Carbide in Iron Austenite. *Journal of Japan Institute of Metals*, 52:1089–1094, 1972.

[125] E. Povoden-Karadeniz, R. Radis and Ernst Kozeschnik. Unpublished Research. Thermodynamic Assesment of the Fe-Nb-C System, 2009.

[126] W. Huang. A Thermodynamic Evaluation of the Fe-Nb-C System. *Zeitschrift für Metallkunde*, 81:397–404, 1990.

[127] W. Huang and M. Selleby. Thermodynamic Assessment of the Nb-W-C System. *Zeitschrift für Metallkunde*, 88(1):55–62, 1997.

[128] S. Matsuda and N. Okumura. Effect of Distribution of TiN Precipitate Particles on Austenite Grain-Size of Low-Carbon Low-Alloy Steels. *Transactions of the Iron and Steel Institute Japan*, 18(4):198–205, 1978.

[129] J. Kunze. Solubility Product of Titanium Nitride in γ-Iron. *Metal Science*, 16:217–218, 1982.

[130] H. Wada and R. D. Pehlke. Nitrogen Solubility and Nitride Formation in Austenitic Fe-Ti Alloys. *Metallurgical Transactions*, 16B:815–822, 1985.

[131] K. Inoue, I. Ohnuma, H. Ohtani, K. Ishida and T. Nishizawa. Solubility Product of TiN in Austenite. *ISIJ International*, 38(9):991–997, 1998.

[132] H. Ohtani and M. Hillert. A Thermodynamic Assessment of the Fe-N-Ti System. *CALPHAD*, 15(1):41–52, 1991.

[133] W. Roberts. No Titel. Technical Report IM 1085, Swedish Institute for Metal Research, 1975.

[134] K. Frisk. Thermodynamic Modelling of Multicomponent Cubic Nb, Ti and V Carbides / Carbonitrides. *CALPHAD*, 32:326–337, 2008.

[135] K. Balasubramanian, A. Kroupa and J. S. Kirkaldy. Experimental Investigation of the Thermodynamics of the Fe-Ti-C Austenite and the Solubility of Titanium Carbide. *Metallurgical Transactions A*, 23A:709–727, 1992.

[136] H. Ohtani, T. Tanaka, M. Hasebe and T. Nishizawa. Calculation of the Fe-C-Ti Ternary Phase Diagram. *CALPHAD*, 12(3):225–246, 1988.

[137] H. F. Beeghly. Determination of Aluminium Nitride Nitrogen in Steel. *Analytical Chemistry*, 21(12):1513–1519, 1949.

[138] A. Brahmi and R. Borrelly. Study of Aluminium Nitride Precipitation in Pure Fe-Al-N Alloy by Thermoelectric Power Measurements. *Acta Materialia*, 45(5):1889–1897, 1997.

[139] T. Mori, K. Fujita, M. Tokizane and K. Yamaguchi. Behavior of Niobium Carbides and Nitrides in Steel. *Tetsu-to-Hagané (Journal of Iron and Steel Institute Japan*, 50:911–917, 1964.

[140] Diffusion Database 'mc_sample', version 1.03, Institute of Materials Science and Technology, Vienna University of Technology.

[141] D. Hull and D. J. Bacon. *Introduction to Dislocations* . Pergamon Press Ltd., Oxford, United Kingdom, 1984.

[142] F. Fazelli, C. W. Sinclar and T. Bastow. The Role of Excess Vacancies on Precipitation Kinetics in an Al-Mg-Sc Alloy. *Metallurgical and Materials Transactions A*, 39A:2297–2305, 2008.

[143] T. Heumann and R. Imm. Self-Diffusion and Isotope Effect in γ-Iron. *Journal of Physics and Chemistry of Solids*, 29(9):1613–1621, 1968.

[144] G. Hettich, H. Mehrer and K. Maier. Self-Diffusion in Ferromagnetic Alpha-Iron. *Scripta Metallurgica*, 11(9):795–802, 1977.

[145] U. Peil und M. Wichers. Schweißen unter Betriebsbeanspruchung - Werkstoffkennwerte zur Temperaturfeldberechnung für einen S 355 J2 G3. *Stahlbau*, 74(4):249–257, 2005.

[146] M. Fukuhara and A. Sanpei. Elastic Moduli and Internal Friction of Low Carbon and Stainless Steels as a Function of Temperature. *ISIJ International*, 33(4):508–512, 1993.

[147] W. H. Hill and K. D. Shimmin. Elevated Temperature Dynamic Elastic Moduli of Various Metallic Materials. Technical Report 60-438, Wright Air Development Division, Wright-Patterson Air Force Base, Ohio, USA, 1961.

[148] E. H. F. Date. Elastic Properties of Steels. *Journal of the Iron and Steel Institute*, pages 988–991, 1969.

[149] B. A. Latella and S. R. Humphries. Young's Modulus of a 2.25Cr-1Mo Steel at Elevated Temperature. *Scripta Materialia*, 51:635–639, 2004.

[150] A. E. Focke. *Metals Handbook.* 9^{th} *ed. Properties and Selection: Irons and Steels*, volume 1. ASM International, Materials Park, Ohio, USA, 1990.

[151] Y. Takeuti, N. Noda, S. Komori, H. Nyuko and T. Kitagawa. Empirical Formulae of Temperature Dependency of Elastic Moduli of Several Steels and Aluminium Alloys. *Journal of the Society of Materials Science (Japan)*, 26:210–214, 1976.

[152] T. Ohba, S. Muneki, H. Tanaka, F. Abe and K. Yagi. High-Temperature Elastic Moduli and Application to Creep Data Analysis for Mod. 9Cr-1Mo Steel. *CAMP-ISIJ*, 8:672–672, 1995.

[153] A. L. Kimball and D. E. Lovell. Variation of Young's Modulus with Temperature from Vibration Measurements. *Physical Review*, 26:121–124, 1925.

[154] K. Harste, T. Suzuki and K. Schwerdtfeger. Thermomechanical Properties of Steel: Viscoplaticity of Gamma Iron and Gamma Fe-C Alloys. *Materials Science and Technology*, 8:23–33, 1992.

[155] M. V. Speight. Growth Kinetics of Grain-Boundary Precipitates. *Acta Metallurgica*, 16:133–135, 1968.

[156] H. O. K. Kirchner. Coarsening of Grain-Boundary Precipitates. *Metallurgical Transactions*, 2:2861–2864, 1971.

[157] A. J. Ardell. On the Coarsening of Grain Boundary Precipitates. *Acta Metallurgica*, 20:601–609, 1972.

[158] J. J. Hoyt. On the Coarsening of Precipitates Located on Grain Boundaries and Dislocations. *Acta Metallurgica et Materialia*, 39(9):2091–2098, 1991.

[159] R. D. Vengrenovitch. On the Ostwald Ripening Theory. *Acta Metallurgica*, 30:1079–1086, 1982.

[160] V. V. Slyozov. Coalescence of a Supersaturated Solid Solution During Diffusion Along Grain Boundaries or Dislocation Lines. *Soviet Physics - Solid State*, 9(4):927–929, 1967.

[161] E. P. Butler and P. R. Swann. In Situ Observations of the Nucleation and Initial Growth of Grain Boundary Precipitates in an Al-Zn-Mg Alloy. *Acta Metallurgica*, 24:343–352, 1976.

[162] T. Fujii, M. Moriyama, M. Kato and T. Mori. Growth of Grain-Boundary Precipitates in Cu-Fe-Co Bicrystals. *Philosophical Magazine A*, 68(1):137–149, 1993.

[163] R. Monzen and T. Echigo. Growth of bcc Fe-Co Precipitate Particles at Boundaries in Cu Bicrystals. *Materials Science Forum*, 294-296:609–612, 1999.

[164] C. Wagner. Theorie der Alterung von Niederschlägen durch Umlösen. *Zeitschrift für Elektrochemie*, 65(7-8):581–591, 1961.

[165] I. M. Lifshitz and V. V. Slyozov. The Kinetics of Precipitation from Supersaturated Solid Solutions. *Journal of Physics and Chemistry of Solids*, 19(1-2):35–50, 1961.

[166] G. A. Duit, A. Hurkmans, J. J. F. Scheffer and T. M. Hoogendoorn. A Model for the Kinetics of Aluminium-Nitride Precipitation. In *Proceedings of the International Conference on Physical Metallurgy of Thermomechanical Proccesing of Steels and other Metals, THERMEC ´88*, pages 114–121, Tokyo, Japan, 1988.

[167] L. M. Cheng, E. B. Hawbolt and T. R. Meadowcroft. Modelling of AlN Precipitation in Low Carbon Steels. *Scripta Materialia*, 41(6):673–678, 1999.

[168] J. Fu, Y. Liu and H. Wu. The Precipitation and Effect of Nano Nitrides in HSLC Steel. *Science in China Series E: Technological Series*, 51(7):989–998, 2008.

[169] L. Zhang, U. Lotter and H. P. Schmitz. Mathematical Modelling of AlN-Precipitation in Hot Strip of Unalloyed Steels During Cooling in the Coil. *Steel Grips*, 4(5/6):375–379, 2006.

[170] N. Y. Zolotorevsky, V. P. Pletenev and Y. F. Titovets. Analysis of Aluminium Nitride Precipitation Proceeding Concurrently with Recrystallization in Low-Carbon Steel. *Modelling and Simulation in Materials Science and Engineering*, 6:383–391, 1998.

[171] E. Kozeschnik, V. Pletenev, N. Zolotorevsky and B. Buchmayr. Aluminium Nitride Precipitation and Texture Development in Batch-Annealed Bake-Hardening Steel. *Metallurgical and Materials Transactions A*, 30A:1663–1673, 1999.

[172] R. Radis and E. Kozeschnik. Kinetics of AlN Precipitation in Microalloyed Steel. *Modelling and Simulation in Materials Science and Engineering*, 18(055003):1–16, 2010.

[173] R. Radis and E. Kozeschnik. Precipitation Kinetics of Aluminium Nitride in Austenite in Microalloyed HSLA Steels. *Materials Science Forum*, 636-637:605–611, 2010.

[174] R. Radis and E. Kozeschnik. Kinetics of AlN Precipitation in the Ferrite Phase Field of Microalloyed (HSLA) Steels. In *139th Annual Meeting & Exhibition TMS, Vol. 2: Materials Characterization, Computation, Modeling and Energy*, pages 341–348, Seattle, Washington, USA, February 2010.

[175] R. Radis and E. Kozeschnik. Precipitation Kinetics of Aluminium Nitride in Austenite in Microalloyed HSLA Steels. In *Vth International Materials Symposium MATERIAIS*, page paper 224 on CD, Lisbon, Portugal, April 2009.

[176] R. Radis and E. Kozeschnik. Numerical Analysis of AlN Precipitation Kinetics in Microalloyed Austenite. In *4th International Conference ASIA STEEL*, pages 13–24, Busan, South Korea, May 2009.

[177] I. Biron, R. Borrelly, P. Delaneau and B. J. Thomas. Application des Mesures de Pouvoir Thermoélectrique au Contrôle de la Précipitation du Nitrure d'Aluminium dans les Aciers Extra-Doux. *Mémoires et Études Scientifiques Revue de Métallurgie*, 11:725–733, 1991.

[178] V. Guetaz, V. Massardier, J. Merlin, D. Ravaine and M. Solar. Determination of Aluminium Nitride or Free Nitrogen in Low Carbon Steel. *Steel Research*, 72(7):245–249, 2001.

[179] X. G. Lu, M. Selleby and B. Sundman. Assessments of Molar Volume and Thermal Expansion for Selected bcc, fcc and hcp Metallic Elements. *CALPHAD*, 29:68–89, 2005.

[180] R. J. Bruls, H. T. Hintzen, G. de With, R. Metselaar and J. C. van Miltenburg. The Temperature Dependency of the Grüneisen Parameters of MgSiN2, AlN and Beta-Si3N4. *Journal of Physics and Chemistry of Solids*, 62:783–792, 2001.

[181] Y. N. Gornostyrev, O. Y. Kontsevoi, K. Y. Khromov, M. I. Katsnelson and A. J. Freeman. The Role of Thermal Expansion and Composition Changes in the Temperature Dependence of the Lattice Misfit in two - Phase γ/γ' Superalloys. *Scripta Materialia*, 56:81–84, 2007.

[182] F. D. Fischer, J. Svoboda, E. Gamsjäger, E. Kozeschnik and B. Sonderegger. Modelling of Precipitation Kinetics with Simultanous Stress Relaxation. In *Materials Research Society Symposium Proceedings*, volume 979, Warrendale, Pennsylvania, USA, 2007. MRS. paper no. 0979-HH11-04.

[183] R. Radis and E. Kozeschnik. Concurrent Precipitation of AlN and VN in Microalloyed Steel. *Steel Research International*, 81(8):681–685, 2010.

[184] R. Radis and E. Kozeschnik. Simulation of Concurrent AlN and VN Precipitation During Thermal Treatment of Microalloyed Steels. In *3rd International Conference on Simulation and Modelling of Metallurgical Processes in Steelmaking STEELSIM*, pages 326–331, Leoben, Austria, September 2009. Austrian Society for Metallurgy and Materials - ASMET.

[185] E. Kozeschnik. Intermediate Report RFCS. Technical report, Institute for Materials Science, Welding and Forming, 2007.

[186] M. Pudar. *Untersuchung der Duktilitätseigenschaften von stranggegossenen mikrolegierten Stählen*. PhD thesis, Graz University of Technology, May 2008.

[187] M. Pudar, S. Zamberger, K. Spiradek-Hahn, R. Radis and E. Kozeschnik. Computational Analysis of Precipitation During Continuous Casting of Microalloyed Steel. *Steel Research International*, 81(5):372–380, 2010.

[188] R. Radis, S. Zamberger and E. Kozeschnik. Simulation of the Precipitation of Nitrides and Carbides Taking into Account the Segregation of Alloying Elements During Solidification. Technical Report B2-09-01, Christian Doppler Laboratory 'Early Stages of Precipitation', 2009.

[189] S. Riaz, J. Komenda, N. Triolet, G. Alvarez de Toledo Bandeira, S. Zamberger, E. Erdem. Precipitation: Behaviour of Microalloyed Steels during Solidification and Cooling. Technical Report EUR 24204, 2010. ISBN: 978-92-79-14428-8.

[190] E. Kozeschnik. A Scheil-Gulliver Model with Back Diffusion Applied to the Microsegregation of Chromium in Fe-Cr-C Alloys. *Metallurgical and Materials Transactions A*, 31A:1682–1684, 2000.

[191] E. Kozeschnik, W. Rindler and B. Buchmayr. Scheil-Gulliver Simulation with Partial Redistribution of Fast Dinusers and Simultaneous Solid-Solid Phase Transformation. *International Journal of Materials Research*, 98(9):826–831, 2007.

Appendix

A MatCalc Script for the Calculation of the Precipitation Kinetics of Nitrides and Carbides in Steel

Employing the software package MatCalc, precipitation kinetics calculations can be performed by executing script files, which also ensure the documentation of the used parameters. In the following a script file is presented for the calculation of the precipitation of nitrides and carbides during the production process of a hypothetical microalloyed steel, according to a hypothetical heat treatment shown in figure A.1.

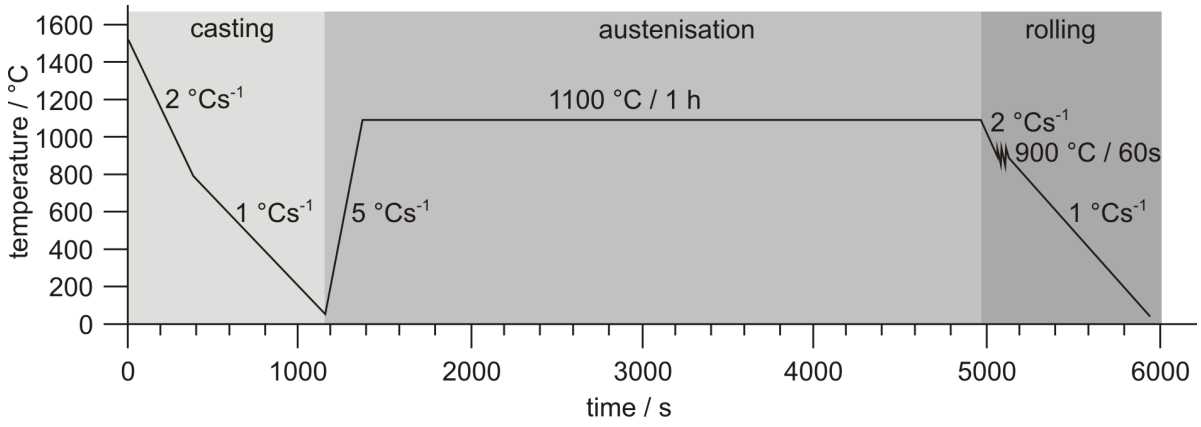

Figure A.1: Heat treatment used for the simulation of the production process of a hypothetical steel during the stages casting, austenisation and rolling.

The simulation of AlN and VN is performed according to the descriptions given in sections 4.7 and 4.8, whereas the calculation of the precipitation kinetics of other precipitates must be considered as a first estimation and is not verified yet.

```
$ ********************************************************************************************************
$ ************************************* GENERAL INFORMATION ************************************************
$ ********************************************************************************************************
$ Simulation of the production process of a hypothetical microalloyed steel
$ Database: mc_steel_1.86.tdb, mc_sample_fe.ddb
$ Author: R. Radis
$ Creation date: 2010-05-27
$ This is a script for MatCalc version 5.30
$ ********************************************************************************************************
$ ************************************* SETUP INFORMATION **************************************************
$ ********************************************************************************************************

new-workspace                                                    $open new workspace

set-workspace-info +Selected elements:                           $give some information about the script
set-workspace-info +C, Si, Mn, Al, V, Nb, N, Cr, Mo, Ni
set-workspace-info +
set-workspace-info +Matrix phases: Ferrite (BCC_A2), Austenite (FCC_A1)
set-workspace-info +Precipitate phases: AlN, VN, VC, NbN, NbC, M23C6, M7C3 and M3C (Cementite)
set-workspace-info +
set-workspace-info +-----------------------------------------------
set-workspace-info +More information about MatCalc on
set-workspace-info +     http://www.matcalc.at
set-workspace-info +-----------------------------------------------

use-module core                                                  $select core module for kinetic simulation

$********************************************************************************************************
$ ************************************** SYSTEM SETUP ******************************************************
$ ********************************************************************************************************

$********************************************************************************************************
$                                  DATABASES, CHEMICAL COMPOSITION, SELECTED PHASES
$ ********************************************************************************************************

open-thermo-database mc_steel_1.86.tdb                           $open thermodynamic database
select-elements Al C Cr Fe Mn Mo N Nb Si V                       $select elements
select-phase bcc_a2 fcc_a1 m23c6 m7c3 cementite aln vn vc nbn nbc Cr2N  $select phases
set-reference-element fe                                         $set fe as reference element
read-thermodyn-database                                          $read thermodynamic database
enter-composition wp al=0,02 c=0,1 cr=1,5 mn=1 n=0,01 nb=0,03 si=0,3 v=0,2$system setup
read-mobility-database mc_sample_fe.ddb                          $read diffusion data

$ ********************************************************************************************************
$                                  HEAT TREATMENTS, VARIABLES, TABLES & FUNCTIONS
$ ********************************************************************************************************

$ ------------------------------------------------------------ HEAT TREATMENTS ---------------------------------------------------

create-heat-treatment ht                                         $create a new heat treatment
append-ht-segment ht                                             $append new segment to heat treatment
edit-ht-segment ht . d n austenite                               $set precipitation domain to austenite
edit-ht-segment ht . s 1550                                      $set start temperature of heat treatment
edit-ht-segment ht . 1 800 2                                     $cool to 800°C with a cooling rate of 2°C/s

                                                                 $nucleation is defined to occur in austenite
edit-ht-segment ht . r + set-precipitation-parameter aln_p0 n s g  $nucleation of aln at gb in austenite
edit-ht-segment ht . r + set-precipitation-parameter aln_p1 n s d  $nucleation of aln at d in austenite
edit-ht-segment ht . r + set-precipitation-parameter aln#01_p0 n s n  $no nucleation of aln at gb in ferrite
edit-ht-segment ht . r + set-precipitation-parameter aln#01_p1 n s n  $no nucleation of aln at d in ferrite
```

```
edit-ht-segment ht . r + set-precipitation-parameter vn_p0 n s d          $nucleation of vn at d in austenite
edit-ht-segment ht . r + set-precipitation-parameter vn#01_p0 n s n       $no nucleation of vn in ferrite
edit-ht-segment ht . r + set-precipitation-parameter vc_p0 n s d          $nucleation of vc at d in austenite
edit-ht-segment ht . r + set-precipitation-parameter vc#01_p0 n s n       $no nucleation of vc in ferrite
edit-ht-segment ht . r + set-precipitation-parameter nbn_p0 n s d         $nucleation of nbn at d in austenite
edit-ht-segment ht . r + set-precipitation-parameter nbn#01_p0 n s n      $no nucleation of nbn in ferrite
edit-ht-segment ht . r + set-precipitation-parameter nbc_p0 n s d         $nucleation of nbc at d in austenite
edit-ht-segment ht . r + set-precipitation-parameter nbc#01_p0 n s n      $no nucleation of nbc in ferrite
edit-ht-segment ht . r + set-precipitation-parameter m7c3_p0 n s n        $no nucleation of m7c3 in ferrite
edit-ht-segment ht . r + set-precipitation-parameter m23c6_p0 n s n       $no nucleation of m23c6 in ferrite
edit-ht-segment ht . r + set-precipitation-parameter Cr2N_p0 n s n        $no nucleation of cr2n in ferrite
edit-ht-segment ht . r + set-precipitation-parameter cementite_p0 n s n   $no nucleation of cementite in ferrite

append-ht-segment ht                                                      $append new segment to heat treatment
edit-ht-segment ht . d n ferrite                                          $change precipitation domain
edit-ht-segment ht . 1 25 1                                               $cool to 25°C with a cooling rate of 1°C/s

                                                                          $change nucleation to occur in ferrite
edit-ht-segment ht . r + set-precipitation-parameter aln_p0 n s n         $no nucleation of AlN at gb in austenite
edit-ht-segment ht . r + set-precipitation-parameter aln_p1 n s n         $no nucleation of AlN at d in austenite
edit-ht-segment ht . r + set-precipitation-parameter aln#01_p0 n s g      $nucleation of AlN at gb in ferrite
edit-ht-segment ht . r + set-precipitation-parameter aln#01_p1 n s d      $nucleation of AlN at d in ferrite
edit-ht-segment ht . r + set-precipitation-parameter vn_p0 n s n          $no nucleation of VN in austenite
edit-ht-segment ht . r + set-precipitation-parameter vn#01_p0 n s d       $nucleation of VN at d in ferrite
edit-ht-segment ht . r + set-precipitation-parameter vc_p0 n s n          $no nucleation of VC in austenite
edit-ht-segment ht . r + set-precipitation-parameter vc#01_p0 n s d       $nucleation of VC at d in ferrite
edit-ht-segment ht . r + set-precipitation-parameter nbn_p0 n s n         $no nucleation of NbN in austenite
edit-ht-segment ht . r + set-precipitation-parameter nbn#01_p0 n s d      $nucleation of NbN at d in ferrite
edit-ht-segment ht . r + set-precipitation-parameter nbc_p0 n s n         $no nucleation of NbC in austenite
edit-ht-segment ht . r + set-precipitation-parameter nbc#01_p0 n s d      $nucleation of NbC at d in ferrite
edit-ht-segment ht . r + set-precipitation-parameter m7c3_p0 n s d        $nucleation of M7C3 at d in ferrite
edit-ht-segment ht . r + set-precipitation-parameter m23c6_p0 n s d       $nucleation of M23C6 at d in ferrite
edit-ht-segment ht . r + set-precipitation-parameter Cr2N_p0 n s d        $nucleation of Cr2N at d in ferrite
edit-ht-segment ht . r + set-precipitation-parameter cementite_p0 n s d   $nucleation of cementite at d in ferrite

append-ht-segment ht                                                      $append new segment to heat treatment
edit-ht-segment ht . d y                                                  $use inherent precipitation domain
edit-ht-segment ht . 1 800 5                                              $heat to 800°C with a heating rate of 5°C/s

append-ht-segment ht                                                      $append new segment to heat treatment
edit-ht-segment ht . d n austenite                                        $change precipitation domain
edit-ht-segment ht . 1 1100 5                                             $heat to 1100°C with a heating rate of 5°C/s

                                                                          $change nucleation to occur in austenite
edit-ht-segment ht . r + set-precipitation-parameter aln_p0 n s g         $nucleation of AlN at gb in austenite
edit-ht-segment ht . r + set-precipitation-parameter aln_p1 n s d         $nucleation of AlN at d in austenite
edit-ht-segment ht . r + set-precipitation-parameter aln#01_p0 n s n      $no nucleation of AlN at gb in ferrite
edit-ht-segment ht . r + set-precipitation-parameter aln#01_p1 n s n      $no nucleation of AlN at d in ferrite
edit-ht-segment ht . r + set-precipitation-parameter vn_p0 n s d          $nucleation of VN at d in austenite
edit-ht-segment ht . r + set-precipitation-parameter vn#01_p0 n s n       $no nucleation of VN in ferrite
edit-ht-segment ht . r + set-precipitation-parameter vc_p0 n s d          $nucleation of VC at d in austenite
edit-ht-segment ht . r + set-precipitation-parameter vc#01_p0 n s n       $no nucleation of VC in ferrite
edit-ht-segment ht . r + set-precipitation-parameter nbn_p0 n s d         $nucleation of NbN at d in austenite
edit-ht-segment ht . r + set-precipitation-parameter nbn#01_p0 n s n      $no nucleation of NbN in ferrite
edit-ht-segment ht . r + set-precipitation-parameter nbc_p0 n s d         $nucleation of NbC at d in austenite
edit-ht-segment ht . r + set-precipitation-parameter nbc#01_p0 n s n      $no nucleation of NbC in ferrite
edit-ht-segment ht . r + set-precipitation-parameter m7c3_p0 n s n        $no nucleation of M7C3 in ferrite
edit-ht-segment ht . r + set-precipitation-parameter m23c6_p0 n s n       $no nucleation of M23C6 in ferrite
edit-ht-segment ht . r + set-precipitation-parameter Cr2N_p0 n s n        $no nucleation of Cr2N in ferrite
edit-ht-segment ht . r + set-precipitation-parameter cementite_p0 n s n   $no nucleation of cementite in ferrite
```

```
append-ht-segment ht                                                    $append new segment to heat treatment
edit-ht-segment ht . d y                                                $use inherent precipitation domain
edit-ht-segment ht . 3 1100 3600                                        $isothermal annealing at 1100°C for 1h

append-ht-segment ht                                                    $append new segment to heat treatment
edit-ht-segment ht . d y                                                $use inherent precipitation domain
edit-ht-segment ht . 1 900 2                                            $cool to 900°C with a cooling rate of 2°C/s

append-ht-segment ht                                                    $append new segment to heat treatment
edit-ht-segment ht . d y                                                $use inherent precipitation domain
edit-ht-segment ht . 3 900 60                                           $isothermal annealing at 900°C for 60s
edit-ht-segment ht . r + set-precipitation-parameter austenite d e 1e15 $increase dislocation density due to rolling

append-ht-segment ht                                                    $append new segment to heat treatment
edit-ht-segment ht . d y                                                $use inherent precipitation domain
edit-ht-segment ht . 1 800 2                                            $cool to 800°C with a cooling rate of 2°C/s

append-ht-segment ht                                                    $append new segment to heat treatment
edit-ht-segment ht . d n ferrite                                        $change precipitation domain
edit-ht-segment ht . 1 25 1                                             $cool to 25°C with a cooling rate of 1°C/s

                                                                        $change nucleation to occur in ferrite
edit-ht-segment ht . r + set-precipitation-parameter aln_p0 n s n       $no nucleation of aln at gb in austenite
edit-ht-segment ht . r + set-precipitation-parameter aln_p1 n s n       $no nucleation of aln at d in austenite
edit-ht-segment ht . r + set-precipitation-parameter aln#01_p0 n s g    $nucleation of aln at gb in ferrite
edit-ht-segment ht . r + set-precipitation-parameter aln#01_p1 n s d    $nucleation of aln at d in ferrite
edit-ht-segment ht . r + set-precipitation-parameter vn_p0 n s n        $no nucleation of vn in austenite
edit-ht-segment ht . r + set-precipitation-parameter vn#01_p0 n s d     $nucleation of vn at d in ferrite
edit-ht-segment ht . r + set-precipitation-parameter vc_p0 n s n        $no nucleation of vc in austenite
edit-ht-segment ht . r + set-precipitation-parameter vc#01_p0 n s d     $nucleation of vc at d in ferrite
edit-ht-segment ht . r + set-precipitation-parameter nbn_p0 n s n       $no nucleation of nbn in austenite
edit-ht-segment ht . r + set-precipitation-parameter nbn#01_p0 n s d    $nucleation of nbn at d in ferrite
edit-ht-segment ht . r + set-precipitation-parameter nbc_p0 n s n       $no nucleation of nbc in austenite
edit-ht-segment ht . r + set-precipitation-parameter nbc#01_p0 n s d    $nucleation of nbc at d in ferrite
edit-ht-segment ht . r + set-precipitation-parameter m7c3_p0 n s d      $nucleation of m7c3 at d in ferrite
edit-ht-segment ht . r + set-precipitation-parameter m23c6_p0 n s d     $nucleation of m23c6 at d in ferrite
edit-ht-segment ht . r + set-precipitation-parameter Cr2N_p0 n s d      $nucleation of cr2n at d in ferrite
edit-ht-segment ht . r + set-precipitation-parameter cementite_p0 n s d $nucleation of cementite at d in ferrite

$ ------------------------------------------------------------------------ VARIABLES ------------------------------------------------------------------------

set-variable-value npc 20                                               $number of precipitate classes

$ ------------------------------------------------------------------------ TABLES ---------------------------------------------------------------------------

create-global-table cie_vn                                              $correction factors for CIE of VN
add-table-entry cie_vn          1073            1                       $MC interpolates between defined values
add-table-entry cie_vn          1173            1
add-table-entry cie_vn          1223            0,95
add-table-entry cie_vn          1273            0,78
add-table-entry cie_vn          1373            0,65
add-table-entry cie_vn          1473            0,65

$ ********************************************************************************************************
$                                       PRECIPITATION DOMAINS, PRECIPITATES
$ ********************************************************************************************************

$ ------------------------------------------------------------ PRECIPITATION DOMAINS ------------------------------------------------------------

create-precipitation-domain austenite                                   $austenite is precipitation domain = matrix
```

```
set-precipitation-parameter austenite x fcc_a1                    $matrix phase of domain „austenite“
set-precipitation-parameter austenite d e 1e11                    $dislocation density (=1e11 m^-2)
set-precipitation-parameter austenite g 100e-6                    $austenite grain size (=100e-6 m)
set-precipitation-parameter austenite t (193000-73,333*T$C)*1e6   $temperature dependent young's modulus
create-precipitation-domain ferrite                               $ferrite is precipitation domain = matrix
set-precipitation-parameter ferrite x bcc_a2                      $matrix phase of domain „ferrite“
set-precipitation-parameter ferrite d e 1e12                      $dislocation density (=1e12 m^-2)l
set-precipitation-parameter ferrite g 10e-6                       $ferrite grain size (=100e-6 m)
set-precipitation-parameter ferrite t (210000-75*T$C)*1e6         $temperature dependent young's modulus

$ ---------- PRECIPITATE PHASES IN AUSTENITE ----------

create-new-phase aln p                                            $new precipitate phase aln_p0 in austenite
set-precipitation-parameter aln_p0 c npc                          $use variable npc for number of prec. classes
set-precipitation-parameter aln_p0 d austenite                    $austenite is precipitation domain
set-precipitation-parameter aln_p0 n s g                          $nucleation sites are grain boundaries
set-precipitation-parameter aln_p0 i y                            $use calculated interfacial energy (CIE)
set-precipitation-parameter aln_p0 z y                            $use automatic size correction for CIE
set-precipitation-parameter aln_p0 s g (10^(11-0,005*T$C))        $ratio between diffusion at gb and bulk
set-precipitation-parameter aln_p0 s n (10^(11-0,005*T$C))        $ratio between diffusion at gb and bulk

create-new-phase aln p                                            $new precipitate phase aln_p1 in austenite
set-precipitation-parameter aln_p1 c npc                          $use variable npc for number of prec. classes
set-precipitation-parameter aln_p1 d austenite                    $austenite is precipitation domain
set-precipitation-parameter aln_p1 n s d                          $nucleation sites are dislocations
set-precipitation-parameter aln_p1 i y                            $use calculated interfacial energy (CIE)
set-precipitation-parameter aln_p1 z y                            $use automatic size correction for CIE
set-precipitation-parameter aln_p1 t m n 0,19                     $use volumetric misfit between prec./matrix
                                                                  $use 0.27 instead 0.19 for MC versions ≥ 5.40
set-precipitation-parameter aln_p1 n f y                          $take into account volume misfit in nucleation

create-new-phase vn p                                             $ new precipitate phase vn_p0 in austenite
set-precipitation-parameter vn_p0 c npc                           $use variable npc for number of prec. classes
set-precipitation-parameter vn_p0 d austenite                     $austenite is precipitation domain
set-precipitation-parameter vn_p0 n s d                           $nucleation sites are dislocations
set-precipitation-parameter vn_p0 i N cie$vn*cie_vn(T)            $correction of CIE due to entropic contr.
set-precipitation-parameter vn_p0 z y                             $use automatic size correction for CIE

create-new-phase vc p                                             $new precipitate phase vc_p0 in austenite
set-precipitation-parameter vc_p0 c npc                           $use variable npc for number of prec. classes
set-precipitation-parameter vc_p0 d austenite                     $austenite is precipitation domain
set-precipitation-parameter vc_p0 n s d                           $nucleation sites are dislocations
set-precipitation-parameter vc_p0 i y                             $use calculated interfacial energy (CIE)
set-precipitation-parameter vc_p0 z y                             $use automatic size correction for CIE

create-new-phase nbn p                                            $ new precipitate phase nbn_p0 in austenite
set-precipitation-parameter nbn_p0 c npc                          $use variable npc for number of prec. classes
set-precipitation-parameter nbn_p0 d austenite                    $austenite is precipitation domain
set-precipitation-parameter nbn_p0 n s d                          $nucleation sites are dislocations
set-precipitation-parameter nbn_p0 i y                            $use calculated interfacial energy (CIE)
set-precipitation-parameter nbn_p0 z y                            $use automatic size correction for CIE

create-new-phase nbc p                                            $new precipitate phase nbc_p0 in austenite
set-precipitation-parameter nbc_p0 c npc                          $use variable npc for number of prec. classes
set-precipitation-parameter nbc_p0 d austenite                    $austenite is precipitation domain
set-precipitation-parameter nbc_p0 n s d                          $nucleation sites are dislocations
set-precipitation-parameter nbc_p0 i y                            $use calculated interfacial energy (CIE)
set-precipitation-parameter nbc_p0 z y                            $use automatic size correction for CIE
```

```
$ ---------- PRECIPITATE PHASES IN FERRITE ----------

remove_phase fcc_A1#01                                  $remove the fcc_A1#01 precipitate phase

create-new-phase aln e                                  $ new equilibrium phase for aln#01
create-new-phase vn e                                   $ new equilibrium phase for vn#01
create-new-phase vc e                                   $ new equilibrium phase for vc#01
create-new-phase nbn e                                  $ new equilibrium phase for nbn#01
create-new-phase nbc e                                  $ new equilibrium phase for nbc#01

create-new-phase aln#01 p                               $ new precipitate phase aln#01_p0 in ferrite
set-precipitation-parameter aln#01_p0 c npc             $use variable npc for number of prec. classes
set-precipitation-parameter aln#01_p0 d ferrite         $ferrite is precipitation domain
set-precipitation-parameter aln#01_p0 n s g             $nucleation sites are grain boundaries
set-precipitation-parameter aln#01_p0 i y               $use calculated interfacial energy (CIE)
set-precipitation-parameter aln#01_p0 z y               $use automatic size correction for CIE
set-precipitation-parameter aln#01_p0 s g (10^(12-0,01*T$C))  $ratio between diffusion at gb and bulk
set-precipitation-parameter aln#01_p0 s n (10^(12-0,01*T$C))  $ratio between diffusion at gb and bulk

create-new-phase aln#01 p                               $new precipitate phase aln#01_p1 in ferrite
set-precipitation-parameter aln#01_p1 c npc             $use variable npc for number of prec. classes
set-precipitation-parameter aln#01_p1 d ferrite         $ferrite is precipitation domain
set-precipitation-parameter aln#01_p1 n s d             $nucleation sites are dislocations
set-precipitation-parameter aln#01_p1 i y               $use calculated interfacial energy (CIE)
set-precipitation-parameter aln#01_p1 z y               $use automatic size correction for CIE
set-precipitation-parameter aln#01_P1 t m n 0,19        $use volumetric misfit between prec./matrix
                                                        $use 0.27 instead 0.19 for MC versions ≤ 5.40
set-precipitation-parameter aln#01_p1 n f y             $take into account volume misfit in nucleation

create-new-phase vn#01 p                                $ new precipitate phase vn#01_p0 in ferrite
set-precipitation-parameter vn#01_p0 c npc              $use variable npc for number of prec. classes
set-precipitation-parameter vn#01_p0 d ferrite          $ferrite is precipitation domain
set-precipitation-parameter vn#01_p0 n s d              $nucleation sites are dislocations
set-precipitation-parameter vn#01_p0 i y                $use calculated interfacial energy (CIE)
set-precipitation-parameter vn#01_p0 z y                $use automatic size correction for CIE

create-new-phase vc#01 p                                $new precipitate phase vc#01_p0 in ferrite
set-precipitation-parameter vc#01_p0 c npc              $use variable npc for number of prec. classes
set-precipitation-parameter vc#01_p0 d ferrite          $ferrite is precipitation domain
set-precipitation-parameter vc#01_p0 n s d              $nucleation sites are dislocations
set-precipitation-parameter vc#01_p0 i y                $use calculated interfacial energy (CIE)
set-precipitation-parameter vc#01_p0 z y                $use automatic size correction for CIE

create-new-phase nbn#01 p                               $ new precipitate phase nbn#01_p0 in ferrite
set-precipitation-parameter nbn#01_p0 c npc             $use variable npc for number of prec. classes
set-precipitation-parameter nbn#01_p0 d ferrite         $ferrite is precipitation domain
set-precipitation-parameter nbn#01_p0 n s d             $nucleation sites are dislocations
set-precipitation-parameter nbn#01_p0 i y               $use calculated interfacial energy (CIE)
set-precipitation-parameter nbn#01_p0 z y               $use automatic size correction for CIE

create-new-phase nbc#01 p                               $new precipitate phase nbc#01_p0 in ferrite
set-precipitation-parameter nbc#01_p0 c npc             $use variable npc for number of prec. classes
set-precipitation-parameter nbc#01_p0 d ferrite         $ferrite is precipitation domain
set-precipitation-parameter nbc#01_p0 n s d             $nucleation sites are dislocations
set-precipitation-parameter nbc#01_p0 i y               $use calculated interfacial energy (CIE)
set-precipitation-parameter nbc#01_p0 z y               $use automatic size correction for CIE

create-new-phase m7c3 p                                 $new precipitate phase m7c3_p0 in ferrite
set-precipitation-parameter m7c3_p0 c npc               $use variable npc for number of prec. classes
set-precipitation-parameter m7c3_p0 d ferrite           $ferrite is precipitation domain
```

```
set-precipitation-parameter m7c3_p0 n s d          $nucleation sites are dislocations
set-precipitation-parameter m7c3_p0 i y            $use calculated interfacial energy (CIE)
set-precipitation-parameter m7c3_p0 z y            $use automatic size correction for CIE

create-new-phase m23c6 p                           $ new precipitate phase m23c6_p0 in ferrite
set-precipitation-parameter m23c6_p0 c npc         $use variable npc for number of prec. classes
set-precipitation-parameter m23c6_p0  d ferrite    $ferrite is precipitation domain
set-precipitation-parameter m23c6_p0  n s d        $nucleation sites are dislocations
set-precipitation-parameter m23c6_p0  i y          $use calculated interfacial energy (CIE)
set-precipitation-parameter m23c6_p0  z y          $use automatic size correction for CIE

create-new-phase Cr2N p                            $new precipitate phase m23c6_p0 in ferrite
set-precipitation-parameter Cr2N_p0 c npc          $use variable npc for number of prec. classes
set-precipitation-parameter Cr2N_p0  d ferrite     $ferrite is precipitation domain
set-precipitation-parameter Cr2N_p0  n s d         $nucleation sites are dislocations
set-precipitation-parameter Cr2N_p0  i y           $use calculated interfacial energy (CIE)
set-precipitation-parameter Cr2N_p0  z y           $use automatic size correction for CIE

create-new-phase cementite p                       $cnew precipitate phase cementite in ferrite
set-precipitation-parameter cementite_p0 c npc     $use variable npc for number of prec. classes
set-precipitation-parameter cementite_p0 d ferrite $ferrite is precipitation domain
set-precipitation-parameter cementite_p0 n s d     $nucleation sites are dislocations
set-precipitation-parameter cementite_p0 n c o     $nucleus composition: ortho-equilibrium
set-precipitation-parameter cementite_p0 i y       $use calculated interfacial energy (CIE)
set-precipitation-parameter cementite_p0 z y       $use automatic size correction for CIE

$ ********************************************************************************************************
$ ************************************** SIMULATION SETUP ************************************************
$ ********************************************************************************************************

set-temperature-celsius 1000                       $define something
set-automatic-startvalues                          $initiate equilibrium calculation
calc-equilibrium                                   $calculate equilibrium state
set-simulation-parameter e 1e24                    $set simulation end time
set-simulation-parameter t h ht 10                 $T-control from defined heat treatment
set-simulation-parameter s r                       $simulation starting conditions: reset

$ ********************************************************************************************************
$ ********************************** OUTPUT WINDOWS, PLOTS, ETC. *****************************************
$ ********************************************************************************************************

new-gui-window p1                                  $gernerate new plot: temperature
                                                   $define values for default x-axis
set-gui-window-property . x stepvalue              $default x-axis variable (time)
set-gui-window-property . s u y                    $use default x-axis for all plots: yes
set-gui-window-property . s t time / s             $default x-axis title
set-gui-window-property . s f 1                    $scaling factor is 1
set-plot-option . s n b t$c                        $add series: temperature
set-plot-option . s m -1 t$c T                     $define series legend
set-plot-option . a y 1 t temperture / °C          $y-axis title
set-plot-option . l n                              $no legend

create-new-plot x .                                $create new plot: phase fractions
set-plot-option . s n b f$aln_p0                   $add series: phase fraction aln_p0
set-plot-option . s m -1 f$aln_p0 AlN(gamma,gb)    $rename phase aln_p0 to AlN(gamma,gb)
set-plot-option . s n b f$aln_p1                   $add series: phase fraction aln_p1
set-plot-option . s m -1 f$aln_p1 AlN(gamma,d)     $rename phase aln_p1 to AlN(gamma,d)
set-plot-option . s n b f$vn_p0                    $add series: phase fraction vn_p0
set-plot-option . s m -1 f$vn_p0 VN(gamma)         $rename phase vn_p0 to VN(gamma)
set-plot-option . s n b f$vc_p0                    $add series: phase fraction vc_p0
```

```
set-plot-option . s m -1 f$vc_p0 VC(gamma)                                                    $rename phase vc_p0 to VC(gamma)
set-plot-option . s n b f$nbn_p0                                                              $add series: phase fraction nbn_p0
set-plot-option . s m -1 f$nbn_p0 NbN(gamma)                                                  $rename phase nbn_p0 to NbN(gamma)
set-plot-option . s n b f$nbc_p0                                                              $add series: phase fraction nbc_p0
set-plot-option . s m -1 f$nbc_p0 NbC(gamma)                                                  $rename phase nbc_p0 to NbC(gamma)
set-plot-option . s n b f$aln#01_p0                                                           $add series: phase fraction aln#01_p0
set-plot-option . s m -1 f$aln#01_p0 AlN(alpha,gb)                                            $rename phase aln#01_p0 to AlN(alpha,gb)
set-plot-option . s n b f$aln#01_p1                                                           $add series: phase fraction aln#01_p1
set-plot-option . s m -1 f$aln#01_p1 AlN(alpha,d)                                             $rename phase aln#01_p1 to AlN(alpha,d)
set-plot-option . s n b f$vn#01_p0                                                            $add series: phase fraction vn#01_p0
set-plot-option . s m -1 f$vn#01_p0 VN(alpha)                                                 $rename phase vn#01_p0 to VN(alpha)
set-plot-option . s n b f$vc#01_p0                                                            $add series: phase fraction vc#01_p0
set-plot-option . s m -1 f$vc#01_p0 VC(alpha)                                                 $rename phase vc#01_p0 to VC(alpha)
set-plot-option . s n b f$nbn#01_p0                                                           $add series: phase fraction nbn#01_p0
set-plot-option . s m -1 f$nbn#01_p0 NbN(alpha)                                               $rename phase nbn#01_p0 to NbN(alpha)
set-plot-option . s n b f$nbc#01_p0                                                           $add series: phase fraction nbc#01_p0
set-plot-option . s m -1 f$nbc#01_p0 NbC(alpha)                                               $rename phase nbc#01_p0 to NbC(alpha)
set-plot-option . s n b f$m23c6_p0                                                            $add series: phase fraction m23c6_p0
set-plot-option . s m -1 f$m23c6_p0 M<sub>23</sub>C<sub>6</sub>(alpha)                        $rename phase m23c6_p0 to M23C6(alpha)
set-plot-option . s n b f$m7c3_p0                                                             $add series: phase fraction m7c3_p0
set-plot-option . s m -1 f$m7c3_p0 M<sub>7</sub>C<sub>3</sub>(alpha)                          $rename phase m7c3_p0 to M7C3(alpha)
set-plot-option . s n b f$Cr2N_p0                                                             $add series: phase fraction cr2n_p0
set-plot-option . s m -1 f$Cr2N_p0 Cr<sub>2</sub>N(alpha)                                     $rename phase cr2n_p0 to Cr2N(alpha)
set-plot-option . s n b f$cementite_p0                                                        $add series: phase fraction cementite_p0
set-plot-option . s m -1 f$cementite_p0 Cementite(alpha)                                      $rename phase cementite_p0 to Cem. (alpha)
set-plot-option . a y 1 t phase fraction                                                      $change y-axis title
set-plot-option . a y 1 y log                                                                 $use logarithmic scale for y-axis
set-plot-option . a y 1 s 1e-8..                                                              $scale the y-axis from 1e-8..
set-plot-option . l b                                                                         $show legend at the bottom of the figure

create-new-plot x .                                                                           $create new plot: mean radii
set-plot-option . s n b r_mean$aln_p0                                                         $add series: mean radius aln_p0
set-plot-option . s m -1 r_mean$aln_p0 AlN(gamma,gb)                                          $rename phase aln_p0 to AlN(gamma,gb)
set-plot-option . s n b r_mean$aln_p1                                                         $add series: mean radius aln_p1
set-plot-option . s m -1 r_mean$aln_p1 AlN(gamma,d)                                           $rename phase aln_p1 to AlN(gamma,d)
set-plot-option . s n b r_mean$vn_p0                                                          $add series: mean radius vn_p0
set-plot-option . s m -1 r_mean$vn_p0 VN(gamma)                                               $rename phase vn_p0 to VN(gamma)
set-plot-option . s n b r_mean$vc_p0                                                          $add series: mean radius vc_p0
set-plot-option . s m -1 r_mean$vc_p0 VC(gamma)                                               $rename phase vc_p0 to VC(gamma)
set-plot-option . s n b r_mean$nbn_p0                                                         $add series: mean radius nbn_p0
set-plot-option . s m -1 r_mean$nbn_p0 NbN(gamma)                                             $rename phase nbn_p0 to NbN(gamma)
set-plot-option . s n b r_mean$nbc_p0                                                         $add series: mean radius nbc_p0
set-plot-option . s m -1 r_mean$nbc_p0 NbC(gamma)                                             $rename phase nbc_p0 to NbC(gamma)
set-plot-option . s n b r_mean$aln#01_p0                                                      $add series: mean radius aln#01_p0
set-plot-option . s m -1 r_mean$aln#01_p0 AlN(alpha,gb)                                       $rename phase aln#01_p0 to AlN(alpha,gb)
set-plot-option . s n b r_mean$aln#01_p1                                                      $add series: mean radius aln#01_p1
set-plot-option . s m -1 r_mean$aln#01_p1 AlN(alpha,d)                                        $rename phase aln#01_p1 to AlN(alpha,d)
set-plot-option . s n b r_mean$vn#01_p0                                                       $add series: mean radius vn#01_p0
set-plot-option . s m -1 r_mean$vn#01_p0 VN(alpha)                                            $rename phase vn#01_p0 to VN(alpha)
set-plot-option . s n b r_mean$vc#01_p0                                                       $add series: mean radius vc#01_p0
set-plot-option . s m -1 r_mean$vc#01_p0 VC(alpha)                                            $rename phase vc#01_p0 to VC(alpha)
set-plot-option . s n b r_mean$nbn#01_p0                                                      $add series: mean radius nbn#01_p0
set-plot-option . s m -1 r_mean$nbn#01_p0 NbN(alpha)                                          $rename phase nbn#01_p0 to NbN(alpha)
set-plot-option . s n b r_mean$nbc#01_p0                                                      $add series: mean radius nbc#01_p0
set-plot-option . s m -1 r_mean$nbc#01_p0 NbC(alpha)                                          $rename phase nbc#01_p0 to NbC(alpha)
set-plot-option . s n b r_mean$m23c6_p0                                                       $add series: mean radius m23c6_p0
set-plot-option . s m -1 r_mean$m23c6_p0 M<sub>23</sub>C<sub>6</sub>(alpha)
set-plot-option . s n b r_mean$m7c3_p0                                                        $add series: mean radius m7c3_p0
set-plot-option . s m -1 r_mean$m7c3_p0 M<sub>7</sub>C<sub>3</sub>(alpha)
set-plot-option . s n b r_mean$Cr2N_p0                                                        $add series: mean radius cr2n_p0
```

```
set-plot-option . s m -1 r_mean$Cr2N_p0 Cr<sub>2</sub>N(alpha)        $rename phase cr2n_p0 to Cr2N(alpha)
set-plot-option . s n b r_mean$cementite_p0                          $add series: mean radius cementite_p0
set-plot-option . s m -1 r_mean$cementite_p0 Cementite(alpha)        $rename phase cementite_p0 to Cem.(alpha)
set-plot-option . a y 1 t mean radius / nm                           $change y-axis title
set-plot-option . a y 1 y log                                        $use logarithmic scale for y-axis
set-plot-option . a y 1 f 1e9                                        $scaling factor is 1e9
set-plot-option . l b                                                $show legend at the bottom of the figure

create-new-plot x .                                                  $create new plot: number densities
set-plot-option . s n b num_part$aln_p0                              $add series: number density aln_p0
set-plot-option . s m -1 num_part$aln_p0 AlN(gamma,gb)               $rename phase aln_p0 to AlN(gamma,gb)
set-plot-option . s n b num_part$aln_p1                              $add series: number density aln_p1
set-plot-option . s m -1 num_part$aln_p1 AlN(gamma,d)                $rename phase aln_p1 to AlN(gamma,d)
set-plot-option . s n b num_part$vn_p0                               $add series: number density vn_p0
set-plot-option . s m -1 num_part$vn_p0 VN(gamma)                    $rename phase vn_p0 to VN(gamma)
set-plot-option . s n b num_part$vc_p0                               $add series: number density vc_p0
set-plot-option . s m -1 num_part$vc_p0 VC(gamma)                    $rename phase vc_p0 to VC(gamma)
set-plot-option . s n b num_part$nbn_p0                              $add series: number density nbn_p0
set-plot-option . s m -1 num_part$nbn_p0 NbN(gamma)                  $rename phase nbn_p0 to NbN(gamma)
set-plot-option . s n b num_part$nbc_p0                              $add series: number density nbc_p0
set-plot-option . s m -1 num_part$nbc_p0 NbC(gamma)                  $rename phase nbc_p0 to NbC(gamma)
set-plot-option . s n b num_part$aln#01_p0                           $add series: number density aln#01_p0
set-plot-option . s m -1 num_part$aln#01_p0 AlN(alpha,gb)            $rename phase aln#01_p0 to AlN(alpha,gb)
set-plot-option . s n b num_part$aln#01_p1                           $add series: number density aln#01_p1
set-plot-option . s m -1 num_part$aln#01_p1 AlN(alpha,d)             $rename phase aln#01_p1 to AlN(alpha,d)
set-plot-option . s n b num_part$vn#01_p0                            $add series: number density vn#01_p0
set-plot-option . s m -1 num_part$vn#01_p0 VN(alpha)                 $rename phase vn#01_p0 to VN(alpha)
set-plot-option . s n b num_part$vc#01_p0                            $add series: number density vc#01_p0
set-plot-option . s m -1 num_part$vc#01_p0 VC(alpha)                 $rename phase vc#01_p0 to VC(alpha)
set-plot-option . s n b num_part$nbn#01_p0                           $add series: number density nbn#01_p0
set-plot-option . s m -1 num_part$nbn#01_p0 NbN(alpha)               $rename phase nbn#01_p0 to NbN(alpha)
set-plot-option . s n b num_part$nbc#01_p0                           $add series: number density nbc#01_p0
set-plot-option . s m -1 num_part$nbc#01_p0 NbC(alpha)               $rename phase nbc#01_p0 to NbC(alpha)
set-plot-option . s n b num_part$m23c6_p0                            $add series: number density m23c6_p0
set-plot-option . s m -1 num_part$m23c6_p0 M<sub>23</sub>C<sub>6</sub>(alpha)
set-plot-option . s n b num_part$m7c3_p0                             $add series: number density m7c3_p0
set-plot-option . s m -1 num_part$m7c3_p0 M<sub>7</sub>C<sub>3</sub>(alpha)
set-plot-option . s n b num_part$Cr2N_p0                             $add series: number density cr2n_p0
set-plot-option . s m -1 num_part$Cr2N_p0 Cr<sub>2</sub>N(alpha)     $rename phase cr2n_p0 to Cr2N(alpha)
set-plot-option . s n b num_part$cementite_p0                        $add series: number density cementite_p0
set-plot-option . s m -1 num_part$cementite_p0 Cementite(alpha)      $rename phase cementite_p0 to Cem.(alpha)
set-plot-option . a y 1 t number density / m<sup>-3</sup>            $change y-axis title
set-plot-option . a y 1 y log                                        $use logarithmic scale for y-axis
set-plot-option . a y 1 s 1..                                        $scale the y-axis from 1..
set-plot-option . l b                                                $show legend at the bottom of the figure

move-gui-window . 10 10 600 1000                                     $move window to new position and resize
update-gui-window .                                                  $update the GUI window

$ ------------------------------------------------------------------------ HISTOGRAMM ------------------------------------------------------------------------

new-gui-window p5                                                    $new precipitation distribution plot window

                                                                     $precipitate distribution AlN
set-plot-option . s n p aln_p0                                       $add series: precipitate distribution aln_p0
set-plot-option . s m -1 aln_p0 AlN(gamma,gb)                        $rename phase aln_p0 to AlN(gamma,gb)
set-plot-option . s n p aln_p1                                       $add series: precipitate distribution aln_p1
set-plot-option . s m -1 aln_p1 AlN(gamma,d)                         $rename phase aln_p1 to AlN(gamma,d)
set-plot-option . s n p aln#01_p0                                    $add series: precipitate distr. aln#01_p0
set-plot-option . s m -1 aln#01_p0 AlN(alpha,gb)                     $rename phase aln#01_p0 to AlN(alpha,gb)
```

```
set-plot-option . s n p aln#01_p1                    $add series: precipitate distr. aln#01_p1
set-plot-option . s m -1 aln#01_p1 AlN(alpha,d)      $rename phase aln#01_p1 to AlN(alpha,d)
set-plot-option . a x 1 f 1e9                        $use scaling factor 1e9 for x-axis
set-plot-option . a y 1 s 1e10..1e20                 $scale the y-axis from 1e10..1e20
set-plot-option . a y 1 y log                        $use logarithmic scale for y-axis
set-plot-option . a x 1 t radius / nm                $change x-axis title
set-plot-option . a x 1 s 1..500                     $scale the x-axis from 1..500
set-plot-option . a x 1 y log                        $use logarithmic scale for x-axis
set-plot-option . a y 1 t number density             $change y-axis title

create-new-plot p .                                  $create new plot: precipitate distribution VN
set-plot-option . s n p vn_p0                        $add series: precipitate distribution vn_p0
set-plot-option . s m -1 vn_p0 VN(gamma)             $rename phase vn_p0 to VN(gamma)
set-plot-option . s n p vn#01_p0                     $add series: precipitate distribution vn#01_p0
set-plot-option . s m -1 vn#01_p0 VN(alpha)          $rename phase vn#01_p0 to VN(alpha)
set-plot-option . a x 1 f 1e9                        $use scaling factor 1e9 for x-axis
set-plot-option . a y 1 s 1e10..1e20                 $scale the y-axis from 1e10..1e20
set-plot-option . a y 1 y log                        $use logarithmic scale for y-axis
set-plot-option . a x 1 t radius / nm                $change x-axis title
set-plot-option . a x 1 s 1..500                     $scale the x-axis from 1..500
set-plot-option . a x 1 y log                        $use logarithmic scale for x-axis
set-plot-option . a y 1 t number density             $change y-axis title

create-new-plot p .                                  $create new plot: precipitate distribution VC
set-plot-option . s n p vc_p0                        $add series: precipitate distribution vc_p0
set-plot-option . s m -1 vc_p0 VC(gamma)             $rename phase vc_p0 to VC(gamma)
set-plot-option . s n p vc#01_p0                     $add series: precipitate distribution vc#01_p0
set-plot-option . s m -1 vc#01_p0 VC(alpha)          $rename phase vc#01_p0 to VC(alpha)
set-plot-option . a x 1 f 1e9                        $use scaling factor 1e9 for x-axis
set-plot-option . a y 1 s 1e10..1e20                 $scale the y-axis from 1e10..1e20
set-plot-option . a y 1 y log                        $use logarithmic scale for y-axis
set-plot-option . a x 1 t radius / nm                $change x-axis title
set-plot-option . a x 1 s 1..500                     $scale the x-axis from 1..500
set-plot-option . a x 1 y log                        $use logarithmic scale for x-axis
set-plot-option . a y 1 t number density             $change y-axis title

create-new-plot p .                                  $create new plot: precipitate distribution NbN
set-plot-option . s n p nbn_p0                       $add series: precipitate distribution nbn_p0
set-plot-option . s m -1 nbn_p0 NbN(gamma)           $rename phase nbn_p0 to NbN(gamma)
set-plot-option . s n p nbn#01_p0                    $add series: precipitate distr. nbn#01_p0
set-plot-option . s m -1 nbn#01_p0 NbN(alpha)        $rename phase nbn#01_p0 to NbN(alpha)
set-plot-option . a x 1 f 1e9                        $use scaling factor 1e9 for x-axis
set-plot-option . a y 1 s 1e10..1e20                 $scale the y-axis from 1e10..1e20
set-plot-option . a y 1 y log                        $use logarithmic scale for y-axis
set-plot-option . a x 1 t radius / nm                $change x-axis title
set-plot-option . a x 1 s 1..500                     $scale the x-axis from 1..500
set-plot-option . a x 1 y log                        $use logarithmic scale for x-axis
set-plot-option . a y 1 t number density             $change y-axis title

create-new-plot p .                                  $create new plot: precipitate distribution NbC
set-plot-option . s n p nbc_p0                       $add series: precipitate distribution nbc_p0
set-plot-option . s m -1 nbc_p0 NbC(gamma)           $rename phase nbn_p0 to NbC(gamma)
set-plot-option . s n p nbc#01_p0                    $add series: precipitate distr. nbc#01_p0
set-plot-option . s m -1 nbc#01_p0 NbC(alpha)        $rename phase nbc#01_p0 to NbC(alpha)
set-plot-option . a x 1 f 1e9                        $use scaling factor 1e9 for x-axis
set-plot-option . a y 1 s 1e10..1e20                 $scale the y-axis from 1e10..1e20
set-plot-option . a y 1 y log                        $use logarithmic scale for y-axis
set-plot-option . a x 1 t radius / nm                $change x-axis title
set-plot-option . a x 1 s 1..500                     $scale the x-axis from 1..500
set-plot-option . a x 1 y log                        $use logarithmic scale for x-axis
```

```
set-plot-option . a y 1 t number density                    $change y-axis title

move-gui-window . 615 10 400 1000                           $move window to new position and resize
update-gui-window . $ Update the GUI window                 $update the GUI window

$ ************************************************************************************************
$ ************************************ START PRECIPITATE SIMULATION ******************************
$ ************************************************************************************************

start-precipitate-simulation

$ ************************************************************************************************
$ ************************************ PRECIPITATE SIMULATION FINISHED ***************************
$ ************************************************************************************************
```

B Additional Selected Scientific Investigations carried out from 2007 to 2010

Beside the numerical analysis of the precipitation kinetics of nitrides and carbides in microalloyed steel, the author of the present thesis carried out additional scientific investigations during his time as a PhD student at the Christian Doppler Laboratory 'Early Stages of Precipitation'.

Particularly, the precipitation kinetics of γ' and δ phases in nickel-based superalloys is of great scientific interest. Therefore detailed investigations are performed on the precipitation process of these phases in the commercial nickel-based superalloys UDIMET 720 Li and ATI Allvac®718Plus™, see appendix B1 to B4.

Furthermore, the precipitation kinetics of NiAl particles is studied along with the formation of reverted austenite in a PH 13-8 Mo maraging steel, see appendix B5.

In the following, these additional scientific investigations are presented, which are also published in international accepted journals.

B.1 R. Radis, M. Schaffer, M. Albu, G. Kothleitner, P. Pölt and E. Kozeschnik. Multi-Modal Size Distributions of γ' Precipitates During Continuous Cooling of UDIMET 720 Li. *Acta Materialia*, 57:5739-5747, 2009.

Available online at www.sciencedirect.com
ScienceDirect
Acta Materialia 57 (2009) 5739–5747
Acta MATERIALIA
www.elsevier.com/locate/actamat

Multimodal size distributions of γ′ precipitates during continuous cooling of UDIMET 720 Li

R. Radis [a,b,*], M. Schaffer [c], M. Albu [c], G. Kothleitner [c], P. Pölt [c], E. Kozeschnik [a,d,e]

[a] Christian Doppler Laboratory for "Early Stages of Precipitation", Vienna University of Technology, Favoritenstraße 9-11, A-1040 Vienna, Austria
[b] Institute for Materials Science and Welding, Graz University of Technology, Kopernikusgasse 24, A-8010 Graz, Austria
[c] Research Institute for Electron Microscopy, Graz University of Technology, Steyrergasse 17, A-8010 Graz, Austria
[d] Materials Center Leoben Forschung GmbH, Roseggerstraße 12, A-8700 Leoben, Austria
[e] Institute of Materials Science and Technology, Vienna University of Technology, Favoritenstraße 9-11, A-1040 Vienna, Austria

Received 27 March 2009; received in revised form 12 June 2009; accepted 3 August 2009
Available online 4 September 2009

Abstract

The technological properties of many nickel-based superalloys originate in the morphology and distribution of $Ni_3(Al, Ti)$ particles (γ′ precipitates). Starting from the solution-annealed condition, the distribution and the morphology of γ′ precipitates are investigated experimentally during continuous cooling of the nickel-base superalloy UDIMET 720 Li. Characterization of the precipitates is carried out by scanning electron microscopy and energy-filtered transmission electron microscopy investigations. Depending on cooling rate, monomodal, bimodal and even trimodal size distributions are observed. The experimental observations of the size distributions are confirmed by numerical simulations of the γ′ precipitation kinetics. The theoretical background for occurrence of multimodal size distributions during continuous cooling is discussed.

Keywords: Multimodal; Nickel alloy; Precipitation; Nucleation and growth; Phase transformation kinetics

1. Introduction

The term superalloy is generally used for a large number of different alloys. A major motivation for development of these materials is their applicability for gas turbines in aircraft and power plants. To achieve a high degree of efficiency, these machines operate at elevated temperatures. Usually, Ni-base superalloys combine high strength and good corrosion resistance, which are essential for application in modern gas turbine aero-engines, e.g. for high-speed rotating components, such as high-pressure turbine disks.

Good control of the technological properties of these alloys is inherently related to the control of precipitation of the large amount of finely dispersed, coherent L_{12}-ordered $Ni_3(Al, Ti)$ particles (γ′ precipitates), which provide a large amount of strengthening via precipitation hardening. Depending on the cooling rate, the shape of these particles varies over a wide range, from simple spheres over cubes and octocubes to complex structures, such as octodendrites and dendrites. This large variety of dissimilar morphologies [1–12] caused by the γ/γ′ lattice mismatch [13] is well known.

It is also well known that bimodal distributions of γ′ precipitates in a γ matrix can lead to superior properties in terms of thermomechanical processing [14–16]. Coarse γ′ precipitates located on grain boundaries prevent the growth of γ grains during homogenization heat treatment. A second γ′ population, significantly smaller than the first, precipitates intergranularly on cooling and is responsible for the observed high strength of these alloys. Multimodal microstructures are usually achieved by special multistage

* Corresponding author. Address: Institute for Materials Science and Welding, Graz University of Technology, Kopernikusgasse 24, A-8010 Graz, Austria. Tel.: +43 316 873 4304; fax: +43 316 873 7187.
E-mail address: rene.radis@tugraz.at (R. Radis).

1359-6454/$36.00 © 2009 Acta Materialia Inc. Published by Elsevier Ltd. All rights reserved.
doi:10.1016/j.actamat.2009.08.002

heat treatments, which are generally complex and costly. Some authors have already shown that such bimodal size distributions of γ′ precipitates can also be achieved by two γ′ nucleation bursts during continuous cooling from the solution-annealed state [17–24]. Thereby, the individual particle populations precipitate at different temperatures and from different chemical compositions of the γ matrix.

Similar to the present investigations, Mao et al. [22] have explored the evolution of bimodal γ′ precipitate size distributions during continuous cooling in UDIMET 720 Li. Unfortunately, their experimental methods have concentrated on scanning electron microscopy (SEM) investigations only, and thus did not capture the finer γ′ precipitates formed at higher cooling rates. Nevertheless, these authors have recommended performing further investigations using high-resolution transmission electron microscopy (TEM).

In the present work, experimental investigations using high-resolution techniques as well as theoretical simulations using the software MatCalc [25–27] are both applied to investigate the evolution of γ′ precipitates in the Ni-base superalloy UDIMET 720 Li. A series of experiments with varying cooling rates is performed and the results of the experimental investigations are compared to the predictions of the simulation. Furthermore, the theoretical background for the formation of multimodal size distributions of precipitates is presented and confirmed by experimental results, where we have identified monomodal, bimodal and even trimodal γ′ size distributions.

2. Experiments and simulation

2.1. Material and heat treatment

The precipitate microstructure of 13 samples was evaluated qualitatively and quantitatively to determine the precipitate distribution parameters and the morphology of the precipitates. The samples were cut into cylindrical pieces of 10 mm diameter × 10 mm, except for two samples 5 mm diameter × 10 mm to achieve the fastest cooling rates. The samples were soaked at 1180 °C for 6 h (in Refs. [21,22], the super-solvus solution temperature is recommended with approximately $T_{sol} = 1160$ °C) and then quenched into water. SEM analyses have shown that this heat treatment is suitable for achieving solid solution condition and dissolution of all precipitates.

Depending on the cooling rate, which was varied between 78 and 0.00416 K s^{-1}, different equipment was used for heat treatment. The samples with cooling rates higher than 0.217 K s^{-1} were heat-treated in a high-speed quenching dilatometer; the other samples were cooled continuously in an electric furnace. Temperature was controlled with Pt–Pt/Rh 10% (Typ S) thermo couples. The samples were heated to a temperature of 1180 °C under argon atmosphere as fast as possible, kept at this level for 30 min to dissolve precipitates which formed temporarily before reheating, and then cooled continuously to 400 °C at different cooling rates (see Table 1). Finally, they were quenched into water. Afterwards, the distribution and the morphology of precipitates were studied by SEM and energy-filtered transmission electron microscopy (EFTEM) [28,29]. The relevant precipitation parameters were determined using the stereological correction procedure of Sonderegger [30]. In each case, more than 100 precipitates were measured to characterize the distributions. For this correction, SEM penetration depth data were used from Ref. [31]. The chemical composition of UDIMET 720 Li was analyzed by emission spectroscopy. The results are summarized in Table 2.

2.2. Electron microscopy

For the investigation of the morphology and the precipitate size evolution of γ′ precipitates, backscattered electron (BSE) images as well as EFTEM images were recorded. For the SEM investigations, samples with polished cross-sections, treated with different cooling rates from solid solution temperature, were studied by use of a 4-quadrant backscattered electron detector attached to a Zeiss DSM 982 Gemini scanning electron microscope. Electron energies between 7 and 10 keV were used for recording the BSE images.

The EFTEM investigations were carried out on a Philips CM20 scanning TEM (STEM) and a FEI Tecnai F20, both equipped with Gatan imaging filters (GIFs). The microscopes were operated at 200 kV with a LaB_6 cathode and a Schottky field emitter, respectively. The pictures were recorded with the slow scan CCD camera incorporating a GIF with a local resolution of about 1 nm. All images were processed with a Gatan Digital Micrograph, and corrected for drift, dark current and gain variations. Electron energy loss spectroscopy (EELS) and X-ray dispersive spectroscopy (EDX) were used for precipitate analysis.

2.3. Computer simulations

For the theoretical analysis of the precipitation behavior in UDIMET 720 Li, the simulation software MatCalc

Table 1
Continuous cooling rates of the present investigation.

Sample	Cooling rate (K s^{-1})	Cooling time (s)
1	78	1000
2	19.5	4000
3	6.5	12,000
4	3.25	24,000
5	1.625	48,000
6	0.867	90,000
7	0.433	180,000
8	0.217	360,000
9	0.03333	2,340,000
10	0.01667	4,680,000
11	0.00984	7,920,000
12	0.00619	12,600,000
13	0.00416	18,720,000

Table 2
Chemical composition of UDIMET 720 Li in wt.% [32].

Cr	Ni	Co	Mo	Ti	Al	W	Fe	C	Mn	B
15.92	57.6	14.43	2.96	4.96	2.53	1.26	0.09	0.014	0.02	0.014

[25–27] was used. In this approach, the nucleation kinetics of precipitates was calculated from classical nucleation theory (CNT) [33] extended for multicomponent systems [25,34,35]. Accordingly, the transient nucleation rate J is given as:

$$J = N_0 Z \beta^* \cdot \exp\left(\frac{-G^*}{k \cdot T}\right) \cdot \exp\left(\frac{-\tau}{t}\right). \quad (1)$$

J describes the rate at which nuclei are created per unit volume and time. N_0 represents the total number of potential nucleation sites. The Zeldovich factor Z takes into account that the nucleus is destabilized by thermal excitation as compared to the inactivated state, and is given by [33]:

$$Z = \left[\frac{-1}{2\pi kT}\frac{\partial^2 \Delta G}{\partial n^2}\bigg|_{n*}\right]^{\frac{1}{2}}. \quad (2)$$

ΔG represents the total free energy change on nucleus formation, n is the number of atoms in the nucleus, k is the Boltzmann constant and T is temperature. The derivative of ΔG is taken at the critical nucleus size n^*.

The atomic attachment rate β^* takes into account the long-range diffusive transport of atoms, which is needed for nucleus formation if the chemical composition of the matrix is different from the chemical composition of the precipitate. A suitable multicomponent equation for β^* has been derived by Svoboda et al. [25], and is given by:

$$\beta^* = \frac{4\pi\rho^{*2}}{a^4\Omega}\left[\sum_{i=1}^{n}\frac{(c_{ki}-c_{0i})^2}{c_{0i}D_{0i}}\right]^{-1}, \quad (3)$$

where ρ^* is the critical nucleation radius, a is the atomic distance, Ω is the molar volume, c_{ki} and c_{0i} are the element concentrations in precipitate with index k and matrix, respectively, and D_{0i} is the diffusivity of element i in the matrix. The incubation time τ is given by [33]:

$$\tau = \frac{1}{2\beta^* Z^2}, \quad (4)$$

and the critical energy for nucleus formation G^* is:

$$G^* = \frac{16\pi}{3}\frac{\gamma^3}{(\Delta G_{vol})^2}, \quad (5)$$

with the interfacial energy γ and the volume free energy change ΔG_{vol}. The chemical composition of the critical nucleus is assumed to be identical to the equilibrium composition of the γ' phase at the corresponding temperature.

It is important to note that G^* is an essential quantity in nucleation theory, when compared to the other quantities occurring in Eq. (1). G^* contains the cube of the interfacial energy over the square of the volume free energy change ΔG_{vol}. Since G^* appears in the exponent of the nucleation rate Eq. (1), small changes in γ and/or ΔG_{vol} can lead to huge variations in J, particularly if G^* is of the order of kT. In the present case, these quantities change steadily during continuous cooling and in the course of the precipitation reaction, since both are functions of temperature and chemical composition of matrix and precipitate. These interactions are discussed in detail in the following sections.

Once a precipitate is nucleated, its further growth is evaluated based on the evolution equations for the radius and composition of the precipitate derived by Svoboda et al. [25] based on a mean-field approach utilizing the thermodynamic extremal principle. Accordingly, the growth rate $\dot{\rho}_k$ and the rate of change of chemical composition $\dot{c}_{ki}$ of the precipitate with index k are obtained from solution of the linear system of equations:

$$A_{ij}y_j = B_i, \quad (6)$$

where the variable y_j represents the rates $\dot{\rho}_k$ and $\dot{c}_{ki}$, as well as the Lagrange multipliers from the stoichiometry constraints (see Ref. [25]). The index i comprises the variables for radius and chemical composition of the precipitate as well as the stoichiometry boundary conditions implied from the crystal structure of the precipitate phase. The system of Eq. (6) is solved for each precipitate k separately. The full expressions for the coefficients A_{ij} and B_i, as used in the present work, are given in Ref. [27]. The numerical time integration of $\dot{\rho}_k$ and $\dot{c}_{ki}$ is performed in the software MatCalc, based on the classical numerical Kampmann–Wagner approach [36], and is described in detail Ref. [26].

Using this computational approach, a series of calculations for various cooling rates was carried out and compared with the experiments. Finally, two parameter studies investigated the sensitivity of the simulation results to the input data, i.e. to the independent thermodynamic and diffusion databases [37,38], which were used for our calculations.

3. Results and discussion

3.1. Precipitate morphology

The γ' precipitates observed in this study appear in shapes ranging from simple spheres to cubes and octocubes to rather complex structures such as octodendrites and dendrites. This structural transition is mainly driven by the lattice mismatch between precipitate and matrix [2]. This phenomenon is well known and has been investigated several times (e.g. [1,2,21]). Depending on the cooling rate, which was varied between 78 and 0.0042 K s^{-1}, different morphologies of γ' precipitates in UDIMET 720 Li are observed. Corresponding micrographs are shown in

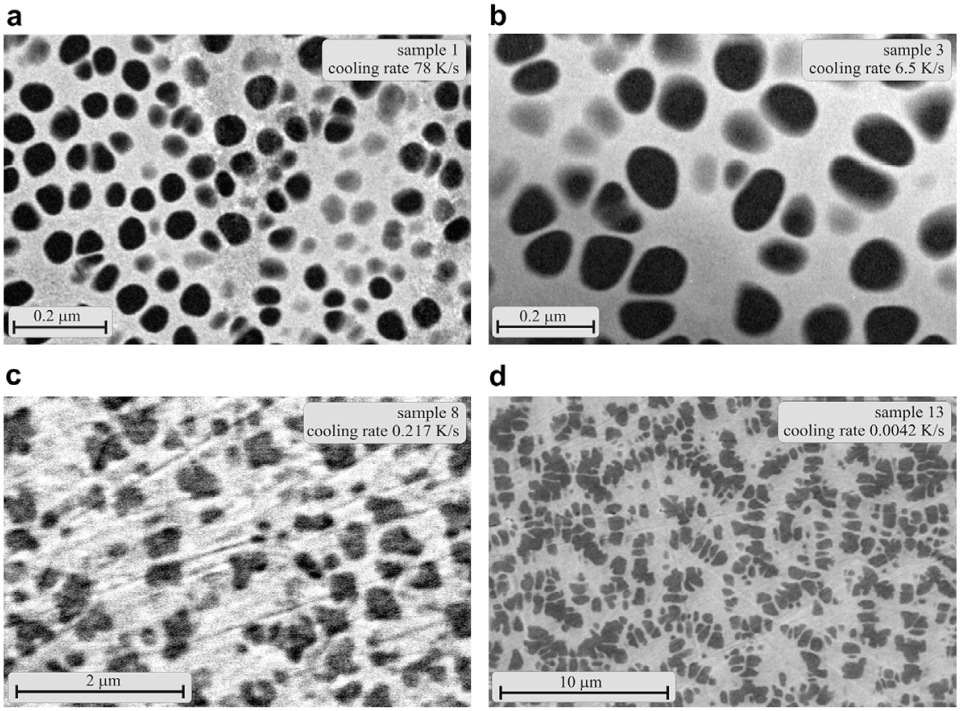

Fig. 1. Morphologies of γ' precipitates in UDIMET 720 Li depending on cooling rate. (a and b) EFTEM (Cr-map) images; (c and d) SEM (BSE) images.

Fig. 1a and b representing EFTEM (Cr maps) images and Fig. 1c and d SEM (BSE) investigations.

Fig. 1a shows the precipitates that form during cooling from 1180 to 400 °C at a rate of 78 K s^{-1}. The shape of these particles is spherical or nearly spherical. On decreasing the cooling rate, an increase of precipitate sizes is observed (Fig. 1b) and the precipitate shapes become more and more irregular. Fig. 1c shows several non-spherical, faceted and sometimes even cuboidal particles. Finally, at the lowest cooling rates, the precipitate–matrix phase boundaries become incoherent [2] and the precipitate shape resembles that of dendrites (Fig. 1d).

Table 3
Measured and stereologically corrected [30] precipitate sizes.

Sample	Cooling rate (K s^{-1})	d_{mean} (nm)	
		Measured	Corrected
1	78	049.4	053.2
2	19.5	058.6	063.8
3	6.5	092.5	098.7
4	3.25	149.6	159.8
5	1.625	165.8	186.4
6	0.867	258.4	278.9
7	0.433	319.0	347.9
8	0.217	379.9	393.5

3.2. Precipitate size evolution

Samples 1–8 (spherical or nearly spherical precipitates) are characterized quantitatively with regard to the mean diameter and the precipitate size distribution. Since the determination of sizes and size distributions of precipitates with non-spherical morphologies is difficult, the quantitative analysis concentrates on samples with a mean precipitate diameter of less than 0.7 µm and close to spherical precipitate shapes. This size limit is well established in literature (e.g. [39]). The measured and corrected mean diameters of the initial population are summarized in Table 3.

In addition to the SEM investigations, the samples are further analyzed with high-resolution EFTEM. Fig. 2 shows a typical example of a second population of smaller precipitates located in the channels between large particles with cubic cross-sections observed after continuous cooling at a rate of 0.217 K s^{-1}. Fig. 3 shows an example of a trimodal size distribution observed after continuous cooling at a rate of 0.0167 K s^{-1}. Next to some octocube precipitates, smaller precipitates of a second population are visible (lower right corner of Fig. 3a). Further magnification of this region reveals the existence of a third precipitate population with even smaller precipitate sizes (Fig. 3b).

3.3. Formation of multimodal size distributions during continuous cooling

Precipitation is commonly considered as occurring in three stages: nucleation, growth, and coarsening. In the

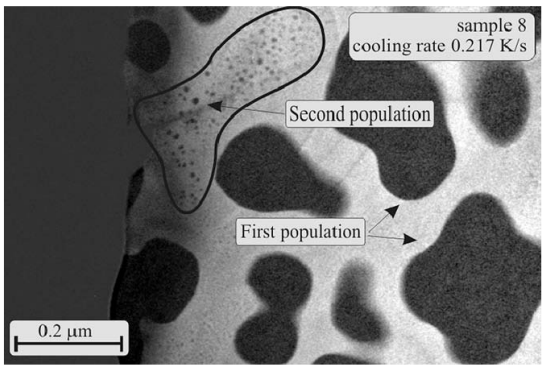

Fig. 2. Bimodal size distribution of γ′ precipitates in Udimet 720 Li (EFTEM (Cr-map) image).

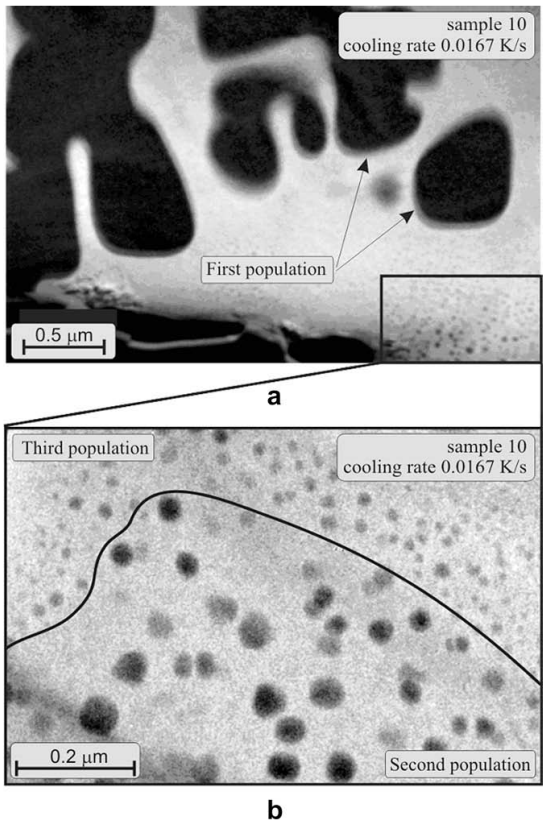

Fig. 3. Multimodal size distribution of γ′ precipitates in Udimet 720 Li (EFTEM (Cr-map) image).

nucleation stage, nuclei of a precipitate phase are formed, usually under the assumption that the matrix composition remains unchanged by this event. Simultaneously, growth of the existing precipitates takes place, depleting the matrix of precipitate-forming solute atoms. Thus, the volume free energy change ΔG_{vol} continuously decreases and the nucleation process comes to a stop (Eqs. (1) and (5)). At this point, the total precipitate density can be obtained from time integration of the nucleation rate J. Continued growth of the precipitates evolves the system into a state close to equilibrium, after which further evolution is driven by the minimization of the total precipitate surface area. This last step is known as coarsening or Ostwald ripening. When comparing precipitation in a continuous cooling regime with isothermal treatment, substantial differences between the two exist. In the case of isothermal aging, supersaturation has a maximum in the beginning of the reaction, after which it steadily decreases during the further process. One of the consequences of this observation is that size distributions observed after isothermal aging are generally monomodal.

In continuous cooling, treatment commonly starts above the solution temperature of the precipitate phase and progresses with a steady reduction in temperature. Below the solution temperature, the volume free energy change ΔG_{vol} continuously increases. At some undercooling, ΔG_{vol} reaches a value at which the nucleation barrier G^* is sufficiently low to render nucleation possible. Since the nucleation rate J is relatively low in this initial stage, the number density of nuclei is rather low, and the distance between the individual precipitates is wide. Fig. 4a schematically shows a sparse distribution of precipitates developed at low undercooling.

Simultaneously with the nucleation of further precipitates, the existing precipitates grow by diffusional transport of atoms towards the precipitates. Depending on the mobility of the atoms and the time available for diffusion as a function of cooling rate, each precipitate can be assigned a characteristic diffusion field, which denotes the region where solute atoms can be gathered. Similar to the

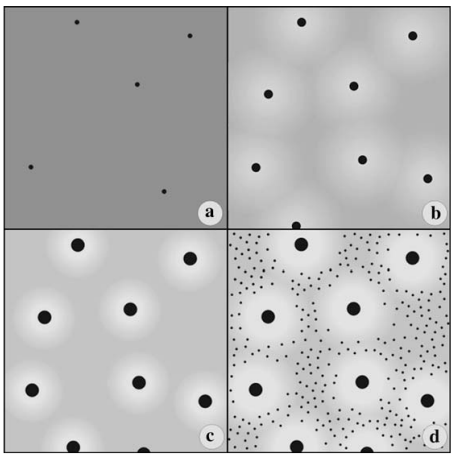

Fig. 4. Interaction between increasing nucleation rate with decreasing temperature, decreasing nucleation rate with solute depletion and development of unaffected channels between growing precipitates (schematic).

isothermal case, due to depletion of the matrix, the nucleation process eventually comes to a stop. This situation is schematically depicted in Fig. 4b.

On further cooling, the extension of the diffusion fields shrinks due to reduced diffusional mobilities. Corridors between the precipitates open, which are essentially unaffected by the continued growth of the existing precipitates (Fig. 4c). In these corridors, supersaturation increases rapidly again until, eventually, a second nucleation burst occurs. This situation is shown in Fig. 4d. As a result of this interaction, size distributions observed after continuous cooling are often multimodal.

It is important to recognize that, during continuous cooling, the three processes of (i) increasing ΔG_{vol} and J with decreasing temperature, (ii) decreasing ΔG_{vol} and J with solute depletion, and (iii) development of unaffected corridors due to reduced diffusional mobilities of solute atoms occur simultaneously. However, the evolution of the resulting multimodal size distributions can be approximately controlled by the cooling rate. This issue is further investigated in the next section, where numerical precipitation kinetics simulation is employed to analyze the experimental observations.

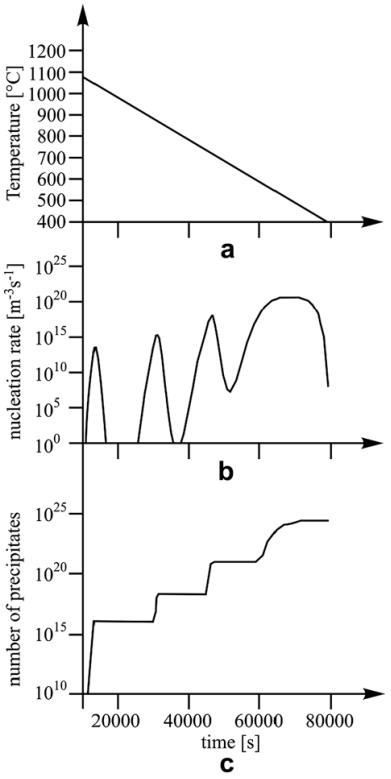

Fig. 5. Temperature profile (a), calculated nucleation rate (b) and number density of γ' precipitates (c) during continuous cooling from 1180 to 400 °C in 79,200 s.

3.4. Simulation

To facilitate interpretation of the experimental results, precipitation kinetics simulations were performed and compared to the observed precipitate distributions. Fig. 5 shows a plot summarizing the simulated precipitation kinetics and demonstrating the occurrence of oscillations in the nucleation rate and, consequently, the occurrence of multimodal size distributions. The top graph displays the time–temperature history for the simulation. The other two plots show the predicted nucleation rate and the integral number density of particles during cooling from 1180 to 400 °C in 79,200 s.

Based on the discussion of mechanisms in the previous section, the shape of the nucleation rate curve is easily interpreted. Below the γ' phase boundary, the volume free energy ΔG_{vol} increases steadily until nucleation initiates. The nucleation rate reaches a maximum value of approximately $10^{14}\,m^{-3}\,s^{-1}$, before it decreases again due to solute depletion of the matrix. This completes the first nucleation wave. The number density of precipitates is relatively low after this first nucleation wave.

On further cooling, corridors between the existing precipitates develop and after approximately 30,000 s, at 900 °C, a second nucleation wave appears. The nucleation rates are significantly higher in this second wave, in agreement with experimental observation. The simulation shows two more nucleation bursts, until the target temperature of 400 °C is reached. Since the total number of precipitates steadily increases, no coarsening of precipitates is observed in our simulation.

3.5. Comparison of simulation and experiment

Fig. 6 compares the observed precipitate distributions for the investigated conditions with the computer simulations. It is apparent that, with decreasing cooling rate, the number of nucleation bursts increases and multimodal size distributions of γ' precipitates develop. Good agreement is observed for the first, largest precipitate population where the precipitate radius as well as the number density coincide well. The experimentally observed second- and higher-order precipitate populations in Fig. 6 are indicated by vertical dashed lines only, since it was not possible to obtain reliable size distributions.

Fig. 7 summarizes and compares the experimental and computational results for the mean precipitate diameter. The continuous solid lines represent the predicted mean diameters of each precipitate population. The dashed lines indicate regions where overlapping of distributions is predicted (see also Fig. 6) and clear separation of the individual precipitate populations is probably difficult. From the results, it is observed that the mean diameter of the precipitates varies linearly with cooling time if plotted on a double-logarithmic scale. This is in agreement with observations of Mao et al. [22], who carried out comparable experiments and derived a phenomenological relation

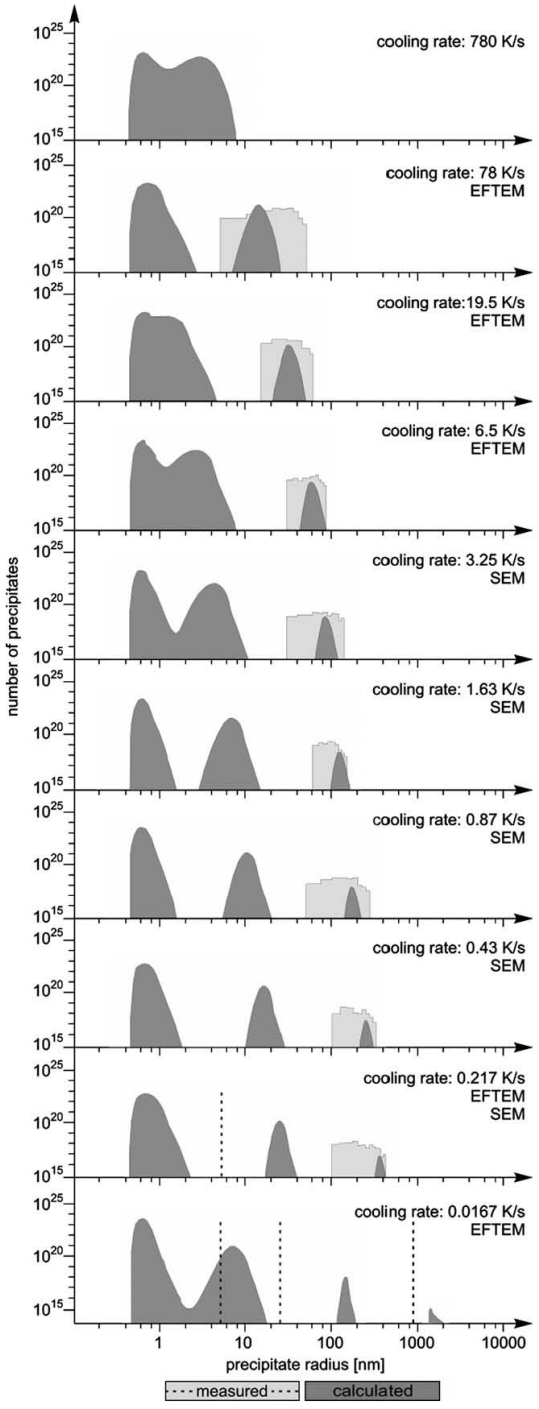

Fig. 6. Comparison of calculated and measured γ' precipitate size distributions (dashed lines are mean values; see text).

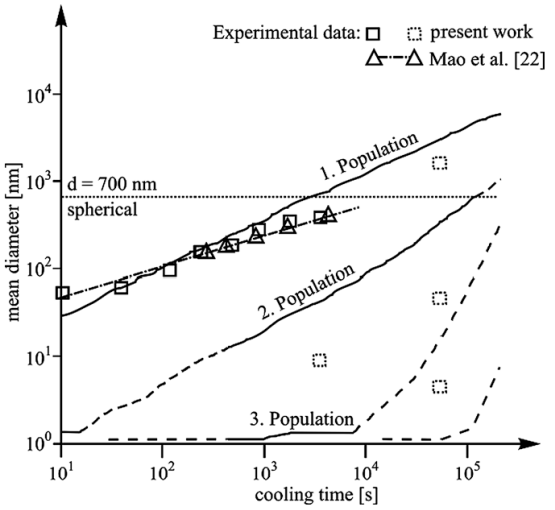

Fig. 7. Average γ' precipitate diameter of each population as a function of cooling time from 1180 to 400 °C.

(Eq. (7)) for the size of the initial γ' precipitate population as a function of cooling rate. This equation is displayed in addition to the results obtained in the present study in Fig. 7.

$$\log D_{\gamma'} = 0.0165 - 0.354 \cdot \log\frac{dT}{dt} \tag{7}$$

The data of Mao et al. [22] coincide very well with our experimental results and both are in good agreement with the present simulations for the initial precipitate population. This latter observation is particularly interesting, since the computer simulations have been carried out without the use of any fitting parameters. All input quantities needed for evaluation of the nucleation and growth equations are calculated from the independent thermodynamic and mobility databases [37,38]. This includes the thermodynamic driving forces as well as the interfacial energies, which are evaluated from a newly developed generalized nearest-neighbor broken-bond approach [40].

Despite the good predictions for the absolute value of the size of the primary precipitate population, discrepancies in the predicted sizes of the second and third population are observed as well as differences in the slope of the size prediction for the first population over cooling time. The measured sizes for the second and third population are generally too small compared to the simulations. The main reason for this discrepancy most probably lies in uncertainties in the underlying thermodynamic and diffusion data. In the Appendix A, a parameter analysis is provided to show the sensitivity of the simulation results to these data. It is shown that, for instance, a variation in diffusion coefficient enters the calculated size distribution almost linearly, thus being a very sensitive quantity for

accurate predictions. The analysis also shows that, interestingly, the value of the interfacial energy has a relatively weak influence on the results, bearing in mind that this quantity occurs in cube form in the exponent of the nucleation rate expression. Another possible source of discrepancy occurs in the mean-field description for precipitate growth, where large distances between the precipitates compared to their size have been assumed in the derivation of the evolution equations [25], as well as deviations from spherical precipitate shape. These are, however, assumed to have only minor influence. The most important parameter in the present simulations seems to be the diffusive mobility of alloying elements where a change of diffusivity by only a factor of 2–3 leads to perfect agreement between simulation and experiment. No attempt to optimize these parameters has been made, however, since mainly a physical understanding of the phenomenon has been sought in this study.

4. Summary and conclusions

In the present work, the morphology and size distribution of γ' precipitates in UDIMET 720 Li were investigated. A series of continuous cooling experiments was performed and characterized using high-resolution SEM and EFTEM methods. Depending on the cooling rate, monomodal, bimodal and multimodal size distributions were observed. The results are compared to computer simulations carried out with the software package MatCalc.

The physical background for the occurrence of multimodal size distributions in the course of diffusion-controlled precipitation processes are discussed. They are identified in the simultaneous processes of (i) increasing ΔG_{vol} and J with decreasing temperature, (ii) decreasing ΔG_{vol} and J with solute depletion, and (iii) development of unaffected channels between existing precipitates due to reduced diffusional mobilities of solute atoms.

The experimental observations are found to be in good agreement with the theoretically predicted precipitate distributions. This is particularly true for the initial nucleation wave, yielding the largest precipitates. The deviations between prediction and experiment for this first wave can most likely be attributed to inaccuracies in the input parameters for the diffusional mobilities of the precipitate-forming elements. A sensitivity analysis on the influence of input parameters shows that only slight modifications of the mobility data by factors of 2–3 suffice to obtain perfect agreement between experiment and simulation.

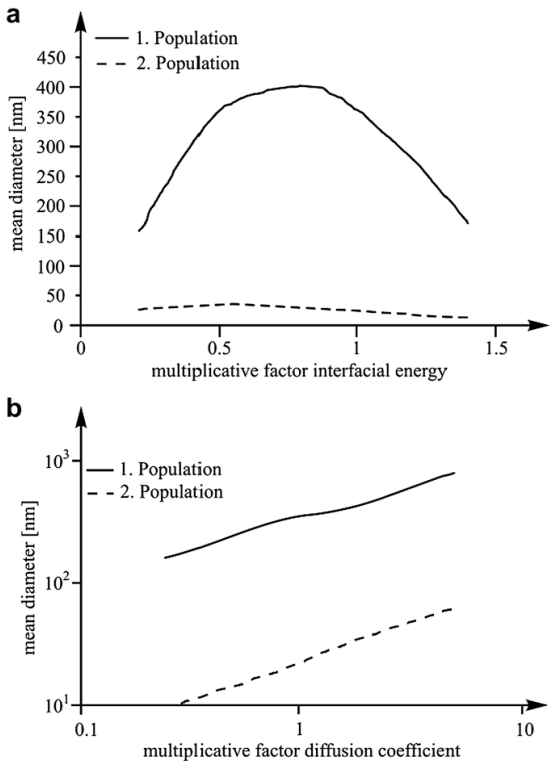

Fig. 8. Sensitivity analysis to determine the influence of interfacial energy (a) and diffusion coefficient (b) on the precipitate size.

Acknowledgement

One of the authors acknowledges financial support by the Österreichische Forschungsförderungsgesellschaft mbH, the Province of Styria, the Steirische Wirtschaftsförderungsgesellschaft mbH and the Municipality of Leoben within research activities of the Materials Center Leoben under the frame of the Austrian Kplus Competence Center Programme.

Appendix A

For a closer investigation of the sensitivity of the simulation results on a variation of input data, a parameter study has been carried out for the interfacial energy and the diffusivity of alloying elements. Both parameter variations are expressed by constant multiplicative factors.

Fig. 8a shows a distinct maximum of the predicted mean precipitate size when varying the value of the interfacial energy. The maximum is observed when multiplying the predicted interfacial energy by a factor of 0.8. A linear dependence of the mean precipitate size is observed on the diffusion coefficient (Fig. 8b), if the curves are plotted on a double-logarithmic scale. A change in the diffusion coefficient by a factor of 2 causes a variation in the mean precipitate size by a factor of approximately 1.5.

References

[1] Ricks RA, Porter AJ, Ecob RC. Acta Metall 1983;31:43.
[2] Grosdidier T, Hazotte A, Simon A. Mater Sci Eng 1998;A256:183.

[3] Hornbogen E, Roth M. Z Metallkd 1967;58:842.
[4] Maebashi T, Doi M. Mater Sci Eng 2004;A373:72.
[5] Maheshwari A, Ardell AJ. Acta Metall Mater 1992;40:2661.
[6] Miyazaki T, Nakamura K, Mori H. J Mater Sci 1979;14:1827.
[7] Miyazaki T, Imamura H, Mori H, Kozakai T. J Mater Sci 1981;16:1197.
[8] Hazotte A, Grosdidier T, Denis S. Scripta Mater 1996;34:601.
[9] Doi M, Miyazaki T. Mater Sci Eng 1986;78:87.
[10] Monajati H, Jahazi M, Bahrami R, Yue S. Mater Sci Eng 2004;A373:286.
[11] Grosdidier T, Hazotte A, Simon A. Scripta Metall Mater 1994;30:1257.
[12] Behrouzghaemi S, Mitchell RJ. Mater Sci Eng 2008;A498:266.
[13] Mitchell RJ, Preuss M, Hardy MC, Tin S. Mater Sci Eng 2006;A423:282.
[14] Jackson MP, Reed RC. Mater Sci Eng 1999;A259:85.
[15] Torster F, Baumeister G, Albrecht J, Lütjering G, Helm D, Daeubler MA. Mater Sci Eng 1997;A234–236:189.
[16] Penkalla HJ, Wosik J, Czyrska-Filemonowicz A. Mater Chem Phys 2003;81:417.
[17] Sarosi PM, Wang B, Simmons JP, Wang Y, Mills MJ. Scripta Mater 2007;57:767.
[18] Babu SS, Miller MK, Vitek JM, David SA. Acta Mater 2001;49:4149.
[19] Simmons JP, Wen Y, Shen C, Wang YZ. Mater Sci Eng 2004;A365:136.
[20] Wen YH, Simmons JP, Shen C, Woodward C, Wang Y. Acta Mater 2003;51:1123.
[21] Furrer DU, Fecht HJ. Scripta Mater 1999;40:1215.
[22] Mao J, Chang KM, Yang W, Ray K, Vaze SP, Furrer DU. Metall Trans A 2001;32:2441.
[23] Mao J, Chang KM, Yang W, Furrer DU, Ray K, Vaze SP. Mater Sci Eng 2002;A332:318.
[24] Gabb TP, Backman DG, Wie DY, Mourer DP, Furrer D, Garg A, et al. γ′ Formation in a nickel-base disk superalloy. Superalloys 2000. Warrendale (PA): TMS; 2000. p. 405.
[25] Svoboda J, Fischer FD, Fratzl P, Kozeschnik E. Mater Sci Eng 2004;A385:166.
[26] Kozeschnik E, Svoboda J, Fratzl P, Fischer FD. Mater Sci Eng 2004;A385:157.
[27] Kozeschnik E, Svoboda J, Fischer FD. Calphad 2005;28:379.
[28] Hofer F, Grogger W, Kothleitner G, Warbichler P. Ultramicroscopy 1997;67:83.
[29] Hofer F, Warbichler P, Grogger W. Ultramicroscopy 1995;59:15.
[30] Sonderegger B. Ultramicroscopy 2006;106:941.
[31] Schmidt PF. Praxis der Rasterelektronenmikroskopie und Mikrobereichsanalyse. Münster: Expert Verlag; 1994.
[32] Stockinger M. Ph.D. Thesis, Technische Universität Graz; 2003.
[33] Russell K. Adv Colloid Sci 1980;13:205.
[34] Janssens KGF, Raabe D, Kozeschnik E, Miodownik MA, Nestler B. Computational materials engineering: an introduction to microstructure evolution. Oxford: Elsevier; 2007.
[35] Kozeschnik E, Svoboda J, Fischer FD. On the role of chemical composition in multi-component nucleation. In: Proceedings of the international conference solid solid phase transformations in inorganic materials, PTM 2005, Phoenix, AZ; 2005. p. 301.
[36] Kampmann R, Wagner R. Acta Scripta Metall Ser 1984;91.
[37] ThermoTech. Ni-base version 3.0 <http://www.thermotech.co.uk/databases.html> [01.08.07].
[38] Campbell CE, Boettinger WJ, Kattner UR. Acta Mater 2002;50:775.
[39] Nembach E, Neite G. Mater Sci 1985;29:177.
[40] Sonderegger B, Kozeschnik E. Metall Mater Trans 2009;40A:499.

B.2 R. Radis, G. A. Zickler, M. Stockinger, C. Sommitsch and E. Kozeschnik. Interaction of the Precipitation Kinetics of δ and γ' Phases in Nickel-Base Superalloy ATI Allvac®718 Plus™. *Materials Science Forum*, 638-642:2712-2717, 2010.

Materials Science Forum Vols. 638-642 (2010) pp 2712-2717

doi:10.4028/www.scientific.net/MSF.638-642.2712

INTERACTION OF THE PRECIPITATION KINETICS OF δ AND γ' PHASES IN NICKEL-BASE SUPERALLOY ATI ALLVAC® 718PLUS™

Rene Radis[1,2,a], Gerald A. Zickler[3,b], Martin Stockinger[4,c],
Christof Sommitsch[2,5,d], Ernst Kozeschnik[1,6,e]

[1]Christian Doppler Laboratory "Early Stages of Precipitation",
Vienna University of Technology, Favoritenstraße 9-11, A-1040 Vienna, Austria

[2]Institute for Materials Science and Welding,
Graz University of Technology, Kopernikusgasse 24, A-8010 Graz, Austria

[3]Christian Doppler Laboratory "Early Stages of Precipitation",
Montanuniversität Leoben, Franz-Josef-Straße 18, A-8700 Leoben, Austria

[4]Böhler Schmiedetechnik GmbH & Co KG,
Mariazeller Str. 25, A-8605 Kapfenberg, Austria

[5]Christian Doppler Laboratory "Materials Modelling and Simulation",
University of Leoben, Franz-Josef-Straße 18, A-8700 Leoben, Austria

[6]Institute of Materials Science and Technology,
Vienna University of Technology, Favoritenstraße 9-11, A-1040 Vienna, Austria

[a]rene.radis@tugraz.at, [b]gerald.zickler@unileoben.ac.at, [c]martin.stockinger@bohler-forging.com,
[d]christof.sommitsch@cdl-mms.at, [e]ernst.kozeschnik@tuwien.ac.at

Keywords: precipitation kinetics, gamma prime, delta, ATI Allvac® 718Plus™, superalloy

Abstract. In this paper, the precipitation behaviour of δ ($Ni_3(Nb,Al)$) and γ' ($Ni_3(Al,Ti,Nb)$) phases in the nickel-base superalloy ATI Allvac® 718Plus™, as well as their kinetic interactions are discussed. Important parameters such as volume fraction, mean radius and number density of precipitates are experimentally determined and numerically simulated as a function of the heat treatment parameters time and temperature. To match the experimentally observed kinetics, the predicted interfacial energy of the precipitates, as calculated for a sharp, planar phase boundary, is adjusted to take into account the interfacial curvature and entropic effects of a diffuse interface. Correction functions for the interfacial energies of δ as well as γ' precipitates are presented. Using these modified interfacial energies, the calculated results show excellent agreement with the experimental measurements.

Introduction

The term superalloy is generally used for a large number of different alloys. A major motivation for the development of nickel-based superalloys is their applicability for gas turbine parts in aircrafts and power plants. The degree of efficiency increases with increasing operation temperatures. Usually, Ni-base superalloys combine high strength and good corrosion resistance, which are essential for the application in modern gas turbine aero-engines, e.g. for high-speed rotating components, such as high-pressure turbine disks [1].

A novel representative of these nickel-base alloys is the superalloy ATI Allvac® 718Plus™ (718Plus™ is a trademark and Allvac® is a registered trademark of ATI Properties, Inc., Monroe, NC, USA), which is a further development of the classical alloy 718 [2]. Compared to alloy 718, the new alloy contains cobalt, tungsten, a higher amount of aluminum and less iron and titanium, see Table 1. According to the chemical composition of ATI Allvac® 718Plus™, the most essential precipitates in this alloy are the $D0_a$-ordered δ ($Ni_3(Nb,Al)$) and the $L1_2$-ordered γ' ($Ni_3(Al,Ti,Nb)$). The precipitation of a suitable quantity and size of coarse δ precipitates is used for controlling grain

growth [3,4], whereas the precipitation of a large amount of fine-dispersed coherent γ' precipitates provides a large quantity of strengthening by precipitation hardening [5,6]. Therefore, knowledge of the precipitation kinetics of both phases is of high technological interest in order to control the evolution of microstructure during processing and to achieve the desired material properties.
In the present work, the precipitation behaviour of the δ and γ' phases is studied numerically and compared to corresponding experiments. A series of isothermal precipitation kinetics simulations at different temperatures is performed using the thermo-kinetic software MatCalc. Furthermore, the kinetic interactions due to a precipitation competition of the alloying elements Nb and Al, is discussed. Finally, a complete time-temperature-precipitation (TTP) diagram for δ and γ' phase in alloy ATI Allvac® 718Plus™ is determined.

Table 1: Chemical composition (wt%) of alloy 718 and ATI Allvac® 718Plus™ [3]

alloy	Ni	Ti	Al	Nb	Cr	Co	Fe	Mo	W	C
alloy 718	base	1.0	0.5	5.4	18.1	-	18.0	2.9	-	0.03
ATI Allvac® 718Plus™	base	0.7	1.5	5.4	18.0	9.0	10.0	2.7	1.0	0.03

Experimental

For the simulation of the precipitation kinetics of the phases δ and γ' in ATI Allvac® 718Plus™, the thermo-kinetic software MatCalc 5.30 (rel 1.036) [7-9] is used. The thermodynamic description and the diffusion data are taken from refs. [10,11]. The numerical time integration procedure for the evolution equations of precipitate nucleation and growth is similar to the classical numerical Kampmann – Wagner model [12]. Nucleation of precipitates is calculated from a multi-component extension of classical nucleation theory [13,14]. The transient nucleation rate *J*,

$$J = N_0 Z \beta^* \cdot e^{\left(\frac{-G^*}{k \cdot T}\right)} \cdot e^{\left(\frac{-\tau}{t}\right)} \quad (1)$$

describes the rate at which nuclei are formed per one unit volume and time, given in units of *[(new nuclei)/(m³s)]*. In Eq. 1, N_0 represents the total number of potential nucleation sites. The Zeldovich factor Z takes into account that the nucleus is destabilized by thermal vibrations compared to the inactivated state and it is often in the order of 1/40 to 1/100. The atomic attachment rate β^* considers the long-range diffusive transport of atoms if the chemical composition of precipitate and matrix is different. k is the Boltzmann constant, T is the absolute temperature and τ stands for the incubation time. The critical nucleation energy G^* is given by

$$G^* = \frac{16\pi}{3} \frac{\gamma^3}{D^2} \quad (2)$$

which is a function of the interfacial energy γ and the total driving force D. The interfacial energy is calculated using a generalized nearest-neighbour broken-bond approach [15,16], assuming a planar and sharp interface. However, corrections regarding the spherical shape of the nucleus and entropic contributions from finite interface thickness must be considered in the interfacial energy. Particularly, close to the solution temperature, these effects can become prominent. This behaviour of the interfacial energy has been observed in a previous work by Pudar et al. [17] and also explained theoretically in ref. [18]. Fig. 1 shows the correction function for the interfacial energy of both phases used in the present simulations.

Subsequently, a series of calculations at different temperatures between 850°C and 975°C, in 25°C intervals, is presented and compared with experimental results. The experimental investigation is described in detail elsewhere [3].

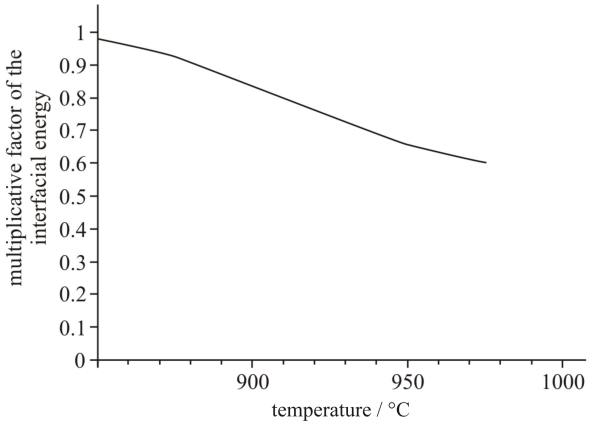

Fig. 1: Temperature-dependent correction of the interfacial energy for planar, sharp interface precipitate/matrix.

Results

Fig. 2 shows the calculated equilibrium phase fractions of the δ and γ' phases in ATI Allvac® 718Plus™ at temperatures between 800°C and 1100°C. In equilibrium, both phases are stable at the same time at temperatures below 975°C, where the following precipitation kinetic simulations are performed.

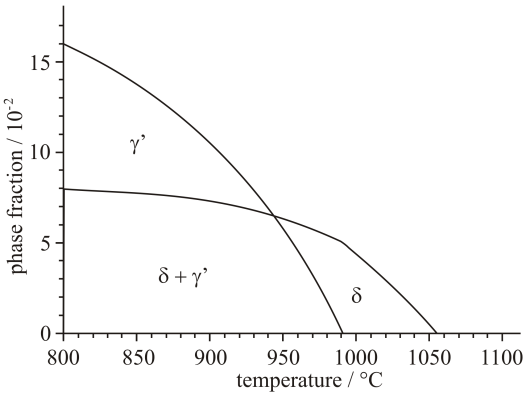

Fig. 2: Calculated equilibrium phase fractions of δ and γ' precipitates at temperatures between 800°C and 1100°C.

Fig. 3 depicts the calculated phase fractions versus time and a comparison with experimental results of δ phase precipitation at temperatures between 850°C and 975°C. The calculations at the two highest temperatures (T=975°C and T=950°C) show that only the δ phase is predicted to appear within a given time span. With decreasing temperature, precipitation of γ' is observed and the kinetics becomes faster with lower temperatures. At a temperature of 875°C the precipitation of both phases occurs simultaneously. After decreasing the temperature to 850°C, partial redissolution follows rapid precipitation of γ', supporting growth of the δ phase.

Materials Science Forum Vols. 638-642 **2715**

Fig. 4 shows the time-temperature-precipitation-diagram for both, the δ and γ' phases in ATI Allvac® 718Plus™. The solid lines mark phase fractions of 2 and 5 vol. % of δ phase, the dashed lines represents 2 vol.% of γ' phase. The calculated results for the δ phase are compared to experimental data (2 vol.% and 5 vol.%).

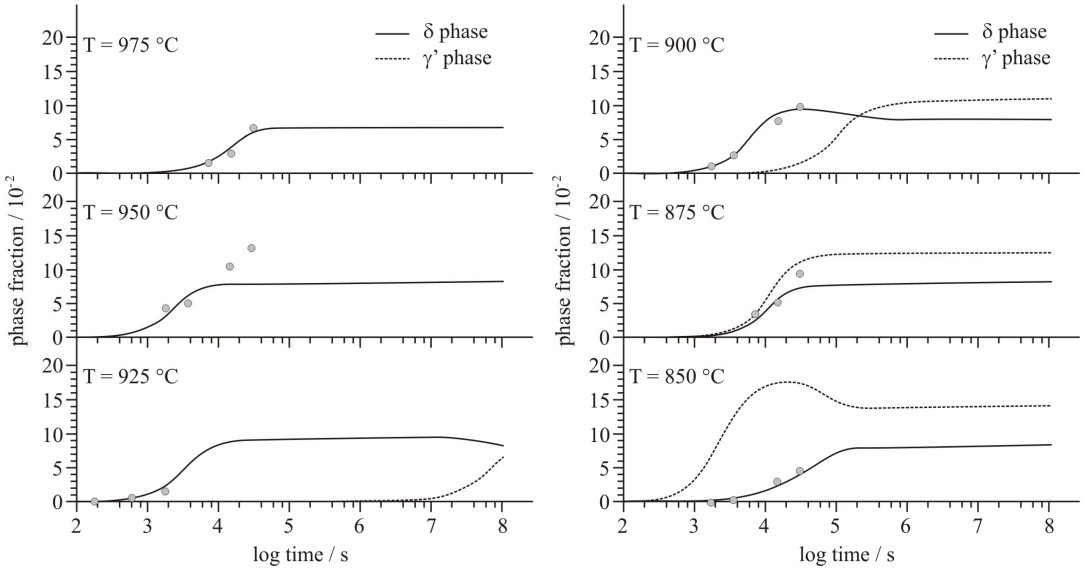

Fig. 3: Calculated δ and γ' phase fractions versus log time and comparison with experimental results of δ phase at temperatures between 850°C and 975°C.

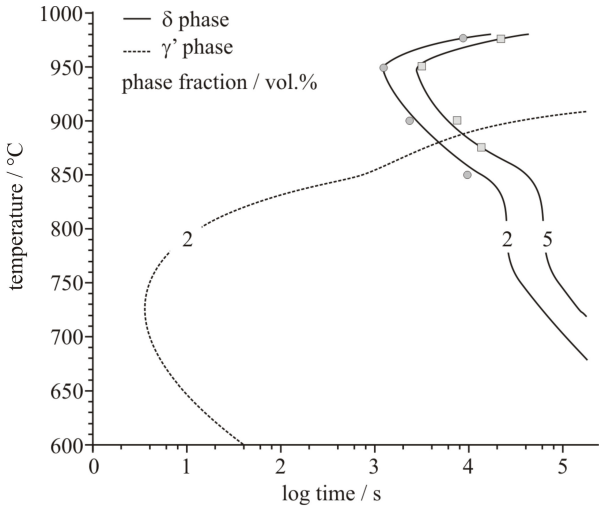

Fig. 4: Calculated time-temperature-precipitation-plot of δ and γ' phases and comparison with experimental results of the δ phase.

Discussion

The numerical calculations in the present work offer important information about the precipitation behaviour of δ and γ' phases in the novel nickel-base superalloy ATI Allvac® 718Plus™, as well as their kinetic interactions. Below the supersolvus temperature of γ', the precipitation kinetics of δ is influenced by the precipitation of γ'. The simultaneous precipitation of both phases leads to a

competition of Nb and Al with respect to the δ and γ' formation. It should be emphasized that a certain amount of Nb is not unusual in γ', which is reported in refs. [19,20] where the chemical composition of γ' in alloy 718 is investigated theoretically and experimentally.
Depending on temperature and time, Al and Nb atoms redistribute to achieve optimum thermodynamic conditions. This is clearly demonstrated in Fig. 5, where the phase fractions of the δ and γ' phases and the mole fractions of the alloying elements of these phases are plotted versus time for an annealing temperature of 850°C. After rapid precipitation, partial redissolution of γ' is observed, supporting the growth of the δ phase. Therefore Nb and Al atoms, previously bonded in γ', are redistributed by diffusional transport, which leads to an increase of the δ phase.

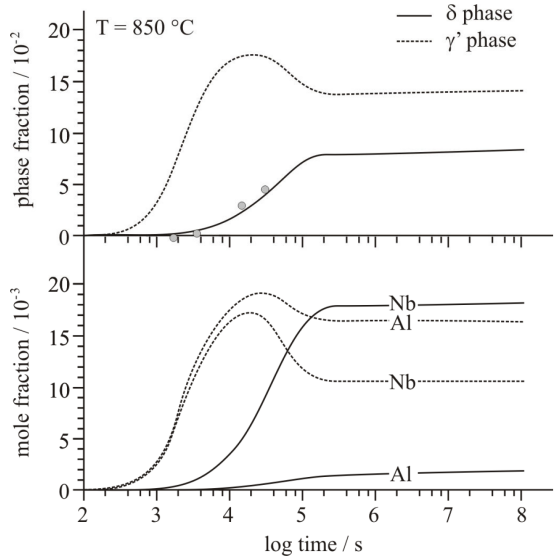

Fig. 5: Calculated phase fraction of the γ' and δ phases as well as the mole fraction of alloying elements versus time at a temperature of 850°C.

The nose temperature for δ phase precipitation is observed at 950°C. The rapid precipitation of γ', faster than the precipitation of δ, leads to a delay in the precipitation kinetics of δ and a discontinuity in the C-curves of the time-temperature-precipitation diagram is observed, see Fig. 4.
To verify the calculated TTP diagram at lower temperatures, additional experimental investigations are suggested for the future. The numerical calculations at temperatures above 850°C show excellent agreement with the experimental investigations.

Summary

The present work deals with the numerical analysis of the precipitation kinetics of δ and γ' phases in the nickel-based superalloy ATI Allvac® 718Plus™. Precipitation kinetics simulations at different temperatures are performed with the thermo-kinetic software MatCalc. The theoretical investigations are compared to experiments. To match the observed kinetics, the predicted interfacial energy of precipitates of planar, sharp interfaces is adjusted to smaller values at temperatures close to the solubility temperature. The correction function for the interfacial energies is presented. Using these modified interfacial energies, the calculated results show excellent agreement with the experimental measurements.
Finally, a complete time temperature precipitation diagram is calculated, which gives important information for controlling the evolution of microstructure during processing in order to achieve the desired material properties.

References

[1] C.T. Sims, N.S. Stoloff and W.C. Hagel, *Superalloys II*, Wiley, New York, 1987.
[2] W.D. Cao, and R. Kennedy, in: Proc. Superalloys 2004, The Minerals, Metals and Materials Society, Warrendale, PA, 2004, 91.
[3] C. Stotter C. Sommitsch, J. Wagner, H. Leitner, I. Letofsky-Papst, G.A. Zickler, W. Prantl and M. Stockinger, Int. J. Mat. Res., 99 (2008), 376.
[4] V. Beaubois, J. Huez, S. Coste, O. Brucelle and J. Lacaze, Mater. Sci. Techn., 20 (2004), 1019.
[5] E. Nembach and G. Neite, Progr. Mater. Sci., 29 (1985), 177.
[6] A.J. Ardell; Metall.Trans., A 16A (1985), 2131.
[7] J. Svoboda, F.D. Fischer, P. Fratzl and E. Kozeschnik, Mater. Sci. Eng., A385 (2004), 166.
[8] E. Kozeschnik, J. Svoboda, P. Fratzl and F.D. Fischer, Mater. Sci. Eng., A385 (2004), 157.
[9] E. Kozeschnik, J. Svoboda and F.D. Fischer, CALPHAD, 28 (4) (2005), 379.
[10] ThermoTech, Ni-Base Version 5.0 http://www.thermotech.co.uk/databases.html (19.01.2009).
[11] C.E. Campbell, W.J. Boettinger, and U.R. Kattner, Acta Mater., 50 (2002), 775.
[12] R. Kampmann and R. Wagner . Acta Scripta Metall series, (1984), 91.
[13] K. Russell Adv. Colloid Sci 13, (1980), 205.
[14] Janssens KGF, Raabe D, Kozeschnik E, Miodownik MA, Nestler B. *"Computational Materials Engineering – An Introduction to Microstructure Evolution"*. Elsevier Academic Press, Oxford, 2007.
[15] B. Sonderegger and E. Kozeschnik, Metall. Mater. Trans., 40A (2009), 499.
[16] B. Sonderegger and E. Kozeschnik, Scripta Mater., in print.
[17] M. Pudar, E. Kozeschnik, A. Sormann and E. Parteder, Steel Res. Int., 79 (8) (2008), 660.
[18] Y.W. Lee and H.I. Aaronson, Acta Metall., 28 (1980), 539.
[19] K. Wu, F. Zhang, S. Chen, W. Cao and Y.A. Chang, in: Superalloys 2008, The Minerals, Metals and Materials Society, Warrendale, PA, 2008, 933.
[20] M.K. Miller and S.S. Babu, in: Superalloys 718, 625, 706 and Various Derivatives, The Minerals, Metals and Materials Society, Warrendale, PA 2001, p. 357.

B.3 G. A. Zickler, R. Schnitzer, R. Radis, R. Hochfellner, R. Schweins, M. Stockinger and H. Leitner. Microstructure and Mechanical Properties of the Superalloy ATI Allvac®718Plus™. *Material Science and Engineering A*, 523:295-303, 2009.

Materials Science and Engineering A 523 (2009) 295–303

Contents lists available at ScienceDirect

Materials Science and Engineering A

journal homepage: www.elsevier.com/locate/msea

Microstructure and mechanical properties of the superalloy ATI Allvac® 718Plus™

Gerald A. Zickler [a,*], Ronald Schnitzer [a], Rene Radis [b,c], Rainer Hochfellner [a], Ralf Schweins [d], Martin Stockinger [e], Harald Leitner [a]

[a] Christian Doppler Laboratory "Early Stages of Precipitation", Department of Physical Metallurgy and Materials Testing, Montanuniversität Leoben, Franz-Josef-Straße 18, A-8700 Leoben, Austria
[b] Christian Doppler Laboratory "Early Stages of Precipitation", Institute of Materials Science and Technology, Vienna University of Technology, Favoritenstraße 9-11, A-1040 Vienna, Austria
[c] Institute for Materials Science and Welding, Graz University of Technology, Kopernikusgasse 24, A-8010 Graz, Austria
[d] Institut Max von Laue - Paul Langevin, DS/LSS group, 6 rue Jules Horowitz, B.P. 156, F-38042 Grenoble, France
[e] Böhler Schmiedetechnik GmbH & Co KG, Mariazeller-Straße 25, A-8605 Kapfenberg, Austria

ARTICLE INFO

Article history:
Received 31 March 2009
Received in revised form 2 June 2009
Accepted 4 June 2009

Keywords:
Nickel-based superalloy
Precipitation kinetics
Atom probe tomography
Small-angle neutron scattering
Strengthening mechanism

ABSTRACT

ATI Allvac® 718Plus™ is a novel nickel-based superalloy, which was designed for heavy-duty applications in aerospace turbines. In the present study the high-resolution investigation techniques, atom probe tomography, electron microscopy and in situ high-temperature small-angle neutron scattering were used for a comprehensive microstructural characterization. The alloy contains nanometer-sized spherical γ′ phase precipitates ($Ni_3(Al,Ti)$) and plate-shaped δ phase precipitates (Ni_3Nb) of micrometer size. The precipitation kinetics of the γ′ phase can be described by a classical model for coarsening. The precipitation strongly influences the mechanical properties and is of high scientific and technological interest.

1. Introduction

For several decades nickel-based alloys, so-called superalloys, have been extensively used for high-duty components of combustion engines, aerospace engines, gas turbines, and nuclear reactors [1]. Nickel–iron–chromium superalloys are especially used as turbine discs in aerospace gas turbines [1], where the materials are operated at relatively high stress environments at elevated temperatures. Superalloys derive their superior mechanical properties essentially from the precipitation of intermetallic phases. Morphology, volume fraction, distribution, and kinetics of precipitation as functions of heat treatment time and temperature are important factors that determine strength and ductility of the superalloys [1]. Therefore, the precipitation kinetics in nickel–iron–chromium alloys, especially in alloy 718, were comprehensively investigated in various studies [2–6]. Nickel–iron–chromium-based superalloys of type alloy 718 precipitate the following phases, which are embedded in the disordered face-centered cubic γ matrix. Firstly, the nanometer-sized γ′ phase, which exhibits an ordered face-centered cubic $Ni_3(Al,Ti)$ crystal structure of type $L1_2$ [7]. This phase mostly accounts for the mechanical properties of superalloys. Secondly, the metastable γ″ phase of chemical composition Ni_3Nb showing a tetragonal crystal structure of type DO_{22} [7–9]. Some studies also reported of γ′/γ″ phase co-precipitates in nickel-based alloys [10–12]. The γ″ phase precipitates are thermodynamically metastable and may eventually transform to the stable δ phase (Ni_3Nb), which has an orthorhombic crystal structure of type DO_a [13,14]. The δ phase precipitation is of high technological importance as it is used to control grain growth during thermo-mechanical processing [6,15]. Additionally small amounts of carbide and carbonitride phases can be found in nickel–iron–chromium-based superalloys, depending on the chemical composition.

In recent years much effort has been directed towards the development of new commercial nickel-based superalloys on the basis of alloy 718, but with higher temperature capabilities and improved mechanical properties. As a part of this effort the new ATI Allvac® 718Plus™ alloy[1] was developed. Table 1 shows a comparison of the chemical composition between the classical and the newly developed alloy. The most significant changes are the addition of cobalt and tungsten, the increase of the aluminum content and the reduction of the amounts of iron and titanium. There exist numerous

* Corresponding author. Tel.: +43 3842 402 4206; fax: +43 3842 402 4202.
E-mail address: gerald.zickler@mu-leoben.at (G.A. Zickler).

0921-5093/$ – see front matter © 2009 Elsevier B.V. All rights reserved.
doi:10.1016/j.msea.2009.06.014

[1] 718Plus™ is a trademark and Allvac® is a registered trademark of ATI Properties, Inc., Monroe, NC, USA.

Table 1
Chemical composition (wt.%) of conventional alloy 718, data taken from Ref. [17], and of ATI Allvac® 718Plus™ alloy as determined by chemical analysis.

Alloy	Ni	Ti	Al	Nb	Cr	Co	Fe	Mo	W	C
Alloy 718	Base	1.00	0.45	5.4	18.1	–	18.0	2.9	–	0.025
ATI Allvac® 718Plus™	Base	0.73	1.42	5.55	18.02	9.11	9.51	2.66	1.05	0.021

studies on the microstructure and the properties of classical alloy 718, however, studies on ATI Allvac® 718 Plus™ are still rare in scientific literature. In recent publications Cao et al. [16–18] provided details about the metallurgical development of ATI Allvac® 718 Plus™ and gave first results on the precipitation kinetics of various phases. Vishwakarma et al. [19] studied the microstructure of fusion and heat-affected zones in electron beam welded ATI Allvac® 718Plus™. In a recent study Stotter et al. [15] investigated the precipitation behavior of the δ phase, where it was shown that the δ phase precipitates in plate-shaped morphology and has a defined crystallographic correlation to the matrix.

For the experimental characterization of the microstructure of nickel-based alloys several high-resolution techniques have been applied. Transmission electron microscopy (TEM) is particularly useful for the identification of individual precipitates of different kinds. However, TEM analysis becomes difficult for precipitate sizes below several nanometers. Moreover, various structures and defects may influence the detailed characterization of materials. In recent years three-dimensional atom probe tomography (APT) provided valuable contributions towards a better understand of the microstructure of nickel-based superalloys [20,21]. APT gives access to three-dimensional imaging and chemical analysis down to the atomic scale. However, the investigated sample volumes of TEM and APT have the dimensions of only a few hundred nanometers, therefore statistically confident results require numerous experiments. Small-angle neutron scattering (SANS) is a powerful experimental technique for obtaining quantitative and statistically relevant data for the characterization of size, shape, arrangement, and volume fraction of intermetallic precipitates in nickel-based alloys [22,23]. The interpretation of SANS patterns usually requires additional microstructural information from complementary methods, e.g. TEM and APT. In the past several studies using SANS reported of the microstructural characterization of nickel-based model alloys [24–26] and various commercial nickel-based superalloys, e.g. alloy PE 16 [27–29], alloy 80a [30,31], alloy 720 [32], alloy 706 [10,11], alloy Re 13 [33], alloy 713 LC [34], and alloy SC 16 [35–37]. The technique of SANS offers the advantage of investigating materials in situ at high temperatures using special furnaces or heating cells. With in situ SANS experiments the entire path of precipitation reactions can be seen on one single specimen, avoiding possible influences from local differences in microstructure and chemical composition. Furthermore, in situ studies allow the detection of rather early stages of precipitation. Recently in situ SANS experiments using special high-temperature furnaces were applied for studying the precipitation behavior of various nickel-based alloys [10,11,26,37].

The aim of the present study is to gain fundamental knowledge of the precipitation behavior of intermetallic phases and its influence on the mechanical properties of the superalloy ATI Allvac® 718Plus™ as a function of heat treatment temperature and aging time. It is aimed at the characterization of the individual phases and their influence on mechanical strength. The combination of SANS, APT and electron microscopy as complementary methods allows a comprehensive microstructural characterization, whereas especially SANS is a powerful experimental tool for obtaining statistically relevant data of nanometer-sized intermetallic precipitates.

2. Experimental

The material used for this investigation was a commercial superalloy ATI Allvac® 718Plus™. Table 1 shows the chemical composition of the as-received material. The material was solution treated (homogenized) at 1283 K for 7200 s in a laboratory furnace and then immediately water-quenched. One sample was used as a homogenized reference specimen. The others were isothermally aged at temperatures of 1048, 1098, 1148, 1173, 1198, and 1223 K. All aging treatments were carried out in ambient atmosphere followed by quenching into water. The mechanical characterization of the differently aged samples were performed by Vickers hardness testing according to the standard EN ISO 10002 using a hardness testing machine EMCO-TEST, M4C-025-G3M.

2.1. Atom probe tomography and electron microscopy

APT was applied for the microstructural characterization of the superalloy ATI Allvac® 718Plus™. For APT small rods with a cross-section of 0.3 mm × 0.3 mm were cut out of the bulk material. The tips were prepared by standard electro polishing in a layer of 85% acetic acid and 15% perchloric acid solution topped over a dielectric liquid in a first step, followed by a second step in an electrolyte of 2% perchloric acid in butoxyethanol. The APT measurements were conducted on the high-performance atom probe microscope Imago LEAP 3000X HR™, operated at 60 K. The measurements were performed in voltage mode with a pulse fraction of 15%. The three-dimensional reconstructions of the measured tips were made by the atom probe data visualization and analysis software IVAS.

Scanning electron microscopy (SEM) was applied for microstructural characterization. Therefore, the samples were mechanically ground and polished using diamond suspension. The SEM investigations were performed on a scanning electron microscope Carl Zeiss EVO® operated in back-scattered electron mode at an acceleration voltage of 8 kV.

For TEM investigations thin foils were mechanically cut, ground and dimpled to a thickness of about 20 μm followed by ion-milling until electron transparency was achieved. TEM studies were carried out using a transmission electron microscope Philips CM 12 operated at an emitter voltage of 120 kV. Digital TEM images were taken with a Gatan BioScan CCD camera.

2.2. Small-angle neutron scattering

The SANS studies of the precipitation kinetics were performed at the small-angle scattering instrument D22 at the Institut Max von Laue - Paul Langevin in Grenoble, France. For the in situ aging experiment a special high-temperature furnace was used, which consisted of an evacuated sample chamber, equipped with entrance and exit windows for the neutron beam. The heating of the furnace was performed by electric current via several wires of niobium, which were positioned around the specimen in the vacuum chamber. The geometry of the measured samples was determined by the special requirements of the sample mounting in the furnace. Therefore, the material was machined to plate-shaped specimens with a thickness of 1.5 mm. To one side, the plates had an extended thickness in order to incorporate an internal thread. By means of this thread, the specimens were screwed on the sample holder, which was equipped with a K-type thermocouple, providing the temperature signal from the core of the material. The samples were heated up with a rate of 1.67 $K s^{-1}$ and then isothermally aged at 1048, 1073, 1098, 1123, 1148, 1173, 1198, and 1223 K, respectively. The cross-section of the primary beam at the sample position

was defined by a circular aperture of cadmium with a diameter of 8 mm. A nominal neutron wavelength $\langle\lambda\rangle = 0.8$ nm ($\Delta\lambda/\lambda = 10\%$) was chosen to avoid double Bragg scattering. SANS patterns were continuously taken during isothermal aging as a function of time t up to 10,800 s. The scattered neutrons were detected by a Reuter-Stokes multi-tube detector, consisting of 128 vertical tubes with 8 mm tube diameter. The spatial resolution of the available 128×128 pixels was 8 mm $\times$ 8 mm. The SANS patterns were measured at a sample-to-detector distance of 8 m, covering a total range in length of scattering vector of $0.06\,\text{nm}^{-1} < q < 1\,\text{nm}^{-1}$. The length of the scattering vector is given by $|\mathbf{q}| = q = (4\pi/\lambda)\sin\theta$, with 2θ being the scattering angle. An exposure time of 60 s yielded excellent counting statistics. All scattering patterns were suitably corrected for parasitic background scattering, detector efficiency, solid angle, flux collimation, sample volume, and sample transmission by using the primary data reduction program GRAS_{ANS}P (Graphical Reduction and Analysis SANS Program for Matlab™). All samples showed isotropic scattering patterns, which were azimuthally averaged for equal radial distances from the central beam. The absolute values for the differential scattering cross-section $\text{d}\Sigma/\text{d}\Omega$ were calculated using the incoherent scattering of the calibration standard water (H_2O).

3. Results

3.1. Mechanical properties

The results of Vickers hardness testing of the superalloy ATI Allvac® 718Plus™ as a function of aging time for various temperatures are illustrated in Fig. 1. After solution treatment at 1283 K for 7200 s, the as-quenched material shows relatively low hardness of 180 ± 5 HV. Isothermal aging in the temperature range of 1048–1198 K leads to an increase of hardness. Hardness values continue to increase for the samples heat treated at 1048 and 1098 K until 10^4 s. The behavior at other temperatures is different. The maximum hardness decreases from about 350 HV at 1048 K to 215 HV at 1198 K in the observed time range. At 1223 K no significant changes compared to the as-quenched state are observed.

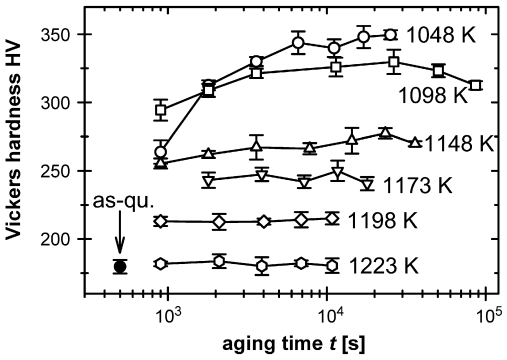

Fig. 1. The Vickers hardness (HV) of ATI Allvac® 718Plus™ alloy in solution treated state (as-quenched) and aged at various temperatures. The data points are averaged values of five indents and the error bars indicate the respective standard deviations.

3.2. Atom probe tomography and electron microscopy

The three-dimensional atom maps of the alloy aged at 1048 K for 3600 s are illustrated in Fig. 2. It can be seen that the ele-

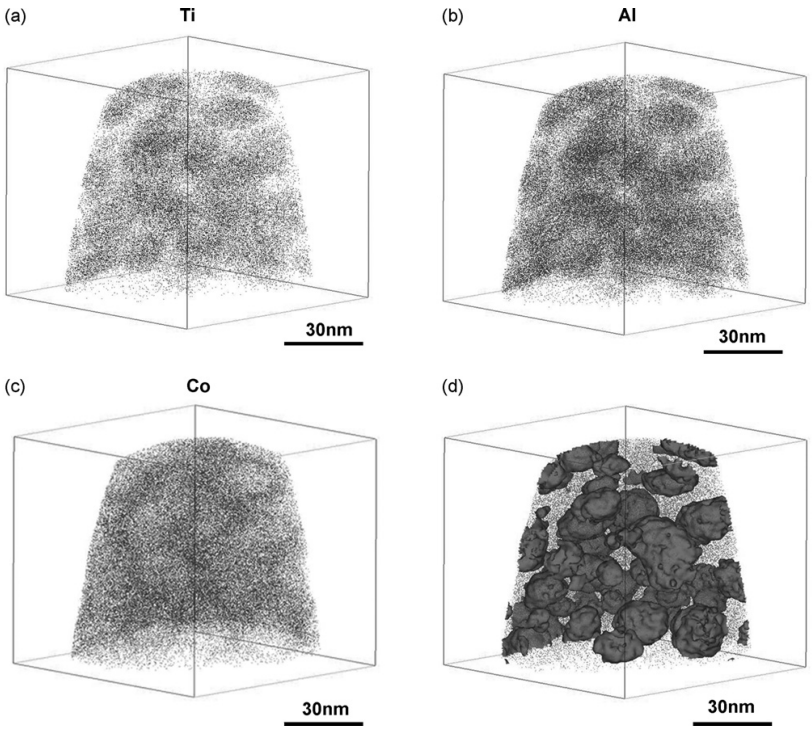

Fig. 2. Three-dimensional reconstructions of the superalloy ATI Allvac® 718Plus™ aged at 1048 K for 3600 s measured by APT. Atom maps for Ti (a), Al (b) and Co (c). (d) Iso-concentration surfaces for Ti + Al = 12 at.% (7 wt.%).

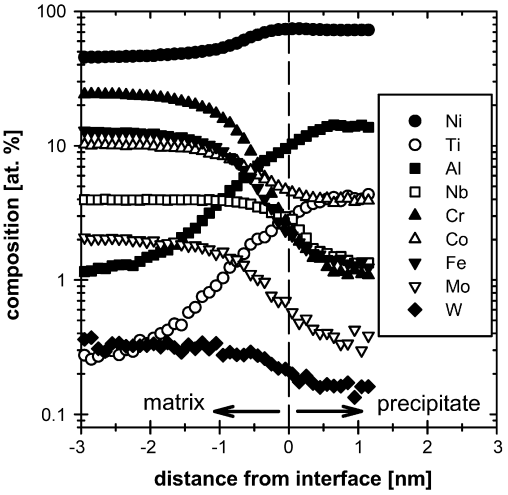

Fig. 3. Proximity histogram over the iso-concentration surfaces illustrated in Fig. 2d (aging treatment: 1048 K, 3600 s). All relevant alloying elements of ATI Allvac® 718Plus™ are shown as function of the distance from the iso-concentration surface (dashed line).

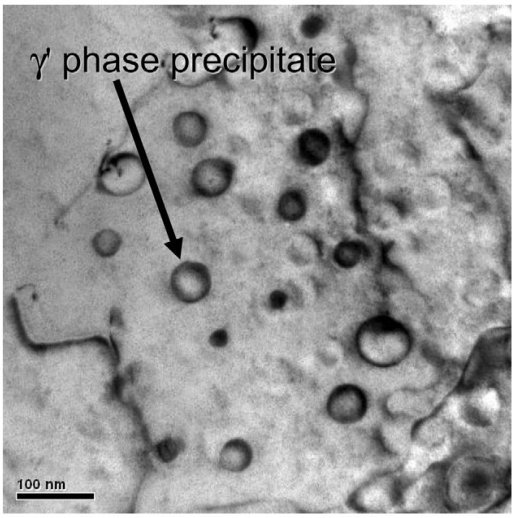

Fig. 4. TEM image of superalloy ATI Allvac® 718Plus™ after aging at 1148 K for 7800 s, showing spherical precipitates of γ′ phase in the γ matrix.

ments titanium (Fig. 2a) and aluminum (Fig. 2b) are clustering, however, cobalt shows depleted zones (Fig. 2c). Fig. 2d shows iso-concentration surfaces of Ti + Al = 12 at.% (7 wt.%). From visual inspection it is obvious that the precipitates are almost spherical with an average radius of 4.5 nm. The chemical composition of the γ′ phase is given by: 73 at.% Ni, 4.1 at.% Ti, 14 at.% Al, 1.3 at.% Nb, 1.1 at.% Cr, 3.9 at.% Co, 1.3 at.% Fe, 0.4 at.% Mo, and 0.1 at.% W. Fig. 3 displays the proximity histogram over the surfaces illustrated in Fig. 2d (aged at 1048 K for 3600 s). All relevant alloying elements are shown as function of the distance from the iso-concentration surface. It can be clearly seen that nickel, aluminum and titanium are enriched in the precipitates. All other alloying elements decrease their concentration in the γ′ phase precipitates and are enriched in the γ matrix.

TEM investigations show that the superalloy ATI Allvac® 718Plus™ contains nanometer-sized spherical γ′ phase precipitates in the γ matrix. Fig. 4 presents a typical result of the microstructure aged at 1148 K for 7800 s, showing the rather high number density of the γ′ phase precipitates.

The results of SEM investigations are presented in Fig. 5, showing plate-shaped precipitates situated mostly at grain boundaries and twin boundaries. Energy dispersive X-ray spectroscopy (EDX) shows that the phase is rich in nickel and niobium, indicating δ phase precipitates (Fig. 5b). For further details of morphology and crystallography of the δ phase in ATI Allvac® 718Plus™ refer to the recent study of Stotter et al. [15].

3.3. Small-angle neutron scattering

Fig. 6 shows typical azimuthally averaged SANS patterns of ATI Allvac® 718Plus™ alloy in the as-quenched and differently aged states. The as-quenched state shows a continuous decrease of scattering intensity with increasing q and it reaches a constant value at larger q. A considerable increase of the differential scattering cross-section $d\Sigma/d\Omega$ is observed after aging, whereas a growing maximum shifts from large q towards smaller values in the investigated time range. There is a small shoulder at the high-q flank, which grows with increasing aging time. These trends are qualitatively similar for the samples aged between 1048 and 1198 K, however, no change of scattering intensity is observed at the highest aging temperature of 1223 K (Fig. 6d).

TEM and APT, as complementary techniques, provide valuable information for the quantitative analysis of the SANS patterns. The alloy contains two types of precipitates on two different length scales: (1) δ phase precipitates of micrometer size and (2)

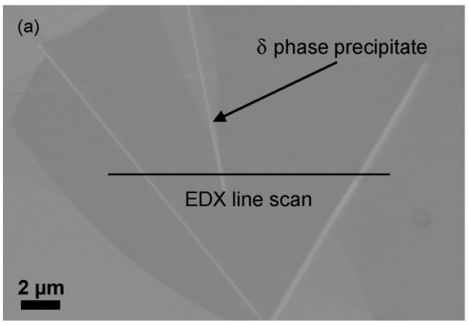

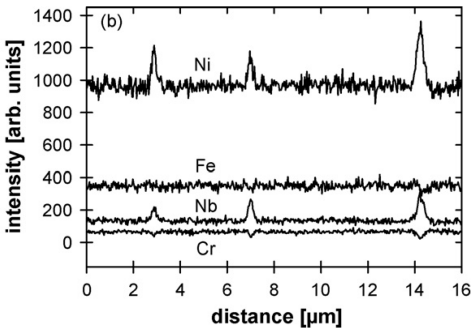

Fig. 5. (a) SEM micrograph (back-scattered electron mode) of the alloy ATI Allvac® 718Plus™ after aging at 1198 K for 3600 s. The plate-shaped precipitates are identified as δ phase. (b) EDX line scan shown in (a).

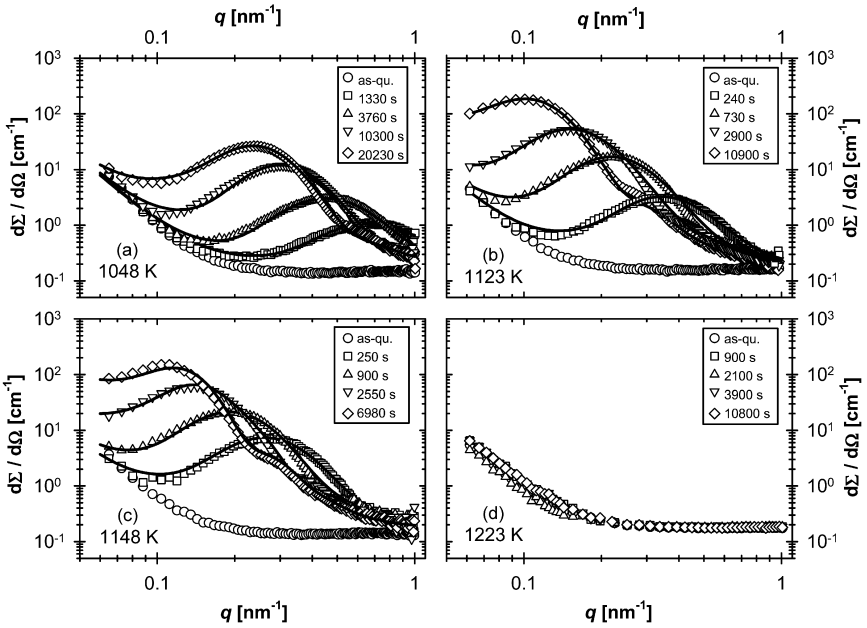

Fig. 6. Azimuthally averaged SANS patterns of ATI Allvac® 718Plus™ alloy aged at 1048 K (a), 1123 K (b), 1148 K (c), and 1223 K (d) for various aging times (see figure legend). The given aging times correspond to the end of the exposure of the detector. The solid lines indicate the least-square fitted model function according to Eq. (1).

nanometer-sized γ′ phase precipitates. Therefore, it is assumed that $\mathrm{d}\Sigma/\mathrm{d}\Omega$ is an adding superposition of the individual scattering contributions of δ phase precipitates $(\mathrm{d}\Sigma/\mathrm{d}\Omega)_\delta$ and γ′ phase precipitates $(\mathrm{d}\Sigma/\mathrm{d}\Omega)_{\gamma'}$, and thus it can be expressed by

$$\frac{\mathrm{d}\Sigma}{\mathrm{d}\Omega} = \left(\frac{\mathrm{d}\Sigma}{\mathrm{d}\Omega}\right)_\delta + \left(\frac{\mathrm{d}\Sigma}{\mathrm{d}\Omega}\right)_{\gamma'} + C. \tag{1}$$

The constant C attributes to additional incoherent scattering contributions and diffuse scattering. The limited q range of the performed SANS experiments does not give access to the entire scattering intensity of rather large microstructural objects, like δ phase precipitates or grain boundaries and various inhomogeneities. However, only the Porod regime [38] of these objects is visible in the SANS patterns, indicated by a decay of intensity with q^{-4} at small values of q. Therefore, $(\mathrm{d}\Sigma/\mathrm{d}\Omega)_\delta = P'q^{-4}$, where P' is the Porod constant [38].

The characteristic peak maximum in the SANS patterns results only from γ′ phase precipitates and was analyzed by applying a microstructural model of densely packed spheres (hard-sphere potential)

$$\left(\frac{\mathrm{d}\Sigma}{\mathrm{d}\Omega}\right)_{\gamma'} = (\Delta\eta)^2 \int_0^\infty n(r)V(r)^2 P(q,r)S(q,r_{\mathrm{HS}},f_{\mathrm{HS}})\,\mathrm{d}r, \tag{2}$$

where $\Delta\eta$ is the difference in scattering length densities between the precipitates and the matrix, $n(r)\,\mathrm{d}r$ is the number density of the precipitates with radius between r and $r+\mathrm{d}r$. A logarithmic normal distribution was chosen for $n(r)$. $V(r)$ is the precipitate volume and $P(q,r) = F(q,r)^2$ is the particle form factor for spherical particles, where the form factor amplitude is given by (see e.g. [39]).

$$F(q,r) = \frac{3[\sin(qr) - qr\cos(qr)]}{(qr)^3}. \tag{3}$$

$S(q,r_{\mathrm{HS}},f_{\mathrm{HS}})$ defines the structure factor of a mono-disperse hard-sphere model describing the effect of the inter-particle interference [39]. r_{HS} is the hard-sphere radius of a precipitate with the radius r, which includes a depleted zone around the particle and is given by $r_{\mathrm{HS}} = \chi_{\mathrm{HS}}\, r$, where χ_{HS} is the hard-sphere constant. The hard-sphere volume fraction f_{HS} is related to the volume fraction of the precipitate f by $f_{\mathrm{HS}} = f(r_{\mathrm{HS}}/r)^3 = f\chi_{\mathrm{HS}}{}^3$).

The difference in scattering length densities $\Delta\eta$ is given by

$$\Delta\eta = \langle\eta_{\mathrm{m}}\rangle - \langle\eta_{\mathrm{p}}\rangle = \sum_{i=1}^{M} \frac{x_i^{\mathrm{m}} b_i}{v_{\mathrm{m}}} - \sum_{j=1}^{N} \frac{x_j^{\mathrm{p}} b_j}{v_{\mathrm{p}}}, \tag{4}$$

where $\langle\eta_{\mathrm{m}}\rangle$ and $\langle\eta_{\mathrm{p}}\rangle$ are the average scattering length densities of the matrix and the precipitates, respectively. b is the scattering length of the individual atoms, x is the atomic concentration in the respective phase and the atomic volume is denoted by v. APT measurements provided numerical values for x of matrix and precipitates, respectively. The numerical values for b were taken from Ref. [40], and the atomic volumes v were calculated from the lattice constants for both phases taken from Ref. [7]. Eventually the difference in scattering length densities was calculated according to Eq. (4) with $\Delta\eta = 8.5 \times 10^9\ \mathrm{cm}^{-2}$.

All experimental SANS patterns were least-square fitted by the structural model given in Eq. (1). A custom-written computer software program based on the programming package Mathematica® (Wolfram Research) was used for model fitting, utilizing a built-in least-squares fitting routine. The radius of the precipitates, the number density of the particles, the full width at half maximum (FWHM) of the particle size distribution, the Porod constant, and the constant C were used as fitting parameters. Typical examples of the data fitting are presented in Fig. 6, showing that the model function is able to describe the characteristic maximum and the small shoulder over the entire q range of experimental data points.

3.4. Kinetics of γ′ phase precipitation

Fig. 7 shows the main parameters of the least-square model fitting, radius R, number density N, volume fraction f, and the full

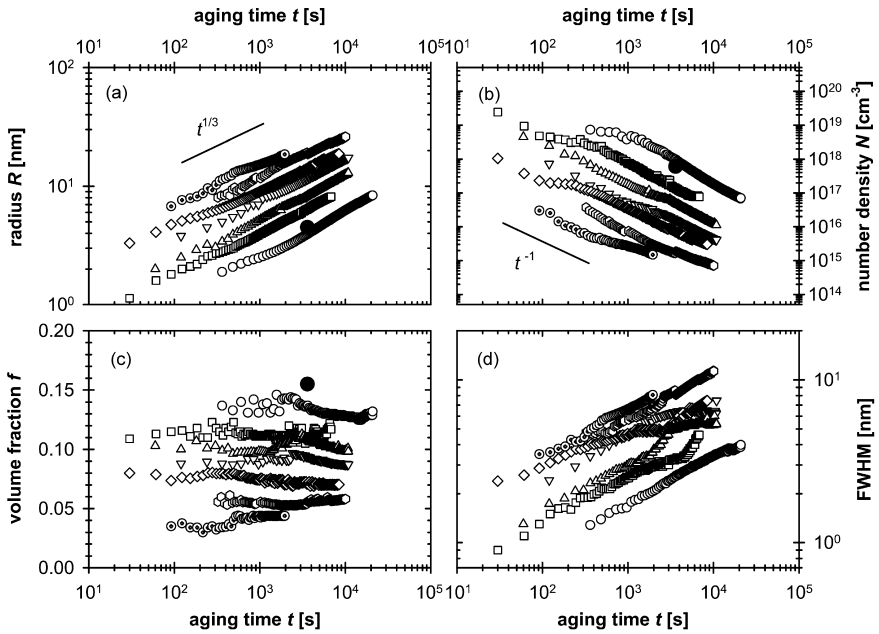

Fig. 7. Radius R (a), number density N (b), volume fraction f (c), and full width at half maximum (FWHM) of the particle size distribution (d) of γ′ phase precipitates in ATI Allvac® 718Plus™ alloy determined by SANS (open symbols) and APT (filled symbols), respectively, as a function of aging time t for various temperatures: 1048 K (circles), 1073 K (squares), 1098 K (triangles up), 1123 K (triangles down), 1148 K (diamonds), 1173 K (hexagons), and 1198 K (dotted circles).

width at half maximum (FWHM) of the particle size distribution of the γ′ phase precipitates as a function of time t for various aging temperatures T. In Fig. 7a it can clearly be seen that R increases with increasing aging time and the growth of the radius is proportional to $t^{1/3}$, as indicated by the solid line. As shown in Fig. 7b, aging at lower temperatures results in higher number densities of precipitates. N decreases for all temperatures proportional to t^{-1} (solid line) with increasing aging time. The entire volume fraction of the precipitates f (Fig. 7c) is highest for aging at the lowest temperature and stays rather constant for the investigated time range. FWHM increases with increasing time, whereas aging at lower temperatures results in lower values of FWHM at the same aging time (Fig. 7d). It is shown that there is good agreement between the values measured by SANS (open symbols) and APT (filled symbols).

4. Discussion

The classical-nickel-iron chromium alloy 718 has been the work horse in the field of high-duty applications for the past four decades. Thus, numerous studies report on the mechanical properties and the microstructure of alloy 718 [1–4]. In recent years the superalloy ATI Allvac® 718Plus™ with improved properties and 718-like processability was developed. Up to now there has been only a few studies on this novel alloy, especially mentioning the first work of Cao et al. [16–18]. The present work is focusing on microstructural investigations of comprehensive understanding of the γ′ phase and its precipitation behavior.

TEM and APT gave detailed information about morphology and chemical composition of the precipitates. The precipitation kinetics of the γ′ phase is studied by in situ SANS using a special high-temperature furnace. It is demonstrated that this experimental method is very powerful for studying the entire path of precipitation on one single specimen. The interpretation of SANS patterns is usually not straightforward and needs additional microstructural information. The present study is a good example of applying results from complementary techniques for SANS data interpretation, i.e. TEM provided information about shape and arrangement of the precipitates and APT gave the chemical composition of matrix and precipitates. In former SANS studies of precipitation kinetics in nickel-based alloys, the numerical value of the difference in scattering length densities $\Delta\eta$ was affected by high uncertainty because of missing chemical information of the phases. The present study overcomes this deficiency by taking data from APT including all chemical elements for the calculation of $\Delta\eta$. Nevertheless, one should keep in mind that the volume measured by APT (Fig. 2) is small and only a very limited number of precipitates are used for the calculation of the chemical composition and the proximity histogram (Fig. 3). Therefore, the value of $\Delta\eta$ might be affected by chemical variance within the material, resulting in an error in the order of 10%. Therefore, the numerical values of number density and volume fraction of the γ′ phase precipitates are affected by this error (Fig. 7).

There are also some drawbacks concerning the in situ SANS experiments. The in situ setup strongly limits the accessible q range, because the entire experiment was performed at only one constant sample-to-detector distance. The limited q range complicates the quantitative evaluation of the SANS patterns by least-square data fitting. Therefore, the structural model for the microstructure had to be simplified, especially concerning the scattering contribution of the δ phase. Nevertheless, the results for the γ′ phase seem to be significant and reliable.

The present study confirms results of earlier studies on ATI Allvac® 718Plus™, but also some discrepancies have been surfaced, where Cao et al. [17,18] reported the presence of γ″ phase precipitates. However, in the present study TEM and APT measurements showed that there was no γ″ phase present in the investigated material. This result is in agreement with the work of Vishwakarma et al. [19], who showed in a TEM study that the alloy contains no γ″ phase precipitates.

4.1. Coarsening of the γ′ phase precipitates

The kinetics of precipitation in nickel-based alloys is of high scientific and technological interest. Therefore, numerous studies of the precipitation behavior in superalloys exist in scientific literature. Lifshitz and Slyozov [41] and Wagner [42] postulated the general theory of particle coarsening (LSW theory), which was consequently advanced by Ardell and Nicholson [43] for describing the coarsening of γ′ phase precipitates in nickel-aluminum alloys. Since then, the LSW theory has been successfully applied in numerous studies on nickel-based alloys. Several modifications of the classical theory exist, which take factors influencing the kinetics of coarsening into account. For an overview of γ′ phase precipitation in nickel-based alloys see Refs. [44,45].

The trends shown in Fig. 7 indicate classical coarsening (Ostwald ripening) of the γ′ phase for the presented aging temperatures in the investigated time range. Therefore, the LSW theory [41,42] was applied to the analysis of the coarsening of the γ′ phase precipitates, which predicts

$$R^3 - R_0^3 = Kt, \tag{5}$$

where R_0 is the radius of the γ′ phase precipitates at the beginning of coarsening and K is the rate constant. The classical LSW theory is valid only at the limit of dilute solutions, however, as indicated by experimental results from TEM, APT and SANS, the number density of the γ′ phase precipitates is high, reaching volume fractions of up to 15% (Fig. 7c). Calderon et al. modified the LSW theory for concentrated alloys, giving a modified rate constant K defined by [46]

$$K = \frac{8D_{\mathrm{eff}}V_{\mathrm{m}}C_{\gamma}(1-C_{\gamma})\sigma}{9R_{\mathrm{g}}T(C_{\gamma'}-C_{\gamma})^2}. \tag{6}$$

V_{m} is the molar volume of the precipitates, σ is the specific interfacial energy between matrix and precipitates, R_{g} is the gas constant, and C_{γ} and $C_{\gamma'}$ are the solubility of the solute in equilibrium with a particle of infinite radius of γ phase and γ′ phase, respectively. The effective diffusion coefficient D_{eff} is defined by

$$D_{\mathrm{eff}} = D_0 \exp\left(-\frac{Q}{R_{\mathrm{g}}T}\right), \tag{7}$$

where D_0 is the diffusion constant and Q is the activation energy for coarsening. The experimental data in Fig. 7a were least-square fitted by Eq. (5), yielding the fit parameter K for the various aging temperatures. Fig. 8 shows an Arrhenius plot according to Eqs. (6) and (7), where it can be clearly seen that there is a linear relationship between $\ln(TK)$ and T^{-1}. Least-square fitting of the data in the Arrhenius plot (Fig. 8) yielded the activation energy Q for coarsening of the γ′ phase precipitates of 303 kJ mol^{-1}, which is higher than the activation energy of 260 ± 13 kJ mol^{-1} for diffusion of aluminum in a matrix of nickel [47]. However, this value lies well in the range for coarsening of γ′ phase precipitation in various other nickel-based alloys (Table 2). A closer look at Table 2 clearly indicates the rather large limits of variation within the same class of alloys, e.g. Q for simple binary Ni–Al model alloys differ by more than a factor of two. Microstructural studies on various commercial superalloys also show significant diversity in Q. However, most values are in the range from about 270 to 390 kJ mol^{-1}.

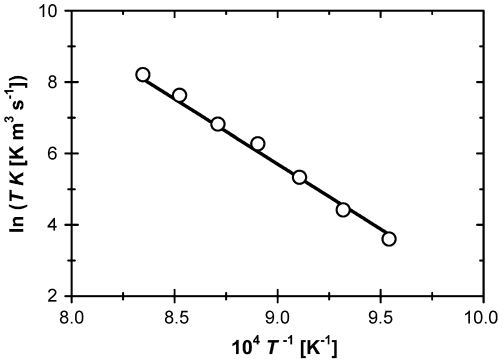

Fig. 8. Arrhenius plot for the derivation of the activation energy for coarsening (303 kJ mol^{-1}) of γ′ phase precipitates in the superalloy ATI Allvac® 718Plus™.

The interfacial energy σ is determined from Eqs. (6) and (7). The molar volume of the γ′ phase is calculated from the crystal lattice constant $a_{\gamma'} = 0.3605 \pm 0.0002$ nm, given by Ref. [7]. The values of C_{γ} and $C_{\gamma'}$ are taken from the chemical composition of the matrix and the precipitates measured by APT. The derivation of a reliable value for D_0 is difficult, because diffusion constants in ATI Allvac® 718Plus™ are not reported in the literature. Nevertheless, an estimate for the diffusion constant can be made by adopting $D_0 = 1.9$ cm^2 s^{-1} for binary nickel-aluminum alloys [48]. One should keep in mind that D_0 is affected by a rather large experimental variation [47,58]. Consequently, a value of 47 mJ m^{-2} for σ is calculated. Table 3 gives an overview of various studies for interfacial energies in nickel-based alloys, from which it can be seen

Table 2
Experimentally determined values for the activation energy Q for coarsening of γ′ phase precipitates in binary Ni–Al model alloys and various industrially processed superalloys.

Alloy	Investigated temperature range [K]	Experimental techniques	Activation energy Q [kJ mol^{-1}]	Reference
ATI Allvac® 718Plus™	1048–1223	SANS	303	Present study
Ni–13.5 at.% Al	898–1048	TEM	270	[43]
Ni–12.3 at.% Al	943–968	TEM	374[a]	[48]
Ni–12.5 at.% Al	823–973	XRD	160[a]	[49]
Alloy PE 16	973–1123	TEM	280	[50]
Alloy PE 16	900–1313	SANS	342	[28]
Alloy PE 16	973–1113	TEM, SANS	339[a]	[29]
Alloy PE 16	943–1113	TEM	331[a]	[51]
Alloy 80a	1023–1203	TEM	274.1	[52]
Alloy 80a	973–1123	TEM	392[a]	[51]
Alloy 80a	1023–1173	SANS	388	[31]
Alloy IN 738	1023–1123	TEM	269	[53]
Alloy IN 738	1023–1223	TEM	269	[54]
Alloy IN 738	1123–1373	TEM	330	[55]
Alloy SC 16	1123–1373	TEM	340	[55]
Alloy 700	1144–1366	TEM	270	[56]
Alloy Mar-M247	1143–1293	TEM	272	[57]
Alloy TM-321	1143–1293	TEM	277	[57]

[a] Activation energy calculated from data given in reference.

Table 3
Experimentally determined values for the interfacial energy σ between γ' phase precipitates and γ phase matrix for binary Ni–Al model alloys and various industrially processed superalloys.

Alloy	Investigated temperature range [K]	Experimental techniques	Interfacial energy σ [mJ m^{-2}]	References
ATI Allvac® 718Plus™	1048–1198	SANS	47	Present study
Ni–13.5 at.% Al	898–1048	TEM	30	[43]
Ni–13.5 at.% Al	898–1048	TEM	14	[59]
Ni–12.3 at.% Al	943–968	TEM	19.5[a]	[49]
Ni–14 at.% Al	823	APT	19	[60]
Ni–12.5 at.% Al	823–973	XRD	16.4[a]	[50]
Ni–13 at.% Al	723–823	SANS	13.5	[25]
Alloy 80a	1023–1173	SANS	12	[31]
Alloy 80a	1073	TEM	61.13	[61]
Alloy PE 16	873–1073	TEM	90	[62]
Alloy PE 16	1023	SANS	1	[27]
Alloy PE 16	1073	TEM	90.92	[61]
Alloy 105	1073	TEM	57.69	[61]
Alloy 700	1073	TEM	71.10	[61]
Various alloys	1073–1418	TEM	140	[63]

[a] Averaged value.

that, for binary nickel-aluminum model alloys, σ is in the range of 20 mJ m^{-2}. However, for commercial superalloys the values for σ are significantly higher. The experimental result of 47 mJ m^{-2} for ATI Allvac® 718Plus™ lies in the range of the field of commercial superalloys. Table 3 also illustrates the large variation of σ in the same classes of alloys. In conclusion, the numerical values of Q and σ should be dealt with caution, due to possible influences from measured temperature ranges, experimental methods, the uncertainty of D_0, and various other uncertainties.

4.2. Mechanical properties

The mechanical characterization by hardness testing already indicates the strong influence of the applied heat treatment. Aging at temperatures from 1048 to 1198 K leads to a significant increase of hardness compared to the as-quenched state. The lower aging temperatures result in higher values of hardness than higher aging temperatures.

Especially for technological applications it would be desirable to calculate the mechanical properties of nickel-based superalloys on the basis of microstructural information of the γ' phase precipitates. There are several established models for the calculation of mechanical strength on the basis of interaction between dislocations and precipitates, whereby the dislocations (1) bow around the particles (Orowan mechanism) or (2) cut through the precipitates [1,64].

The adapted form of the Orowan mechanism is given by [65]

$$\sigma_\gamma = \sigma_0 + \frac{2Gb_{0,\gamma}\phi}{4\pi(\Lambda - 2R)} \ln\left(\frac{\Lambda - 2R}{2b_{0,\gamma}}\right), \quad (8)$$

where σ_γ is the tensile yield strength of the precipitation-hardened alloy, σ_0 is the tensile yield strength of the matrix phase, G is the shear modulus of the matrix phase and $b_{0,\gamma}$ is the length of its Burger's vector $\mathbf{b}_{0,\gamma}$. Λ denotes the inter-particle spacing between the precipitates and R is their radius. The parameter ϕ is related to the Poisson's ratio μ of the γ phase matrix by $\phi = 1/2[1 + (1-\mu)^{-1}]$. Eq. (8) was used to estimate the strengthening by intermetallic γ' phase precipitates in ATI Allvac® 718Plus™. The inter-particle spacing is calculated from microstructural data (Fig. 7) by $\Lambda = R/\sqrt{3f/\pi}$. The numerical values for the parameters are taken from the literature: $b' = 0.254$ nm [7], $G = 77$ GPa and $\mu = 0.3$ [1].

The increase of mechanical strength due to cutting of precipitates is described by [66]

$$\sigma_\gamma = \sigma_0 + \frac{M_T G' b_{0,\gamma'}}{R\sqrt{\pi\omega_q}} \sqrt{f}\left(\frac{2\gamma_0\omega_r R}{G' {b_{0,\gamma'}}^2}\right)^{3/2}, \quad (9)$$

where $M_T = 2.75$ is the Taylor factor, G' is the shear modulus of the precipitates and $b_{0,\gamma'}$ is the length of its Burger's vector. γ_0 denotes the energy density of the planar anti-phase boundary due to cutting of the precipitates. $\omega_q = 0.75$ and $\omega_r = 0.82$ are constants [66]. Eq. (9) was applied for calculating the strengthening by cutting of γ' phase precipitates. Therefore, the numerical values for the parameters are taken from the literature: $G' = 55$ GPa [1] and $b' = 0.255$ nm [7]. As far as can be ascertained, the literature does not report γ_0 for ATI Allvac® 718Plus™. Thus, $\gamma_0 = 104$ mJ m^{-2} [1] for γ' phase precipitates in a nickel–chromium–aluminum alloy was assumed to be a reasonable estimate for the present study.

The experimental values for yield strength are calculated from the Vickers hardness HV measurements (Fig. 1) by the correlation "strength [MPa] = 3.2 HV", which is of course a rather crude approximation, but should provide the right tendency. Fig. 9 shows a comparison between the calculated values (Eqs. (8) and (9)) and the experimental data from hardness testing. The analysis indicates that Eq. (9) is in fair agreement with the experimental values at the early stages of aging. However, Eq. (8) (Orowan mechanism) shows a decrease of strength from about 3000 to 1300 MPa with increasing aging time, which clearly does not represent the accurate trend of the experimental data. Strictly speaking, Eq. (8) is only valid under the condition $R/b_0 > 30$, which is fulfilled for aging times over 3000 s in the present case. At later stages the calculated curve (Eq. (8)) heads towards the experimental data. This finding indicates that

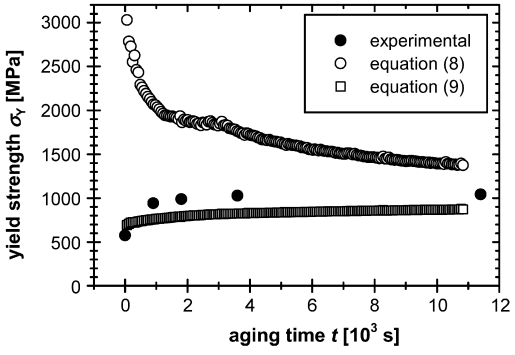

Fig. 9. Comparison between the experimental data and the calculations of yield strength σ_γ on the basis of microstructural parameters for ATI Allvac® 718Plus™ aged at 1098 K. The experimental values were estimated from Vickers hardness measurements (Fig. 1). The calculations were performed on the basis of a modified Orowan mechanism (Eq. (8)) and a model for cutting of the precipitates (Eq. (9)).

strengthening by Orowan mechanism might take place only in the later stages, whereas other mechanisms, e.g. cutting of particles, are dominant in the early stages. One should keep in mind that the radii of the γ′ phase precipitates have a certain variance (see FWHM in Fig. 7d), which leads to concurring strengthening mechanisms at the same stage. Nevertheless, it is shown that mechanical properties might be calculated from microstructural parameters by rather simple correlations, which represents a challenging task especially for technological applications of superalloys. Therefore, further work in this field is in progress.

5. Summary

The precipitation behavior and the mechanical properties of the superalloy ATI Allvac® 718Plus™ were studied as a function of heat treatment temperature and aging time by hardness testing, electron microscopy, atom probe tomography, and in situ high-temperature small-angle neutron scattering. The results are summarized as follows:

(1) Aging heat treatments of the superalloy ATI Allvac® 718Plus™ lead to a significant increase of hardness, which is due to precipitation of intermetallic phases.
(2) The microstructure of the alloy contains two types of intermetallic phases, namely γ′ phase and δ phase. The γ′ phase shows the morphology of nanometer-sized spherical particles, which are homogeneously distributed in the matrix.
(3) Experimental results from SANS indicate that γ′ phase precipitates show coarsening in the investigated time range, which can be described by a modified LSW theory for concentrated alloys. The numerical value for the activation energy for coarsening and the interfacial energy between matrix and precipitates are in the range of other commercial superalloys.
(4) The mechanical properties are calculated by a modified Orowan model and a model for cutting of the precipitates, which provide reasonable results, however, the strengthening mechanism seems to be more complex than these two simple models.

Acknowledgements

The authors would like to thank C.D. Dewhurst from the Institut Max von Laue - Paul Langevin, Grenoble for his support at the SANS measurements and valuable discussions on data treatment and evaluation. Technical support from G. Hawranek and S. Pölzl from the Department of Physical Metallurgy and Materials Testing, Leoben is gratefully acknowledged.

References

[1] C.T. Sims, N.S. Stoloff, W.C. Hagel (Eds.), Superalloys II, Wiley, New York, 1987.
[2] H.L. Eiselstein, Am. Soc. Test. Mater. Spec. Tech. Publ. 396 (1965) 62–77.
[3] W.J. Boesch, H.B. Canada, J. Met. 21 (1969) 34–38.
[4] D.F. Paulonis, J.M. Oblak, D.S. Duvall, ASM Trans. Q. 62 (1969) 611–622.
[5] C. Slama, C. Servant, G. Cizeron, J. Mater. Res. 12 (1997) 2298–2316.
[6] V. Beaubois, J. Huez, S. Coste, O. Burcelle, J. Lacaze, Mater. Sci. Technol. 20 (2004) 1019–1026.
[7] R. Cozar, A. Pineau, Metall. Trans. 4 (1973) 47–59.
[8] S.J. Hong, W.P. Chen, T.W. Wang, Metall. Mater. Trans. A 32 (2001) 1887–1901.
[9] K. Kusabiraki, H. Komatsu, S. Ikeuchi, Metall. Mater. Trans. A 29 (1998) 1169–1174.
[10] D. Mukherji, P. Strunz, D. Del Genovese, R. Gilles, J. Rösler, A. Wiedenmann, Metall. Mater. Trans. A 34 (2003) 2781–2792.
[11] D. Del Genovese, P. Strunz, M. Mukherji, R. Gilles, J. Rösler, Metall. Mater. Trans. A 36 (2005) 3439–3450.
[12] V. Kindrachuk, N. Wanderka, J. Banhart, Mater. Sci. Eng. A 417 (2006) 82–89.
[13] T. Fang, S.J. Kennedy, L. Quan, T.J. Hicks, J. Phys. Condens. Matter 4 (1992) 2405–2414.
[14] S. Azadian, L.-Y. Wei, R. Warren, Mater. Charact. 53 (2004) 7–16.
[15] C. Stotter, C. Sommitsch, J. Wagner, H. Leitner, I. Letofsky-Papst, G.A. Zickler, W. Prantl, M. Stockinger, Int. J. Mater. Res. (formerly Z. Metallkd.) 99 (2008) 376–380.
[16] W.D. Cao, R.L. Kennedy, Acta Metall. Sin. 18 (2005) 39–46.
[17] W.-D. Cao, in: E.A. Loria (Ed.), Superalloys 718, 625, 706 and Derivatives, The Minerals, Metals & Materials Society, Warrendale, 2005, pp. 165–177.
[18] X. Xie, C. Xu, G. Wang, J. Dong, W.-D. Cao, R. Kennedy, in: E.A. Loria (Ed.), Superalloys 718, 625, 706 and Derivatives, The Minerals, Metals & Materials Society, Warrendale, 2005, pp. 193–202.
[19] K.R. Vishwakarma, N.L. Richards, M.C. Chaturvedi, Mater. Sci. Eng. A 480 (2008) 517–528.
[20] E. Cadel, D. Lemarchand, S. Chambreland, D. Blavette, Acta Mater. 50 (2002) 957–966.
[21] M.K. Miller, Micron 32 (2001) 757–764.
[22] G. Kostorz, J. Appl. Cryst. 24 (1991) 444–456.
[23] R. Gilles, Z. Metallkd. 96 (2005) 325–334.
[24] A.D. Sequeira, H.A. Calderon, G. Kostorz, J.S. Pedersen, Acta Metall. Mater. 43 (1995) 3427–3439.
[25] P. Staron, R. Kampmann, Acta Mater. 48 (2000) 701–712.
[26] M. Kompatscher, M. Bär, J. Hecht, C. Muheim, J. Kohlbrecher, G. Kostorz, W. Wagner, Nucl. Instrum. Methods Phys. Res. A 495 (2002) 40–47.
[27] R.E. Beddoe, P. Haasen, G. Kostorz, Z. Metallkd. 75 (1984) 213–216.
[28] K. Ali, S. Messoloras, R.J. Stewart, J. Phys. F. Met. Phys. 15 (1985) 487–505.
[29] H.P. Degischer, W. Hein, H. Strecker, W. Wagner, R.P. Wahi, Z. Metallkd. 78 (1987) 237–249.
[30] B. Tian, O. Paris, G.A. Zickler, C. Lind, G. Wasle, R.P. May, Scripta Mater. 47 (2002) 25–30.
[31] G.A. Zickler, B. Tian, C. Lind, O. Paris, J. Appl. Cryst. 36 (2003) 484–488.
[32] P. Bianchi, F. Carsughi, D. D'Angelo, M. Magnani, A. Olchini, R. Rustichelli, M. Stafanon, Physica B 156&157 (1989) 688–690.
[33] P. Strunz, D. Mukherji, R. Gilles, A. Wiedenmann, H. Fuess, J. Appl. Cryst. 34 (2001) 541–548.
[34] D. Schwahn, W. Kesternich, H. Schuster, Metall. Trans. A 12 (1981) 155–165.
[35] H. Lemke, Y. Wang, D. Mukherji, W. Chen, A. Wiedenmann, R.P. Wahi, Z. Metallkd. 87 (1996) 286–294.
[36] R. Gilles, D. Mukherji, P. Strunz, A. Wiedenmann, R.P. Wahi, Z. Metallkd. 88 (1997) 518–521.
[37] N. Ratel, G. Bruno, B. Demé, J. Phys. Condens. Matter 17 (2005) 7061–7075.
[38] G. Porod, in: O. Glatter, O. Kratky (Eds.), Small Angle X-ray Scattering, Academic Press, London, 1982, pp. 17–51.
[39] D.J. Kinning, E.L. Thomas, Macromolecules 17 (1984) 1712–1718.
[40] H. Rauch, W. Waschkowski, in: A.-J. Dianoux, G. Lander (Eds.), Neutron Data Booklet, Old City Publishing, Philadelphia, 2003, pp. 1.1-1–1.1-17.
[41] I.M. Lifshitz, V.V. Slyozov, J. Phys. Chem. Solids 19 (1961) 35–50.
[42] C. Wagner, Z. Elektrochem. 65 (1961) 581–591.
[43] A.J. Ardell, R.B. Nicholson, Acta Metall. 14 (1966) 1295–1309.
[44] C.S. Jayanth, P. Nash, J. Mater. Sci. 24 (1989) 3041–3052.
[45] A. Baldan, J. Mater. Sci. 37 (2002) 2379–2405.
[46] H.A. Calderon, P.W. Voorhees, J.L. Murray, G. Kostorz, Acta Metall. Mater. 42 (1994) 991–1000.
[47] W. Gust, M.B. Hintz, A. Lodding, H. Odelius, P. Predel, Phys. Stat. Sol. 64 (1981) 187–194.
[48] T. Hirata, D.H. Kirkwood, Acta Metall. 25 (1977) 1425–1434.
[49] C. Marsh, H. Chen, Acta Metall. Mater. 38 (1990) 2287–2298.
[50] K.B.S. Rao, V. Seetharaman, S.L. Mannan, P. Rodriguez, Mater. Sci. Eng. 58 (1983) 93–106.
[51] B. Reppich, G. Schumann, Mater. Sci. Eng. A 101 (1988) 171–182.
[52] P.K. Footner, B.P. Richards, J. Mater. Sci. 17 (1982) 2141–2153.
[53] R.A. Stevens, P.E.J. Flewitt, Mater. Sci. Eng. 37 (1979) 237–247.
[54] P.J. Henderson, M. McLean, Acta Metall. 31 (1983) 1203–1219.
[55] T. Malow, J. Zhu, R.P. Wahi, Z. Metallkd. 85 (1994) 9–19.
[56] E.H. van der Molen, J.M. Oblak, O.H. Kriege, Metall. Trans. 2 (1971) 1627–1633.
[57] H.T. Kim, S.S. Chun, X.X. Yao, Y. Fang, J. Choi, J. Mater. Sci. 32 (1997) 4917–4923.
[58] R.A. Swalin, A. Martin, Trans. Am. Inst. Min. Met. Eng. 206 (1956) 567–572.
[59] A.J. Ardell, Acta Metall. 16 (1968) 511–516.
[60] H. Wendt, P. Haasen, Acta Metall. 31 (1983) 1649–1659.
[61] X. Li, N. Saunders, A.P. Miodownik, Metall. Mater. Trans. A 33 (2002) 3367–3373.
[62] R.J. White, S.B. Fisher, Mater. Sci. Eng. 33 (1978) 149–157.
[63] R.A. Ricks, A.J. Porter, R.C. Ecob, Acta Metall. 31 (1983) 43–53.
[64] E. Nembach, G. Neite, Prog. Mater. Sci. 29 (1985) 177–319.
[65] M.F. Ashby, Acta Metall. 14 (1966) 679–681.
[66] V. Mohles, D. Rönnpagel, E. Nembach, Comput. Mater. Sci. 16 (1999) 144–150.

B.4 G. A. Zickler , R. Radis, R. Schnitzer, E. Kozeschnik, M. Stockinger and H. Leitner. The Precipitation Behavior of Superalloy ATI Allvac®718Plus™. *Advanced Engineering Materials*, 12:176-183, 2010.

ADVANCED ENGINEERING MATERIALS

DOI: 10.1002/adem.200900282

The Precipitation Behavior of Superalloy ATI Allvac 718Plus

By *Gerald A. Zickler*, Rene Radis, Ronald Schnitzer, Ernst Kozeschnik, Martin Stockinger* and *Harald Leitner*

ATI Allvac 718Plus is a novel nickel-based superalloy, which was designed for heavy-duty applications in aerospace gas turbines. The precipitation kinetics of the intermetallic δ (Ni_3Nb) and γ′ ($Ni_3(Al,Ti)$) phases in this alloy are of scientific as well as technological interest because of their significant influence on the mechanical properties. Important parameters like grain size are controlled by coarse δ precipitates located at grain boundaries, whereas small γ′ precipitates are responsible for strengthening by precipitation hardening. In the present study, the microstructure is investigated by three-dimensional atom probe tomography and simulated by computer modeling using the thermo-kinetic software MatCalc. The results of numerical simulations and experimental data are compared and critically discussed. It is shown that the chemical compositions of the phases change during isothermal aging, and the precipitation kinetics of δ and γ′ phases interact with each other as shown in a time temperature precipitation (TTP) plot. The TTP plot shows C-shaped curves with characteristic discontinuities in the temperature range, where simultaneous and concurrent precipitation of the δ and γ′ phases occurs. This leads to a competition in the diffusion of Nb and Al, which are partly present in both phases. Thus, the present study gives important information on heat treatments for ATI Allvac 718Plus in order to achieve the desired microstructure and mechanical properties.

Nickel-iron-chromium-based superalloys are widely used in applications requiring high strength and toughness at elevated temperatures. Gas turbines, especially aerospace gas turbine disks are classical fields of application.[1] Therefore, nickel-iron-chromium-based superalloys are of high scientific and technological interest. The classical nickel-iron-chromium-based alloy 718 has been the work horse in the field of high-duty applications for several decades.[2,3] Recently, the novel superalloy ATI Allvac 718Plus[a] was developed on the basis of alloy 718 by Cao et al.[4–6]. ATI Allvac 718Plus shows an improved combination of advanced mechanical properties, long-time stability at elevated temperatures and processability, i.e., good forgeability, weldability and machineability, when compared to classical nickel-based alloys. Therefore, the alloy was intensively studied, especially focusing on metallurgical and mechanical aspects,[4–6] microstructural phases,[7,8] grain growth and recrystallization,[9] and various degradation mechanisms, e.g., fissuring in welding zones,[10,11] and grain boundary cracking.[12,13]

ATI Allvac 718Plus gains its extraordinary properties from its complex microstructure, where two types of intermetallic phases are embedded in a disordered face-centered cubic γ matrix. Firstly, the γ′ phase $Ni_3(Al,Ti)$ with its $L1_2$-ordered face-centered cubic crystal structure[14] acting as nanometer-sized obstacles for the migration of dislocations and therefore primarily accounting for the mechanical properties of the alloy.[8] Secondly, the δ phase Ni_3Nb[15] of orthorhombic crystal structure, which precipitates in plate-shaped morphology predominantly at grain boundaries. The δ phase is of technological importance as it is used for controlling the grain

[*] *Dr. G. A. Zickler, Dr. R. Schnitzer, Dr. H. Leitner*
Department of Physical Metallurgy and Materials Testing, Christian Doppler Laboratory "Early Stages of Precipitation" Montanuniversität Leoben, Franz-Josef-Straße 18, A-8700 Leoben, Austria
E-mail: gerald.zickler@mu-leoben.at
R. Radis, Prof. E. Kozeschnik
Christian Doppler Laboratory "Early Stages of Precipitation", Institute of Materials Science and Technology, Vienna University of Technology
Favoritenstraße 9-11, A-1040 Vienna, Austria
R. Radis
Institute for Materials Science and Welding, Graz University of Technology
Kopernikusgasse 24, A-8010 Graz, Austria
Dr. M. Stockinger
Böhler Schmiedetechnik GmbH & Co KG
Mariazeller-Straße 25, A-8605 Kapfenberg, Austria

[a] *Allvac 718Plus is a registered trademark of Allegheny Technologies Inc. (ATI), Monroe, NC, USA.*

ADVANCED ENGINEERING MATERIALS

growth during processing, e.g., hot forging.[7] γ'' precipitates and γ'/γ'' co-precipitates, which are common in alloy 718 and several derivatives,[1] are not reported for ATI Allvac 718Plus. Apart from qualitative information about the prevailing phases, quantitative data, i.e., size, number density, and volume fraction of the precipitates, as function of heat treatment temperature and time are needed for the proper adjustment of the alloy's microstructure and its properties. Time temperature precipitation (TTP) plots provide valuable quantitative information about the precipitation behavior as guide for heat treatments of the alloy. TTP plots for ATI Allvac 718Plus are still very rare in scientific literature, especially mentioning the studies of Cao et al.[5,6] and Stotter et al.[7] However, none of these studies gave deeper insight into the simultaneous precipitation behavior of both γ' and δ phases, and how their precipitation kinetics interfere, thus leaving important questions in the precipitation behavior of this novel nickel-iron-chromium-based superalloy still open.

The aim of the present study is to gain fundamental knowledge of the precipitation behavior of the intermetallic γ' and δ phases in ATI Allvac 718Plus from combined experimental investigations and thermo-kinetic computer simulations. Experimental data are provided from atom probe tomography (APT) and two recently published studies on the γ' phase[8] and the δ phase.[7] It is focused on the influence of heat treatments on the precipitation kinetics and the interaction between precipitates of different phases.

Experimental

The chemical composition of the as-received superalloy ATI Allvac 718Plus is given in Table 1. The material was homogenized (solution treated) at a temperature of 1283 K for 7200 s followed by isothermally aging at 1048 K for 60, 300, 3600, and 10 800 s. All heat treatments were performed on cylindrical samples with a diameter of 5 mm and a length of 15 mm in a quenching dilatometer Bähr 805 A/D (Bähr Thermoanalyse, Hüllhorst, Germany) in vacuum $<5 \times 10^{-4}$ mbar.

Atom Probe Tomography

For APT investigations small rods with a cross section of 0.3 mm × 0.3 mm were cut from the heat-treated samples. Standard electro polishing was applied for the preparation of thin tips using a layer of 85% acetic acid ($C_2H_4O_2$) and 15% perchloric acid ($HClO_4$) solution topped over a dielectric liquid in a first step, followed by a second step in an electrolyte of 2% perchloric acid ($HClO_4$) in 2-butoxyethanol ($C_6H_{14}O_2$).[16] The APT measurements were conducted on the high-resolution atom probe microscope Imago LEAP 3000X HR (Imago Scientific Instruments, Madison, WI, USA).

Table 1. Chemical composition of the superalloy ATI Allvac 718Plus as determined by chemical analysis (wt%).

Ni	Ti	Al	Nb	Cr	Co	Fe	Mo	W	C
base	0.73	1.42	5.55	18.02	9.11	9.51	2.66	1.05	0.021

The investigations were performed at a temperature of 60 K in voltage mode with a pulse fraction of 15%. The three-dimensional reconstructions of the measured volumes were made by the atom probe visualization and analysis software IVAS.

Thermo-kinetic Simulations of Precipitation Kinetics

The precipitation behavior of the superalloy ATI Allvac 718Plus was numerically simulated with the software program MatCalc, [17–19] using a novel theoretical approach, which was developed for the simulation of the precipitation kinetics in multi-component multi-phase alloys. In this simulation the theoretical foundation of precipitate growth is based on a mean-field formulation utilizing the thermodynamic extremal principle of maximum entropy production.[20] The numerical time integration procedure for the evolution equations is based on the classical model of Kampmann and Wagner.[18,21] The nucleation of the precipitates is calculated from the extended classical nucleation theory for multi-component systems[17]. In this approach the transient nucleation rate J of the precipitates is given by

$$J = N_0 \, Z \, \beta^* \, \exp\left(\frac{-G^*}{k_B T}\right) \exp\left(\frac{-\tau}{t}\right) \quad (1)$$

where N_0 is the total number of possible nucleation sites. The Zeldovich factor Z takes into account the destabilization of the nucleus due to thermal vibration. The atomic attachment rate β^* accounts for the long-range diffusion transport of atoms, which is necessary for the formation of nuclei if the chemical compositions of matrix and precipitates are different. k_B is the Boltzmann constant, T is the absolute temperature, τ is the incubation time, and t represents time. The critical nucleation energy G^* is given by

$$G^* = \frac{16\pi}{3} \frac{\gamma_0^3}{\Delta G_{vol}^2} \quad (2)$$

where γ_0 is the specific interfacial energy and ΔG_{vol} is the total driving force. The interfacial energy is calculated from the chemical compositions of precipitates and matrix, respectively, by applying a generalized nearest-neighbor broken-bond model, assuming planar, sharp, and coherent interfaces.[22] However, corrections taking into account the spherical shape of the nucleus are considered as a function of the precipitate radius.[23] Entropic contributions from the finite interface thickness are taken into account by temperature-dependent correction functions (Figure 1) as observed,[24] see also a previous study by Pudar et al.[25]. The latter corrections become particularly prominent close to the solution temperature of the precipitates. For numerical simulations, data for thermodynamics and diffusion were taken from the respective databases.[26,27]

Results

Precipitation Kinetics

In order to get a first insight into the precipitation behavior, numerical simulations were compared with experimental

ADVANCED ENGINEERING MATERIALS

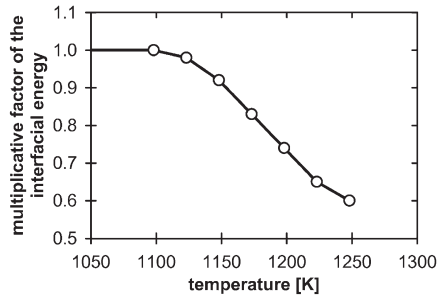

Fig. 1. Temperature-dependent correction factor of the interfacial energy between matrix and precipitates.

data. Figure 2 shows numerical simulations and experimental data[8] for radius R, number density N, and volume fraction f of the γ' phase precipitates in ATI Allvac 718Plus as a function of time t for aging temperatures of 1123 K (Fig. 2(a–c)) and 1173 K (Fig. 2(d–f)). For reasons of comparability, the identical heat treatments were simulated as experimentally performed in reference.[8] The simulation takes into account the solution heat treatment and the heating ramp of 100 K min^{-1} to the respective aging temperatures. It can be seen that the radius R increases with aging time and the growth rate is proportional to $t^{1/3}$ in the late stages (Fig. 2(a, d)). The number density N leaps to values of about 10^{20} cm^{-3} at the nucleation of the γ' phase precipitates, followed by a continuous decrease of N, which shows proportionality to t^{-1} in the late stages of precipitation (Fig. 2(b, e)). The volume fraction of the precipitates f (Fig. 2(c, f)) increases simultaneously with N and then stays rather constant for the investigated time range. The kinetics of R, N, and f for the γ' phase precipitates indicates classical coarsening, which is described in detail in reference.[8] The results of Figure 2 demonstrate the excellent agreement between numerical simulations and experimental data. The minor fluctuations in the simulated curves are due to numerical effects.

Besides the precipitation of the γ' phase, the evolution of the δ phase was also simulated and compared to experimental data. Figure 3 depicts calculated volume fractions of the δ precipitates and experimental data[7] as a function of aging time for various temperatures from 1123 to 1248 K. For reasons of comparability, the identical heat treatments were simulated as applied in reference.[7] The precipitation of the δ phase occurs in the time range of 10^3 to 10^4 s for all investigated temperatures, and it is unambiguous that the kinetics of the δ phase precipitation is slower than that of the γ' phase (Fig. 2). At later stages of the heat treatments the volume fractions stay constant for all aging temperatures. For further experimental details of the δ phase in ATI Allvac 718Plus see reference.[7]

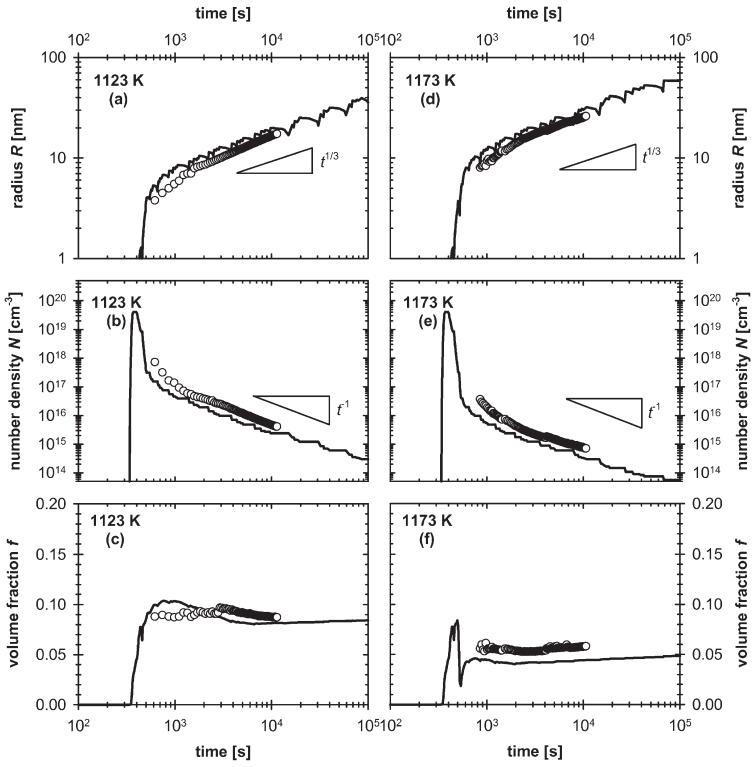

Fig. 2. Radius R, number density N, and volume fraction f of γ' precipitates in ATI Allvac 718Plus as a function of aging time at 1123 K (a–c) and 1173 K (d–f), respectively. Solid lines represent the thermo-kinetic simulations of the precipitation kinetics and circles indicate experimental data taken from reference.[8]

The precipitation behavior of both γ' and δ phases is shown in a TTP plot in Figure 4, where the calculated results for the δ phase are compared with experimental data.[7] The TTP plot illustrates that the C-shaped precipitation curves of the γ' and δ phase show their maxima at 1000 and 1220 K, respectively. The rapid precipitation of the γ' phase is faster than the precipitation of the δ phase, which leads to a delay in the kinetics of the δ phase and a discontinuity in the curves of the TTP plot.

Chemical Composition of the Phases

APT measurements were performed investigating the changes of chemical composition of the γ' phase precipitates during aging heat treatments. Figure 5(a) shows three-dimensional atom maps of ATI Allvac 718Plus aged

ADVANCED ENGINEERING MATERIALS

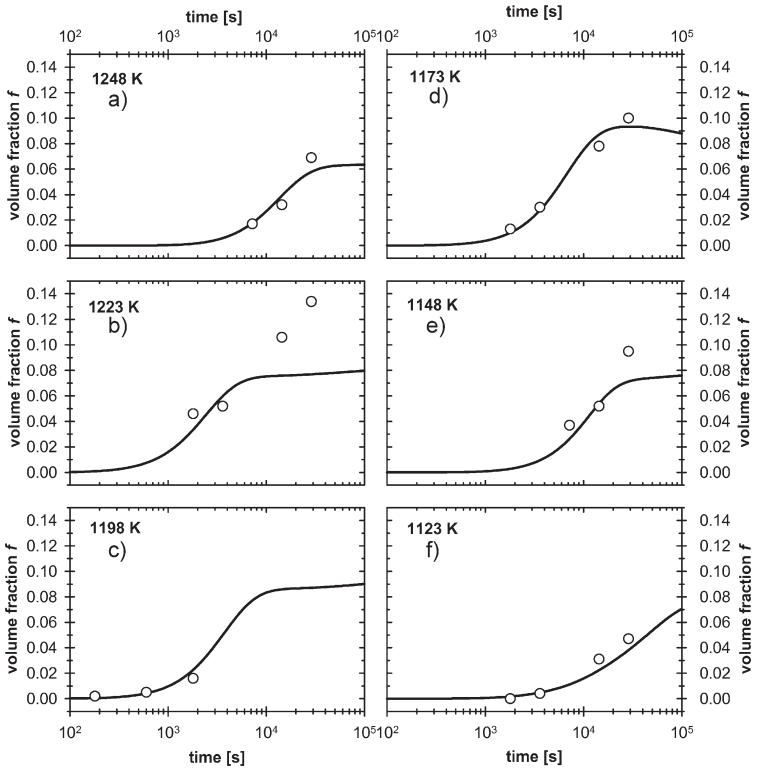

Fig. 3. The volume fraction of δ precipitates in ATI Allvac 718Plus as a function of aging time at various temperatures. Solid lines represent the thermo-kinetic simulations of the precipitation kinetics and circles indicate experimental data taken from reference.[7]

at 1048 K for 60 s. Visual inspection does not give any evidence for precipitates and the spatial distribution of the elements seems to be completely homogeneous in the early stages of aging. By applying a cluster-search algorithm[28] for Ti and Al, respectively, it is possible to reconstruct clusters or small precipitates inside the scanned volume. The algorithm allows the identification of clusters and provides chemical information for both clusters and matrix. For the cluster-search algorithm, the parameters separation distance, surrounding distance, and erosion distance[28] were set to 0.42 nm. It can be seen that the clusters of Ti (Fig. 5(b)) and Al (Fig. 5(c)) atoms have the same spatial distribution in the measured sample, indicating a correlation between Ti and Al. Figure 5 clearly demonstrates that there is elemental decomposition already in the early stages of aging at 1048 K.

Representative examples of three-dimensional atom maps of the sample aged at 1048 K for 3600 s are illustrated in Figure 6. In the late stages of aging it can be clearly seen that the spatial distributions of the elements Al (Fig. 6(a)) and Ti (Fig. 6(b)) are not homogeneous in the investigated volume. From visual inspection it is obvious that the clusters of Al and Ti are sited at the same positions in the alloy, which already indicates the presence of precipitates. For better illustration, iso-concentration surfaces for Al + Ti = 12 at.% are set in Figure 6(c), clearly showing the almost spherical shape of the precipitates. Figure 7 shows a proximity histogram, which is calculated over the iso-concentration surfaces shown in Figure 6(c). Therein the chemical elements are displayed as a function of the distance from the iso-concentration surfaces.

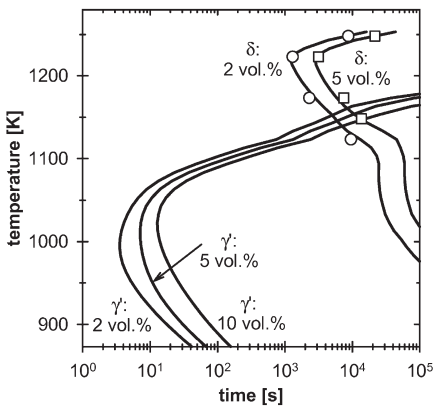

Fig. 4. Isothermal TTP plot for the superalloy ATI Allvac 718Plus calculated by thermo-kinetic simulations. Experimental data points indicate 2 vol% (circles) and 5 vol% (squares) of the δ phase taken from reference.[7]

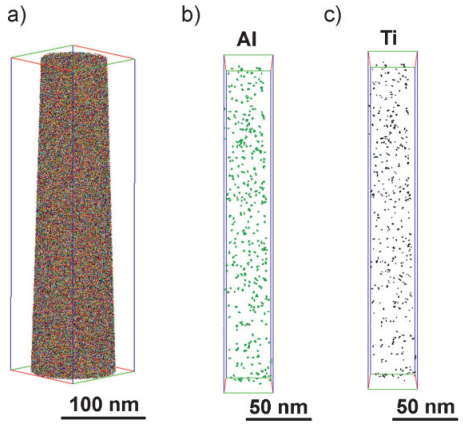

Fig. 5. (a) Three-dimensional volume reconstruction of the superalloy ATI Allvac 718Plus isothermally aged at 1048 K for 60 s. Clusters of Al (b) and Ti (c) atoms.

ADVANCED ENGINEERING MATERIALS

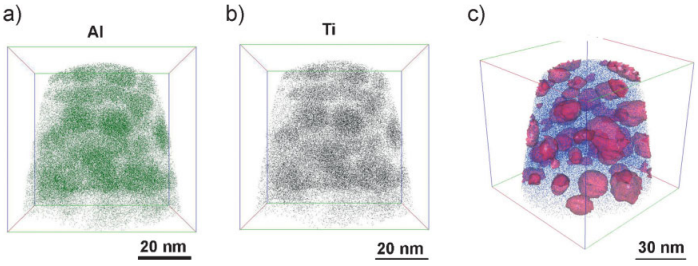

Fig. 6. Three-dimensional volume reconstruction of the superalloy ATI Allvac 718Plus isothermally aged at 1048 K for 3600 s. Atom maps for Al (a) and Ti (b). Iso-concentration surfaces set at Al + Ti = 12 at% (c).

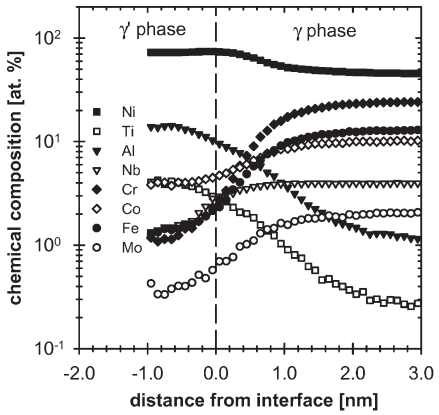

Fig. 7. Proximity histogram of the iso-concentration surfaces (Al + Ti = 12 at.%) illustrated in Figure 6(c) (heat treatment: 1048 K for 3600 s) for ATI Allvac 718Plus. The alloying elements are shown as a function of the distance from the iso-concentration surface (vertical line).

At first glance it is unambiguous that the precipitates in ATI Allvac 718Plus do not have a simple stoichiometric composition. Figure 7 illustrates that Ni, Al, and Ti are the main elements of the precipitates, which indicates the presence of the γ' phase. However, the phase also contains considerable amounts of Co and Nb. As can be seen in Figure 7, the proximity histogram does not show a sharp interface between the precipitates and the matrix. There is a rather broad transition zone in the order of 2 nm, where Ni, Al, and Ti are enriched in the γ' phase precipitates, whereas all other alloying elements decrease their concentrations toward the core.

Table 2 shows the average chemical composition of the γ' precipitates and the γ matrix gained from APT. It can be seen that the chemical composition for both phases strongly depends on the applied aging heat treatments. The results for the γ' precipitates and the γ matrix are summarized as follows:

(a) γ' precipitates: In the early stages of aging the γ' precipitates are mainly Al-rich clusters with an Al concentration of 50.98 at% (1048 K, 60 s). The Ti concentration of 12.67 at% is also much higher than in the late stages, but the Ni concentration of 23.31 at% is rather low. After aging at 1048 K for 300 s the chemical concentration of Al and Ti in the precipitates decreases, however, the concentrations have not reached quasi equilibrium values. In the later stages (1048 K, 3600 s and 1048 K, 10800 s) the chemical concentrations of Al and Ti decrease to rather constant values of about 12.7 at% and 3.7 at%, respectively, and the Ni concentration increases to about 75 at%. The concentration of Nb in the precipitates shows an interesting trend, starting with a relatively high value of 2.32 at% at the beginning of aging, which decreases to 1.11 at% at 10 800 s. This finding indicates that Nb is needed in the early stages for the precipitation of the γ′ phase, however, it is replaced by other atoms, e.g., Al and Ti, in the late stages. The Cr content increases from 4.7 at% in the early stages to 10.0 at% after aging at 1048 K for 300 s, and then decreases to a rather constant level of about 1.3 at% at long aging times.

(b) γ matrix: The γ phase shows a more or less stable concentration of Ni and decreasing contents of Al and Ti, which are consumed by formation of γ' precipitates. The trend of Nb is opposite, showing an increase of the element in the γ matrix with increasing in aging time at 1048 K.

Table 2. Chemical composition (at.%) of the γ matrix and the γ' precipitates of ATI Allvac 718Plus determined by APT.

Aging heat treatment	Phase	Ni	Cr	Co	Fe	Ti	Al	Nb	W	Mo
1048 K/60 s	γ	53.62 ± 0.02	19.77 ± 0.02	8.95 ± 0.01	10.67 ± 0.01	0.85 ± 0.01	3.23 ± 0.01	0.40 ± 0.01	0.29 ± 0.01	1.72 ± 0.01
1048 K/60 s	γ'	23.31 ± 0.43	4.73 ± 0.22	2.64 ± 0.17	2.55 ± 0.16	12.67 ± 0.35	50.98 ± 0.52	2.32 ± 0.06	0.11 ± 0.03	0.56 ± 0.08
1048 K/300 s	γ	49.215 ± 0.032	21.043 ± 0.019	9.454 ± 0.012	11.306 ± 0.014	0.673 ± 0.003	2.704 ± 0.006	3.473 ± 0.002	0.265 ± 0.002	1.644 ± 0.005
1048 K/300 s	γ'	66.098 ± 0.098	9.936 ± 0.032	6.215 ± 0.025	5.797 ± 0.024	1.693 ± 0.013	6.256 ± 0.025	2.584 ± 0.005	0.217 ± 0.005	1.014 ± 0.010
1048 K/3600 s	γ	48.630 ± 0.035	21.460 ± 0.022	9.548 ± 0.014	11.521 ± 0.015	0.521 ± 0.003	2.152 ± 0.006	3.840 ± 0.002	0.293 ± 0.002	1.753 ± 0.006
1048 K/3600 s	γ'	73.807 ± 0.131	1.366 ± 0.015	4.211 ± 0.026	1.508 ± 0.016	3.696 ± 0.025	12.834 ± 0.048	1.974 ± 0.005	0.182 ± 0.005	0.273 ± 0.007
1048 K/10800 s	γ	47.819 ± 0.028	22.050 ± 0.017	9.738 ± 0.011	11.879 ± 0.012	0.422 ± 0.002	1.833 ± 0.005	3.857 ± 0.002	0.304 ± 0.002	1.819 ± 0.005
1048 K/10800 s	γ'	75.107 ± 0.091	1.271 ± 0.010	4.071 ± 0.018	1.529 ± 0.011	3.620 ± 0.017	12.619 ± 0.033	1.114 ± 0.002	0.126 ± 0.003	0.282 ± 0.005

ADVANCED ENGINEERING MATERIALS

The δ precipitates are too large for being studied by conventional APT preparation techniques. Therefore, local preparation by focused ion beam techniques would be desired, which are currently not available. However, further studies in this challenging field are in progress.

Discussion

The present study is aimed at providing comprehensive understanding of the γ' and δ phase precipitation behavior in ATI Allvac 718Plus. The precipitation behavior of intermetallic γ' and δ phases are simulated by thermo-kinetic calculations and the results are compared to experimental data. As seen in Figures 2 and 3, there is good agreement between the experimentally determined precipitation kinetics and the numerical simulations. The time and temperature dependences of the precipitation kinetics are summarized in a TTP plot (Fig. 4). As can be clearly seen, the C-shaped TTP curves of both phases show discontinuities in their shape in the temperature region of 1050 to 1150 K. These discontinuities are of special interest and will be discussed in more detail in the following. Therefore, experimental data and results of numerical simulations for the chemical composition of the γ' precipitates and γ matrix are shown as a function of aging time at a temperature of 1048 K in Figure 8. The precipitation reactions are manifested by changes of chemical concentrations in Figure 8. The simulations predict the precipitation of the γ' phase at about 10^2 s and the δ phase at about 5×10^4 s at an aging temperature of 1048 K (for comparison see Fig. 4). The results for the γ' precipitates (Fig. 8(a–c)) and the γ' matrix (Fig. 8(d–e)) are summarized as follows:

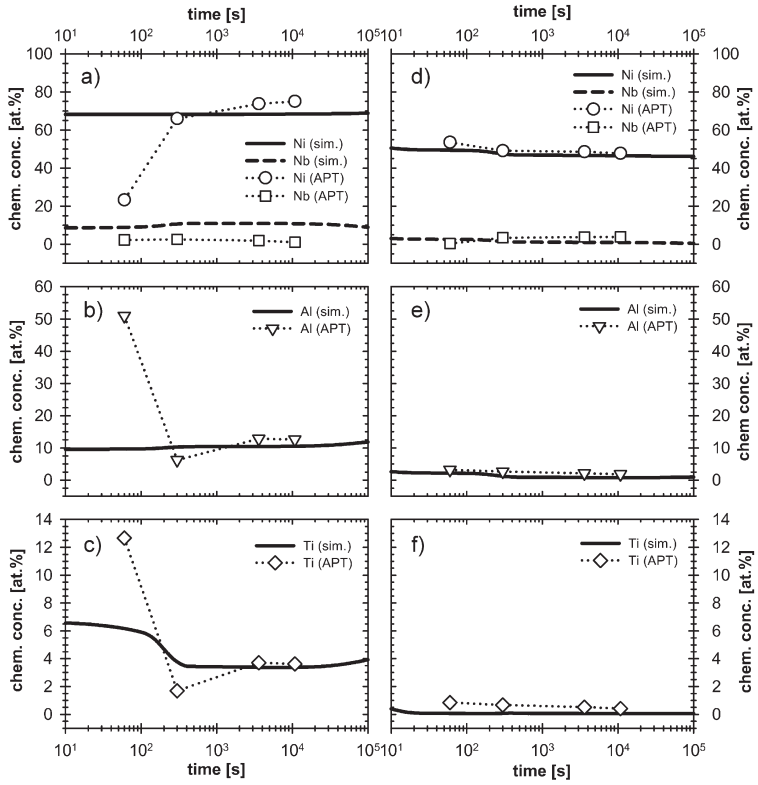

Fig. 8. The chemical composition of the γ' precipitates (a–c) and the γ matrix (d–f) of ATI Allvac 718Plus as a function of aging time at a temperature of 1048 K. Solid and dashed lines represent the thermo-kinetic simulations of the chemical composition and symbols indicate experimental data determined by APT.

(a) γ' precipitates: As can be seen in Figure 8(a–c), the qualitative trends of experiments and numerical simulation are in reasonable agreement in the late stages of aging. However, at the early stages the simulation does not account for the high concentrations of Al (Fig. 8(b)) and Ti (Fig. 8(c)) in the γ' phase. At this point it has to be mentioned that the results from the cluster-search algorithm depend on the chemical element selected for the algorithm (see Section 3.2.). Therefore, one should keep in mind that a search for Al and Ti atoms will also deliver clusters which are rich in these elements. The simulations predict an increase in the Nb content during the precipitation of the γ' phase, which stays rather constant until the precipitation of the δ phase, leading to a decrease in content. The experimental data also show that the concentration of Nb in the γ' phase decreases in the time range from 60 to 10 800 s. The trends for Nb in the experimental data and the simulation are qualitatively identical. However, the simulation overestimates the absolute numerical values (Fig. 8(a)).

(b) γ matrix: For the γ phase (Fig. 8(d–f)), the qualitative trends of experimental data and numerical simulations for Ni, Al, and Ti are also in reasonable agreement. Al (Fig. 8(e)) and Ti (Fig. 8(f)) both show a decrease of chemical concentration. However, the simulation underestimates the absolute numerical values. The simulations predict a decrease of Nb content in the γ phase at the precipitation of the γ' phase ($\sim 10^2$ s) and the δ phase ($\sim 5 \times 10^4$ s). This trend seems to be physically meaningful but it is not reproduced by the experimental data (Fig. 8(d)). The discrepancy is probably due to the fact that the volumes investigated by APT are small and might not be completely representative of the behavior of the alloy.

ADVANCED ENGINEERING MATERIALS

Nb is of special interest for the precipitation behavior because it is present in the γ, γ', and δ phases. It should be emphasized that a certain amount of Nb is not unusual in γ' phase precipitates, which was also reported for conventional alloy 718.[29] Thus, Nb atoms, previously incorporated in γ' precipitates, are redistributed by diffusional transport, which leads to a delayed precipitation of the δ phase, finally resulting in a discontinuity in the TTP curve. The simultaneous precipitation of the γ' and δ phases promotes a competing growth of both phases. Depending on heat treatment temperature and time, Nb and Al atoms redistribute to achieve optimum thermodynamic conditions. At higher aging temperatures above the γ' phase precipitation no competitive diffusion process occurs, resulting in faster precipitation of the δ phase, which is verified by experimental data.[7] The discontinuity in the C-shaped precipitation curves can also be explained in terms of driving force ΔG_{vol} (Eq. 2). Thermo-kinetic simulations were performed at an aging temperature of 1048 K for two cases: Firstly, simultaneous precipitation of γ' and δ phases and secondly, exclusive precipitation of the δ phase. The comparison of the two cases showed that the driving force ΔG_{vol} for the δ phase is decreased by about 10% when the γ' phase is precipitated simultaneously. Reduced values of ΔG_{vol} for the δ phase in the temperature range of about 1050 to 1150 K are responsible for the discontinuity in the precipitation curves in the TTP plot.

Summary

The present study deals with the precipitation behavior of intermetallic phases in the novel nickel-iron-chromium-based superalloy ATI Allvac 718Plus. Numerical simulations of the precipitation kinetics of the γ' and δ phases were performed by using the thermo-kinetic software Matcalc. The simulated behavior was compared to experimental data from APT measurements and literature data from two recent studies on the same alloy. The main results may be summarized as follows:

(1) The thermo-kinetic simulations of the precipitation behavior are in good agreement with experimental data for γ' and δ phase precipitation.
(2) A complete TTP plot for both phases is calculated, which provides important information for controlling the evolution of the alloy microstructure during heat treatments in order to achieve the desired material properties.
(3) The TTP plot shows C-shaped curves with characteristic discontinuities in the temperature range, where both phases are precipitated. The discontinuity is due to the fact that simultaneous precipitation of the γ' and δ phases leads to a competition in the diffusional transport of the chemical elements Nb and Al.

Received: October 19, 2009
Final Version: December 17, 2009

[1] E. E. Brown, D. R. Muzyka, in: *Superalloys II* (Eds: C. T. Sims, N. S. Stoloff, W. C. Hagel), Wiley, New York **1987**, 165.
[2] H. L. Eiselstein, *Am. Soc. Test. Mater. Spec. Tech. Publ.* **1965**, *396*, 62.
[3] D. F. Paulonis, J. M. Oblak, D. S. Duvall, *ASM Trans. Q.* **1969**, *62*, 611.
[4] W. D. Cao, R. L. Kennedy, *Acta Metall. Sin.* **2005**, *18*, 39.
[5] W.-D. Cao, in *Superalloys 718, 625, 706 and Derivatives*, (Ed: E. A. Loria), The Minerals, Metals & Materials Society, Warrendale **2005**, 165.
[6] X. Xie, C. Xu, G. Wang, J. Dong, W.-D. Cao, R. Kennedy, in *Superalloys 718, 625, 706 and Derivatives* (Ed: E. A. Loria), The Minerals, Metals & Materials Society, Warrendale **2005**, 193.
[7] C. Stotter, C. Sommitsch, J. Wagner, H. Leitner, I. Letofsky-Papst, G. A. Zickler, W. Prantl, M. Stockinger, *Int. J. Mater. Res. (formerly Z. Metallkd.)* **2008**, *99*, 376.
[8] G. A. Zickler, R. Schnitzer, R. Radis, R. Hochfellner, R. Schweins, M. Stockinger, H. Leitner, *Mater. Sci. Eng., A* **2009**, *523*, 295.
[9] C. Sommitsch, D. Huber, F. Ingelman-Sundberg, S. Mitsche, M. Stockinger, B. Buchmayr, *Int. J. Mater. Res. (formerly Z. Metallkd.)* **2009**, *100*, 1088.
[10] K. R. Vishwakarma, N. L. Richards, M. C. Chaturvedi, *Mater. Sci. Eng., A* **2008**, *480*, 517.
[11] K. R. Vishwakarma, M. C. Chaturvedi, *Mater. Sci. Technol.* **2009**, *25*, 351.
[12] R. W. Hayes, *Metall. Mater. Trans. A* **2008**, *39*, 2596.
[13] R. Hayes, E. Thompson, K. Johnson, A. Aichlmayr, *Mater. Sci. Eng., A* **2009**, *510*, 256.
[14] R. Cozar, A. Pineau, *Metall. Trans.* **1973**, *4*, 47.
[15] T. Fang, S. J. Kennedy, L. Quan, T. J. Hicks, *J. Phys. Condens. Matter* **1992**, *4*, 2405.
[16] M. K. Miller, A. Cerezo, M. G. Hetherington, G. D. W. Smith, in *Atom Probe Field Ion Microscopy*, Clarendon Press, Oxford **1996**.
[17] J. Svoboda, F. D. Fischer, P. Fratzl, E. Kozeschnik, *Mater. Sci. Eng., A* **2004**, *385*, 166.
[18] E. Kozeschnik, J. Svoboda, P. Fratzl, F. D. Fischer, *Mater. Sci. Eng., A* **2004**, *385*, 157.
[19] E. Kozeschnik, J. Svoboda, F. D. Fischer, *CALPHAD* **2004**, *28*, 379.
[20] J. Svoboda, I. Turek, F. D. Fischer, *Philos. Mag.* **2005**, *85*, 3699.
[21] R. Kampmann, R. Wagner, in *Kinetics of Precipitation in Metastable Binary Alloys – Theory and Applications, Acta Scripta Metall. Series, Decomposition of Alloys: the Early Stages* (Eds: P. Haasen, V. Gerold, R. Wagner, M. F. Ashby), Pergamon Press, Oxford **1984**, 91.
[22] B. Sonderegger, E. Kozeschnik, *Scr. Mater.* **2009**, *60*, 635.
[23] B. Sonderegger, E. Kozeschnik, *Metall. Mater. Trans. A* **2009**, *40*, 499.

[24] Y. W. Lee, H. I. Aaronson, *Acta Metall.* **1980**, *28*, 539.
[25] M. Pudar, E. Kozeschnik, A. Sormann, E. Parteder, *Steel Res. Int.* **2008**, *79*, 660.
[26] C. E. Campbell, W. J. Boettinger, U. R. Kattner, *Acta Mater.* **2002**, *50*, 775.
[27] Thermotech Sente Software, http://www.thermotech.co.uk **2009**.
[28] A. Cerezo, L. Davin, *Surf. Interface Anal.* **2007**, *39*, 184.
[29] M. K. Miller, S. S. Babu, M. G. Burke, *Mater. Sci. Eng., A* **2002**, *327*, 84.

B.5 R. Schnitzer, R. Radis, M. Nöhrer, M. Schober, R. Hochfellner, S. Zinner, E. Povoden-Karadeniz, E. Kozeschnik and H. Leitner. Reverted Austenite in PH 13-8 Mo Maraging Steels. *Materials Chemistry and Physics*, 122:138-145, 2010.

Materials Chemistry and Physics 122 (2010) 138–145

Contents lists available at ScienceDirect

Materials Chemistry and Physics

journal homepage: www.elsevier.com/locate/matchemphys

Reverted austenite in PH 13-8 Mo maraging steels

Ronald Schnitzer[a,*], Rene Radis[b,c], Matthias Nöhrer[a], Michael Schober[d], Rainer Hochfellner[a], Silvia Zinner[e], E. Povoden-Karadeniz[b], Ernst Kozeschnik[b], Harald Leitner[a,d]

[a] Christian Doppler Laboratory for Early Stages of Precipitation, University of Leoben, Franz-Josef-Strasse 18, A-8700 Leoben, Austria
[b] Christian Doppler Laboratory for Early Stages of Precipitation, Vienna University of Technology, Favoritenstrasse 9-11, A-1040 Vienna, Austria
[c] Institute for Materials Science and Welding, Graz University of Technology, Kopernikusgasse 24, A-8010 Graz, Austria
[d] Department of Physical Metallurgy and Materials Testing, University of Leoben, Franz-Josef-Strasse 18, A-8700 Leoben, Austria
[e] Böhler Edelstahl GmbH & Co KG, Mariazeller Strasse 25, A-8605 Kapfenberg, Austria

ARTICLE INFO

Article history:
Received 26 June 2009
Received in revised form 29 January 2010
Accepted 23 February 2010

Keywords:
Maraging steel
Reverted austenite
Atom probe
Transmission electron microscopy

ABSTRACT

The mechanical properties of maraging steels are strongly influenced by the presence of reverted austenite. In this study, the morphology and chemical composition of reverted austenite in a corrosion resistant maraging steel was characterized using transmission electron microscopy (TEM) and atom probe tomography (APT). Two types of austenite, i.e. granular and elongated, are present after aging at 575 °C, whereby the content of the latter increases during aging. The investigations revealed that the austenite phase is enriched in Ni, which prevents the transformation to martensite during cooling. Inside and next to the austenitc areas, Mo and Cr-rich carbides, which form during the aging treatment, were found. Various aging treatments were performed to obtain the activation energy for the formation of reverted austenite. Additionally, the experimental data are compared with thermodynamic and kinetic simulations. Based on these results and the chemical composition changes of the phases, a model for the formation of reverted austenite is presented. It is concluded that precipitation of B2-ordered NiAl and formation of reverted austenite take place simultaneously during aging and that dissolution of precipitates is not essential for the initial formation of reverted austenite.

1. Introduction

The development and production of martensitic hardenable steels (maraging steels) started in the early 1960s in the USA with steels containing 18% Ni and 8–9% Co [1,2]. Due to the sharp drop of the availability and the raising costs of Co, alternatives to cobalt containing maraging steels were in demand. Much effort was laid on developing Co-free maraging steels with appropriate mechanical properties [3]. This resulted in a variety of steels with different precipitating elements, e.g. Al, Ti, Cu and also alloys with lowered Ni content. One example for these developments are the PH 13-8 Mo types, which are hardened by the presence of ordered intermetallic β-NiAl phases (CsCl structure) [4]. These alloys possess a good resistance to stress corrosion cracking [5] and superior mechanical properties compared to the 17-4 PH and 15-5 PH types [6]. Its excellent combination of strength and toughness offers a wide range of applications, e.g. dies for plastic moulds, landing gear parts and parts in petrochemical plants [7–9].

A lot of research was conducted on the characterization of the microstructure, especially on the precipitation sequences in maraging steels and on their influence on the mechanical properties [10–14]. An intensive atom probe tomography (APT) investigation on a PH 13-8 Mo alloy was conducted by Ping et al. [6] and by Guo et al. [7], who described the evolution of intermetallic NiAl precipitates. However, from literature it is also well known that, in maraging steels, partial reversion from martensite to austenite takes place during aging treatments [15–20] and this so-called reverted austenite has a strong influence on the mechanical properties. For high toughness requirements, high amounts of reverted austenite are beneficial and therefore, the material is subjected to higher aging temperatures [11,21]. On prolonged aging, coarsening of precipitates results also in an increase of ductility and loss of strength. However, it was reported that the influence of austenite reversion is much more pronounced on softening than the influence of coarsening of precipitates [9,11].

This work focuses on the characterization of reverted austenite in PH 13-8 Mo maraging steels. This type of austenite has to be distinguished from retained austenite, which can also be present in PH 13-8 Mo alloys after cooling from the solution annealing temperature [8]. Depending on the alloy composition and the applied heat treatment, different morphologies of reverted austenite are reported in maraging steels. Generally, reverted austenite could be of granular or elongated shape. Shiang and Wayman [16] classified the observed austenite morphologies into three types, i.e. matrix

* Corresponding author. Tel.: +43 3842 4024214; fax: +43 3842 4024202.
E-mail address: ronald.schnitzer@unileoben.ac.at (R. Schnitzer).

0254-0584/$ – see front matter © 2010 Elsevier B.V. All rights reserved.
doi:10.1016/j.matchemphys.2010.02.058

austenite, lath-like austenite and recrystallized austenite. Matrix austenite grows from retained austenite or nucleates on prior austenite grain boundaries. Lath-like austenite can develop within the martensite lath or grow along the lath boundaries of martensite. Recrystallized austenite forms at higher aging temperatures or longer aging times, and is characterized by a very low density of defects and dislocations. In high Ni alloyed and Ti-containing maraging steels, which are hardened by Ni_3Ti precipitates, the occurrence of Widmanstätten austenite is also mentioned [22,23]. However, it has been shown that the particular type of austenite depends on the applied aging temperature [19]. The orientation relationship between austenite and martensite is generally reported to be of Kurdjumow–Sachs or Nishiyama–Wassermann type [17,24,25].

The formation mechanism of reverted austenite in maraging steels is often related to a diffusion-controlled process. Hereby, it is assumed that the formation of reverted austenite is determined by dissolution of precipitates during aging, which results in a local enrichment of austenite stabilizing elements [23,26–30]. Sinha et al. [17] exclude the mechanism of dissolution of precipitates for the formation of reverted austenite. They suppose that Ni diffuse to dislocations and defects, resulting in microsegregation of austenite stabilizing elements in localized areas. Kim and Wayman [22] suggested that the formation of lath-like austenite in high Ni maraging alloys is shear dominated but assisted by a diffusion-controlled process. However, to the author's best knowledge, there exists no investigation about the formation mechanism of reverted austenite in PH 13-8 Mo alloys. There is a lack of information concerning the morphology, size and chemical composition of reverted austenite in such kind of steels.

The aim of this work is to characterize reverted austenite in a PH 13-8 Mo alloy by the two complementary methods transmission electron microscopy (TEM) and atom probe tomography. Based on experimental results and simulations, the formation mechanism of reverted austenite is discussed.

2. Experimental

The chemical composition of the investigated PH 13-8 Mo maraging steel is given in Table 1. The alloy was commercially produced and provided by the company Böhler Edelstahl GmbH & Co KG as a rolled bar. The material was subjected to solution annealing at 900 °C for 1.5 h and subsequent cooling in air. Aging was performed at 575 °C for various times, up to 1000 h. TEM investigations and APT were conducted on samples, which have been aged for 3 h, 5 h, 10 h and 100 h. The determination of the austenite phase fraction was conducted by X-ray diffraction measurements on a Siemens D500 using Cu$K\alpha$ radiation. For evaluation of the diffraction scans, the method of direct comparison of the integrated intensities of the martensite and austenite peaks [31] was applied. The TEM investigations were performed on polished and electrolytically etched samples on a Phillips CM12 microscope, which was operated at 120 kV.

For APT, small rods were cut from the bulk material and then etched to sharp needles by a standard two-step electro polishing technique [32]. The second polishing step was conducted in a 2% perchloric acid in 2-butoxyethanol. APT was performed on a LEAP™ 3000X HR atom probe in laser mode at a base temperature of 20 K. The laser energy was adjusted to 0.2 nJ and the repetition rate was set to 200 kHz. Data reconstruction was conducted using the software package IVAS™.

Thermodynamic and kinetic simulations were performed with the software package MatCalc 5.30 (rel 1.075) [33–35] and the corresponding thermodynamic and diffusion databases 'mc_steel' [36] and 'mc_sample_fe' [37], respectively. The calculations were performed taking into account the phases FCC_A1 (austenite), BCC_A2 (ferrite) and BCC_B2 (ordered bcc NiAl) and based on the entire time-temperature history of the experiment. For the NiAl precipitates, homogeneous bulk nucleation was assumed, while, for the reverted austenite, only the grain boundaries and subgrain boundaries were considered. A measured prior austenite grain diameter of 25 μm and a subgrain diameter of 1 μm were utilized. Furthermore, a shape factor of H/D = 0.2 (see ref. [38]) was used for the reverted austenite to take into account the elongated shape. For the precipitation simulation, the interfacial energy of the precipitate phases was calculated using the generalized nearest-neighbor broken-bond approach [39], and taking into account size effects for the critical nucleus [40]. Entropic contributions to the interfacial energy stemming from finite interface thickness and mixing across the interface are taken into account by a constant factor of 0.8 for the NiAl phase. No corrections were made for the FCC precipitates at grain boundaries and subgrain boundaries.

Table 1
Chemical composition of the investigated PH 13-8 Mo maraging steel.

	C	Cr	Ni	Mo	Al	Fe
wt.%	0.03	12.70	8.20	2.20	1.10	Bal.
at.%	0.14	13.52	7.73	1.27	2.26	Bal.

3. Results

Aged samples and a solution-annealed sample as reference material were characterized in order to reveal the phase fraction and morphology of austenite, the presence of carbides and the chemical composition of austenite and precipitates.

3.1. Phase fraction of austenite

To determine the amount of reverted austenite present after the applied aging treatments, X-ray diffraction experiments were conducted. Fig. 1 shows the phase fraction of austenite versus aging time for an aging temperature of 575 °C. After solution annealing, the material contains no retained austenite or the amount is below the detection limit of X-ray diffraction of about 3 vol.%. Aging up to 100 h leads to a nearly linear increase of the austenite phase fraction. This is due to the reverse transformation of martensite into austenite during isothermal aging at 575 °C. After 100 h of aging, the austenite phase fraction reaches a plateau at 29 vol.%. No further increase of the austenite phase fraction is observed, even after 1000 h of aging.

3.2. TEM investigations

TEM investigations have been conducted on samples in the as-quenched state as well as after aging at 575 °C for 3 h, 5 h, 10 h and 100 h. The sizes of reverted austenite resulting from evaluation of numerous TEM images are summarized in Table 2. The evaluation of the reverted austenite size was performed separately for granular and elongated shapes. The solution-annealed state did not show any retained austenite and is therefore not depicted here. Furthermore, no carbides were found in the solution-annealed state. Fig. 2 illustrates a bright-field TEM image of a sample aged at 575 °C for 3 h. Small austenite grains with an elliptic shape are present on prior austenite grain boundaries or triple points. The dominant

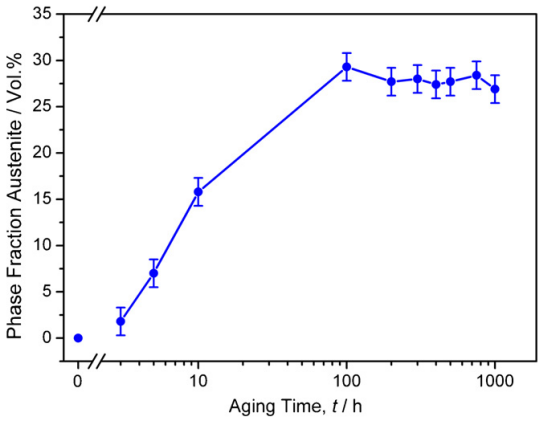

Fig. 1. Phase fraction of austenite as function of aging time. The aging temperature was kept constant at 575 °C.

Table 2
Average values of the size dimensions of reverted austenite after different aging times (aging temperature = 575 °C). The 100 h aged sample exhibit lath-like austenite which can have a length dimension of more than 2000 nm.

Aging time	Austenite morphology	Length [nm]	Width [nm]
3 h	Granular	342	133
	Elongated	469	115
5 h	Granular	340	190
	Elongated	542	143
10 h	Granular	263	151
	Elongated	798	140
100 h	Granular	412	183
	Elongated	≈2000	227

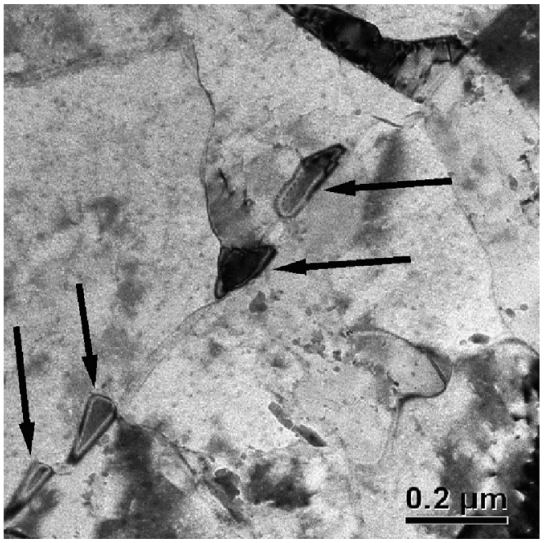

Fig. 2. Bright-field TEM image of a sample aged at 575 °C for 3 h. Matrix austenite (marked with arrows) on prior austenite grain boundaries can be seen.

austenite morphology after 3 h of aging is a granular one with a length of approximately 340 nm and a width of 130 nm. EDS analyses of the austenite grains revealed that the austenite is enriched in Ni, showing a content of approximately 13 at.% Ni compared to 4 at.% Ni in the martensitic matrix. In Fig. 3 TEM images of a sample aged at 575 °C for 5 h are displayed. Clear evidence of different types of austenite was available from the TEM micrographs. The austenite visible in Fig. 3a shows a granular morphology and it has formed within a martensite lath. However, it is noticeable that these austenite regions sometimes contain precipitates (marked with an arrow in Fig. 3a). The TEM image in Fig. 3b shows another type of austenite. It is located along martensite lath boundaries and exhibits an elongated shape. This austenite type grew to an average length of 540 nm and an average width of 140 nm, corresponding to an aspect ratio of 0.25. Fig. 4 provides bright-field TEM images of a sample, which has been aged for 10 h. It can be seen that the fraction of both the elongated austenite (Fig. 4a) as well as the granular (Fig. 4b) has increased. However, in this condition the content of the elongated austenite exceeds the content of the granular one. Mainly the length of the elongated austenite has increased to almost 800 nm resulting in a lowered aspect ratio of 0.18. Fig. 5a and b are illustrations of the microstructure after 100 h of aging, which was observed by TEM investigations. Several austenite laths can be seen inside one martensite lath. Thus, aging at 575 °C for 100 h led to a lamellar structure of alternating austenite and martensite laths. The austenite laths have grown to a length of more than 2000 µm, whereas the increase of the width is small. This results in an aspect ratio of almost 0.10. However, in this condition, almost no granular austenite can be found inside the martensite laths (see Fig. 5b). Fig. 5c also reveals that fine precipitates are present in the austenite. EDS analyses indicate an enrichment of Mo.

However, there is no indication for NiAl precipitates inside the austenite phase. EDS analyses of the austenite grains on the different aged samples have shown that the content of the alloying elements remain constant during aging.

3.3. Atom probe investigations

The chemical composition changes between matrix, precipitates and reverted austenite are in the nm-scale and were therefore analyzed by APT. In Fig. 6, the three-dimensional reconstruction of the atomic positions of a sample aged at 575 °C for 100 h is illustrated. The left image shows the measured volume and the rectangle on the right provides a detail of this volume with the atom positions of Ni, Al and Cr. It can be seen that the analyzed volume consists of different enriched areas, which correspond to different phases. The Ni-enriched area on the top of the analyzed volume is followed by a region with a lower Ni content. In this region small spherical enrichments of Ni and Al are present. These areas correspond to the bcc-B2-ordered NiAl precipitates in the martensitic matrix. On the lower site of the tip, again, a Ni-enriched area can be observed. According to EDS analyses in TEM, it is con-

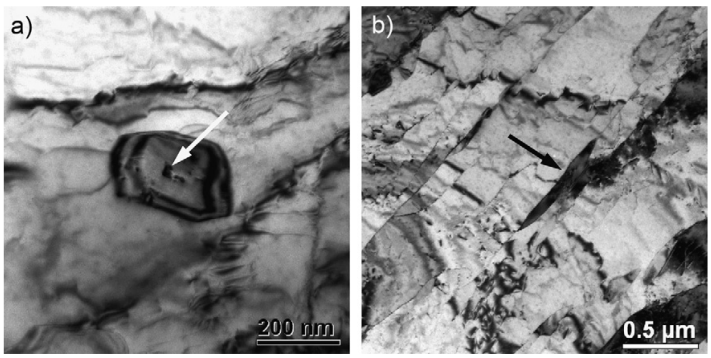

Fig. 3. Bright-field TEM images of a sample aged at 575 °C for 5 h. (a) A Cr-enriched precipitate (marked with an arrow) can be seen inside a granular austenite grain. (b) The arrow indicates elongated austenite, which has grown along a martensite lath boundary.

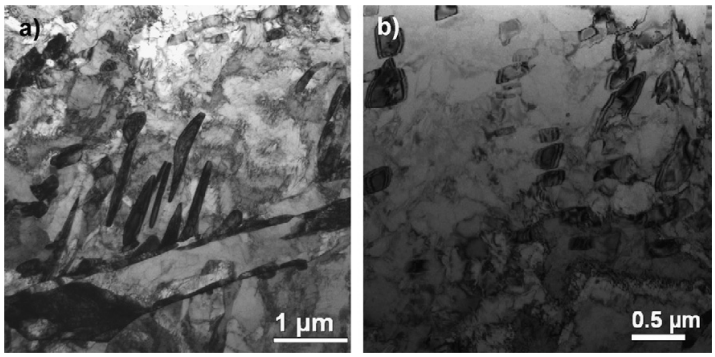

Fig. 4. TEM images of a sample aged at 575 °C for 10 h. (a) Elongated austenite along and inside the martensite lath can be seen. (b) Bright-field TEM image of an area with granular austenite.

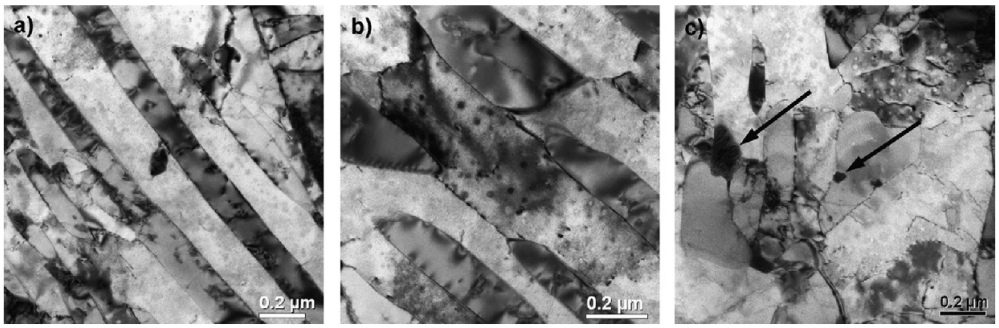

Fig. 5. Bright-field TEM images of a sample aged at 575 °C for 100 h. (a) Lath-like austenite can be seen. (b) NiAl precipitates are only visible in the martensite laths. The austenitic phase is free of this precipitates. (c) Mo-enriched particles inside or next to austenite are shown.

cluded that this Ni-enriched area corresponds to the austenite phase. The measurement shows that this analyzed volume is free of NiAl precipitates. A one-dimensional concentration profile (Fig. 7) along the analysis direction was obtained by positioning a box of 5 nm × 5 nm × 250 nm through the different regions as shown in the left image in Fig. 6. It can be seen that the Ni content in the austenite is increased to about 14 at.% and the aluminium content remains almost the same as in the martensitic matrix. In contrast, both the Ni and Al content are increased in the precipitate. The Ni content in the core of the precipitates reaches the stoichiometric 50 at.%, whereas the Al content is much lower due to a high amount of Fe incorporated in the precipitates.

In Fig. 8, a three-dimensional reconstruction of the atom positions of a sample aged for 10 h is illustrated. The atom positions reveal four different regions by visual inspection. The lower half of the analyzed volume consists of a region where spherical Ni-

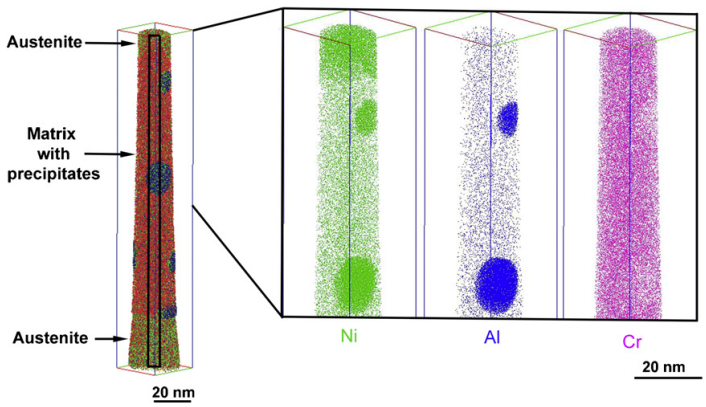

Fig. 6. Three-dimensional reconstruction of a sample aged at 575 °C for 100 h. In the left image the different phases are marked. The large rectangle shows a detail of the measured volume and the distribution of the Ni, Al and Cr atoms. The box in the left image corresponds to a volume, which was analyzed separately to gain details of the chemical variations.

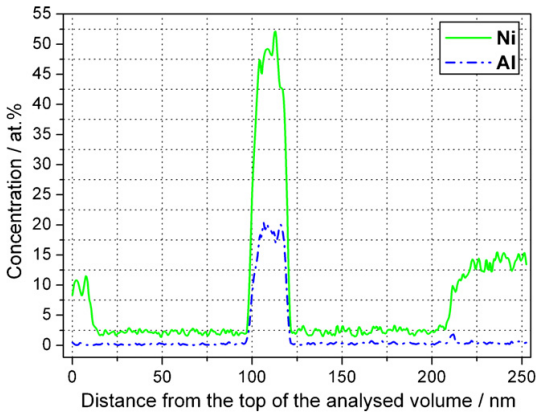

Fig. 7. One-dimensional concentration profile of Ni and Al along the analysis axis of the marked volume from Fig. 6. The areas with Ni increased only represent the reverted austenite.

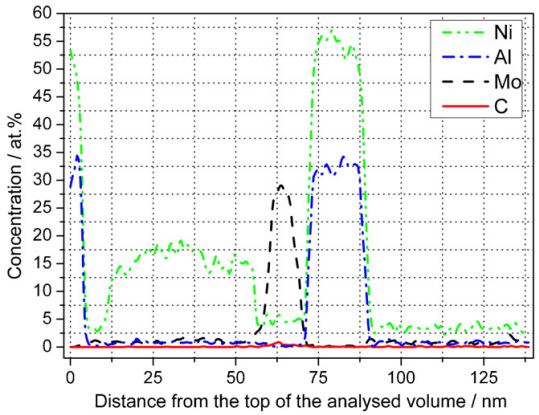

Fig. 9. One-dimensional concentration profile of Ni, Al, Mo and C along the analysis axis of the marked volume from Fig. 8. The area where only the Ni content is increased represents reverted austenite and the one with an increased Mo content corresponds to Mo carbides.

Table 3
Results of the NiAl precipitates obtained by atom probe data analysis with isosurfaces.

	Radius [nm]	Number density [m^{-3}]	vol.%
3 h*	3.4 ± 1.1	1.98E+23	3.3
5 h*	4.0 ± 1.6	1.16E+23	3.2
10 h	5.2 ± 2.1	6.2E+22	3.5
100 h**	9.4	1.1E+22	3.5

* Not depicted here.
** Values with higher uncertainty because of poor statistics.

and Al-enriched volumes are present. This area corresponds to the martensitic matrix with NiAl precipitates. On the upper half of the analyzed volume, a Ni-enriched region, supposed to be reverted austenite, can be recognized. Attached to this region, a Mo- and C-enriched area can be observed. Fig. 9 provides a one-dimensional concentration profile along the analysis axis of a box of 5 nm × 5 nm × 150 nm as shown in Fig. 8a. In the area where austenite is present, a higher Ni content of approximately 15 at.% is observed and the region enriched in Mo shows also a slightly higher C content. The increased Ni and Al content in the precipitates are also visible. A Ni content of about 50 at.% and an Al content of about 30 at.% are reached in the core of the precipitates.

The evaluated radius, number density and volume fraction of the NiAl precipitates after different aging conditions are summarized in Table 3. An increase of the radius, a decrease of the number density and an approximately constant volume fraction of the precipitates with prolonged aging time are observed.

4. Discussion

4.1. Microstructure evolution during aging

Reverted austenite was characterized by transmission electron microscopy on samples, which had been aged for various times. By using TEM, on the one hand, it is possible to gain information about the shape, distribution and size of reverted austenite, on the other hand it is difficult to obtain chemical information in the sub-nm range. By applying atom probe tomography, compositional changes with near atomic resolution can be measured.

The investigations showed that, in the as-quenched state, this alloy contains no retained austenite. Thus, it is assumed that the entire austenite, which is present in the aged conditions, can be related to reverted austenite. This is in disagreement to the results reported by Mittra et al. [8], who have found retained austenite in the as-quenched state. The reason for that might be the higher solution annealing temperature and the fast quenching rate applied in the study by Mittra et al. [8].

TEM investigations revealed two morphologies of reverted austenite in the investigated steel, namely granular and elongated austenite. Following the classification of Shiang and Wayman [16],

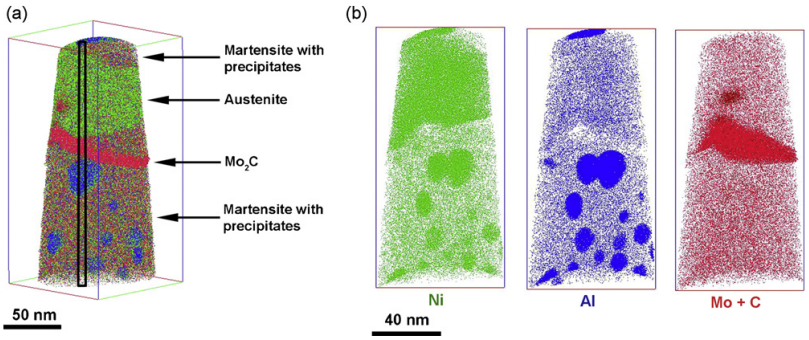

Fig. 8. (a) Three-dimensional reconstruction of sample aged at 575 °C for 10 h. The different measured phases are marked with arrows. The box corresponds to a volume which was analyzed separately to gain details of the chemical variations. (b) Distribution of the Ni, Al and Mo + C atoms.

Table 4
Chemical composition of reverted austenite obtained by TEM and APT of samples aged at 575 °C for 10 h and 100 h (APT data taken from Table 5, all values in at.%).

	10 h		100 h	
	APT	TEM	APT	TEM
Al	0.8	1.0 ± 0.1	0.7	1.4 ± 0.5
Cr	14.1	15.0 ± 1.0	13.6	14.0 ± 1.2
Ni	16.0	13.7 ± 2.3	13.3	13.5 ± 1.4
Mo	0.9	1.4 ± 0.3	0.9	0.6 ± 0.7
Fe	68.2	68.9 ± 2.4	71.5	70.5 ± 2.7

the observed austenite belongs to matrix austenite and lath-like austenite. However, there was no evidence of recrystallized austenite or Widmanstätten austenite, as had been observed in high Ni containing maraging alloys [23]. Non-recrystallized austenite is difficult to distinguish from recrystallized austenite as it is only possible via the dislocation density. The investigations did not reveal austenitic areas showing significant differences in dislocation density. This could be due to the applied aging temperature of 575 °C, which might be too low for recrystallization of austenite. The fractions of the two observed types of austenite change with prolonged aging. After 3 h of aging, only matrix austenite is present. Aging for 10 h leads to additional formation of lath-like austenite, being the dominant morphology after 100 h of aging. The preferred formation of matrix austenite at short aging times might be caused by the low nucleation energy at the prior austenite grain boundaries. Nucleation within the martensite laths might be caused by the high dislocation density, providing numerous low-energy sites for nucleation. The size of the granular austenite during aging is almost constant. In contrast, the elongated austenite increases in size. The growth rate parallel to the lath boundaries is much faster. This indicates that matrix austenite is formed at the beginning of aging and the increase of the phase fraction of austenite during aging can be attributed to the formation and grow of lath-like austenite. A similar behaviour was reported by Shiang and Wayman [16]. These authors assumed that the restricted growth perpendicular to the length axis is due to the inhibition of adjacent austenite laths. However, probably, this is also the reason for the preferred growth direction of reverted austenite in this study. An influence of carbides that hinder the growth of austenite can be excluded because of their minor content present in this alloy.

In addition to TEM investigations, APT measurements were performed to gain information on the processes occurring during reverted austenite formation. The measured chemical compositions of reverted austenite for the 10 h and 100 h aged states are listed in Table 4. The Ni content of reverted austenite varies on different sites between 11 and 16 at.%, which might be an effect of locally different nucleation and growth conditions. The content of other alloying elements in the austenite remains almost constant during aging, which suggests that no redistribution of alloying elements between martensite and austenite takes place. In this study, also, Mo- and Cr-rich carbides located on lath boundaries between austenite and martensite as well as within the austenite were found. This nucleation inside or next to the austenite is due to the higher solubility of C in austenite compared to martensite. In contrast to Mittra et al. [8], who reported the presence of primary carbides in this type of steel, it is assumed that these carbides precipitate during aging, since no carbides were observed in the as-quenched state.

4.2. Formation of reverted austenite

In order to understand the formation mechanism of reverted austenite, it is essential to consider the distribution of alloying elements during aging. Table 5 shows the chemical composition of the present phases, which have been obtained by separation during atom probe data evaluation. The NiAl precipitates were defined by isosurfaces, austenite and martensite were exported to separate volumes. For the 3 h and 5 h aged samples, only the chemical composition of the martensitic matrix and the precipitates are listed, because no reverted austenite has been detected in atom probe in a random run mode. The values for the 100 h aged sample are connected with high uncertainty, due to the limited number of large precipitates measured by APT. The NiAl precipitates contain a significant amount of Fe in all aging conditions. However, the amount of Al increases at the expense of Fe with prolonged aging. According to our calculations, the diffusion of Al atoms is approximately 10 times faster compared to the diffusion of Ni atoms in a PH 13-8 Mo alloy. The amount of Ni in the martensitic matrix decreases slightly during aging, whereas the Fe content increases. The amount of all other alloying elements remains almost constant in the martensitic matrix during aging.

To aid interpretation of the experimental data and to gain information on the initial states of austenite formation, thermodynamic and kinetic calculations were performed. The experimental results, i.e. phase fraction of NiAl precipitates and reverted austenite are compared to values obtained by simulations, using the software package MatCalc 5.30 (rel 1.075) [33–35]. For the simulations, both, the BCC_B2 phase (ordered bcc-B2 NiAl) as well as the FCC_A1 (austenite) are defined as precipitate phases, which can form in the ferritic matrix (BCC_A2). The comparison of the computed results and the experimental measurements (taken from Fig. 1 and Table 3) are presented in Fig. 10. It can be seen that the simulation describes the obtained experimental data quite well. In accordance with the experimental results, the phase fraction of austenite (Fig. 10) increases after 3 h of aging and reaches a constant value after approximately 100 h. It seems that the amount of 30 vol.% is the equilibrium phase fraction of austenite at 575 °C, as this amount remains constant even after 1000 h of aging. The formation of NiAl precipitates and reverted austenite is predicted to start from the

Table 5
Chemical composition of the phases detected by atom probe tomography (all values in at.%).

at.%		Fe	Cr	Ni	Mo	Al	Mn	Si	C
3 h*	Matrix	79.65 ± 0.03	12.99 ± 0.01	5.02 ± 0.01	1.06 ± 0.003	0.77 ± 0.002	0.06 ± 0.001	0.04 ± 0.001	0.02 ± 0.0004
	Precipitates	28.39 ± 0.09	3.32 ± 0.03	41.46 ± 0.11	0.29 ± 0.01	25.93 ± 0.08	0.53 ± 0.01	0.06 ± 0.003	0.02 ± 0.002
5 h*	Matrix	80.16 ± 0.04	13.21 ± 0.01	4.78 ± 0.01	1.05 ± 0.004	0.70 ± 0.003	0.06 ± 0.0009	0.04 ± 0.0007	0.003 ± 0.0002
	Precipitates	24.67 ± 0.10	2.82 ± 0.03	43.84 ± 0.15	0.31 ± 0.01	27.77 ± 0.11	0.50 ± 0.01	0.05 ± 0.004	0.01 ± 0.002
10 h	Matrix	81.75 ± 0.04	12.51 ± 0.01	3.98 ± 0.01	0.92 ± 0.003	0.72 ± 0.003	0.07 ± 0.001	0.04 ± 0.001	0.01 ± 0.0004
	Precipitates	23.67 ± 0.08	2.29 ± 0.02	43.21 ± 0.12	0.28 ± 0.01	29.91 ± 0.10	0.50 ± 0.01	0.10 ± 0.01	0.03 ± 0.003
	Austenite	68.05 ± 0.13	14.03 ± 0.05	16.01 ± 0.05	0.90 ± 0.01	0.84 ± 0.01	0.13 ± 0.004	0.05 ± 0.003	0.001 ± 0.0005
100 h	Matrix	82.40 ± 0.09	12.26 ± 0.03	3.43 ± 0.01	0.79 ± 0.01	1.01 ± 0.01	0.05 ± 0.002	0.04 ± 0.001	0.02 ± 0.0005
	Precipitates	19.15 ± 0.10	1.00 ± 0.02	45.23 ± 0.16	0.15 ± 0.01	33.88 ± 0.13	0.47 ± 0.01	0.09 ± 0.01	0.03 ± 0.003
	Austenite	71.21 ± 0.18	13.59 ± 0.06	13.33 ± 0.06	0.86 ± 0.02	0.72 ± 0.01	0.15 ± 0.01	0.06 ± 0.004	0.08 ± 0.004

* Not depicted here.

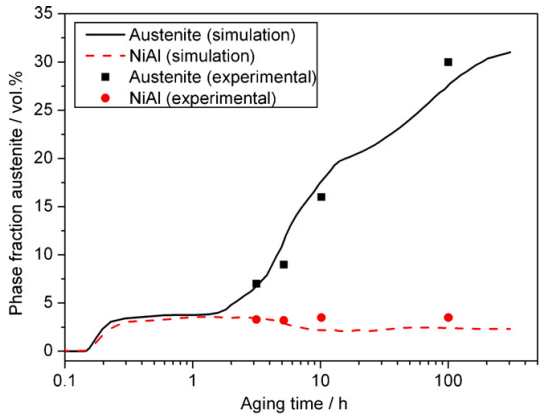

Fig. 10. Thermodynamic simulation showing the phase fraction of NiAl precipitates and reverted austenite (aging temperature = 575 °C).

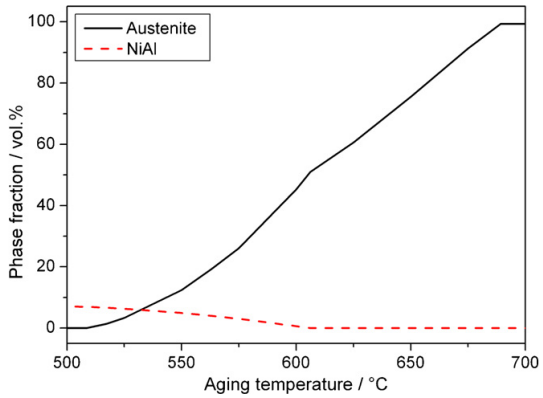

Fig. 11. Calculated equilibrium phase fractions of reverted austenite and bcc-B2 NiAl.

very beginning of aging. Thus, the simulations indicate that the formation of precipitates and reverted austenite occurs widely independent of each other. The formation of both, austenite and NiAl nuclei, is thermodynamically possible in the virgin martensitic matrix. Thus, dissolution of precipitates is not necessarily the initial driving factor for the formation of reverted austenite.

If the formation of reverted austenite is diffusion controlled, its activation energy can be determined based on an equation of Arrhenius type:

$$\ln(t) = Q/RT + \text{constant} \quad (1)$$

In Eq. (1), t is the time to attain a fixed amount of reverted austenite at a specific temperature T, R is the universal gas constant and Q is the activation energy.

As the equilibrium phase fraction of reverted austenite strongly depends on the applied aging temperature, which can be seen in Fig. 11 showing the results from thermodynamic simulations, aging experiments had to be conducted. In this study, the time necessary to achieve 20% of the equilibrium amount of austenite at each temperature was determined. The results are presented in Fig. 12 and it can be seen that the data fit well to a straight line. Based on this analysis, an activation energy of $234 \pm 20\,\mathrm{kJ\,mol^{-1}}$ was obtained. Slightly different values for the activation energy for the formation of reverted austenite were reported by Nakagawa et al. [41] and Sinha et al. [17]. They found an activation energy of about $250\,\mathrm{kJ\,mol^{-1}}$, which is in the range of the activation energy for diffusion of Ni in pure iron [42]. Calculation of the activation energy for the diffusion of Ni atoms in a PH13-8 Mo steel based on the mobility database 'mc_sample_fe' yielded $213\,\mathrm{kJ\,mol^{-1}}$, which is in the range of the measured one. The calculated activation energy for diffusion of Al atoms in a PH 13-8 Mo steel is $218\,\mathrm{kJ\,mol^{-1}}$, which is nearly the same as for the diffusion of Ni atoms. Therefore, it is concluded that diffusion of both elements is decisive for the growth of reverted austenite.

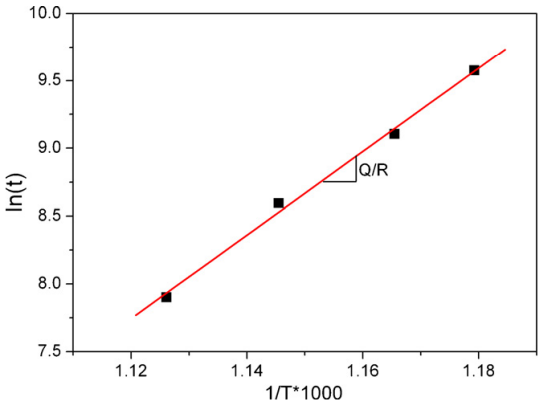

Fig. 12. Arrhenius plot used for determination of the activation energy for austenite formation.

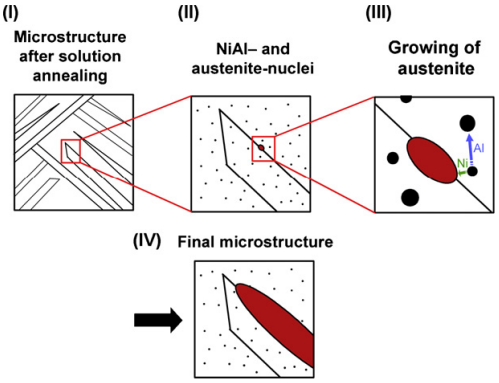

Fig. 13. Proposed model for the formation of reverted austenite.

Based on the experimental results and the simulations, the following sequence of mechanisms is proposed for the formation of reverted austenite. Fig. 13 shows a schematic drawing of the proposed mechanism, describing the four different stages of the model as follows:

(I) The initial microstructure, i.e. after quenching from the solution-annealed state, consists of lath martensite with high dislocation density.
(II) From the very beginning of aging, NiAl precipitates nucleate homogeneously in the martensitic matrix. Austenite forms preferentially on prior austenite grain boundaries or on martensite lath boundaries. However, in this stage, the formation of precipitates and reverted austenite occur independent

of each other. The formation of both austenite and NiAl nuclei is thermodynamically possible.

(III) Growth of reverted austenite on prolonged aging leads to dissolution of adjacent NiAl precipitates. Ni stemming from the dissolved precipitates diffuses to reverted austenite and promotes its further growth. In contrast, Al, which has a higher diffusion coefficient than Ni, is assumed to diffuse to precipitates inside the martensitic matrix, as the Al content in the precipitates increases significantly during aging. The Al content in the austenite is approximately the same as in the matrix. A clear evidence for the dissolution of precipitates is, that reverted austenite is completely free of NiAl precipitates. Since, after short aging times, the same areas are full of homogenously and densely distributed precipitates, the conclusion is drawn that the NiAl precipitates dissolve during aging when reverted austenite grows.

(IV) The final microstructure consists of a martensitic matrix with bcc-B2-ordered NiAl precipitates and a significant amount of reverted austenite.

5. Conclusions

The characterization of reverted austenite by TEM and APT and the investigations of its formation mechanism lead to the following conclusions:

(1) Matrix austenite and lath-like austenite were observed in the investigated PH 13-8 Mo maraging steel during aging at 575 °C. The fraction of the lath-like austenite increases during aging and it represents the dominant morphology after aging for 100 h.

(2) The size of reverted austenite at 575 °C after short aging times is in the range of a few hundred nanometers. The lath-like austenite has a preferred growth direction, which is parallel to the martensite lath boundaries.

(3) TEM and APT showed that reverted austenite is enriched in Ni, which stabilizes austenite. Mo- and Cr-rich carbides were observed inside and next to the austenitic areas.

(4) Reverted austenite is completely free of NiAl precipitates.

(5) Thermodynamic and kinetic simulations of NiAl precipitation and reverted austenite formation showed good accordance with experimental values. Furthermore, simulations have revealed that the precipitation of NiAl and the formation of reverted austenite take place simultaneously and independently. Dissolution of precipitates is not a necessary premise for the formation of reverted austenite.

(6) The activation energy for the formation of reverted austenite was found to be $234 \pm 20\,\mathrm{kJ\,mol^{-1}}$, which is in the range of the calculated activation energies for diffusion of Al and Ni atoms in PH 13-8 Mo alloys.

(7) Growth of reverted austenite on prolonged aging leads to dissolution of adjacent NiAl precipitates. Ni from the precipitates diffuses towards the reverted austenite and promotes its growth. In contrast, the Al content in the austenite is approximately the same as in the matrix. Therefore, Al, which has a higher diffusion coefficient in Fe than Ni, is assumed to diffuse to precipitates inside the martensitic matrix, as the Al content in the precipitates increases significant during aging.

References

[1] C.G. Bieber, Met. Prog. 78 (1960) 99–100.
[2] R.F. Decker, S. Floreen, in: R.K. Wilson (Ed.), Maraging Steels: Recent Developments and Applications, TMS, Warrendale, PA, USA, 1988, pp. 1–38.
[3] E.L. AuBuchon, R.V. London, Met. Prog. 119 (1981) 35–37.
[4] V. Seetharaman, M. Sundararaman, R. Krishnan, Mater. Sci. Eng. 47 (1981) 1–11.
[5] L.W. Tsay, H.H. Chen, M.F. Chiang, C. Chen, Corros. Sci. 49 (2007) 2461–2473.
[6] D.H. Ping, M. Ohnuma, Y. Hirakawa, Y. Kadoya, K. Hono, Mater. Sci. Eng. A 394 (2005) 285–295.
[7] Z. Guo, W. Sha, D. Vaumousse, Acta Mater. 51 (2003) 101–116.
[8] J. Mittra, G.K. Dey, D. Sen, A.K. Patra, S. Mazumder, P.K. De, Scripta Mater. 51 (2004) 349–353.
[9] J.-M. Cloue, B. Viguier, E. Andrieu, Metall. Mater. Trans. 36 A (2005) 2633–2639.
[10] W. Sha, A. Cerezo, G.D.W. Smith, Metall. Trans. 24 A (1993) 1221–1256.
[11] P.W. Hochanadel, C.V. Robino, G.R. Edwards, M.J. Cieslak, Metall. Mater. Trans. 25 A (1994) 789–798.
[12] M. Hättestrand, J.-O. Nilsson, K. Stiller, P. Liu, M. Andersson, Acta Mater. 52 (2004) 1023–1037.
[13] K. Liu, Y. Shan, Z. Yang, J. Liang, L. Lu, K. Yang, J. Mater. Sci. Technol. 23 (2007) 312–318.
[14] S. Hossein Nedjad, S. Meimandi, A. Mahmoudi, T. Abedi, S. Yazdani, H. Shirazi, M. Nili Ahmadabadi, Mater. Sci. Eng. A 501 (2004) 182–187.
[15] D.T. Peters, Trans. ASM 61 (1968) 62–74.
[16] L.T. Shiang, M. Wayman, Metallography 21 (1988) 425–451.
[17] P.P. Sinha, D. Sivakumar, N.S. Babu, K.T. Tharian, A. Natarajan, Steel Res. 66 (1995) 490–494.
[18] J.M. Pardal, S.S.M. Tavares, M.P.C. Fonseca, H.F.G. Abreu, J.J.M. Silva, J. Mater. Sci. 41 (2006) 2301–2307.
[19] N.D. Zemtsova, I.G. Kabanova, E.I. Anufrieva, Phys. Met. Metall. 105 (2008) 19–35.
[20] J.M. Pardal, S.S.M. Tavares, M.P.C. Fonseca, Proceedings of the Conference on New Developments on Metallurgy and Applications of High Strength Steels, Buenos Aires, Argentinia, 2008, pp. 1327–1336.
[21] U.K. Viswanathan, G.K. Dey, V. Sethumadhavan, Mater. Sci. Eng. A 398 (2005) 367–372.
[22] S.J. Kim, C.M. Wayman, Mater. Sci. Eng. A 128 (1990) 217–230.
[23] X. Li, Z. Yin, Mater. Lett. 24 (1995) 239–242.
[24] N. Atsmon, A. Rosen, Metallography 14 (1981) 163–167.
[25] U.K. Viswanathan, G.K. Dey, M.K. Asundi, Metall. Trans. 24 A (1993) 2429–2442.
[26] U.K. Viswanathan, S. Banerjee, R. Krishnan, Mater. Sci. Eng. A 104 (1988) 181–189.
[27] V.I. Zel'dovich, N.Y. Frolova, Phys. Met. Metall. 69 (1990) 175–183.
[28] C.N. Hsiao, C.S. Chiou, J.R. Yang, Mater. Chem. Phys. 74 (2002) 134–142.
[29] S. Höring, D. Abou-Ras, N. Wanderka, H. Leitner, H. Clemens, J. Banhart, Steel Res. Int. 80 (2009) 84–88.
[30] M. Farooque, H. Ayub, A. Ul Haq, A.Q. Khan, J. Mater. Sci. 33 (1998) 2927–2930.
[31] G. Faninger, U. Hartmann, HTM 27 (1972) 233–244.
[32] M.K. Miller, A. Cerezo, M.G. Hetherington, G.D.W. Smith, Atom Probe Field Ion Microscopy, Clarendon Press, Oxford, 1996, pp. 476–481.
[33] J. Svoboda, F.D. Fischer, P. Fratzl, E. Kozeschnik, Mater. Sci. Eng. A 385 (2004) 166–174.
[34] E. Kozeschnik, J. Svoboda, P. Fratzl, F.D. Fischer, Mater. Sci. Eng. A 385 (2004) 157–165.
[35] E. Kozeschnik, J. Svoboda, F.D. Fischer, Calphad 28 (4) (2005) 379–382.
[36] Thermodynamic Database 'mc_steel', version 1.83, Institute of Materials Science and Technology, Vienna University of Technology.
[37] Mobility Database 'mc_sample_fe', version 1.03, Institute of Materials Science and Technology, Vienna University of Technology.
[38] E. Kozeschnik, J. Svoboda, F.D. Fischer, Mater. Sci. Eng. A 441 (2006) 68–72.
[39] B. Sonderegger, E. Kozeschnik, Metall. Mater. Trans. 40A (2009) 499–510.
[40] B. Sonderegger, E. Kozeschnik, Scripta Mater. 60 (8) (2009) 635–638.
[41] H. Nakagawa, T. Miyazaki, H. Yokota, J. Mater. Sci. 35 (2000) 2245–2253.
[42] H. Mehrer (Ed.), Londolt-Boernstein, Volume 26, Diffusion in Solid Metals and Alloys, Springer-Verlag, Berlin, 1990, p. 129.